Terahertz Spectroscopy of Charge-Carrier Dynamics in One-Dimensional Nanomaterials

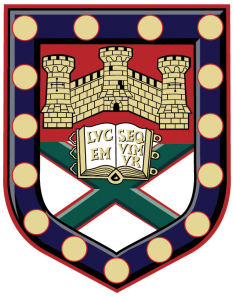

Peter Karlsen

School of Physics

University of Exeter

A thesis submitted for the degree of

Doctor of Philosophy

February 2018

Terahertz Spectroscopy of Charge-Carrier Dynamics in One-Dimensional Nanomaterials

Submitted by Peter Karlsen to the University of Exeter as a thesis for the degree of Doctor of Philosophy in Physics
February 2018

This thesis is available for Library use on the understanding that it is copyright material and that no quotation from the thesis may be published without proper acknowledgement.

I certify that all material in this thesis which is not my own work has been identified and that no material has previously been submitted and approved for the award of a degree by this or any other University.

(Signature).....

Peter Karlsen
February 2018

Jeg vil gerne dedikere denne PhD-afhandling til de følgende personer:

Til mine forældre, Aksel Karlsen og Lene Graversen, til mine bedsteforældre, Inger og Holger Graversen, til mine søskende, Anders og Pernille Karlsen: Uden jeres kærlighed og støtte var jeg ikke blevet den person jeg er idag. Til mine studie-venner fra min tid ved Aalborg Universitet, med hvem jeg har nydt mange gode stunder af videnskabelige og politiske diskussioner. Sidst, men ikke mindst, til min kæreste skat, Kimberly Bryan, for at have elsket og støttet mig gennem alle de hårde tider i løbet af denne PhD.

I would like to dedicate this thesis to the following people:

To my parents, Aksel Karlsen and Lene Graversen, my grandparents, Holger and Inger Graversen, and my siblings, Anders and Pernille Karlsen, without whom I would not be the man I am today. To my friends from Aalborg University, with whom I enjoyed countless hours of scientific and political discussions. Last, but not least, to my dearest Kimberly Bryan, for being my pillar of love and support throughout the ups and downs of doing this PhD.

Acknowledgements

First and foremost I would like to acknowledge my supervisors, Euan Hendry and Mikhail Portnoi, for giving me the opportunity to study at Exeter University. I give my thanks to Euan for his advice through the three years of this PhD, both in navigating an ultrafast laserlab and the world of academia in general. Thanks to my colleagues in the ultrafast laserlab, who helped me when various equipment broke down, who kept me company during the many hours working in the laser lab, and who took the time to chat with me in general.

Thanks to the NOTEDEV fellows in the Marie Curie initial training network. You gave me friendship when I needed it the most.

Thanks to my family and friends back in Denmark. To my parents, Aksel Karlsen and Lene Graversen, my grandparents, Holger and Inger Graversen, and my siblings, Anders and Pernille Karlsen, without whom I would not be the man I am today. To my friends from Aalborg University, with whom I enjoyed countless hours of scientific and political discussions.

Last, but not least, thanks to min kæreste skat, Kimberly Bryan, for being my pillar of love and support throughout the ups and downs of doing this PhD.

Collaborators

I would like to acknowledge the contributions of my collaborators to this thesis:

- In chapters 6 and 7, the WS_2 nanotubes (INT) were provided by Reshef Tenne at the Department of Materials and Interfaces, Weizmann Institute of Science, Israel. The *s*-, *m*-, *met*-, and *sem*-CNT films, as well as the *m*−CNT/INT composites were prepared by Dzmitry I. Yuko and Mikhail Shuba at the Institute for Nuclear Problems, Belarus State University. The *l*-CNT films were provided by Albert G. Nasibulin at the Skolkovo Institute of Science and Technology, Moscow, and Department of Applied Physics, Aalto University, Finland. The 99% semiconducting CNTs were provided by Patrizia Lamberti at the Department of Information and Electrical Engineering and Applied Mathematics, University of Salerno, Italy.

- In chapter 6, Chris Beckerleg (University of Exeter) assisted with the SEM measurements in figure 6.4. Mikhail Shuba provided the theoretical analysis of the CNTs in section 6.2, including the calculated conductivity spectra in figures 6.2 and 6.3. Furthermore, he and Dzmitry I. Yuko supplied the Raman spectra in figure 6.5; the broadband optical density and conductivity spectra in figures 6.6, 6.7, and 6.10; and the high temperature (>300 K) THz conductivity spectra in figure 6.9.

- In chapter 8, WO_x nanowire fabrication, preparation and structural characterisation described in section 8.2, was performed by Kunyapat Thummavichai, under supervision of Prof. Yanqiu Zhu, at the College of Engineering, University of Exeter.

The Mathematica and Matlab code used for performing the Transfer Matrix calculations in chapter 5 was initially adapted from the Mathematica code written by Steven Byrnes.

Finally I would like to acknowledge that the project that this thesis is based on has received funding from the European Unions Seventh Framework Programme for research, technological development and demonstration under grant agreement no 607521.

Abstract

One-dimensional (1D) nanomaterials are of great importance for a number of potential applications. However, in order to realize this potential a thorough understanding of the charge-carrier dynamics in these materials is required, since these largely determine the optoelectronic properties of the materials in question. This thesis investigates the charge-carrier dynamics of two 1D nanomaterials, single-walled carbon nanotubes (CNTs) and tungsten-oxide nanowires (WO_xNWs), with the goal of better understanding the nature of their optoelectronic responses, and how nanomaterial geometry and morphology influence these responses. We do this using terahertz time-domain spectroscopy (THz-TDS) and optical pump - terahertz probe time-domain spectroscopy (OPTP).

Firstly, we discuss how to properly analyse and interpret the data obtained from these experiments when measuring 1D nanomaterials. While the data obtained from THz-TDS is fairly straight-forward to analyse, OPTP experimental data can be far from trivial. Depending on the relative size of the sample geometry compared to the probe wavelength, various approximations can be used to simplify the extraction of their ultrafast response. We present a general method, based on the transfer matrix method, for evaluating the applicability of these approximations for a given multilayer structure, and show the limitations of the most commonly used approximations. We find that these approximations are only valid in extreme cases where the thickness of the sample is several orders of magnitude smaller or larger than the wavelength, which highlight the danger originating from improper use of these approximations.

We then move on to investigate how the charge-carrier dynamics of our CNTs is influenced by nanotube length and density. This is done through studying the nature of the broad THz resonance observed in finite-length CNTs, and how the nanotube length and density affects this resonance. We do this by measuring the conductivity spectra of thin films comprising bundled CNTs of different average lengths in the frequency range 0.3–1000 THz and temperature interval 10–530 K. From this we show that the observed temperature-induced changes in the terahertz conductivity spectra depend strongly on the average CNT length, with a conductivity around 1 THz that increases/decreases as the temperature increases for short-/long tubes. This behaviour originates from the temperature dependence of the electron scattering rate, which results in a subsequent broadening of the observed THz conductivity

peak at higher temperatures and a shift to lower frequencies for increasing CNT length. Finally, we show that the change in conductivity with temperature depends not only on tube length, but also varies with tube density. We record the effective conductivities of composite films comprising mixtures of WS_2 nanotubes and CNTs vs CNT density for frequencies in the range 0.3–1 THz, finding that the conductivity increases/decreases for low/high density films as the temperature increases. This effect arises due to the density dependence of the effective length of conducting pathways in the composite films, which again leads to a shift and temperature dependent broadening of the THz conductivity peak.

Next, we investigate the conflicting reports regarding the ultrafast photoconductive response of films of CNTs, which apparently exhibit photoconductivities that can vastly differ, even in sign. Here we observe explicitly that the THz photoconductivity of CNT films is a highly variable quantity which correlates with the length of the CNTs, while the specific type of CNT has little influence. Moreover, by comparing the photo-induced change in THz conductivity with heat-induced changes, we show that both occur primarily due to heat-generated modification of the Drude electron relaxation rate, resulting in a broadening of the plasmonic resonance present in finite-length metallic and doped semiconducting CNTs. This clarifies the nature of the photo-response of CNT films and demonstrates the need to carefully consider the geometry of the CNTs, specifically the length, when considering them for application in optoelectronic devices.

We then move on to consider our WO_xNWs. We measure the terahertz conductivity and photoconductivity spectra of thin films compromising tungsten-oxide (WO_x) nanowires of average diameters 4 nm and 100 nm, and oxygen deficiencies $WO_{2.72}$ and WO_3 using THz-TDS and OPTP. From this we present the first experimental evidence of a metal-to-insulator transition in WO_x nanowires, which occurs when the oxygen content is increased from $x = 2.72 \rightarrow 3$ and manifests itself as a massive drop in the THz conductivity due to a shift in the Fermi level from the conduction band down into the bandgap. Furthermore we present the first experimental measurements of the photoexcited charge-carrier dynamics of WO_x nanowires on a picosecond timescale and map the influence of oxygen-content and nanowire diameter. From this we show that the decay-dynamics of the nanowires is characterized by a fast decay of <1 ps, followed by slow decay of 3-10 ps, which we attribute to saturable carrier trapping at the surface of the nanowires.

Publications

This thesis is based on the following publications:

- **P. Karlsen** and E. Hendry.
  "Approximations used in the analysis of signals in pump-probe spectroscopy"
  (In preparation)

- **P. Karlsen**, M.V. Shuba, C Beckerleg, D.I. Yuko, P.P. Kuzhir, S.A. Maksimenko, V. Ksenevich, Ho Viet, A.G. Nasibulin, R. Tenne, and E. Hendry.
  "Influence of nanotube length and density on the plasmonic terahertz response of single-walled carbon nanotubes"
  Journal of Physics D: Applied Physics, vol. 51, no. 1, p. 14003, January 2018 (Special Issue on ultrafast spectroscopy: applications).

- **P. Karlsen**, M.V. Shuba, P.P. Kuzhir, A.G. Nasibulin, P. Lamberti, and E. Hendry.
  "Sign inversion in the terahertz photoconductivity of single-walled carbon nanotube films"
  Submitted to *Physical Review Letters*, January 2018.

- **P. Karlsen**, T. Thummavichai, Y. Zhu, and E. Hendry.
  "Influence of Diameter and Oxygen Content on the Terahertz Conductivity of Tungsten-Oxide Nanowires"
  (In preparation)

Contents

List of Figures

List of Abbreviations

$\Delta\tau$	Pump-probe delay time
ϵ	Complex permittivity
γ	Scattering rate
$\hbar$	Reduced Planck constant
λ	Wavelength
ν	Frequency
ω	Angular frequency
ϕ	Volume-fraction
σ	Complex conductivity
τ	Scattering/relaxation time
c	Speed of light in vacuum
d	Thickness
d_p	Penetration depth
E	Energy
e	Fundamental unit of electric charge
E_F	Fermi level
E_g	Bandgap
h	Planck constant

k	Wave-vector
n	Complex refractive index
t	Time
1D	One-dimensional
2D	Two-dimensional
3D	Three-dimensional
CNT	Carbon nanotube
CVD	Chemical vapour deposition
DC	Direct/static Current (i.e. 0 Hz)
DS	Drude-Smith
EM	Electromagnetic
EMT	Effective medium theory
EO	Electro-optic
HiPco	High-pressure carbon monoxide
INT	(Inorganic) WS_2 nanotube
IR	Infrared
K	Kelvin
NW	Nanowire
OPTP	Optical pump - terahertz probe time-domain spectroscopy
PCA	Photoconductive antenna
SEM	Scanning electron microscopy
THz	Terahertz
THz-TDS	Terahertz time-domain spectroscopy
TMM	Transfer matrix method

UV	Ultraviolet
VHS	Van-Hove Singularity
Vis	Visible
WO_xNW	Tungsten-oxide nanowire

Chapter 1

Introduction

Charge-carriers in semiconductors and metals provide the basis for a variety of important technologies, including computers, lasers, light emitting devices, gas-sensors and so on [15, 16]. There is a constant drive to reduce the physical size of these devices, which requires increasingly smaller building blocks in electronics. Nanomaterials with sizes well below 100 nm, such as nanotubes and nanowires, are ideal candidates for such building blocks. At the same time, these nanomaterials open up new avenues of research and potential applications due to their increased surface to volume ratio and exotic one-dimensional (1D) nature, leading to interesting and novel charge-carrier behaviour. As such, there is both a technological and fundamental interest in the properties of charge-carriers in nanostructured materials.

The common characteristic of any charge-carriers is that they all exhibit a distinct response in the low-frequency range of the electromagnetic spectrum, specifically for terahertz (THz) frequencies (1 THz $\sim$ 333 μm $\sim$ 1 ps $\sim$ 4.1 meV). The ability to probe charge-carriers in the terahertz frequency range therefore allows for detailed characterization through their distinct spectral signatures in the this range [15–17]. However, with the advancement of nanotechnologies and nanomaterials, the ability to characterize electrical properties in a non-contact fashion with sub-picosecond temporal resolution is increasingly necessary in the field of nanoscale electronics and optoelectronics, where it is very challenging, if not impossible, to use conventional probes. In this regard, terahertz time-domain spectroscopy (THz-TDS) constitutes a contact-free probe of the frequency-dependent dielectric properties of a material, which are determined by key parameters such as the carrier density and mobility. THz-TDS has been proven useful for investigating a multitude of different charge-carriers such as free charge plasmas [18], plasmons [19], excitons [20, 21], transient molecular dipoles [22], and phonons in crystalline solids [23].

One particular advantage of THz-TDS is the possibility to combine the approach with a

time-synchronized femtosecond excitation pulse, a technique known as optical pump - THz probe time-domain spectroscopy (OPTP). This makes the method well suited for the investigation of electronic charge transport under non-equilibrium conditions, particularly for nanomaterials [15, 16]. This allows THz spectroscopy to circumvent many of the constraints of conventional transport measurement techniques. From this much progress has been made in the past several decades in understanding the physics of elementary electronic excitations. OPTP not only allows for the characterization of charge-carriers under steady-state conditions, but is also ideally suited for non-equilibrium measurements: using a time-resolved THz spectroscopy setup, an optical pulse can be used to create charge-carriers and the subsequent evolution of charge-carriers can be monitored on the femtosecond time scale. In this way, one has direct access to the time scales and mechanisms of carrier cooling, trapping, and recombination, as well as the dynamics of formation of quasiparticles such as excitons and plasmons [15, 16]. As such, THz-TDS and OPTP are ideal tools for investigating the charge-carrier dynamics of 1D nanomaterials.

1.1 1D nanomaterials: Carbon nanotubes and Semiconductor Nanowires

Nanotubes and nanowires are structures with an significant aspect-ratio, typically with diameters less than 100 nm and lengths up to several hundred microns. This 1D nature allows for a number of novel device applications, and the ability to combine new materials and create atomically sharp interfaces without dislocations provides direct control of key properties, such as the density of states and electronic transitions, which are purely determined by the geometry of the nanomaterials, rather than material composition. The 1D nature of these materials also provides a platform to examine properties inaccessible in conventional planar semiconductors.

1.1.1 Single-Walled Carbon Nanotubes

A single-walled carbon nanotubes (CNT) can be imagined as a rolled-up sheet of graphene (a single layer of carbon atoms in a honeycomb structure), resulting in a hollow cylinder with a diameter of a few nanometers and a length that can range between hundreds of nanometers and micrometers [2, 3, 24]. The myriad of possible rolling directions and diameters give rise to a multitude of possible CNT configurations with different bandstructures and conductivities. CNTs are effectively one-dimensional structures due to their typical diameters of $1-2$ nm, as opposed to the two-dimensional nature of graphene, leading to a range of beneficial properties

in terms of their optoelectronic properties, such as strong exciton formation and ballistic conductivity at room temperature [3]. Since CNTs were first observed in 1991 in the carbon soot of graphite electrodes [25], a multitude of fabrication techniques have been developed [26, 27], and the optical and electronic properties of CNTs have been under intense investigation due to their fascinating physical properties and exciting potential for advanced applications [28–32]. Understanding the ultrafast dynamics of photoexcited charge-carriers in CNTs is critical due to their potential applications in photonics and optoelectronics [33–36]. For this reason, many groups have utilized time-resolved measurements to study the ultrafast response of CNTs due to optical photoexcitation, documenting, for example, the presence of excitons in photoexcited CNTs [37, 38, 38–42]. Yet despite this attention, much of the charge-carrier dynamics in CNTs still remain a mystery, particularly in THz frequency range.

1.1.2 Tungsten-Oxide Nanowires

Tungsten-oxide (WO_x, $2 < x < 3$) is a transition metal oxide made up of perovskite-like units with a wide band gap ranging from 2.62 eV to 3.25 eV. It is of great interest because of its nonstoichiometric properties, as the lattice can withstand a considerable amount of oxygen deficiency [43]. Only a partial loss of the WO_3 oxygen content is needed to affect its electronic band structure and increase its conductivity by a large amount [8, 44]. Fully oxidized WO_3 is a n-type semiconductor with an indirect bandgap E_g corresponding to the difference between the energy levels of the valence band, originating from filled O 2p orbitals, and the conduction band originating from empty W 5d orbitals [8, 45, 46]. Because of these properties, WO_x has been used in a number of practical applications such as smart windows [47], photocatalysts [48, 49], and gas/temperature sensors [50, 51], and much effort has been expended to synthesize 1D tungsten-oxide materials with various morphologies and phases using either physical or chemical routes [52–63]. Despite this, the study of tungsten-oxide's optoelectronic properties is fairly limited in the THz range, especially in terms of how the low dimensionality of the WO_x differs from its bulk counterpart.

1.2 This Thesis

The overall goal of this thesis is to investigate the charge-carrier dynamics of 1D-nanomaterials, specifically single-walled carbon nanotubes (CNTs) and tungsten-oxide nanowires (WO_xNWs), with the goal of better understanding the nature of their optoelectronic responses, and how nanomaterial geometry and morphology influences these responses. We do this using THz-TDS and OPTP, where we also discuss how to properly analyse and interpret the data

obtained from these experiments by considering the limitations of commonly used approximations for these types of experiments.

In **chapter 2** we introduce the fundamental principles of 1D nanomaterials, specifically the background theory relating to bandstructure and the conductivity models used to describe the THz response of our materials, as well as common scattering and recombination mechanisms of charge-carriers in these materials. **Chapter 3** gives an overview of the equipment and techniques used by our collaborators to fabricate and prepare the numerous CNT and WO_xNW thin-films investigated in later chapters. In **chapter 4** we present a detailed description of THz spectroscopy, where we discuss the different techniques used for THz generation and detection, as well as the two main spectroscopy techniques used in this thesis; terahertz time-domain spectroscopy (THz-TDS) and optical pump - THz probe spectroscopy (OPTP).

Chapter 5 discusses how to properly analyse the data obtained from THz-TDS and OPTP experiments. While the former is fairly straight-forward, the latter can be far from trivial. Depending on the relative size of the sample geometry compared to the probe wavelength, various approximations can be used to simplify the extraction of their ultrafast response. We present a general method, based on the transfer matrix method, for evaluating the applicability of these approximations for a given multilayer structure, and show the limitations of the most commonly used approximations. We find that these approximations are only valid in extreme cases where the thickness of the sample is several orders of magnitude smaller or larger than the wavelength, which highlight the danger originating from improper use of these approximations.

In **chapter 6** we investigate the nature of the broad THz resonance observed in finite-length CNTs, specifically the influence of nanotube length and density. We do this by measuring the conductivity spectra of thin films comprising bundled CNTs of different average lengths in the frequency range 0.3–1000 THz and temperature interval 10–530 K. From this we show that the observed temperature-induced changes in the terahertz conductivity spectra depend strongly on the average CNT length, with a conductivity around 1 THz that increases/decreases as the temperature increases for short/long tubes. This behaviour originates from the temperature dependence of the electron scattering rate, which results in a subsequent broadening of the observed THz conductivity peak at higher temperatures and a shift to lower frequencies for increasing CNT length. Finally, we show that the change in conductivity with temperature depends not only on tube length, but also varies with tube density. We record the effective conductivities of composite films comprising mixtures of WS_2 nanotubes and CNTs vs CNT density for frequencies in the range 0.3–1 THz, finding that the conductivity increases/decreases for low/high density films as the temperature increases.

This effect arises due to the density dependence of the effective length of conducting pathways in the composite films, which again leads to a shift and temperature dependent broadening of the THz conductivity peak.

In **chapter 7** we investigate the conflicting reports regarding the ultrafast photoconductive response of films of CNTs, which apparently exhibit photoconductivities that can differ vastly, even in sign. Here, we observe explicitly that the THz photoconductivity of CNT films is a highly variable quantity which correlates with the length of the CNTs, while the specific type of CNT has little influence. Moreover, by comparing the photo-induced change in THz conductivity with heat-induced changes, we show that both occur primarily due to heat-generated modification of the Drude electron relaxation rate, resulting in a broadening of the plasmonic resonance present in finite-length metallic and doped semiconducting CNTs. This clarifies the nature of the photo-response of CNT films and demonstrates the need to carefully consider the geometry of the CNTs, specifically the length, when considering them for application in optoelectronic devices.

In **chapter 8** we measure the terahertz conductivity and photoconductivity spectra of thin films compromising tungsten-oxide (WO_x) nanowires of average diameters 4 nm and 100 nm, and oxygen deficiencies $WO_{2.72}$ and WO_3 using THz-TDS and OPTP. From this we present the first experimental evidence of a metal-to-insulator transition in WO_x nanowires, which occurs when the oxygen content is increased from $x = 2.72 \rightarrow 3$ and manifests itself as a massive drop in the THz conductivity due to a shift in the Fermi level from the conduction band down into the bandgap. Furthermore we present the first experimental measurements of the photoexcited charge-carrier dynamics of WO_x nanowires on a picosecond timescale and map the influence of oxygen-content and nanowire diameter. From this we show that the decay-dynamics of the nanowires is characterized by a fast decay of <1 ps, followed by slow decay of 3-10 ps, which we attribute to saturable carrier trapping at the surface of the nanowires.

Finally, the conclusions and potential for future work can be found in chapter 9, where we summarize the work done in this thesis and give an outlook on future studies into the charge-carrier dynamics of CNTs and WO_xNWs.

Chapter 2

Fundamental Principles of 1D Nanomaterials

This chapter introduces the fundamental principles of 1D nanomaterials, specifically the background theory relating to bandstructure and conductivity models, as well as common scattering and recombination mechanisms of charge-carriers in these materials. We then introduce the fundamental optoelectronic properties of the two materials of interest in this thesis; single-walled carbon nanotubes (CNTs) and tungsten-oxide nanowires (WO_xNWs).

2.1 Electronic Structure of Materials

In the quantum mechanical picture, the wave nature of the electron gives rise to specific electronic states, each characterized by a specific wavelength, which depends on the electron's energy (E) and wave-vector ($k = p/\hbar$), where p is the momentum and $\hbar = 1.055 \times 10^{-34}$ J/s is the reduced Planck constant. In a crystal, these electron waves can interact with the periodic lattice potential, causing the waves to interfere either constructively or destructively. The states where the forward travelling electron wave is completely cancelled out by destructive interference are referred to as (band) gap states, since the wave is essentially forbidden from propagating through the crystal.

According to the Pauli exclusion principle, each electron state can only be occupied by one electron at any one time, leading to a build up of occupied states with increasing energy (see figure 2.1). Here the Fermi energy E_F indicates the energy of highest occupied state in the bandstructure at 0 K. Solid materials are broadly classified as either metals, semiconductors, or insulators, which is determined by the location of the Fermi level and whether or not a band-gap is present. Away from the band-gap energies, the density of states is very high,

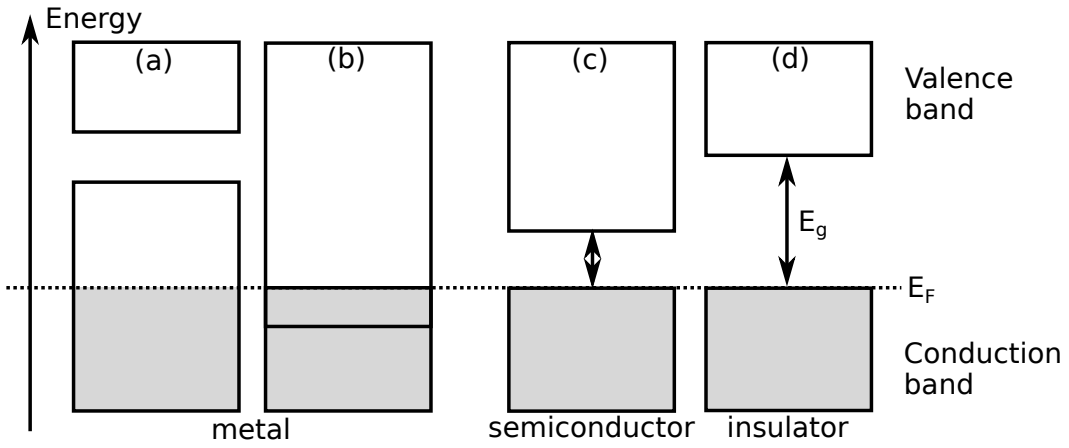

Figure 2.1: Possible energy band diagrams of a solid. Solids are broadly classified as either **(a)**-**(b)** metals, **(c)** semiconductors, or **(d)** insulators. The Fermi level (E_F) indicates the energy of the highest occupied state in the bandstructure at 0 K. A metal appears as either a half filled band, or two overlapping bands, while a semiconductor and insulator appear as a full (valence) band and empty (conduction) band, separated by a bandgap. The size of the bandgap E_g determines whether the material is considered a semiconductor or an insulator.

and can be approximated by a continuum. A metal appears as either a half filled band, or two overlapping bands, where the electrons are free to transition to nearby states and thus can contribute to the material conductivity. On the other hand, a pure semiconductor and insulator appear as a full (valence) band and empty (conduction) band, separated by a band-gap. The size of the band-gap determines whether the material is considered a semiconductor or an insulator: A rule of thumb is $E_g < 2$ eV for a semiconductor and $E_g > 2$ eV for an insulator, although this definition is somewhat arbitrary. Furthermore, the band-gap can be classified as either direct or indirect, depending on the location of the conduction- and valence-band edges with respect to each other. In the former case, both edges are situated at the same k-value, while the opposite is true in the latter. Whether the band-gap is direct or indirect has a strong effect on the photon absorption and emission properties of the material.

In any case the electrons in the valence band have no available states to transition into, and so they cannot contribute to the material conductivity. Thus the dark conductivity (i.e. the conductivity in the absence of light) is effectively zero for pure semiconductors and insulators. Only by receiving enough energy to transition across the band-gap can the electrons contribute to the material conductivity, for example by absorbing an incident photon. These transitions are commonly known as “interband transitions”, while transitions within the same band are known as “intraband transitions”. Photoexciting a semiconductor (or insulator) with photons of energy (E_{ph}) larger than E_g can generate excited mobile

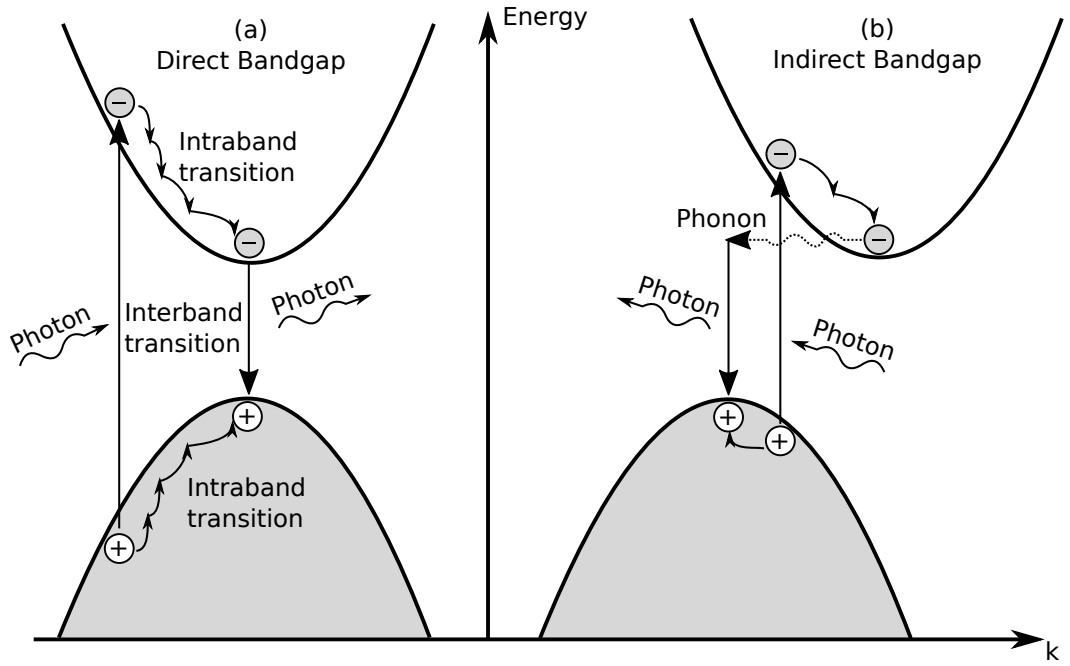

Figure 2.2: Diagram of the typical photoexcited charge-carrier evolution in a **(a)** direct and **(b)** indirect band-gap material plotted vs energy and wave-vector, k. An incident photon is absorbed by an electron in the valence band of the material, thereby creating an electron-hole pair and promoting the electron to the conduction band via an interband transition. The electron and hole proceed to relax to the bottom of the conduction band and top of the valence band, respectively, via a series of intraband transitions, typically enabled by electron-phonon scattering. Finally the electron-hole pair recombine across the band-gap under emission of a photon with an energy corresponding to the bandgap. In case of the indirect band-gap material, the electron must additionally receive a change in wave-vector, typically via an electron-phonon scattering event.

electrons in the conduction band, and can increase the conductivity by orders of magnitude. Here, the vacancy left by the electron is also mobile, and is referred to as a hole, which can effectively be considered a positively charged electron. As shown in figure 2.2, these initially "hot" charge-carriers then proceed to "cool" (i.e. relax) within their respective bands through carrier-carrier and carrier-phonon scattering before recombining across the band-gap at the edges of the conduction and valence bands, which typically occurs on the order of picoseconds [15].

Finally it is important to note that just above or below the bandgap, these mobile electrons and holes no longer behave as in a vacuum, as the electron and hole wavefunctions experience interference due to their interaction with the periodic lattice. To address this, an effective mass m^* is introduced, which describes the mass that an electron or hole appears to have

when moving through a crystal. As the wavelength of an electron in the conduction band differs slightly from that of a hole in the valence band, the wave interference often results in a larger effective mass for holes than for electrons. The size of this effective mass has a direct effect on the mobility of the particle through the material. For example, as holes are often much heavier than electrons, they move more slowly through the material and thereby possess a lower mobility. The electron and hole effective masses also vary from material to material, as they are purely dependent on the electronic bandstructure and material crystal structure. This leads to an inherent difference in mobilities for different semiconducting materials, with a limit placed on the mobility dependent on the material's crystal structure.

2.2 Charge-Carriers and Quasiparticles

Throughout the history of material science, a wide range of different charge-carriers and quasi-particles have been discovered. Each type of particle has its own unique properties in terms of the interaction with the crystal lattice, which in turn determines the optoelectronic properties of that material [64]. In this section we briefly introduce the charge-carriers and quasiparticles that are commonly found in 1D nanomaterials.

2.2.1 Free Electrons and Holes

As mentioned in section 2.1, mobile electrons can be introduced into the conduction band via photoexcitation or doping of the material. For the case of photoexcitation, the excited electron leaves behind a vacancy or "gap" state in the valence band, which can also become mobile. This "gap" state acts like a positively charged electron, forming a quasi-particle, which is referred to as a "hole", see figure 2.2. Both the electron and hole has an associated effective mass m^*, which is determined by the material. Free electrons and holes move independently of each other and the ions in the lattice, and can contribute to a conductivity until they recombine at some later time, with scattering via the lattice (i.e. phonons, impurities, defects, surfaces and so on) being the main limiting factors on mobility of the carriers. Mechanisms such as electron-electron scattering and the mutual coulomb interaction between the electron-hole pair do not have a significant effect on the carriers.

2.2.2 Plasmons

A plasmon is the quantization of the collective oscillations of the electron density in a material, much like a photon is a quantization of the oscillating electric field. As such, plasmons only occur in materials with a significant presence of free electrons. They arise due to the restoring

force experienced by electrons from the positively charged ions in the lattice, as the electrons are displaced from their rest position in the lattice under the application of an electric field. As a result, the electrons oscillate back and forth within the material at a frequency labelled the plasma frequency, ω_p. The value of this plasma frequency largely determines a material's optical properties in a given frequency range. Surface plasmons are a subset of plasmons that are localized at the interface between two materials. Localized surface plasmons (LSPs) are a common occurrence in nanomaterials with a significant charge-carrier concentration, such as metal spheres or wires, or photoexcited semiconductor nanomaterials. Here the confined nature of such systems lead to a build-up of charges at the boundaries of the material which then proceed to oscillate with a resonance frequency determined by the dimensions of the nanomaterial and the charge-carrier density.

2.2.3 Phonons

Phonons are the quantization of the lattice vibrations in a material. The displacement of atoms from their equilibrium positions produces lattice waves within the crystal, for which the wave amplitude is equal to the magnitude of the displacement. For crystals with at least two atoms in a unit cell ($N \geq 2$), there are two types of phonon modes: acoustic and optical, as shown in figure 2.3. In the optical mode, two adjacent atoms move in the opposite direction to each other, whereas in the acoustic mode, they move together. For crystals with $N \geq 2$, there are two transverse acoustic modes, one longitudinal acoustic mode and $3N - 3$ optical modes. Mobile charge-carriers can interact or "scatter" off these modes, causing a decrease in carrier mobility. In terms of the bandstructure of materials, phonon-scattering can mediate the intraband transitions of charge-carriers, for example when initially "hot" photoexcited electrons thermalize with the surrounding lattice and relax to the bottom of their respective bands.

2.2.4 Excitons

The behaviour of electrons, holes, and ions in the lattice is largely determined by their mutual Coulomb interactions. In many materials, this Coulomb interaction between electrons and holes is strong enough to create an "exciton", a bound electron-hole pair with a binding energy of E_b and an average electron-hole separation distance labelled the "exciton Bohr radius" (r_B), see figure 2.4a. Depending on the strength of the electron-hole interaction, excitons can be treated in two limiting cases [65]: Frenkel excitons, where r_B is smaller than the lattice constant, and Mott-Wannier excitons, where r_B is greater than the lattice constant. Mott-Wannier excitons are usually created in polarisable lattices with a high permittivity,

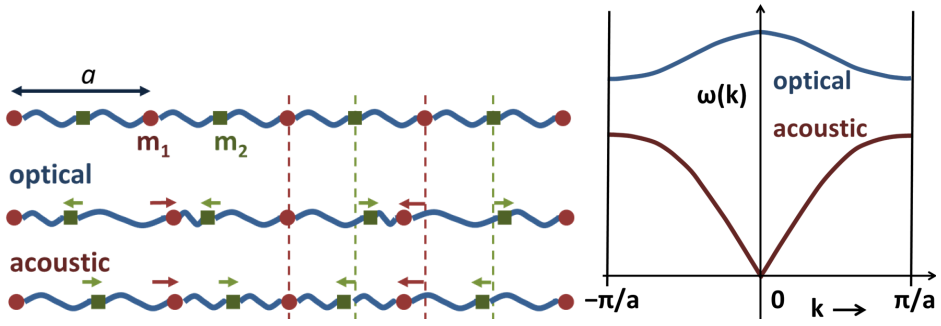

(a) (b)

Figure 2.3: **(a)** Schematic diagram of atomic displacements in the lattice for optical and acoustic modes. **(b)** Corresponding dispersion curves of the angular frequency $\omega(k) = E(k)/\hbar$ against k for optical and acoustic modes. Image source: https://en.wikipedia.org/wiki/Phonon

as the electron-hole attraction is screened, resulting in an exciton binding energy that is typically less than 0.1 eV. In this case r_B tends to extend over several unit cells and therefore the effect of the lattice potential creates a low exciton effective mass. In contrast, Frenkel excitons form in materials with low permittivity that are not easily polarised. Here they have high exciton binding energies and r_B is on the order of the crystal lattice spacing. Excitons are in many ways similar to atoms in the sense that they also form discrete energy states defined by the size of E_b. For strongly bound excitons, discrete energy levels with large energy level spacing are observed, while weakly bound excitons have far denser energy levels, to the point where there is no longer any electron-hole coupling and the electron-hole pair is essentially free. In terms of the material bandstructure, the exciton states appear below the conduction band due to the additional electron-hole binding energy, with the energy level of the lowest exciton state E_x defined by $E_x = E_g - E_b$, see figure 2.4b.

Excitons in nanoscale systems are formed by light absorption in molecules such as polyacenes and polyenes, conjugated polymers, quantum dots, molecular aggregates, carbon nanotubes and so on. In bulk semiconductors, E_b is usually comparable to or much smaller than the energy at room temperature (∼26 meV), and it is difficult to observe distinct excitonic optical transition peaks at room temperature. However, in 1D nanomaterials such as CNTs, significantly large binding energies of approximately 500 meV have been observed experimentally [38], owing to the exotic 1D nature of these systems. Furthermore, the physical size and shape of a nanomaterial strongly influences the nature and dynamics of the exciton. Therefore, a unique property of excitons in nanoscale systems is that the exciton size is dictated not by the electron-hole Coulomb interaction, but by the physical dimensions of the material.

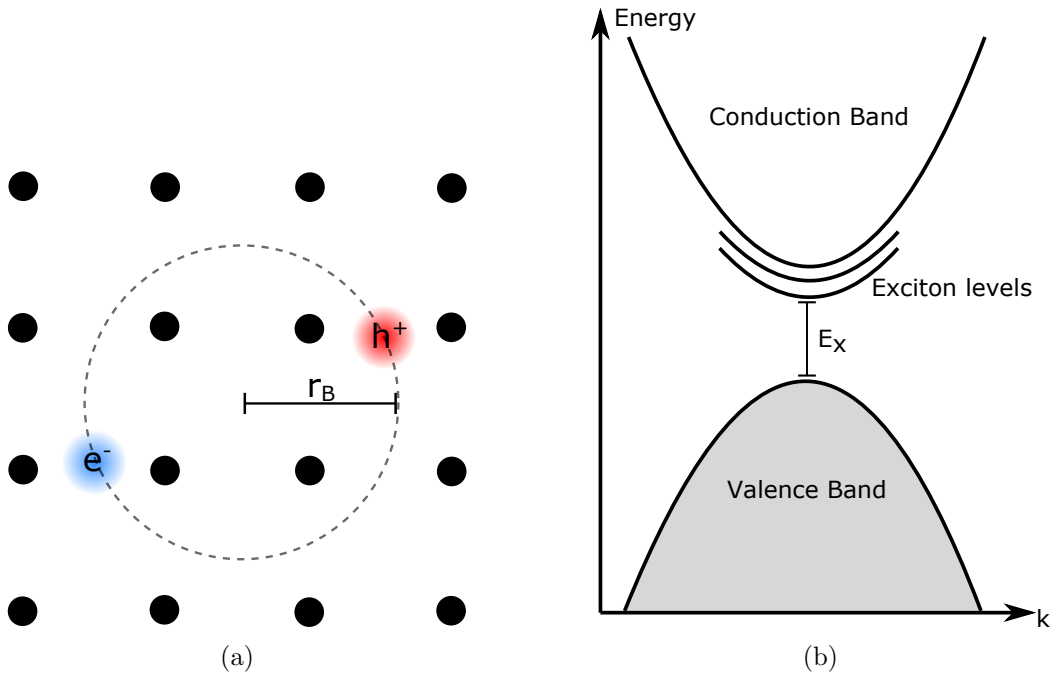

Figure 2.4: **(a)** Schematic of an exciton. The electron and hole are bound together by their mutual Coulomb interaction, with the strength of this interaction determining the type of exciton. As a rule of thumb, if their separation distance (r_B), a.k.a. the exciton Bohr radius, is smaller than the lattice constant, it is considered a Frenkel exciton, while if r_B is larger than the lattice constant, it is considered a Mott-Wannier exciton. **(b)** Schematic of the exciton states in the semiconductor bandstructure. The lowest energy exciton state is defined by $E_x = E_g - E_b$.

2.2.5 Polarons

Polarons are quasi-particles that form in highly polarisable semiconductors where the ions of the lattice can no longer be considered rigid in their position. In this case the Coulomb interactions between the electrons and the charged ions will deform the lattice around the electron, pushing away negative ions and attracting positive ions as shown in figure 2.5. This lattice deformation essentially forms a local potential well around the electron as it propagates through the material, increasing its effective mass. This electron dressed with lattice deformations is known as a "polaron". As with excitons, one typically distinguishes between small and large polarons, depending on the strength of the coupling between the electron and lattice. When the coupling-strength is weak, large polarons with spatially extended wavefunctions are formed, which propagate more or less like free carriers, but with increased effective mass. When the coupling-strength is strong, small polarons are formed, in which the

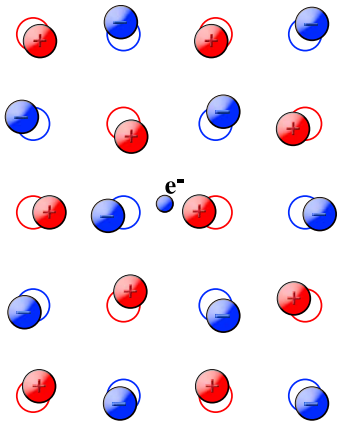

Figure 2.5: Schematic of a polaron. Due to the polarizability of the lattice, the electron attracts/repels positively/negatively charged ions, respectively, resulting in an increased effective mass of the electron. Image source: https://en.wikipedia.org/wiki/Polaron.

electron is essentially trapped within the potential well formed by the lattice deformation. In this case, charge transport only occurs via tunnelling or hopping between lattice sites.

2.3 Fundamental Models of Matter

The fundamental goal of THz spectroscopy is to measure the response of a material to an applied electric field. This is quantified in terms of the complex conductivity $\sigma(\omega)$, which relates the applied electric field $E(\omega)$ to the current density $J(\omega)$:

$$J(\omega) = \sigma(\omega)E(\omega), \tag{2.1}$$

where $\omega = 2\pi\nu$ is the angular frequency, and ν is the frequency. The conductivity is a complex and frequency-dependent value, i.e. $\sigma(\omega) = \sigma_r(\omega) + i\sigma_i(\omega)$, where the real part relates to the resistance experienced by a charge-carrier in the material, and the imaginary part relates to the reactance of the material. Another equivalent way of representing the dielectric response of a material is via the complex refractive index $n(\omega)$ or the complex permittivity $\epsilon(\omega)$, which are related via the following equations:

$$n(\omega) = \sqrt{\epsilon(\omega)\mu(\omega)}, \tag{2.2}$$

$$\epsilon(\omega) = \epsilon_b + \frac{i\sigma(\omega)}{\omega\epsilon_0}, \tag{2.3}$$

where $\epsilon_0 = 8.85 \times 10^{-12} Fm^{-1}$ is the vacuum permittivity, ϵ_b is the background permittivity, and $\mu(\omega)$ is the permeability of the material. In this thesis we only work with non-magnetic materials, so $\mu = 1$. Note that we set $\epsilon_b = 1$ so that the σ in equation (2.3) contains contributions from the lattice, which some authors choose to write into ϵ_b instead. The real and imaginary part of the complex refractive index $n = n_r + i\kappa$ describes the classical refractive index $n_r = c/v_{phase}$ and the extinction coefficient κ, respectively, where c is the vacuum speed of light and v_{phase} is the phase velocity of light in the medium. Likewise, ϵ describes the polarizability of a material:

$$P(\omega) = (\epsilon(\omega) - \epsilon_0)\, E(\omega), \tag{2.4}$$

where $P(\omega)$ is the polarization of the material. Whether one uses n, ϵ or σ for describing the dielectric response of a material is a matter of preference, since the same information is contained in either one of them. In this thesis we mainly refer to the complex conductivity unless otherwise noted. The question is now how the microscopic behaviour of charge-carriers and quasi-particles can be related to the measurable macroscopic conductivity $\sigma(\omega)$.

2.3.1 The Drude Model

As mentioned in section 2.1, the motion of electrons in the quantum-mechanical picture is that of waves propagating through a periodic lattice potential, where the motion of the electrons is interrupted by scattering events caused by lattice vibrations, impurities, defects, grain boundaries, vacancies, surfaces, and any other deviation from a perfectly periodic lattice. These travelling waves provide the physical basis for conduction in the material. The motion of the electrons between scattering events is essentially free, subject only to external forces, usually applied electric or magnetic fields. A theory can then be developed that relates macroscopic and measurable quantities such as conductivity or mobility to the microscopic scattering processes. The simplest of these transport models is the so-called *Drude model*; a purely classical model based on the application of kinetic theory to a non-interacting electron gas. Principle in this theory is the concept of *mean free time* τ which is the average time between scattering events. Equivalently, $\gamma = \tau^{-1}$ is the *scattering rate*, i.e. the average probability per unit time that an electron is scattered.

There are two important velocity quantities that must be distinguished. The first is the *mean speed* u or *thermal velocity* v_{th} which, as the name implies, is the average speed of the electrons. u is quite large being on the order of $\sqrt{3k_BT/m^*} \approx 10^5$ m/s for electrons in a nondegenerate semiconductor and $\sqrt{2E_F/m^*} \approx 10^6$ m/s for electrons in a metal, where k_B is Boltzmann's constant, T is the temperature, E_F is the Fermi energy of the metal, and m^*

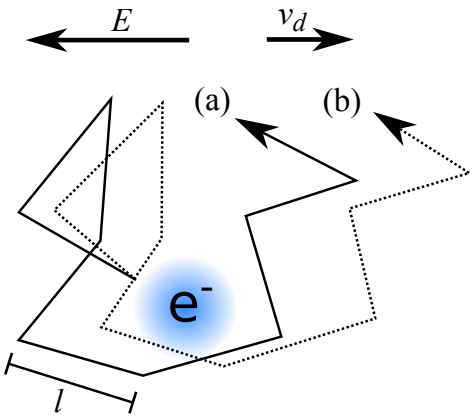

Figure 2.6: In the Drude model, the electron is considered free, only interacting with the lattice through elastic collisions with ions. In the absence of an electric field (solid line, (a)) the velocity of the electron remains constant in-between the momentum altering scattering events. The electron then follows a random walk through the lattice, described by a mean free path l. Since the scattering events are random, the time-averaged velocity is zero. In the presence of a static electric field E, the electrons are accelerated in-between the scattering events (dotted line, (b)) such that the time averaged velocity (drift-velocity $\boldsymbol{v}_d$) has a non-zero component in the opposite direction to the applied field.

is the electron effective mass. The distance an electron travels between scattering events is called the free path. It is straightforward to show that the average or *mean free path* for an electron is simply $l = u\tau$. The second velocity is the mean or *drift velocity* $\boldsymbol{v}_d$, which is simply the vector average over the velocities of all N electrons,

$$\boldsymbol{v}_d = \frac{1}{N}\sum_{i=1}^{N}\boldsymbol{v}_i. \tag{2.5}$$

With no external forces applied to the material, the electron motion is random and thus the drift velocity is zero. When subject to external forces like an electric field, the electrons acquire a net drift velocity as shown in figure 2.6. In most cases, the magnitude of the drift velocity is much smaller than u so that the mean speed of the electron is not affected to any practical extent by the external forces.

The drift velocity gives rise to an electric current. If the density of electrons is N then the current density $\boldsymbol{J}$ is

$$\boldsymbol{J} = -eN\boldsymbol{v}_d, \tag{2.6}$$

where $e = 1.602 \times 10^{-19}$ C is the fundamental unit of electric charge. For the case of an

applied electric field $\boldsymbol{E}$, the solutions of the semi-classical equations give a drift velocity that is proportional to $\boldsymbol{E}$. The proportionality constant is the *mobility* μ (not to be confused with the permeability mentioned earlier):

$$\boldsymbol{v}_d = -\mu \boldsymbol{E}. \tag{2.7}$$

The mobility might be a constant or it might depend on the applied field (usually only if the field is large). Ohm's Law defines the conductivity σ of a material as $\boldsymbol{J} = \sigma \boldsymbol{E}$, resulting in a simple relation to the mobility

$$\sigma = eN\mu. \tag{2.8}$$

As mentioned previously, the Drude model makes the simple assumption that the scattering randomizes the electron's velocity. The equation of motion for the drift velocity $\boldsymbol{v}_d$ then reduces to a simple form

$$\frac{d\boldsymbol{v}_d}{dt} + \frac{\boldsymbol{v}_d}{\tau} = \frac{\boldsymbol{F}(t)}{m^*}, \tag{2.9}$$

where $\boldsymbol{F}(t)$ is the sum of all external forces acting on the electrons. The effect of the scattering is to introduce a frictional term into what otherwise would be just Newton's Law. Solutions of equation (2.9) depend on $\boldsymbol{F}(t)$. In the simplest case of a constant applied electric field, the steady-state solution is trivial,

$$\boldsymbol{v}_d = -\mu \boldsymbol{E}. \tag{2.10}$$

The mobility and conductivity can then be related to the scattering time as

$$\mu = \frac{e\tau}{m^*} \qquad \text{and} \qquad \sigma = \frac{Ne^2\tau}{m^*}. \tag{2.11}$$

The carrier mobility is therefore directly proportional to the scattering time τ. If we assume a time-varying sinusoidal electric field $E = E_0 e^{-i\omega t}$, equation (2.9) has the following solution:

$$\boldsymbol{v}_d = -\frac{e\tau}{m^*} \frac{1}{1 - i\omega\tau} E_0 e^{-i\omega t}, \tag{2.12}$$

leading to

$$\mu(\omega) = -\frac{e\tau}{m^*}\frac{1}{1-i\omega\tau}, \tag{2.13}$$

$$\sigma(\omega) = \frac{\epsilon_0\omega_p^2\tau}{1-i\omega\tau}, \qquad \omega_p^2 = \frac{e^2N}{\epsilon_0 m^*}, \tag{2.14}$$

where ω_p is the plasma frequency, and ϵ_0 is the vacuum permittivity. It should be noted that the Drude model in its current form contain many simplifications, for example: (i) interactions between the electrons and lattice only occur via scattering, meaning it only applies for non-polarizable materials. (ii) electrons are considered to be independent of each other, which is not true for very high carrier densities, where electron-electron interactions become significant. (iii) the mass and scattering time of the electrons are considered to be independent of the velocity, and assumed to be isotropic. Because of these simplifications, the Drude model breaks down at high field strengths and for high carrier densities, but even so the model can fairly accurately explain a wide range of observations regarding the conductivity of metals and semiconductors. In the context of nanomaterials such as nanotubes and nanowires, the Drude model does not account for several transport phenomena that arises due to the finite nanoscale dimensions of these materials, such as backscattering of electrons at nanotube surfaces, surface depletion and accumulation fields at the boundaries, carrier localisation, and nanotube polarisability. Therefore, extensions to the Drude model are needed to accurately describe the nanomaterial conductivity response.

2.3.2 The Lorentzian Oscillator

The Drude response in equation 2.14 is a signature of free carriers, with the maximum of $\mathrm{Re}(\sigma)$ located at $\omega = 0$ and the maximum of $\mathrm{Im}(\sigma)$ located at $\omega = \gamma$, see figure 2.7. However, in most materials the observed conductivity response at THz frequencies is typically that of one or more resonances located at finite frequencies. The simplest resonance response is that of a Lorentzian centered at a resonance frequency ω_0:

$$\sigma(\omega) = \frac{-i\omega A}{\omega^2 - \omega_0^2 + i\omega\gamma}, \tag{2.15}$$

where A is the amplitude of the resonance and γ determines the width of the resonance. In this case the imaginary part of the conductivity is no longer purely positive, but starts negative for $\omega < \omega_0$ and becomes positive for $\omega > \omega_0$, as shown in figure 2.7. As such, the Drude response is simply a Lorentzian centered at zero frequency. The THz frequency regime covers many fundamental excitations including rotations, vibrations, and low-lying electronic

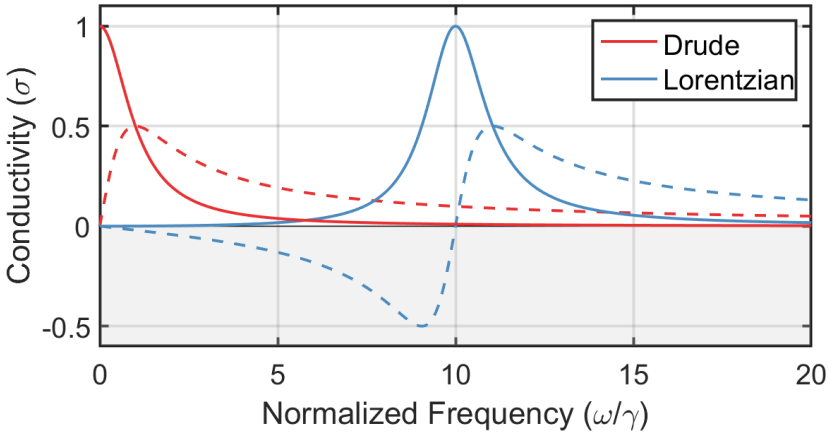

Figure 2.7: Conductivity plot of a Drude response and Lorentzian response, plotted against the normalized frequency (ω/γ). Full and dashed lines represent real and imaginary values, respectively. In this case, the Lorentzian response has a resonance frequency $\omega_0/\gamma = 10$. Note that the Drude response is simply a Lorentzian centered at zero frequency.

transitions in molecules and collective modes in condensed matter such as phonons, plasma, magnons, energy gaps associated with superconductivity, intraexcitonic transitions for excitons [15, 66–69]. A response with a resonance at finite frequencies also occurs for a number of other situations, including the effective medium-type response [70–72], the plasmon-type response [73], the Drude-Smith response [74], and the response associated with "dispersive" transport in percolating networks [1]. As it turns out, most of these responses can to a large extend be described as Lorentzian responses. For the rest of this section we will introduce some of the common material models used to describe the Lorentzian resonances observed in nanomaterials.

2.3.3 The Plasmon Model

The plasmon model is an extension to the Drude model, where it is assumed that the charge-carriers are subjected not only to an applied electromagnetic field but also to an electrostatic restoring force. This is achieved by adding a restoring force, $F(x) = m\omega_0^2 x$, to the equation of motion (2.9) (written here in terms of the displacement, x, of the charge-carrier):

$$\frac{d^2x}{dt^2} + \gamma\frac{dx}{dt} + \omega_0^2 x = \frac{eE}{m^*}. \tag{2.16}$$

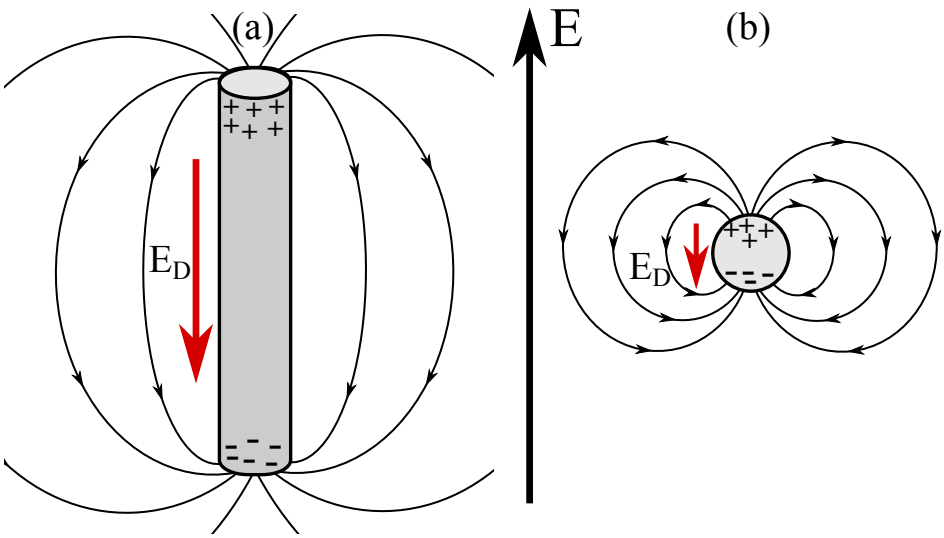

Figure 2.8: Schematic of a nanotube with an electric field E applied along the **(a)** long and **(b)** short axis of a nanotube. The applied field leads to a build-up of positive and negative charges in opposite ends, resulting in a depolarization field E_D that gives rise to the plasmon oscillation.

By solving this equation of motion, the plasmon response for the conductivity becomes:

$$\sigma = \frac{i\omega\omega_p^2}{\omega^2 - \omega_0^2 + i\omega\gamma}, \qquad \omega_p^2 = \frac{e^2 N}{\epsilon_0 m^*}. \tag{2.17}$$

where ω_0 denotes the plasmon resonance frequency, and γ is the scattering rate that defines the width of the resonance.

Applying an electric field to nanowires and nanotubes leads to build-up of positive charge on one side of the nanotube and a negative charge on the other side. This creates an electric dipole, as shown in figure 2.8, whose electric field, known as the depolarisation field (E_D), is in opposition to the applied electric field. In our plasmon model, the depolarisation field acts as the electrostatic restoring force, causing the carriers to undergo harmonic oscillation. The resonance frequency is linked to the plasma frequency by $\omega_0^2 = g^2\omega_p^2$, where g is a geometrical factor associated with the material geometry. Note that in this case the resonance frequency is expected to scale with the carrier density in the material as $\omega_0 \propto \sqrt{N}$. Because of this, the resonance frequencies of metallic nanostructures typically occur in the ultraviolet, visible and near-infrared ranges, while semiconductor nanostructures exhibit resonances in the THz range. However, this is only true for "normal" materials with a non-linear bandstructure near the Fermi level. In the case of a linear bandstructure, the dimensions of the material determines the proportionality between ω_p and N, such that $\omega_p \propto N^{1/3}$ for 3D (bulk) ma-

terials and $\omega_p \propto N^{1/4}$ for 2D materials such as graphene [75]. For 1D nanomaterials with a linear bandstructure such as carbon nanotubes, a curious phenoma occurs where the plasmon frequency is actually independent of N [75], which underlines the exotic nature of these materials, however we note that only a subset of carbon nanotubes (metallic CNTs) have a linear bandstructure.

2.3.4 Drude-Smith Model

The Drude-Smith model is another extension of the Drude model, which was developed to describe materials in which localisation and disorder disrupt long-range transport of carriers. While the Drude model only describes isotropic carrier scattering, the Drude-Smith model allows scattering in preferential directions. The conductivity is expressed as [74]:

$$\sigma_{DS} = \frac{Ne^2}{m^*} \frac{\tau_{DS}}{1 - i\omega\tau_{DS}} \times \left(1 + \sum_{j=1}^{\infty} \frac{c_j}{(1 - i\omega\tau_{DS})^j} \right), \tag{2.18}$$

where τ_{DS} is the Drude-Smith scattering time and c_j is the fraction of the carrier's initial velocity retained after the scattering event j. This c_j parameter is known as the persistence of velocity parameter and accounts for the anisotropy of carrier scattering. For completely isotropic Drude-like scattering, $c_j = 0$; for forward scattering, c_p is positive; and for backward scattering, c_j is negative, with $c_p \pm 1$ for complete forward and backward scattering, respectively. A key assumption of the model is that the persistence of velocity is retained for only one collision, i.e., only the first scattering event $j = 1$ is considered. While this approximation is quite primitive, the model can reproduce the negative imaginary component observed in nanomaterial conductivity spectra, giving a similar spectral shape to the Lorentzian response shown in figure 2.7, as seen for the plasmon model. Therefore, it has been widely applied in analysis of THz conductivity spectra of semiconductor nanowires and CNTs, with the fitted parameter c_1 generally yielding a negative value, indicating preferential backscattering of electrons at the nanowire surfaces. The c_1 parameter is often used to indicate a degree of localisation, with greater localisation giving a value closer to -1. However, it is important to note that the single-scattering approximation has no proper physical basis, since it assumes carrier scattering is only anisotropic for the first scattering event and is isotropic thereafter, which has lead to criticism of this model for analysis of nanostructure conductivity [76].

2.3.5 Beyond the Drude Model

Using the Drude model and its expanded variants described in the previous sections, it is possible to model and interpret the majority of observed nanomaterial responses in the THz range. Even so, it is important to recognize the limitations of these models, which are all based on classical mechanics. Quantum mechanical effects, such as a finite density of available states or an energy-dependent scattering rate, are not taken into account. Similarly, the Drude model is unable to describe strongly confined systems, where diffusive transport break down and carrier transport only occurs via hopping or tunnelling. Thus, if one wishes to go beyond the Drude model, the next step is to derive a conductivity expression from quantum-mechanical theories such as the Boltzmann transport equation or Linear response theory, which accounts for various quantum mechanical effects, see [16] for a description of these conductivity models in the context of THz spectroscopy and nanomaterials.

2.4 Charge-Carrier Scattering Mechanisms

In order to understand the optoelectronic properties of a material, in particular its conductive properties, one must understand the mechanisms that limit this conductivity. In general, the conduction electron, whether in a metal or in a semiconductor, can be scattered by a number of mechanisms such as lattice vibrations, impurities, lattice defects such as dislocations, grain boundaries, vacancies, surfaces, or any other deviation from a perfectly periodic lattice. Thankfully, the total scattering rate of a system can generally be written as a sum of the individual contributions (Matthiessen's Rule [77, 78]):

$$\gamma_{tot} = \sum_i \gamma_i, \tag{2.19}$$

where γ_i is the i'th scattering mechanism, making it possible to consider the individual contributions of each mechanism. In this section we briefly introduce each of these scattering mechanisms.

2.4.1 Phonon Scattering

Phonon scattering is catagorized by the phonon-modes involved in the scattering event, in most cases acoustic phonons and longitudinal optical (LO) phonons, see section 2.2.3.

For **longitudinal-optical phonons**, the out of phase vibrations of the lattice produce an effective dipole moment proportional to the bond polarity. For this reason optical phonon scattering is also known as *polar phonon scattering*, since the dipole moment can interact with

an incident electromagnetic field. Due to the polarization in polar semiconductor crystals induced by the optical vibration mode, the electrons are scattered through the interaction with the field of the lattice polarization waves. Since a sub-lattice is necessary for optical modes, this scattering mechanism is not present in elemental semiconductors such as Si, Ge, or diamond.

Acoustic phonon scattering comes from long wavelength oscillations in the crystal, involving small displacements of tens to thousands of atoms. The wavelength depends on the material and its elastic properties. Such modes are very similar to sound vibrations and are thus referred to as acoustic modes. The associated atomic displacements correspond to an effective built-in strain, with local change in the lattice potential causing carrier scattering known as *deformation potential acoustic phonon scattering*. Since the change in potential is relatively small, the scattering efficiency is relatively low compared with optical phonon scattering in bulk materials. However, in 1D nanomaterials both electrons and acoustic phonons experience confinement effects, leading to an increased electron-acoustic phonon interaction, as has been predicted for small rectangular ($\sim 5 \times 5$ nm) Si nanowires [79] and cylindrical GaAs nanowires [80]. As such, acoustic-phonon scattering is significantly stronger in 1D nanomaterials, and the anisotropy of some semiconductor materials can further have a strong influence on the acoustic phonon scattering rate, depending on the growth direction of the nanowires [81].

Finally it should be noted that the temperature dependency of the two scattering mechanisms is significantly different; LO-phonon scattering has been shown to grow exponentially with temperature $\gamma_{LO} \propto e^{-\hbar\omega_s/(kT)}$, where ω_s is the frequency of LO phonon mode s [82], while acoustic-phonon scattering generally scales with the temperature as $\gamma_{ac} \propto T^{3/2}$ [83]. As such, LO-phonon scattering tends to dominate at room temperature in bulk materials where these modes are present.

2.4.2 Impurity Scattering

As the name implies, this scattering occurs due to impurities and defects in the material, essentially anything that breaks the periodic structure of the lattice, whether they be charged ions from doping, or structural defects due to missing atoms in the crystal structure, see figure 2.9a. Impurities can either be neutral or charged/ionized. Impurities influence electron behaviour in two ways; they provide additional states in the bandstructure for the carriers to occupy, sometimes located in the bandgap, as well as contributing additional electrons/holes. They also scatter the charge-carriers, leading to changes in their motion under the influence of an electric field. Impurity scattering is present at all temperatures, but is most important

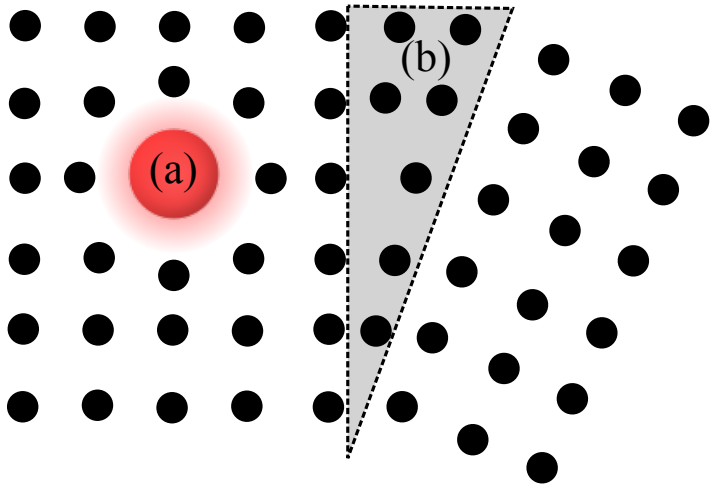

Figure 2.9: Schematic of a **(a)** Impurity and **(b)** interface (grain boundary) in a lattice structure, which break the periodic structure of the lattice and contribute to carrier scattering.

at low temperatures where phonon scattering is minimal. For sufficiently large doping levels, this regime may extend to room-temperature. For materials dominated by ionised impurity scattering, the mobility has been found to be proportional to $T^{3/2}/N_I$, where N_I is the density of ionised impurities [84, 85].

2.4.3 Interface and Surface Scattering

Surface or interface scattering is an elastic scattering process of the free charge-carriers with an imperfect interface or rough surface, see figure 2.9b. These scattering interfaces can either be grain boundaries inside the material, or simply the physical edge of the material, where dangling bonds and adsorbed molecules can significantly alter the bandstructure of the material. These imperfections in the lattice act to displace the charge density, causing an increase in scattering. As one might expect, surface scattering is a major factor in 1D nanomaterials, where the surface to volume ratio can be quite substantial. As such, surface scattering have been found to have significant effect on the mobility of thin semiconductor films. As with impurity scattering, surface scattering can dominate at low temperatures, where phonon scattering is minimal [79, 86–88].

2.5 Charge-Carrier Recombination

So far, we have discussed the various charge-carrier scattering mechanisms in materials, which largely determines the mobility of these carriers. For photoexcited carriers, the final

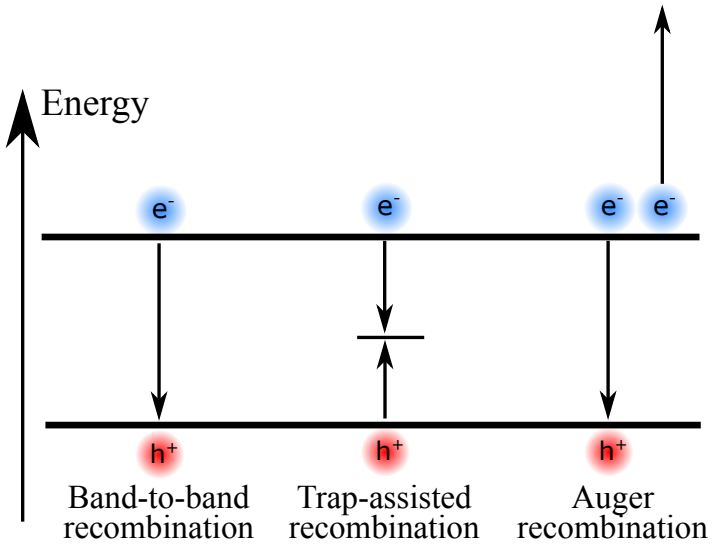

Figure 2.10: Carrier recombination mechanisms in semiconductors.

stage before returning to their equilibrium state is charge-carrier recombination, in which the photogenerated electrons and holes recombine across the material band-gap, see figure 2.10. For any recombination process, the energy difference between the initial and final state of the electron is released during this process. As such, carrier recombination mainly determines the luminescent properties of a material and the lifetimes of the photogenerated carriers. In the case of *radiative recombination*, the energy is emitted in the form of a photon. In the case of *non-radiative recombination*, it is passed on to one or more phonons, and in the case of *Auger recombination* it is given off in the form of kinetic energy to another electron. For many semiconductor crystals, the process of carrier recombination can be quite complex, with the carrier lifetime altered by carrier trapping, defects and surface effects. For nanostructures in particular, the large surface-to-volume ratio leads to the surface effects such as trap states and defects dominating transport properties. Thus, the various types of radiative and non-radiative recombination must be taken into account in order to understand the photoexcited charge-carrier dynamics in semiconductor materials [15, 89].

Band-to-band recombination occurs when an electron moves from its conduction band state into the empty valence band state associated with the hole. This band-to-band transition is typically also a radiative transition in direct bandgap semiconductors and is the reverse process of photon absorption. Band-to-band recombination depends on the density of available electrons and holes and both carrier types need to be available in the recombination process. Therefore, the recombination rate is expected to be proportional to the product of the electron and hole concentrations.

Trap-assisted recombination occurs when an electron falls into a "trap", an energy level within the bandgap caused by the presence of a foreign atom or a structural defect. Once the trap is filled it cannot accept another electron. The electron occupying the trap, in a second step, moves into an empty valence band state, thereby completing the recombination process. One can envision this process as a two-step transition of an electron from the conduction band to the valence band or as the annihilation of the electron and hole, which meet each other in the trap. This process is also known as Shockley-Read-Hall (SRH) recombination.

Surface recombination occurs at surfaces and interfaces, and can have a significant impact on the behaviour of semiconductor devices. This is because surfaces and interfaces typically contain a large number of recombination centers because of the abrupt termination of the semiconductor crystal, which leaves a large number of electrically active states in the form of dangling bonds. In addition, the surfaces and interfaces are more likely to contain impurities since they are exposed during sample fabrication and preparation. As such, recombination rates are typically faster in semiconductor nanomaterials as opposed to bulk crystals.

Auger recombination is a process in which an electron and a hole recombine in a band-to-band transition, but the resulting energy is given off to another electron or hole. The excited electron or hole then transfers its excess kinetic energy through collisions with the crystal (phonons), relaxing back to the bandedge. Auger recombination can involve either multiple electrons and a hole, or multiple holes and an electron. The probability of Auger recombination increases with a higher concentration of carriers, as it relies on the interchange of energy between multiple charge-carriers. Thus the process can be observed in semiconductors with high concentrations of photoexcited carriers, for example immediately after photoexcitation.

Exciton Recombination forms the dominant carrier recombination mechanism in semiconductors, where the exciton pair is tightly bound. Exciton recombination occurs when the coupled electron and hole recombine with each other to produce a photon [65]. As the exciton binding energy is less than that of the uncoupled electron and hole and is usually lower than the bandgap energy of the material, a photon of energy lower than the bandgap is produced. Excitons usually possess short carrier lifetimes due to the proximity of the electrons and holes involved in the recombination process, and as such the exciton lifetime is dependent on the exciton Bohr radius and its binding energy. For Mott-Wannier excitons, which are weakly bound and possess exciton radii many orders of magnitude larger than the distance of the unit cell, the recombination rate is small due to the large separation between the electron and hole, while for Frenkel excitons, which are tightly bound and have exciton radii on the

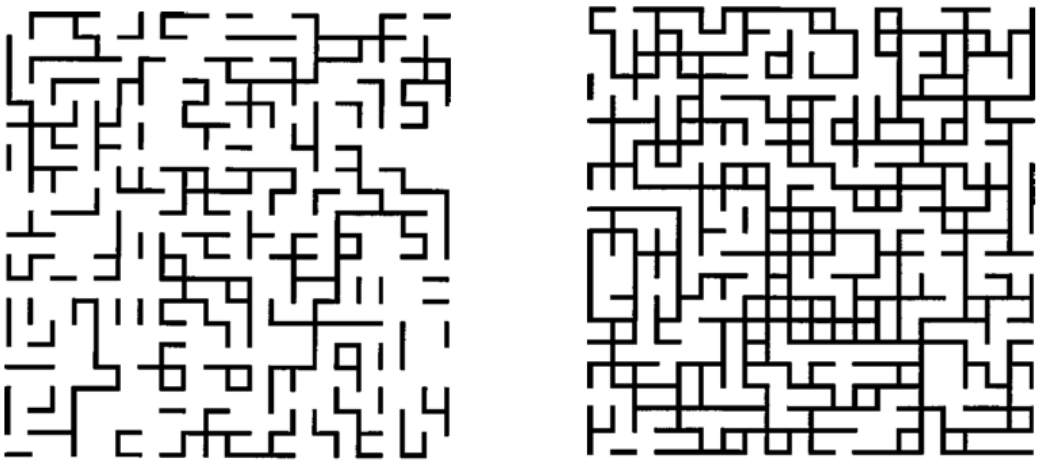

(a) $p < p_c$ (b) $p > p_c$

Figure 2.11: Percolation in two dimensions. Here the nanotube components are situated on an underlying square lattice (not shown). The black lines represent a connection between neighbouring nanotubes, allowing conduction between them. **(a)** The density of nanotubes p is smaller than the percolation threshold p_c, meaning the nanotubes are fairly isolated and it is not possible to form a connection across the entire sample. **(b)** $p > p_c$ and diffuse transport across the network is possible. Image source: [1].

order of the atomic scale, there is a much greater probability of radiative recombination due to the strong Coulomb-interaction.

2.6 Percolation and Effective Medium Theory

So far we have only considered homogeneous materials, however in reality nanowires and nanotubes are typically dispersed in a host material (usually air or an inert polymer), resulting in a percolating network of nanotubes, depending on the density of the tubes, see figure 2.11. This means that the measurable dielectric response is that of the entire network, as opposed to the local response of the individual nanotubes. As such, contact resistance between nanotubes, nanotube geometry, concentration, alignment, and so on, can heavily influence the *effective* conductivity response of a nanomaterial network. In terms of THz spectroscopy, when the diffraction-limited spot size of THz radiation is far larger than the material's dimension (1 THz $\approx$ 333 μm in air), these effects start to dominate. In this case, an effective medium theory (EMT) can be used to model the composite material's permittivity. Numerous models exist, depending on the geometry and optoelectronic properties of the constituent materials, and the geometry of the system [70, 72, 76, 90].

The goal of any EMT is to relate the effective permittivity, ϵ_{eff}, (or equivalently, the conductivity) of the composite material to the permittivity, ϵ_{CNT}, of the nanostructured material (in this case CNTs), the permittivity, ϵ_h, of the host medium (often air) in which they are embedded and the volume fraction, f, which they occupy. When these parameters are known, one can in principle model the effective response of the composite material, which is the measurable quantity in experiments. When this EMT is applied in reverse, the permittivity of the constituent CNTs, ϵ_{CNT} can then be extracted from the measured permittivity of the composite, ϵ_{eff}. The two most commonly used EMTs are the Maxwell-Garnett and the Bruggeman EMTs [70, 90, 91], where the former is applicable when f is relatively small (isolated nanotubes), and the latter when f is relatively large (percolating network). The two formulas are given by:

$$\frac{\epsilon_{eff}-\epsilon_h}{\epsilon_{eff}+2\epsilon_h} - f\frac{\epsilon_{CNT}-\epsilon_h}{\epsilon_{CNT}+2\epsilon_h} = 0 \qquad \text{(Maxwell-Garnett)}, \tag{2.20}$$

$$f\frac{\epsilon_{CNT}-\epsilon_{eff}}{g\epsilon_{CNT}+(1-g)\epsilon_{eff}} + (1-f)\frac{\epsilon_h-\epsilon_{eff}}{g\epsilon_h+(1-g)\epsilon_{eff}} = 0 \qquad \text{(Bruggeman)}, \tag{2.21}$$

where g is a depolarisation factor, which depends on the CNT geometry. We note that in most cases prepared samples of CNTs and semiconductor nanowires form percolating networks, making the Maxwell-Garnet EMT a poor choice. Therefore, in the case of large f, the Bruggeman approximation is more appropriate and can provide more accurate results for the CNT conductivity.

2.7 Carbon Nanotube Morphology and Bandstructure

In this chapter we have so far discussed the fundamental bandstructure theory and conductivity models used to explain the charge-carrier dynamics in nanomaterials. The rest of this chapter is dedicated to introducing the fundamental structure and properties of the two materials of interest in this thesis, carbon nanotubes and tungsten-oxide nanowires.

A single-walled carbon nanotubes (CNT) can be imagined as a rolled-up sheet of graphene (a single layer of carbon atoms in a honeycomb structure), resulting in a hollow cylinder with a diameter of a few nanometers and a length that can range between hundreds of nanometers and hundreds of micrometers [2, 3, 24], see figure 2.12. The myriad of possible rolling directions and diameters give rise to a multitude of possible CNT configurations, where the rolling-direction and diameter largely determines the bandstructure of the resulting CNT as seen in figure 2.13. CNTs are effectively one-dimensional structures due to their typical diameters of $1-2$ nm, as opposed to the two-dimensional nature of graphene, and since their

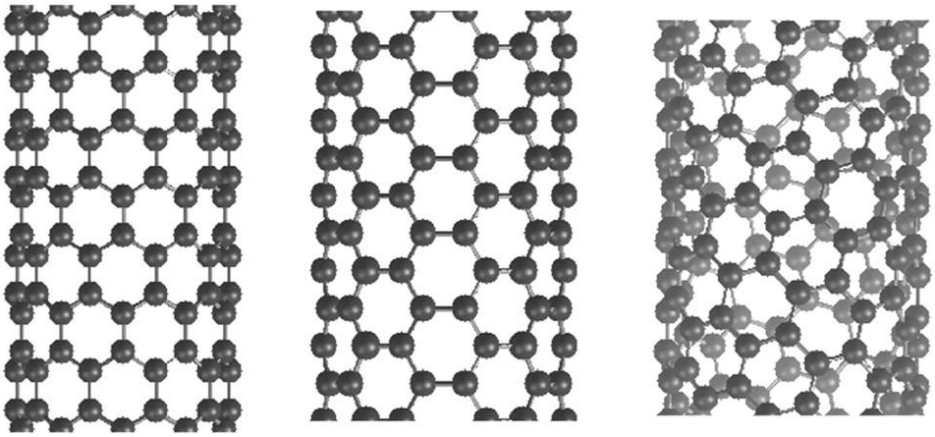

Figure 2.12: "zigzag nanotubes" (left) and "armchair nanotubes" (center), whose names derive from the pattern formed by the carbon lattice along the short axis of the nanotube. Any other CNT is known as a "chiral nanotube" (right). Image source: [2].

morphology are closely linked to that of graphene, they are labelled in terms of the graphene lattice vectors. The lattice constant is $a = \sqrt{3}a_{CC} \approx 2.46$ Å, where $a_{CC} = 1.42$ Å is the distance between neighbouring carbon atoms in the honeycomb lattice. The basis vectors $\boldsymbol{a}_1$ and $\boldsymbol{a}_2$ are given by

$$\boldsymbol{a}_1 = \left(\frac{\sqrt{3}}{2}, \frac{1}{2}\right) a, \tag{2.22}$$

$$\boldsymbol{a}_2 = \left(\frac{\sqrt{3}}{2}, -\frac{1}{2}\right) a. \tag{2.23}$$

Since the characteristics of a CNT is largely determined by the diameter and rolling-angle, we can specify this in terms of a chiral vector $\boldsymbol{C}_h$:

$$\boldsymbol{C}_h = n\boldsymbol{a}_1 + m\boldsymbol{a}_2 \equiv (n, m), \tag{2.24}$$

where (n, m) are the chiral indices with $0 \leq |m| \leq n$. The tube diameter can be calculated from the chiral vector as

$$d_t = \frac{|\boldsymbol{C}_h|}{\pi} = \frac{a}{\pi}\sqrt{n^2 + nm + m^2}. \tag{2.25}$$

The simplest way of describing the electronic properties of CNTs is by applying circumferential boundary conditions to the bandstructure of graphene. The electronic structure of graphene was first studied in 1946 by P. R. Wallace [92] and uses a nearest-neighbour tight

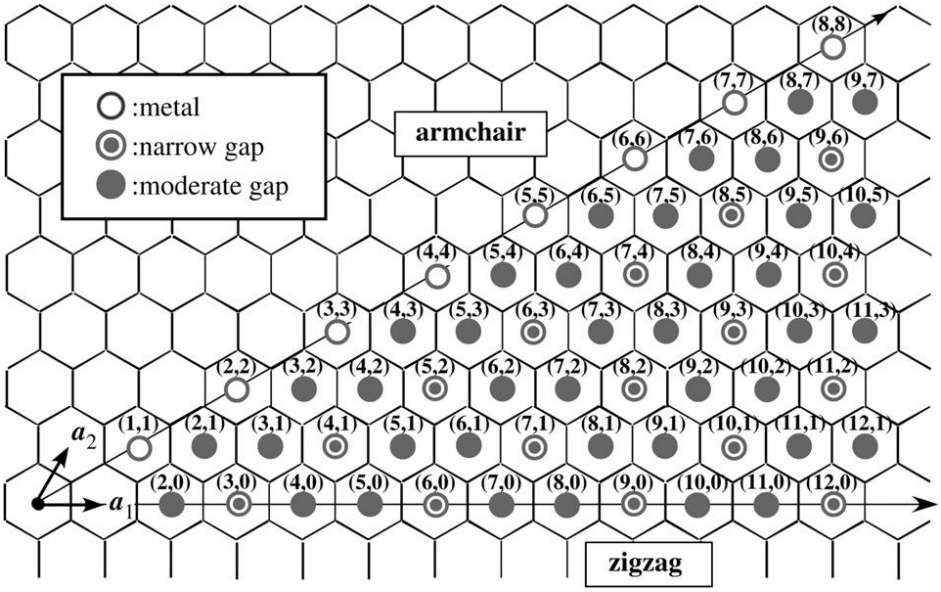

Figure 2.13: Circumferential vector map of carbon nanotubes and their electronic transport properties, specifically the relative size of their bandgap. Image source: [2].

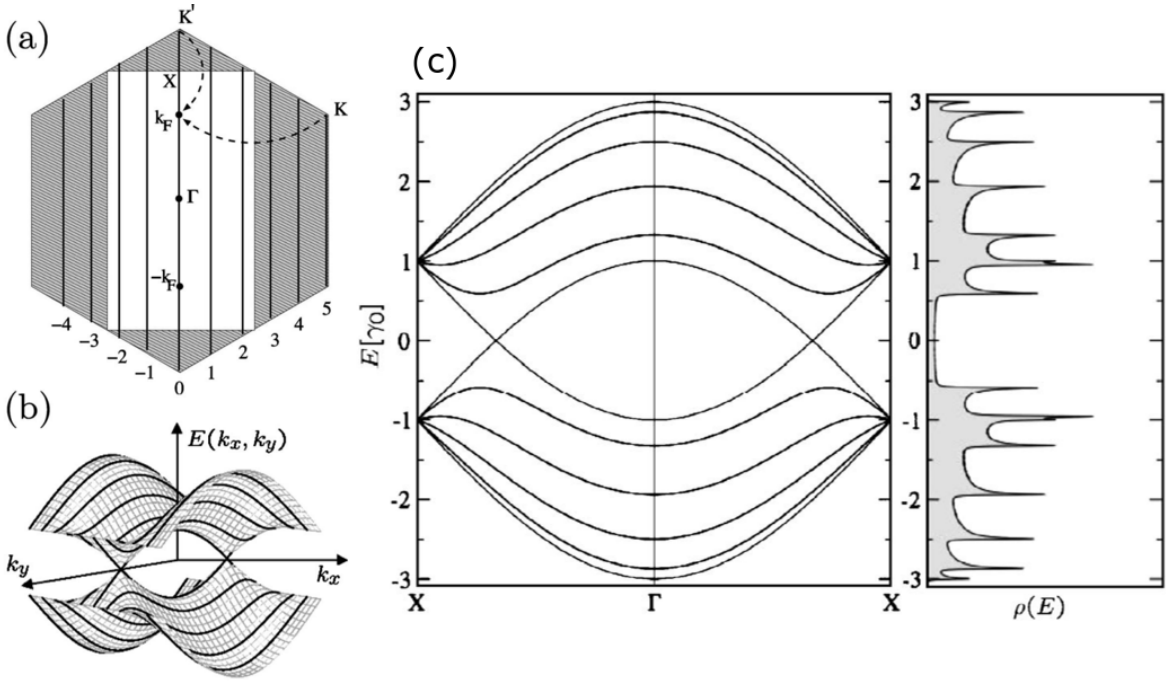

Figure 2.14: Schematic of (a) the Brillouin zone of graphene with allowed wavevectors for the SWCNT, (b) dispersion relation for graphene, and (c) the electronic bandstructure and density of states of a metallic CNT. Image source: [3].

binding approximation. The two atoms in the unit cell give rise to a valence band and a conduction band that touch at six points at the edges of the Brillouin zone as shown in figures 2.14a and 2.14b. Due to symmetry, these points can be reduced to a pair of conical energy bands K and K', where close to the K and K points the energy dispersion, $E(k)$, is linear:

$$E(k) = \pm v_F \hbar k, \tag{2.26}$$

where $k = |\boldsymbol{k}|$ is the absolute value of the wavevector, $v_F = \frac{3t}{2\hbar} a_{CC} \approx 10^6$ ms^{-1} is the Fermi velocity and $t \approx 2.8$ eV is the nearest neighbour hopping energy. By applying periodic boundary conditions along the circumferential direction of the CNT, we get a set of discrete values for the allowed wave vectors $k_\perp$, while in the axial direction of the CNT the wave vectors $k_\parallel$ remain continuous (assuming the CNT is infinitely long) [3]. By plotting the allowed wave vectors in the Brillouin zone of a graphene sheet, a series of parallel lines are generated, with length, number, and orientation that depend on the chiral indexes (n,m) of the CNT as seen in figures 2.14a and 2.14b. In other words, this can be imagined as slicing the Dirac cones along a certain direction determined by the rolling-angle of the CNT, where the spacing of the lines increases with decreasing diameter. This is the known as the zone-folding approximation, where the electronic band structure of a CNT with a specific chirality is given by the superposition of the "sliced" energy bands along the corresponding allowed wave-vectors, see figur 2.14c. Therefore, the electrical bandgap in CNTs depends on the chiral angle: a nanotube is metallic if the allowed wave-vectors cross the zero-gap K point in the graphene Brillouin lattice, which occurs when $n-m = 3j$ ($j = 1, 2, 3, \dots$), or equivalently when $2n + m \equiv 0 \pmod 3$. Thus, 2/3 of the chiralities correspond to semiconducting CNTs, while 1/3 correspond to "metallic" ones [2, 3]. Out of the latter, only "arm-chair" ($n = m$) CNTs are truly metallic in the sense that they are completely without a bandgap. The rest of the "metallic" CNTs do in fact have a small curvature-induced bandgap of approximately 1-40 meV (which coincidentally is in the range of THz frequencies), where the size of the gap scales inversely with the diameter of the CNT [93, 94]. These are commonly known as "small-gap" or "quasi-metallic" CNTs. Additional influences on the electronic bandstructure include many-body effects [95], coupling effects between adjacent tubes (bundles) [96], as well as ambient contamination and doping due to water and oxygen molecules [97, 98].

The density of states (DOS) of a semiconducting and a metallic CNT is plotted in figure 2.15. In both cases a number of "spikes" can be observed, corresponding to energy levels of the subband edges. These "spikes" in the DOS are called Van Hove singularities (VHSs) and arise due to the 1D nature of the CNTs, since the DOS is known to have a strong dependence on the dimensionality of a system [3]. This in turn largely defines the allowed optical transitions

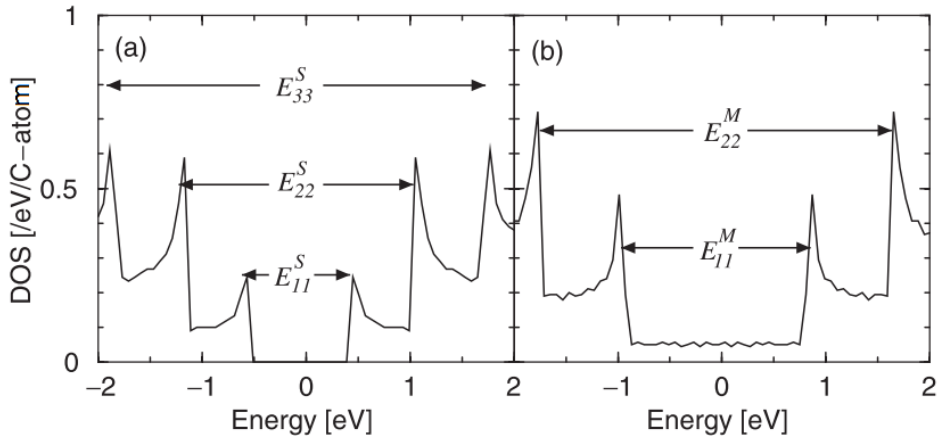

Figure 2.15: Electronic density of states for (a) a semiconducting CNT and (b) a metallic CNT. The Fermi energy (E_F) is located at $E = 0$. An optical transition is possible between VHS peaks in the valence and conduction bands. Energy separations between two VHS peaks are labelled from smallest to largest for semiconducting tubes by E_{11}^S, E_{22}^S, E_{33}^S,..., and for metallic tubes by E_{11}^M, E_{22}^M, E_{33}^M, ... Image source: [2].

in CNTs, where selection rules determine that the strongest optical transitions take place between subbands with the same angular momentum when the incident light is polarized parallel to the long axis of the CNT [99, 100]. In other words, if the notation E_{ij} represents the optical transition from valence subband i to the conduction subband j, the strongest transitions occur for $i = j$, i.e. E_{11}^S, E_{22}^S, E_{33}^S,... for semiconducting CNTs, and E_{11}^M, E_{22}^M, E_{33}^M, ... for metallic CNTs. On the other hand, if the incident light is polarized perpendicular to the long nanotube axis, this would lead to transitions between different subbands, such as E_{12}, however with much smaller absorption cross-section with respect to those for parallel polarization. Such studies were summarized in the well-known Kataura plot [101] shown in figure 2.16, where the E_{ii} transition energies are displayed as a function of the CNT diameter. The Kataura plot is quite useful in spectroscopy studies, since one typically knows the diameter distribution of the CNT sample. Using figure 2.16, one can then easily determine the energy-range of the optical transitions in the CNT sample.

2.8 Tungsten-Oxide Morphology and Bandstructure

Tungsten-oxide (WO_x, $2 \leq x \leq 3$) is a transition metal oxide made up of perovskite-like units, which is well-known for its nonstoichiometric properties, as the lattice can withstand a considerable amount of oxygen deficiency [43]. Only a partial loss of the WO_3 oxygen content is needed to affect its electronic band structure and increase its conductivity by a large amount

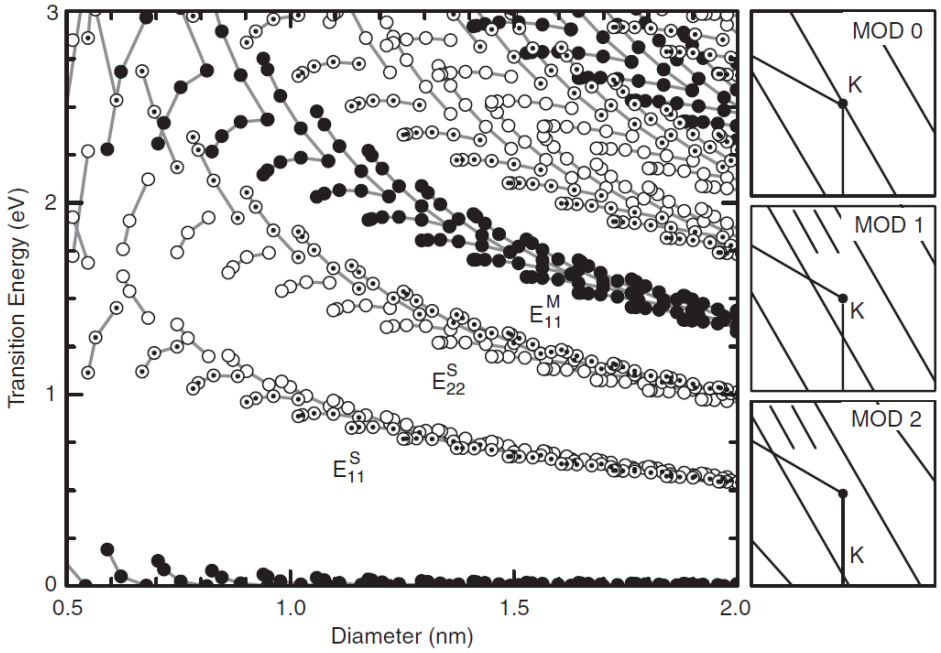

Figure 2.16: Plot of the transition energies E_{ii} vs. d_t for all (n, m) values occurring for $0.5 \leq d_t \leq 2$ nm (Kataura plot) where S and M denote semiconducting (open and open-dot circles) and metallic (closed circles) nanotubes, respectively. On the right, cutting lines are shown for M tubes (MOD 0), and S tubes of two types, MOD 1 and MOD 2, for open and open-dot circles respectively. Here the "MOD x" notation refers to the condition $2n+m \equiv x$ (mod 3), which determines the type of CNT. Image source: [2].

[8, 44]. In this section we review the fundamental morphology and bandstructure of WO_x.

2.8.1 Crystal Structure and Substoichiometry

The "ideal" WO_3 crystals can be represented as a cubic structure consisting of corner-sharing WO_6 octahedra, see figure 2.17a-2.17b. However, cubic WO_3 has never been observed experimentally due to its instability; instead, various polymorphs of WO_3 exist, which are derived from the "ideal" cubic structure through lattice distortions, depending on the titling angles and rotation directions of the WO_6 octahedra [4]. One common example is hexagonal tungsten trioxide (h-WO_3), which is metastable and cannot form from other phases by crystal-phase transitions, but usually exists as a dehydration product of tungsten oxide hydrate [102]. In this phase three different types of "tunnels" are present, which are constructed from corner-sharing WO_6 octahedra, with the formation of trigonal and hexagonal voids in the ab plane and square windows along the c axis (Figure 2.17c-2.17d) [103]. In general, the different phases of WO_x contain at least one of these types of tunnels, making

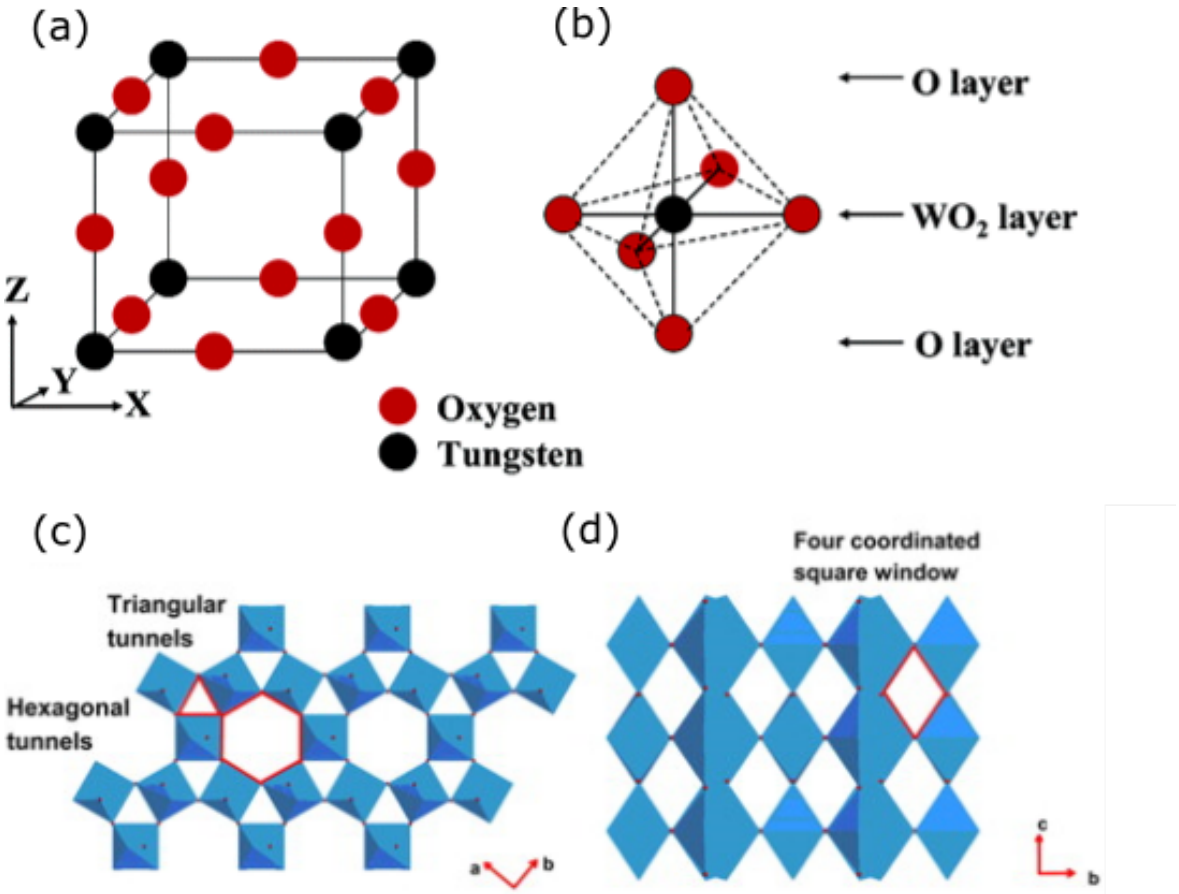

Figure 2.17: (a) The cubic structure of WO_3 and (b) the WO_6 octahedra unit. (c) The structure of hexagonal WO_3 with its c axis perpendicular to the lattice plane (001) and (d) parallel to the plane. Image sources: [4, 5].

WO_3 an excellent material for applications involving intercalation of smaller ions such as Li^+ or H^+ [104–106]. The counterpart of h-WO_3 is amorphous WO_3, which shares similar building blocks with the crystalline ones, but with disordered bond lengths and bond angles, to the point where it is difficult to make a detailed physical description due to the dangling bonds and defects that exist in such distorted structures [107]. Like other metal oxides, WO_3 crystal phase transitions can take place during annealing and cooling. For bulk WO_3, phase transformation occurs in the following sequence [108, 109], see figure 2.18: monoclinic II (ϵ-WO_3, $<-43°C$) $\rightarrow$ triclinic (δ-WO_3, $-43°C-17°C$) $\rightarrow$ monoclinic I (γ-WO_3, $17°C-330°C$) $\rightarrow$ orthorhombic (β-WO_3, $330°C-740°C$) $\rightarrow$ tetragonal ($\alpha-WO_3$, $> 740°C$). However, the phase transition behaviour in nanostructured WO_x can be quite complex, as it mainly depends on the material's morphology, which is greatly affected by the nanostructure synthesis

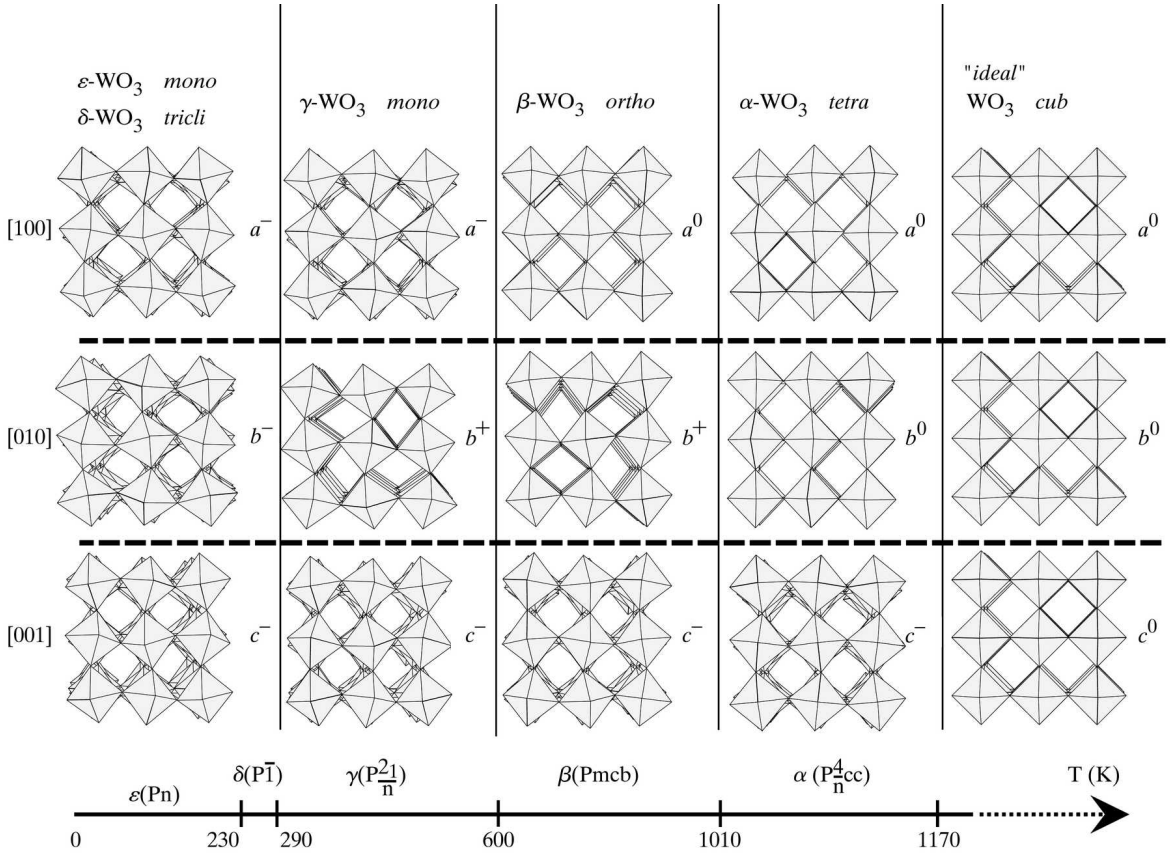

Figure 2.18: Tilt patterns and stability temperature domains of the different phases of WO_3. Image source: [6].

process and the initial precursors used [110].

In addition to the numerous phases supported by the WO_3 perovskite-like crystal structure, several substoichiometric (i.e. oxygen deficient) phases of WO_x exist as well, with x ranging from 2.625 to 2.92. These oxygen-deficient phases are also built up of edge-sharing WO_6 octahedra, however, they are split by crystallographic shear planes (ordered oxygen defect planes) [111]. For example, a substoichiometric phase with tunnel structure similar to those of h-WO_3 is the $W_{18}O_{49}$ ($WO_{2.72}$), in which the well-ordered edge-sharing WO_6 lattice is organized such that three different types of tunnels form within one plane, specifically hexagonal, quadrilateral, and trigonal tunnels [7], see figure 2.19. Since the existence of substoichiometric tungsten oxide was first suggested by Glember and Sauer [112], numerous stable substoichiometric phases, known as Magnéli phases, have been experimentally observed, including $WO_{2.72}$ ($W_{18}O_{49}$), $WO_{2.8}$ (W_5O_{14}), $WO_{2.83}$ ($W_{24}O_{68}$), and $WO_{2.9}$ ($W_{20}O_{58}$) [8]. Furthermore, if sufficient oxygen vacancies are introduced, WO_x undergoes a

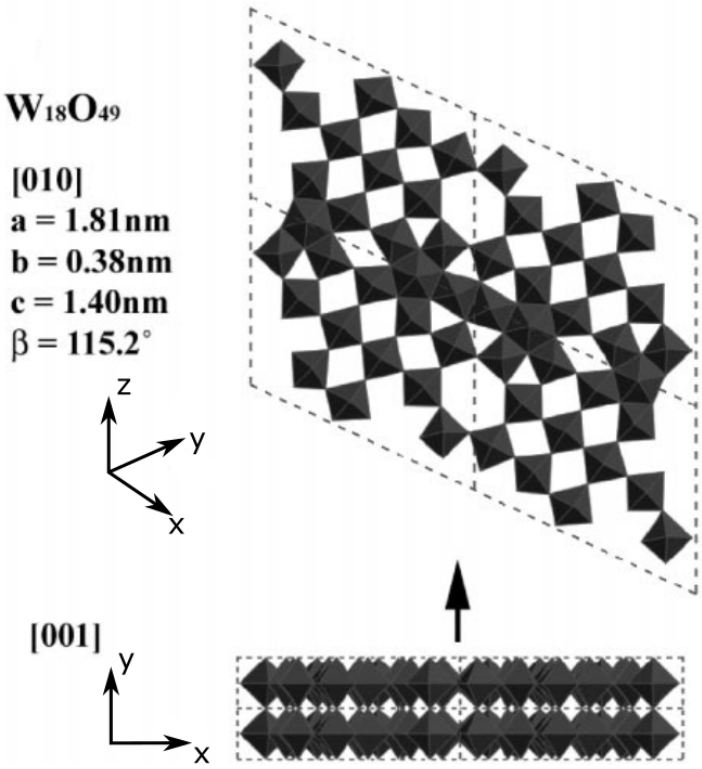

Figure 2.19: Cross section ([010] and [001] direction) of a $W_{18}O_{49}$ ($WO_{2.72}$) phase. Image source: [7].

metal-insulator transition around $x = 2.9$, in which the addition/removal of oxygen atoms into/from the lattice affects the Fermi-level position of tungsten oxide, as well as its energy gap and free-electron density [8].

2.8.2 Bandstructure and Conductivity

WO_3 is an n-type semiconductor with indirect bandgap (E_g) between the valence and conduction bands, where the valence band (VB) is formed by filled O 2p orbitals and the conduction band (CB) is composed mainly of empty W 5d orbitals. The bandgap of WO_3 can be significantly changed by phase transitions, as the occupancy level of its W 5d orbitals alters with lattice distortion. For example, amorphous WO_3 with a large lattice distortion exhibits a relatively large bandgap of approximately 3.4 eV, while the value for the monoclinic crystalline is typically around 2.6 eV in its bulk form [113]. The bandgap of WO_3 is size-dependent due to the quantum confinement (QC) effect, observed experimentally as a blueshift of the absorption edge. A strong QC effect can be observed especially when the particle size is

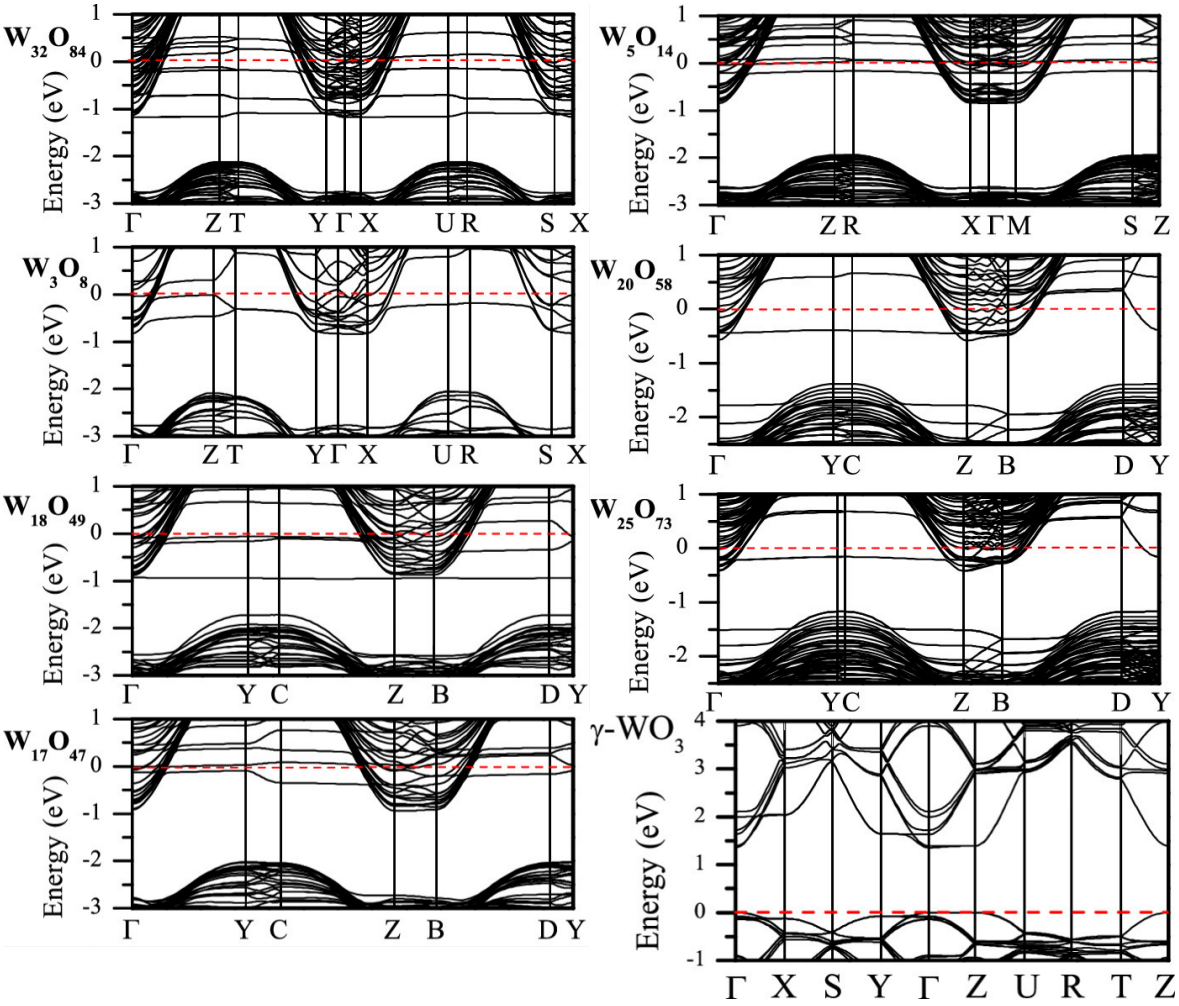

Figure 2.20: The band structures of all Magnéli phases of tungsten oxides, as well as γ-WO_3. Zero at the energy scale corresponds to the Fermi energy. Image source: [8].

close to or smaller than the exciton Bohr radius of the material, approximately 3 nm for WO_3, resulting in direct change in electron wave functions. For a crystal size larger than the exciton Bohr radius, the QC effect results in an indirect perturbation of the electron wave functions due to Coulomb effects, meaning the bandgap is only slightly affected [114].

In terms of the substoichiometric phases of WO_x, only a partial loss of the WO_3 oxygen content is needed to affect its electronic band structure and increase its conductivity by a large amount, since new defect states located in the forbidden energy gap can be introduced by oxygen vacancies, thus narrowing the bandgap [8, 44, 115]. The influence of oxygen deficiency upon the bandstructure can be observed visually by the strong colour change that occurs from white WO_3 to the deep blue colour of $WO_{2.72}$. Similarly, tungsten-oxide exhibits a strong

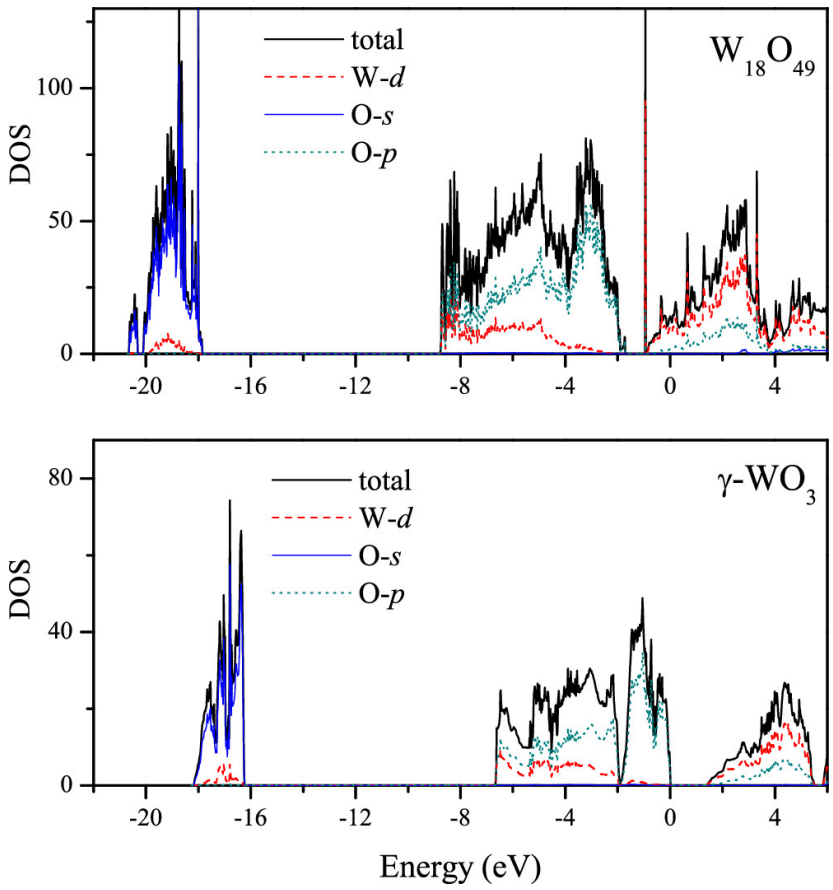

Figure 2.21: The total and projected DOS (states per electron volt per unit cell) of $W_{18}O_{49}$ ($WO_{2.72}$) and γ-WO_3. Zero at the energy scale corresponds to the Fermi energy. Image source: [8].

colour change upon intercalation of small ions such as Li^+ or H^+ [104]. For $2.9 < x < 3$ in bulk WO_x, the electrical and optical properties are dominated by localized electrons involved in polarons, which are quasiparticles consisting of a charge-carrier and its polarization field in a lattice. Bulk WO_x undergoes a metal-insulator transition at $x = 2.9$, as the localized polaronic wave functions begin to overlap and form delocalized states [116]. This transition corresponds to the Fermi-level shifting from the band-gap and up into the conduction band [8], see figures 2.20 and 2.21. As a result, for $x < 2.9$ in bulk WO_x, the electrical and optical properties are dominated by free electrons. The metal-insulator transition has been firmly established in bulk WO_x, both theoretically [8] and experimentally by a combination of temperature-dependent conductivity measurements [117], reflectivity measurements of the bulk plasma frequency [118], and X-ray photoelectron spectroscopy (XPS) [119]. Thus, there

is a wide range of known phenomena from the bulk that may exhibit interesting size- and shape-dependent behaviour at the nanoscale.

Studies of nanoscale WO_x have so far led to some contradictory results. For instance, $WO_{2.72}$ nanowires appear to be semiconducting on the basis of electrical transport [120] and photoluminescence studies [53, 121–125]. At the same time there is some evidence that $WO_{2.72}$ bulk is characterized by a metal-like dependence of electrical resistivity on temperature [118], which has also been confirmed theoretically [8]. Likewise, $WO_{2.8}$ nanowires appear to be metallic on the basis of XPS and electrical transport measurements [126], and it was demonstrated that nanoscale $WO_{2.83}$ can support strong localized surface plasmon resonances (LSPRs) [127], which can only appear in materials with a relatively high charge-carrier concentration.

Chapter 3

Sample Fabrication and Preparation

In this chapter we give an overview of the equipment and techniques used by our collaborators to fabricate and prepare the various nanotube and nanowire thin-films investigated in later chapters.

3.1 Fabrication of Carbon Nanotube Thin Films

Carbon nanotubes (CNTs) were first observed in 1991 in the carbon soot of graphite electrodes during an arc discharge that was intended to produce fullerenes [25], and the first macroscopic production of carbon nanotubes was made in 1992 by Ebbesen and Ajayan at NEC's Fundamental Research Laboratory [128] using the same method. Since then a multitude of fabrication techniques have been developed, including laser ablation, high-pressure carbon monoxide disproportionation (HiPco), and chemical vapour deposition (CVD), each with their own advantages and disadvantages, see [26, 27] for a review of each method. In this section we briefly introduce the techniques used to fabricate and prepare our CNT films.

3.1.1 Chemical Vapour Deposition Method (CVD)

Chemical vapour deposition (CVD) is the most common method for direct growth of CNT thin films due to its simplicity and low cost. In the CVD method, catalyst nanoparticles on substrates are used as seeds for CNT growth. CNTs are produced from the carbon containing source (usually a hydrocarbon gas) as it decomposes at elevated temperature and passes over the transition metal catalyst (typically Fe, Co or Ni) [9, 129, 130], see figure 3.1. Depending

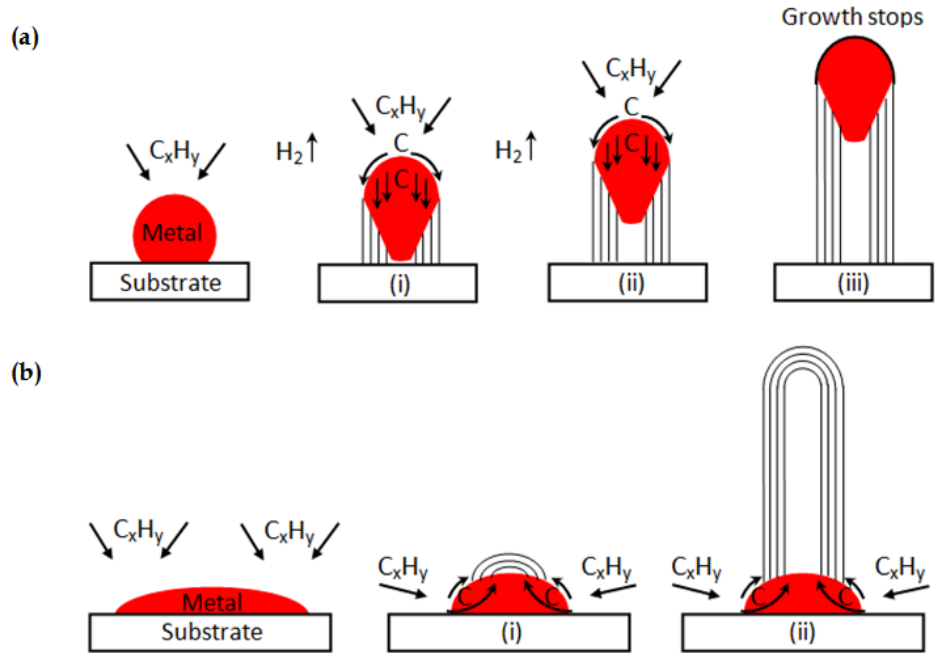

Figure 3.1: The two possible CVD growth mechanisms for CNTs, where CNTs are produced from a carbon containing gas as it decomposes at elevated temperature and passes over the metal catalyst: (a) tip-growth model, where CNTs grow underneath the metal catalyst, and (b) base-growth model, where the CNTs grow on top of the metal catalyst. Image source: [9].

on the strength of the interaction between the catalyst and substrate, the CNTs will either push up the nanoparticles as they grow, or grow on top of the nanoparticles, as shown in figure 3.1a and 3.1b, respectively. The key parameters that control the growth kinetics are the hydrocarbon carrier gas, the growth time and temperature, and the catalyst composition [9, 130]. CVD grown CNTs are generally more structurally defective than those produced by arc or laser evaporation methods, however a high yield of nanotubes can be achieved by this method and the product tends to be purer, i.e. there are far fewer impurities in the form of nanoparticles of graphite or metal. Secondly, the growth occurs at a lower temperature ($550 - 1000°C$) [129], making the process both cheaper and more accessible for lab applications. Finally, since the metal catalyst can be held on a substrate, this allows for growth of aligned nanotubes in a desired direction with respect to the substrate.

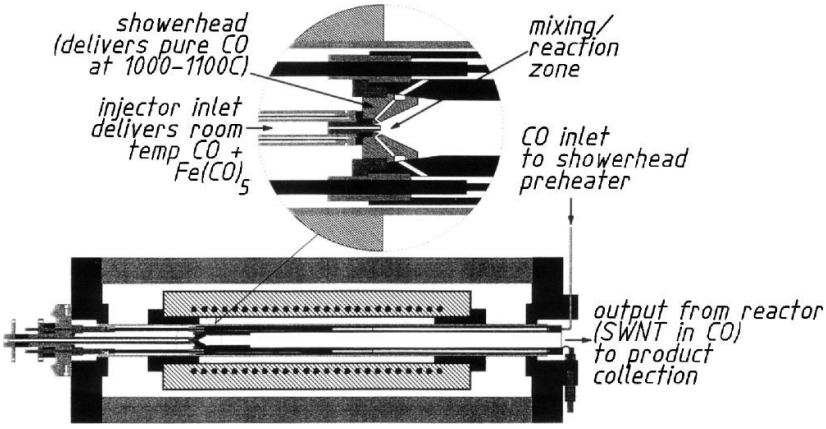

Figure 3.2: Schematic of the HiPco reactor used by Smalley et al. at Rice University to synthesise the CNTs, with the mixing/reaction zone shown enlarged. Image source: [10].

3.1.2 High-Pressure Carbon Monoxide Method (HiPco)

High-pressure carbon monoxide disproportionation (HiPco) is a method developed by Smalley et al. at Rice University in 1999 for the production of carbon nanotubes [10, 131]. Unlike other methods in which the metal catalysts are deposited or embedded on the substrate before the deposition of the carbon begins (for example CVD), in this method the catalyst is introduced in the gas phase. Both the catalyst and the hydrocarbon gas are fed into a furnace, followed by a catalytic reaction in the gas phase, see figure 3.2. Usually CO gas is used as the hydrocarbon gas which reacts with iron pentacarbonyl ($Fe(CO)_5$) to form CNTs. Similar to the CVD method, this method is suitable for large-scale synthesis, because the nanotubes are free from catalytic supports (i.e. no substrate is required) and the reaction can be operated continuously.

3.1.3 Nanotube Dispersion

Once the CNTs have been fabricated, the next step is to prepare the actual CNT films, which should ideally consist of well-dispersed individual CNTs. Because of their large aspect ratio, CNTs are subject to large van der Waals forces, which cause them to stick together, forming large bundles (often referred to as ropes). Therefore, one of the major challenges in fabricating a CNT film is to separate the tubes, without using covalent chemistries or other harsh conditions, which could lower their electrical conductivity. The most widely used route is to use surfactants, such as sodium-dodecyl-sulfate (SDS), to disperse the CNTs due to their ability to individualize CNTs at high concentrations, and their ability to be rinsed off in subsequent washing of the CNT film [132, 133]. Furthermore, most surfactants are

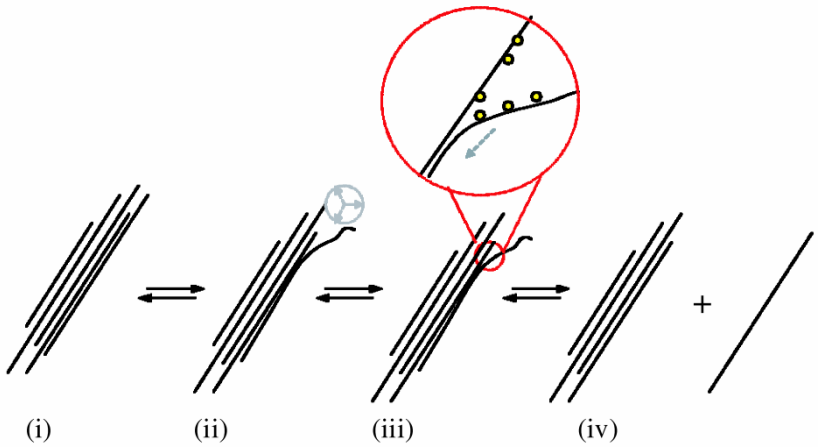

Figure 3.3: Proposed mechanism of CNT isolation from bundles. (i) A bundle of CNTs held together by van der Waals forces. Ultrasonic processing "frays" the bundle end (ii), which then becomes a site for additional surfactant adsorption. This latter process continues in an "unzipping" fashion (iii) that terminates with the release of an isolated, surfactant-coated CNT in solution (iv). Image source: [11].

water-soluble, which allows for aqueous-based CNT dispersions. This is important for fields such as biochemistry and biomedical engineering, in which organic solvents cannot be used due to incompatibilities with living organisms. In practice, sonication is required in order to facilitate the surfactant-assisted dispersion of the CNTs. While the exact mechanism is not entirely understood, it has been proposed that dispersion occurs via an "unzipping" mechanism [11, 132], where sonication "frays" the ends of the CNT bundles, allowing the surfactant to diffuse into the resulting gaps and adsorb to the individual CNTs. This process continues along the bundle length until the CNTs has been completely separated from each other. Figure 3.3 shows this "unzipping" mechanism [134, 135]. The optimal sonication time depends on the CNT preparation, the surfactant choice, CNT and surfactant concentration, the sonication power and amplitude, solution volume and temperature, and pH value [136].

3.1.4 Nanotube Separation and Cutting

In practice, the as-produced CNTs have lengths of tens or even hundreds of micrometers [137] and as we will show in chapters 6 and 7, the length of the individual CNTs has a significant influence on their optoelectronic properties. Therefore it is often desirable to control the individual tube length of the final CNT films. In general, purification of CNTs and their dispersion in solutions by ultrasonication leads to uncontrolled cutting of CNTs until a length of about $0.5-5\ \mu$m [137, 138]. Ultrasonication causes exoergic collapse of bubbles (cavitation)

that produce localized domains of high strain and high temperature, i.e., "hotspots" [139]. These microscopic domains are believed to result in localized attacks on the CNT surfaces, leading to the opening of holes in the nanotube structure and eventual breaking of the tube [140]. To get shorter ($50 - 200$ nm) nanotubes a number of different separation and cutting approaches have been developed. The most popular separation methods, such as gradient ultracentrifugation [141–143] and size-exclusion chromatography [144], are very useful for the generation of CNTs with controllable lengths and narrow length distribution. However, these methods are quite expensive in terms of equipment and chemicals and the yield of short length CNTs is fairly low [142]. Moreover additional procedures must be performed to remove the surfactant and other chemicals after separation, making the procedure time-intensive and labor intensive as well.

Cutting long CNTs into shorter tubes is often a cheaper and simpler approach than CNT sorting, and a number of different cutting methods have been developed, where the simplest and most frequently used method is sonicating the CNTs in a mixture of acids [140, 145–147]. In this case, the defects induced by sonication exposes the nanotubes to the acids, which generate vacancies in the CNT sidewall and consume the oxidized vacancies to yield short, cut nanotubes. Increased sonication time results in increasingly shorter nanotubes. While this method initially had a major disadvantage in terms of degradation of CNTs during the sonication process, Shuba et al. [145] overcame this issue by sonicating the CNT/acid solution at low temperature ($< 8°C$) for several hours, which had previously been done at elevated temperatures. This method is used in the preparation of the CNT films investigated in chapters 6 and 7.

3.1.5 Transfer from Solution to Substrate/Holder

The final step of the CNT film preparation is to transfer the CNTs in solution to a substrate (or a holder in the case of free-standing CNT films). A vacuum filtration technique is used [147], where the solution is filtered through a porous membrane and the CNT film forms on the surface of the membrane. The resulting film is then washed to remove any surfactants and the membrane is dissolved using acetone, leaving the CNT film, which can then be transferred to the desired substrate or holder.

3.1.6 CNT Composite Materials

When preparing the CNT films it may be desirable to mix the CNTs with another material in order to create a composite material, for example in order to reduce the density of the CNT network in the film. Since the observation of a conductivity threshold in polymer/car-

bon nanotube composites [148] much research has been dedicated to fabricating CNT-based composite materials with percolated networks and understanding their optical and electrical responses [149]. Hybrid materials based on carbon and inorganic nanostructures attracted a lot of interest, due to their unique electrical, mechanical, optical and thermal properties [150, 151]. Hybrid nanocomposites have a number of potential applications, including gas sensors, chemical sensors, supercapacitors, batteries and photovoltaic elements [152].

In chapter 6 we investigate the density dependence of composites made from CNTs and non-conductive inorganic WS_2 nanotubes (INT). The INTs were provided by Reshef Tenne at the Weizmann Institute of Science, Israel, and were synthesized in a large scale fluidized bed reactor (see details in [153]). Essentially, the growth mechanism involves conversion of tungsten-oxide particles into WS_2 nanotubes by reacting the particles in a reducing (H_2) and sulfidizing atmosphere (H_2S) at an elevated temperature (840°C) [154]. The INTs have diameters of 20–180 nm and lengths of 1–10 μm; they are semiconducting with a bandgap of 2 eV, and are transparent and non-conductive for THz frequencies. The preparation of the composites are almost the same as for the pure CNT films; the INTs are dispersed using a surfactant by ultrasonication and then centrifugated to remove aggregated INTs. The suspensions of INTs and CNTs are then mixed and filtrated to obtain thin films of CNT/INT composites, with the density of the CNT network determined by the ratio of CNTs and INTs.

3.2 Fabrication of Tungsten-Oxide Nanowire Thin Films

Similar to CNTs, the preparation of tungsten-oxide nanowire (WO_xNW) films involves a growth/fabrication stage, followed by a film-preparation stage. Numerous different approaches for the syntheses of nanostructured WO_x have been implemented using both vapour-phase-based methods, such as sputtering and thermal evaporation, and liquid-phase-based methods, such as sol-gel synthesis, hydrothermal (solvothermal) synthesis, and electrochemical anodization, see [105] for a review of each method. For the sake of brevity, this section will focus on the two methods used to fabricate our WO_xNW thin films, namely the solvothermal method and a solid-vapour reaction method.

3.2.1 Solvothermal Method

The solvothermal method is a cost-effective and well-studied method for preparing a variety of materials such as metals, semiconductors, ceramics, and polymers. The process involves the use of a solvent under moderate to high pressure and temperature that facilitates the interaction of precursors during synthesis, allowing the nucleation and growth of crystallites.

If water is used as the solvent, the method is called "hydrothermal synthesis". The synthesis under hydrothermal conditions is usually performed below the supercritical temperature of water (374°C). The process can be used to prepare many geometries including thin films, bulk powders, single crystals, and nanocrystals, and allows for different crystal morphologies, i.e. spheres (3D), rods (2D), or wires (1D).

In terms of tungsten-oxide nanomaterials, the hydrothermal method can be used to synthesize a variety of high-aspect-ratio 1D WO_x nanostructures, such as nanowires, nanorods, and other interesting configurations, with potentially small (∼4 nm) individual diameters, by low temperature processing of tungsten-containing precursors such as WCl_6, $W(CO)_6$ and WCl_4 in solvents that are usually a mixture of alcohol and water with the addition of acids/bases and surfactants [52]. The type of nanostructure and crystallinity can be controlled through the use of different kinds of sulfates and organic acids [105]. Once synthesis is completed, the resulting nanowire solution is then washed to remove any surfactants and transferred onto a desired substrate. It is noteworthy that $WO_{2.72}$NWs are limited to room-temperature or relatively low-temperature applications due to the fact that they may be oxidized to WO_3 at elevated temperatures [52]. In chapter 8 we exploit this property to convert nanowires of $WO_{2.72}$ into WO_3.

3.2.2 Solid-Vapour Reaction Method

The solid-vapour reaction method is a fairly simple approach allowing synthesis of large ($60 - 150$ nm) diameter $WO_{2.72}$NWs [155]. By heating commercially available WS_2-IF nanoparticles in an oxidation atmosphere, specifically an Ar-flushed furnace with controllable water-vapour content, the nanoparticles go through a sulfide-to-oxide reaction with the water vapour and are converted into $WO_{2.72}$NWs. In this procedure uniform distribution of the precursor is required, which can be achieved via ultrasonic treatment and deposition on a substrate before baking, since the WS_2-IF precursor otherwise agglomerates into large particles with sizes of $40 - 200$ μm, where only the surface of these particles are converted into $WO_{2.72}$. In order to achieve long, thin, and homogeneous nanowires the important parameters are reaction temperature, water vapour, and precursor preparation [155].

Chapter 4

Experimental Measurement Techniques

In this chapter we describe the various experimental techniques used to investigate our nanotube and nanowire thin films, primarily terahertz time-domain spectroscopy (THz-TDS) and optical pump - terahertz probe time-domain spectroscopy (OPTP), which are the two main experimental techniques used in this thesis.

The THz frequency range is commonly defined as being somewhere between the microwave and infrared frequencies, see figure 4.1. The exact range of frequencies that fall within the terahertz region is not well defined, but generally lie between 100 GHz and 10 THz, corresponding to a free-space wavelength of 3 mm - 30 μm, wavenumber of 3.3-333 cm^{-1}, oscillation time of 0.1-10 ps, and photon energies of 0.4-40 meV. For a classical Drude charge-carrier the scattering time is the main parameter determining its transport properties, i.e. the mean time between collision events, which impede the flow of a current under an applied electric field. Since the scattering time of most materials is typically on the order of picoseconds, this makes THz radiation an ideal probe for charge-carriers. Furthermore, the

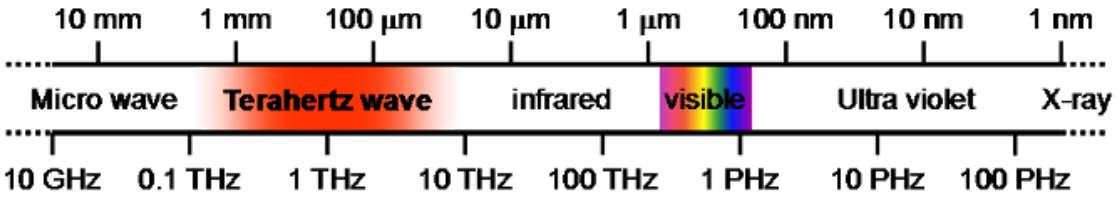

Figure 4.1: The electromagnetic spectrum with corresponding wavelengths and frequencies indicating the regimes of commonly defined types of radiation. Image source: [12].

energy range occupied by typical quasiparticles such as excitons and plasmons fall within the THz range. Thus, terahertz time-domain spectroscopy (THz-TDS) has been proven useful for investigating a multitude of different charge-carriers such as free charge plasmas [18], plasmons [19], excitons [20, 21], transient molecular dipoles [22], and phonons in crystalline solids [23], see [15, 156] for a detailed review.

4.1 THz Generation and Detection

For the past decade there has been a great deal of research dedicated to developing efficient THz emitters and detectors, since the first THz-TDS system was develop by Auston et al. [157–159] and later refined by Grischkowsky et al. [17]. While the so-called "THz gap" has since been closed, current emitters and detectors still have a long way to go in terms of price and efficiency. In this section we describe the most common methods for generating and detecting THz radiation, i.e. using photoconductive antennas and non-linear crystals. However, there are numerous other THz sources such as synchrotrons [160], free-electron lasers [161], quantum cascade lasers [162], and THz detectors such as bolometers [163] and Schottky diodes [164], which we do not cover in this chapter.

4.1.1 Photoconductive Antennas

A basic photoconductive antenna (PCA) consists of two electrodes situated on a high-resistance semiconductor substrate, see figure 4.2. A PCA can function as both an emitter and detector, and both mechanisms rely on creating a transient photoconductivity in the semiconductor gap between the electrodes. When used as an emitter, a bias is applied across the gap, either from a built-in pn-junction in the semiconductor material, or from an external applied bias. An incident high energy femtosecond pulse creates a number of charge-carriers in the gap and the carriers are subsequently accelerated by the bias, thus creating a transient photoconductivity that results in emission of a THz pulse [157–159, 165–168]. When used as a detector, the incident THz pulse acts as the bias that drives the charge-carriers created by the gate pulse, again resulting in a photocurrent at the instant overlap of the two pulses. This photocurrent is directly proportional with the sign and amplitude of the THz pulse [169, 170], which allows us to coherently detect the latter by scanning the "narrow" femtosecond gate pulse over the broader picosecond THz pulse.

In the far field, the emitted THz field is directly proportional to the first time derivative of the transient current. Because of the finite response time of photoconductive materials, this limits the achievable bandwidth of PCAs, which is approximately 5 THz, as opposed to

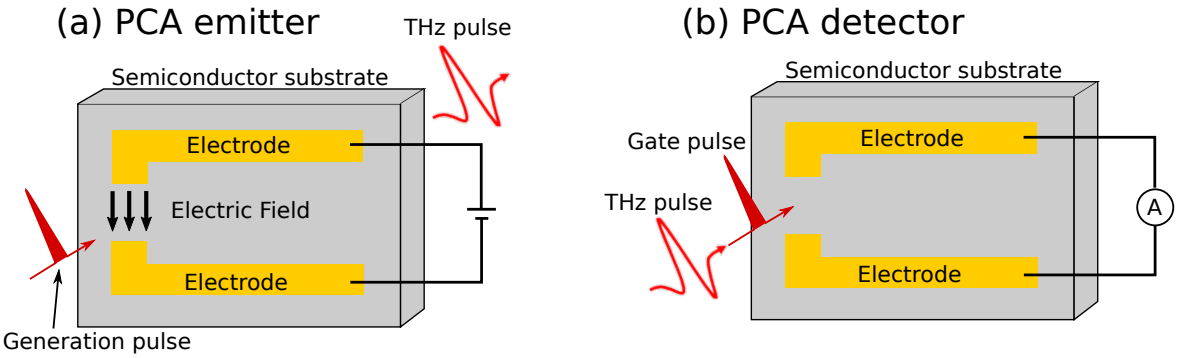

Figure 4.2: Schematic of the photoconductive antenna, which consists of a high-resistance semiconductor substrate with two electrodes. In the emitter setup **(a)** a high energy generation pulse is incident on the gap between the two electrodes and photoexcites a number of electron-hole pairs in the semiconductor substrate. These charge-carriers are subsequently accelerated due to the applied electric field between the electrodes, resulting in emission of a THz pulse. In the detector setup **(b)** the THz pulse functions as the applied electric field that accelerates the charge-carriers generated by the gate pulse. The resulting photocurrent scales with the magnitude and sign of the incident THz electric field and is measured by a lock-in amplifier. The amplitude and phase of the incident THz pulse can then be obtained by scanning the "narrow" gate pulse over the broader THz pulse.

the ideal bandwidth that could be obtained from current state-of-the-art mode-locked laser pulses. For instance, a 10-fs optical pulse (with a corresponding bandwidth of ∼50 THz) should in principle permit generation and detection of electromagnetic transients up to ∼50 THz. However in this regime the comparatively slow response of the carriers in available photoconductive materials significantly limits the high-frequency performance. The THz emission is limited by the recombination lifetime of the semiconductor and the amount of time it takes for the carriers to drift out of the active emitter area [171]. It is also limited by the duration of the optical excitation pulse and the carrier scattering time. Similarly, the temporal resolution, speed and detection bandwidth of a PCA detector is determined by the photoconductivity rise time of the material, while the photoconductivity lifetime sets the noise level [165, 169]. Semiconductor materials are therefore often chosen to be defect-rich, in order to reduce the fall time of the transient current and increase the amount of THz radiation emitted. Currently, low-temperature grown or ion-implanted bulk GaAs, InP and Si samples have been shown to form high-quality, ultrafast PCAs [172–174]. These have since been optimised to a great extent, with improved performance from surface passivation [175] and application of a magnetic field [176, 177]. More recently, these materials have been shown to form effective surface-field emitters, where THz radiation is emitted simply by an optical pulse incident upon the material's surface [178]. While PCAs are limited in

bandwidth, as opposed to non-linear optical processes such as optical rectification (see section 4.1.2), they require comparably less power to function efficiently, making them favourable for low-energy and high repetition rate ultrafast lasers, which are often used in THz imaging, where acquisition time is an important parameter [179].

4.1.2 Optical Rectification

Optical rectification is a second-order non-linear polarization effect, which can be used for generating THz radiation. In this case a DC or low-frequency polarization is developed when an intense laser beam propagates through a non-centro-symmetric crystal [180, 181]. It can be viewed as difference-frequency generation between the frequency components within the band of an optical excitation pulse. Since optical rectification is a nonresonant process, it can withstand higher excitation fluences and generate THz emission with a bandwidth limited only by that of the optical excitation pulse. In the case of our ultrafast laser (100 fs, 800 nm), the bandwidth of the pulses are in the THz frequency range, essentially resulting in a "down-conversion" of the optical pulse (10^{15} Hz) to a THz pulse (10^{12} Hz) [182, 183].

When choosing an appropriate crystal for optical rectification, several factors must be considered: i) the nonlinear crystal must possess a large, second-order, nonlinear susceptibility; ii) it must be transparent in the desired frequency range, so that the interaction length is not limited by absorption; iii) the crystal must have a high damage threshold, as high intensities are required for difference-frequency generation to occur; iv) a phase-matching condition must be satisfied, meaning the group velocity of the excitation pulse must be matched to the phase velocity of all the frequency components of the emitted THz pulse so that all frequency components interfere constructively as they propagate through the crystal [184]. Due to these conditions, various crystals have been optimized for different frequency intervals, namely ZnTe for 0-3 THz, GaP for 2-7 THz, and GaSe for 8-40 THz [185–188].

4.1.3 Electro-Optic Sampling

Electro-optic (EO) sampling, also known as the Pockels effect, is the other main method for coherent detection of THz pulses. Like optical rectification (see section 4.1.2), this is a second-order nonlinear process that occurs in anisotropic crystals that lack inversion symmetry. When an incident electric field such as our THz pulse is applied to an anisotropic crystal, a birefringence is induced in the crystal due to its second-order nonlinear susceptibility. This induced birefringence is proportional to the magnitude of the THz electric field. An optical gate pulse passing through the crystal at the same time as the THz pulse will in this case experience a change in polarization, and since the THz pulses are significantly longer than the

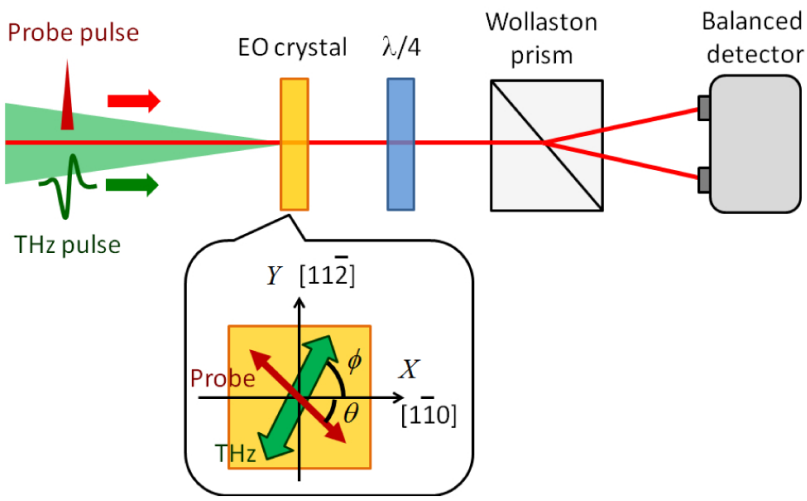

Figure 4.3: Schematic of the EO-sampling method. A anisotropic non-linear crystal such as ZnTe or ZnS with a (111) surface is used for EO sampling. Green and red arrows in the balloon indicate the polarization of the THz and probe pulses, respectively. Image source: [13].

laser pulses (several picoseconds compared to 100 fs), the THz field can be approximated as a static field biasing the detection crystal. The degree of this polarisation rotation can then be measured to obtain the magnitude and phase of the incident THz pulse [183, 189–192]. In practice the non-linear crystal is used together with a quarter-wave plate ($\lambda/4$-plate), a Wollaston prism and balanced detectors as shown in figure 4.3. The balanced detectors consist of two photodiodes that output a signal corresponding to the voltage-difference measured between the two diodes. In the absence of a THz pulse, the $\lambda/4$-plate is calibrated such that the gate beam is circularly polarised as it passes through the Wollaston prism, resulting in equal intensity incident on the two detectors. When a THz pulse is applied, the THz-induced birefringence within the crystal causes the polarisation of the gate pulse to change, so that it exits the $\lambda/4$-plate elliptically polarised. This shift in polarization is then picked up by the balanced detectors. Since the change in birefringence is proportional to the magnitude of the instantaneous THz electric field, the voltage difference measured on the detectors can be used to extract the amplitude of the THz wave [188, 193, 194]. Similarly to the gate technique used for the PCA detector in section 4.1.1, the gate pulse can be scanned over the THz pulse to obtain the full THz waveform as a function of time. Since EO is more or less the reverse process of OR, the considerations regarding the appropriate crystals are the same: the THz and gate pulses must be phase-matched as they propagate through the crystal, which should possess a large, second-order, nonlinear susceptibility and be transparent in the

desired frequency range [170, 195, 196]. Therefore the same type of crystal is typically used for both generation and detection of THz pulses in THz-TDS setups.

4.2 Terahertz Time-Domain Spectroscopy

The fundamental principles of THz-TDS is the ability to generate and coherently detect single-cycle pulses of THz radiation, which typically have an oscillation time of approximately 1 ps, corresponding to a bandwidth of 0.1-2 THz, see figure 4.4. By measuring the THz transmission or reflection through a sample (and an appropriate reference), the change in amplitude and phase induced by the sample can be determined, which in turn allows us to determine the dielectric properties of the sample, specifically the complex-valued refractive index, permittivity and conductivity.

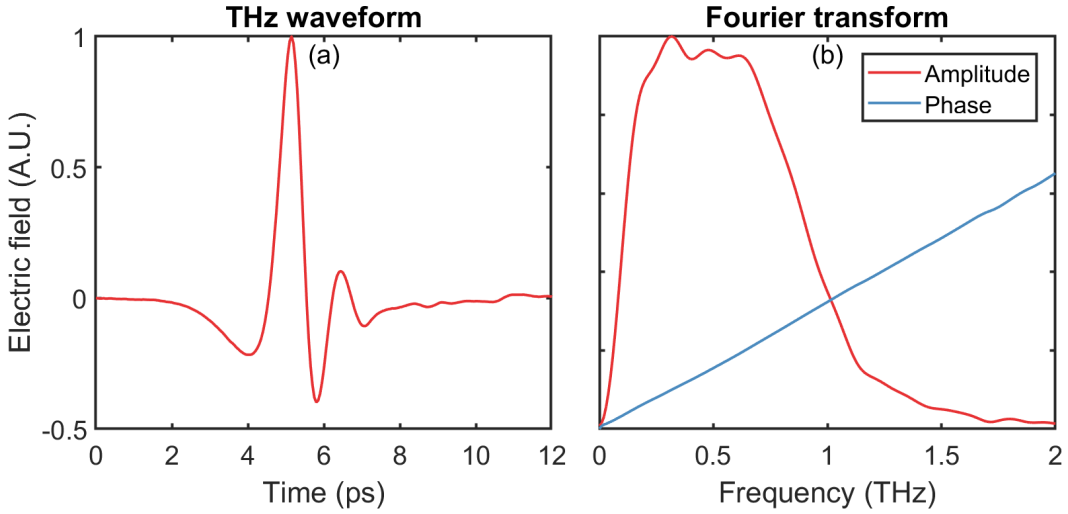

Figure 4.4: (a) Typical time-resolved scan of a THz pulse and (b) the corresponding amplitude and phase plotted in the frequency domain, obtained using Fourier transformation.

The foundation of a THz-TDS setup is based on the ultrafast femtosecond laser, which is able to generate high energy pulses of approximately 100 fs. The center wavelength of these lasers are typically in the optical to near-infrared range, and can have a repetition rate ranging from a few kilohertz to tens of megahertz, depending on the type of ultrafast laser. When used in a THz-TDS setup, the femtosecond pulses are split into an emitter path and gate path that are respectively used to generate and detect the THz pulses, see figure 4.5. Using a delay-stage, the 100 fs gate pulse can be scanned over the THz pulse as it arrives at the detector, allowing us to reconstruct the original time-resolved electric field, and thus obtain the full amplitude and phase information using Fourier transformation. It is possible

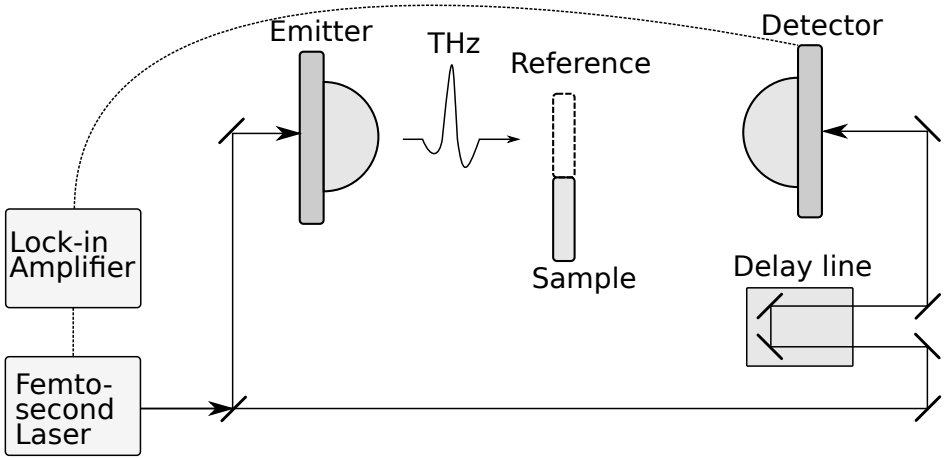

Figure 4.5: Basic diagram of the terahertz time-domain spectroscopy setup. Femto-second pulses are generated by our laser and split into an emitter and detector path, where they are used to generate and coherently detect THz-pulses. The length of the detector path is controlled by a delay-line. The dielectric properties of a sample is obtained by measuring the THz transmission of the sample and an appropriate reference.

to measure either the reflection or transmission of a sample using this method, depending on the geometry of the setup and type of sample. For optically thick samples it is common to measure in reflection geometry, since at least some amount of THz must reach the detector. Therefore the transmission geometry shown in figure 4.5 is typically used for low absorption materials and thin films. In any case, as the THz pulse is transmitted through (or reflected by) the sample, the light-matter interaction between the two results in an attenuation and phase delay of the THz pulse. This change is measured by calibrating the THz setup using an appropriate reference, typically the transmitted THz pulse through either air or a bare substrate, resulting in the complex transmission function $t(\omega)$ of the sample:

$$t(\omega) = \frac{E(\omega)}{E_{ref}(\omega)}, \tag{4.1}$$

where $E(\omega)$ and $E_{ref}(\omega)$ are the transmitted fields of the sample and reference, respectively. From $t(\omega)$ it is then possible to determine the dielectric properties of the sample as we will show in chapter 5.

4.3 Optical Pump - Terahertz Probe Time-Domain Spectroscopy

Optical pump - THz probe time-domain spectroscopy (OPTP) is an extension of THz-TDS and a powerful tool for studying the ultrafast charge-carrier dynamics of materials on a

femtosecond to nanosecond time-scale. It has successfully been applied to a range of different materials including semiconductors, carbon nanotubes, nanowires, and polymers [15, 66, 156, 197]. As with THz-TDS, the power of this method lies in the extraction of the complex material parameters (represented by a complex permittivity, refractive index or conductivity) from photoinduced changes to the THz transmission/reflection of a sample [198–200]. This approach has allowed the study of a wealth of photo-species and phenomena, including exciton dynamics [201], plasmon formation [202], coulomb screening [203] and carrier scattering [204].

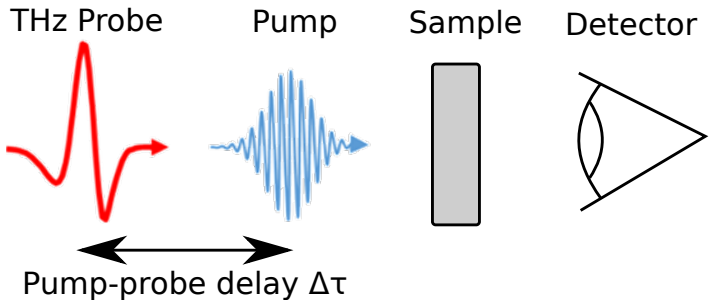

Figure 4.6: Basic diagram of a pump-probe experiment. The sample is photoexcited by an optical pump and afterwards probed by a THz pulse at pump-probe delay time $\Delta\tau$. The change in THz transmission due to photoexcitation is measured by the detector.

By splitting off part of the femtosecond pulses into a pump pulse, which is then used to illuminate the sample directly, it is possible to optically stimulate the sample using the high energy pump, resulting in optical excitation of new charge-carriers, see figure 4.6. These then proceed to relax and recombine through a variety of possible mechanisms, which typically occur on the order of picoseconds. By varying the time delay between the pump and the probe ($\Delta\tau$) using a delay-stage, it is possible to measure the resulting photo-induced change in THz transmission, see figure 4.7:

$$\frac{\Delta E(\omega, \Delta\tau)}{E(\omega)} = \frac{E_{photo}(\omega, \Delta\tau) - E(\omega)}{E(\omega)}, \tag{4.2}$$

where $\Delta E \equiv E_{photo} - E$, and E_{photo} and E are the transmitted electric fields through the photoexcited and unexcited sample, respectively. Similar to THz-TDS, it is then possible to determine the photoinduced changes in the dielectric properties of the sample as a function of frequency and $\Delta\tau$, see chapter 5. There are two possible measurements in this setup: (i) scanning the probe delay-stage (t) in order to obtain the full shape of the THz probe, which can then be fourier transformed to obtain the amplitude and phase information, similar to THz-TDS, and (ii) scanning the pump delay-stage ($\Delta\tau$) to obtain the time-evolution of the THz-probe after photoexcitation by the pump. Ideally the change in THz transmission due

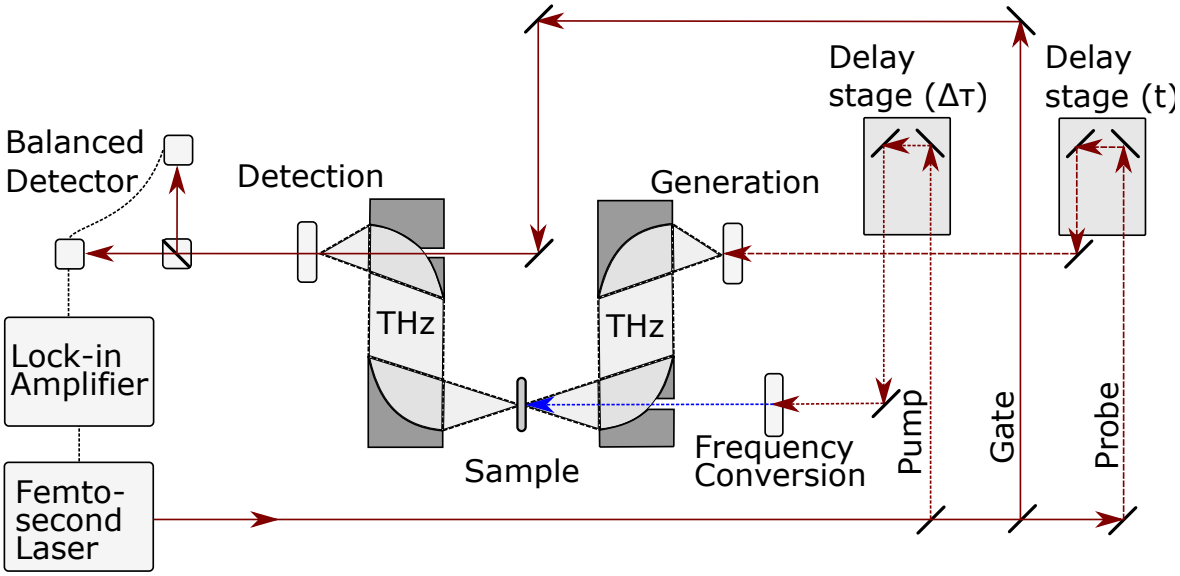

Figure 4.7: The optical pump - THz probe (OPTP) spectrometer: For this setup generation of THz occurs in a ZnTe crystal through optical rectification. Generated THz pulses are first collimated and then focused onto a sample using off-axis parabolic mirrors. The sample can be housed in a closed cycle helium cryostat for temperature control. Transmitted THz pulses are re-collimated and focused onto a detection crystal. THz field waveforms are detected through electro-optical sampling in a second ZnTe crystal by scanning the temporally narrow 800 nm pulse over the THz field using delay stage (t). A pump pulse can be used to excite the sample at pump-probe delay time $\Delta\tau$ using a delay stage, and optionally frequency converted using a non-linear crystal or an optical parametric amplifier.

to photoexcitation is mapped for all t and $\Delta\tau$ in the region of interest, however this is usually quite time-consuming, especially since one typically wants to map over a range of incident pump fluences and pump wavelengths as well. In practice the probe delay-stage t is set to the peak of the THz pulse while scanning over $\Delta\tau$, which obtains the relative change in amplitude of the THz probe as a function of $\Delta\tau$, allowing us to study the decay-dynamics of the sample as a function of time. Similarly, the full THz pulse is scanned for set pump-probe delay times $\Delta\tau$ in order to obtain "snapshots" of the photoexcited dielectric response of the sample for these specific times. Together these measurements reveal all the relevant information about the photoexcited charge-carrier dynamics of the sample in the majority of cases.

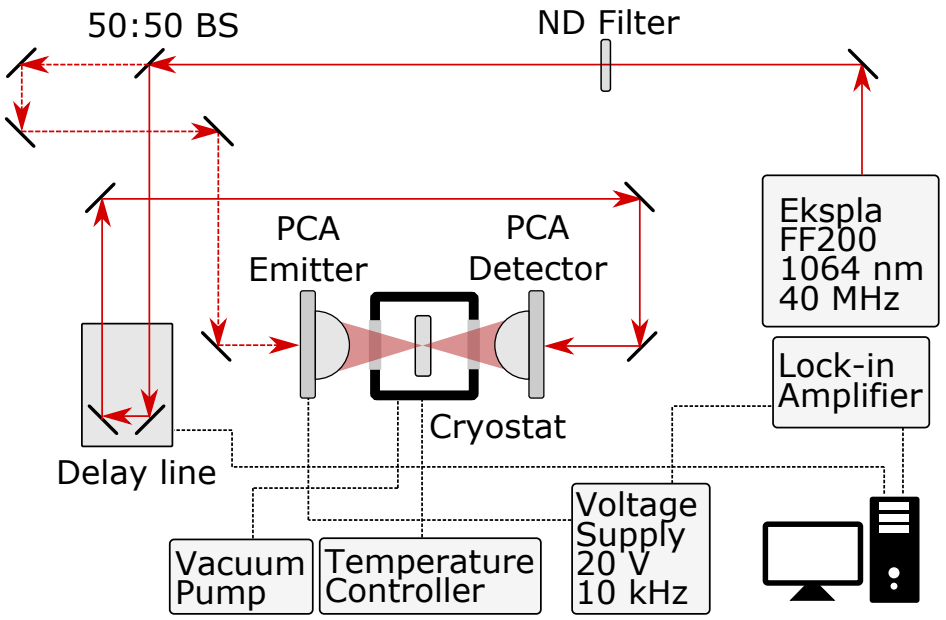

Figure 4.8: Schematic of the PCA based THz-TDS setup used in this thesis. Here BS stands for beam splitter.

4.4 Our Experimental THz Setups

4.4.1 Our THz-TDS Setup

Figure 4.8 shows a schematic of the PCA-based THz-TDS setup used in this thesis to obtain the unexcited dielectric properties of our samples. We carry out transmission measurements over the range 0.2–1.3 THz, where THz pulses are incident normal to our samples. THz pulses are generated and detected by commercially available Photoconductive Antennas (PCAs) (section 4.1.1) from Batop using a model F200, 200 mW, 40 MHz, 1064nm, femtosecond fibre-laser from Ekspla. To investigate the temperature dependence of the THz conductivity in the range 10–300 K, we employed a closed cycle helium cryostat (ARS) with quartz windows. The 1064 nm pulse is split into a detector and emitter path using a 50:50 beamsplitter. The THz signal is modulation at the emitter using a voltage supply applying a 20 V square-wave at 10 kHz, and each PCA receives a power of approximately 20 mW. The emitted THz pulse propagates through the quartz window of the cryostat and is focused onto the sample with a TPX focusing lens ($f = 3$ cm), resulting in a spotsize of a few millimetres. The transmitted pulse then propagates out through the other window and onto the PCA detector, where the resulting current is measured on a Signal Recovery 7230 General Purpose DSP Lock-in Amplifier, measuring with a time constant of 100 ms. Data collection is automated via a

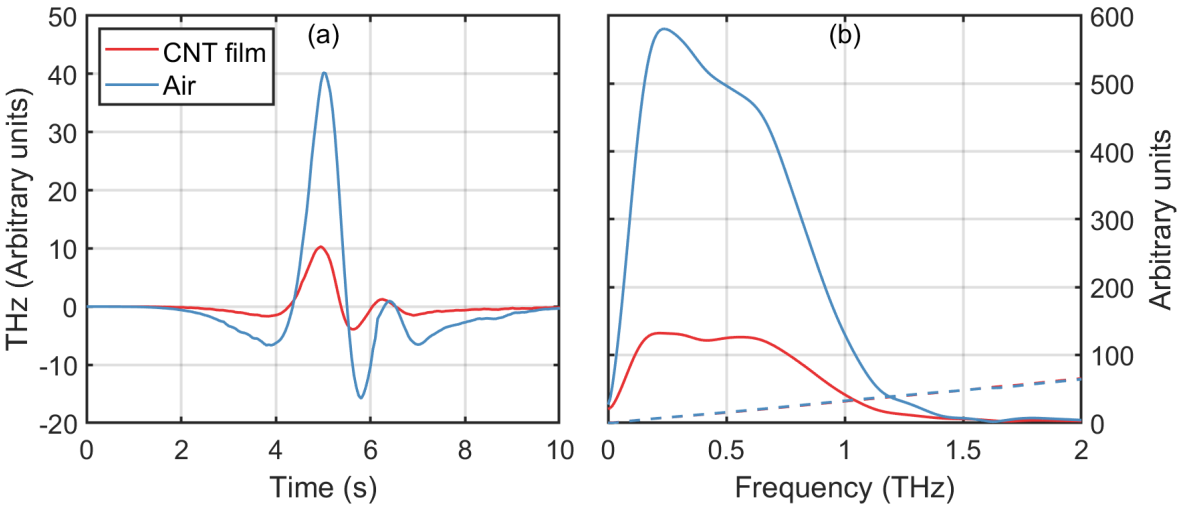

Figure 4.9: **(a)** Time-resolved THz pulse transmitted through air (reference) and a CNT film at 300 K (l-CNT, see chapter 6), and **(b)** the resulting fourier transform, where full and dashed lines are the magnitude and phase, respectively.

computer running LabView, which controls the delay lines and receives the measured signal from the lock-in amplifier. All measurements were done under vacuum in the cryostat, and the temperature was controlled by running a current through heating wires connected at the bottom of the cryostat coldfinger and controlled via a separate temperature controller, see appendix A for pictures of the setup and cryostat. By analysing the frequency dependent transmission amplitude and phase of a sample (see chapter 5), we can determine the complex equilibrium effective conductivity, $\sigma(\nu)$, where ν is the frequency. Figure 4.9 shows a typical THz measurement from this setup, where we have measured a reference scan through air, E_{ref}, and a sample scan through a CNT film, E (specifically l-CNT, see chapter 6 for details). Note that when scanning the THz pulse in figure 4.9a we zero our data after the main pulse, meaning multiple reflections from any substrates such as quartz are ignored. When running the cryostat, cooling time is roughly 1 hour, and temperature-dependence is mapped by slowly heating the sample using the heating wires while running the cryostat. Note that vibrations from running the cryostat results in notably increased noise for these measurements.

4.4.2 Our OPTP Setup

Figure 4.10 shows a diagram of the OPTP setup used in our thesis to measure the photoconductivity spectra of our samples. Pictures of the setup can be found in appendix A. We carry out photoconductivity measurements over the range 0.2–1.3 THz, where THz pulses are incident normal to our samples. To investigate the photoexcited THz response of our

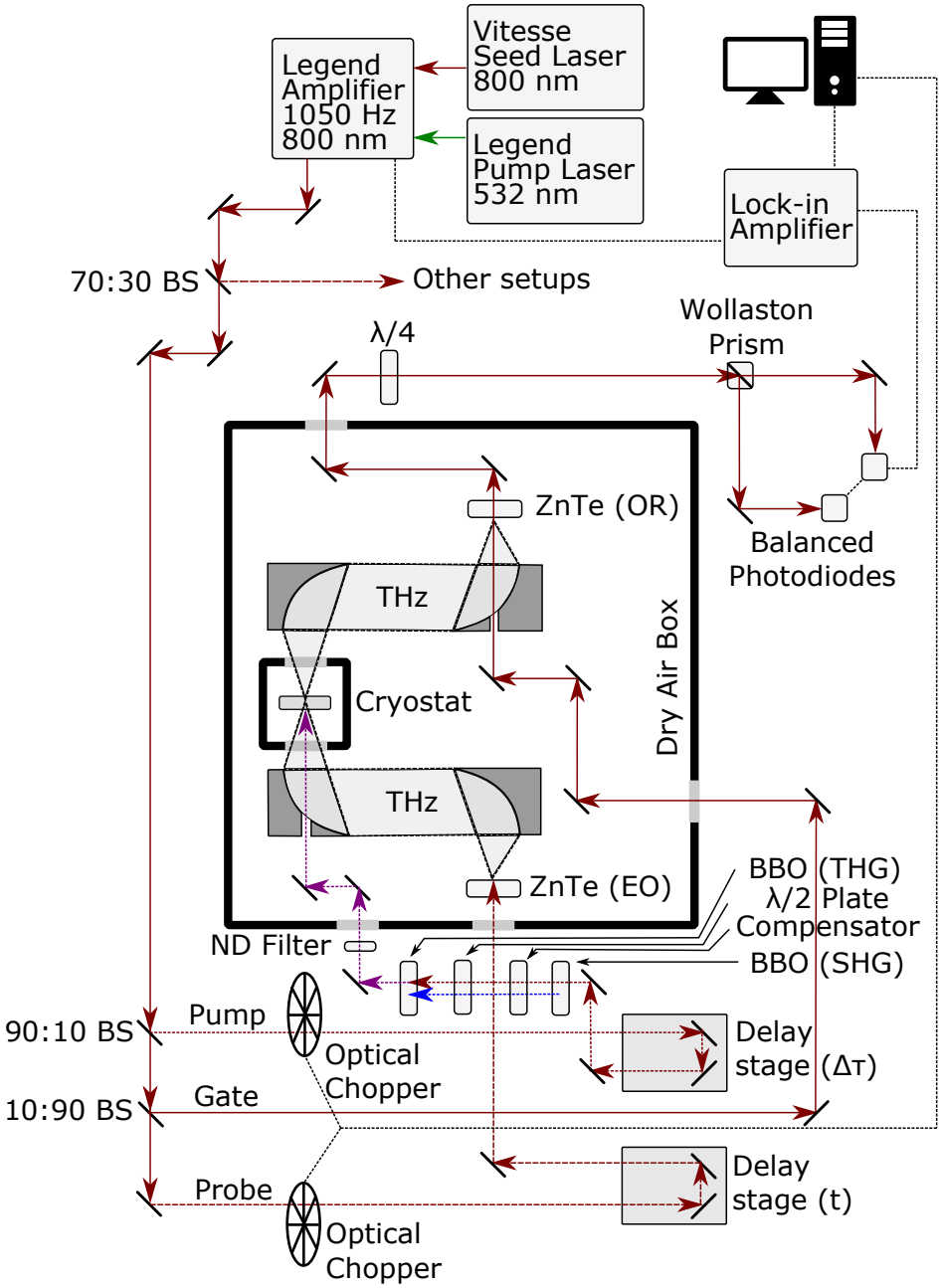

Figure 4.10: Schematic of the optical pump - THz probe (OPTP) spectrometer used in this thesis. Here BS stands for beam splitter.

samples, we employ a 100 fs, 1050 Hz, 800 nm, Coherent Legend Ti:Sapphire amplified laser, which is seeded by a Coherent Vitesse 800 nm femtosecond laser and pumped by a Coherent Legend 532 nm pump laser. The amplified laser outputs 3W of power, with roughly 1 W going to the OPTP setup. The 800 nm beam is then split into three paths; a pump path, gate path and probe path, which respectively receive 90%, 1% and 9% of the 1 W power. The THz pulses are generated and detected by optical rectification (section 4.1.2) and electro-optic sampling (section 4.1.3), respectively, in 1 mm thick ZnTe crystals. The probe beam is used to generate THz radiation in the first ZnTe crystal, which is then guided onto the sample using two aluminium off-axis parabolic mirrors with effective focal lengths (EFL) of 12.5 cm and heights of 10 cm. The transmitted THz field is then collected by another parabolic mirror with EFL of 12.5 cm and directed to a final parabolic mirror with EFL of 5 cm, which focuses the remaining THz pulse onto a second ZnTe crystal. At the same time, the 800 nm gate pulse is directed onto the second ZnTe crystal so that it overlaps with the THz pulse, with the timedelay controlled by a delay stage (t) in the probe path. Past the second ZnTe crystal, the gate pulse is directed through a quarter-wave plate, and then split into two polarizations using a wollaston prism, before being directed onto a pair of balanced photodiodes. The resulting voltage difference on the diodes is measured by a Signal Recovery 7270 Lock-in amplifier with a time-constant of 200 ms, which is passed on to a computer running LabView that also controls the position of the delay-lines. Modulation of the THz signal is achieved by chopping the gate pulse path using an optical chopper, which is frequency-locked at half the repetition rate of the amplified laser (525 Hz). The part of the setup concerning THz generation and detection is placed in a dry-air box in order to remove attenuation from water in the atmosphere.

To photoexcite the sample, we again use 800 nm pulses, which can optionally be frequency converted to 400 nm or 266 nm by way of second- and third-harmonic generation using BBO-crystals purchased from Eksma Optics, or frequency converted to wavelengths ranging from 280 nm to 2500 nm using an optical parametric amplifier purchased from Light Conversion. In practice, the pump pulse is directed onto a second delay stage ($\Delta\tau$), which is also controlled by the computer, and optionally through a BBO crystal, resulting in second harmonic generation (SHG) of 400 nm pulses. Both the 800 nm and 400 nm pulses then propagate through a compensator and half-wave plate to ensure time-overlap and parallel polarization, respectively, before going through a second BBO crystal, resulting in third-harmonic generation (THG) of 266 nm pulses. The final pump-pulse is then directed onto our sample in the cryostat through the back of the second off-axis parabolic mirror. The fluence of the incident pump is controlled using a variable ND filter.

By recording the difference in transmission, $\Delta E = E_{exc} - E$, between a photoexcited

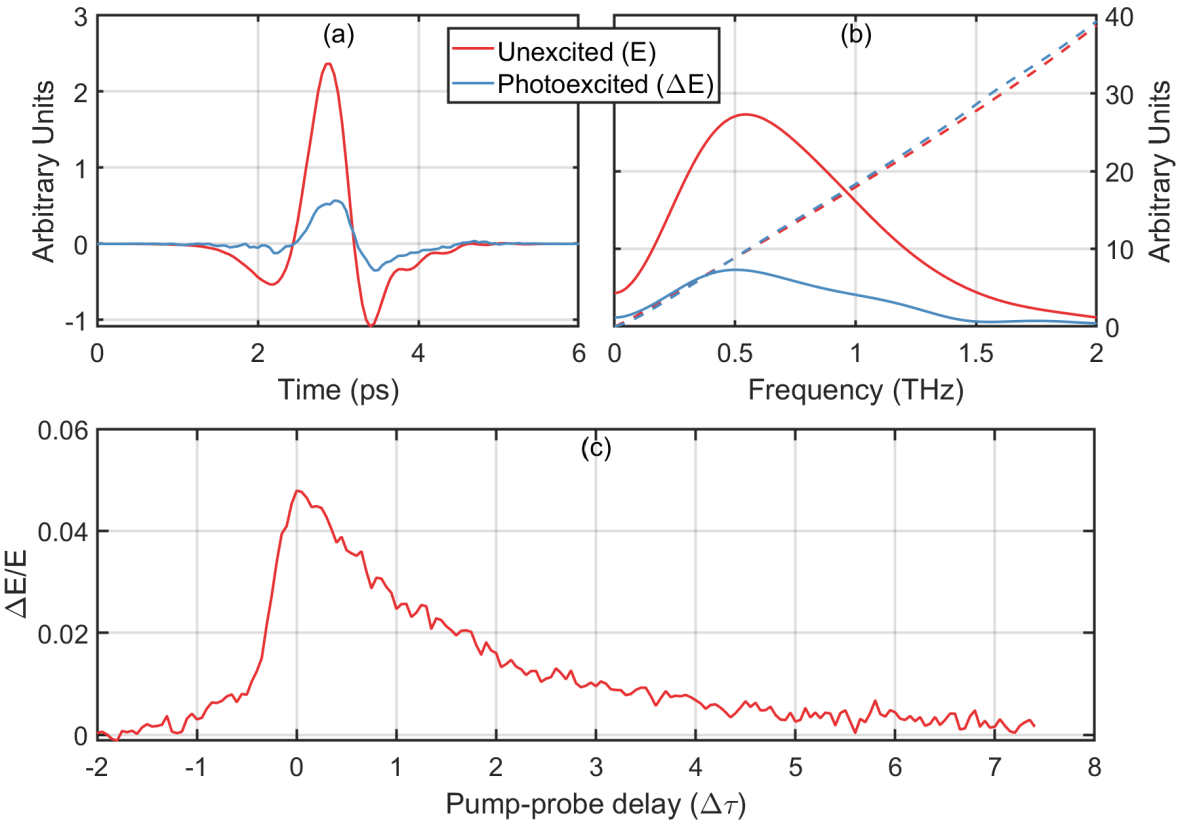

Figure 4.11: **(a)** Time-resolved THz pulse transmitted through an unexcited CNT film (E) at 300 K, and the change in transmitted pulse (ΔE) due to photoexcitation 800 nm pump pulse at $\Delta\tau = 1$ ps and incident fluence of 66 nJ/cm^2. The ΔE data has been scaled by 10. **(b)** The resulting Fourier transform with full and dashed lines corresponding to magnitude and phase, respectively. Again the ΔE data has been scaled by 10. **(c)** Time-scan of $\Delta E/E$ as a function of pump-probe delay time $\Delta\tau$.

(E_{exc}) and unexcited sample (E), a complex photoconductivity $\Delta\sigma_{photo}(\nu, \Delta\tau)$ can be obtained as a function of pump-probe delay-time $\Delta\tau$ (see chapter 5). To measure the relative change in THz transmission ($\Delta E/E$), two scans are performed; (i) the unexcited THz transmission (E), where the pump blocked while chopping the probe pulse and scanning the probe delay-line (t); (ii) the change in transmission ΔE, where the pump is unblocked and chopped and the probe delay-line is scanned for a specific pump-probe delay-time $\Delta\tau$. From these two scans, $\Delta\sigma_{photo}(\nu, \Delta\tau)$ can be obtained for the given $\Delta\tau$. Finally, $\Delta E/E$ can be obtained as a function of $\Delta\tau$ by setting the probe delay-line to the peak of the THz pulse and scanning the pump-delay line while chopping the pump pulse. Figure 4.11 shows an example of these three measurements for the sample CNT film measured in figure 4.9. Note that when scanning the

THz pulse in figure 4.11a we zero our data after the main pulse, meaning multiple reflections from any substrates such as quartz are ignored.

4.4.3 Bandwidth Issues

We note here that many THz-TDS setups typically have bandwidths of 0.2-2.5 THz. Our THz-TDS setups may be limited in several ways, resulting in the reduced bandwidth:

1. The quartz windows in the cryostat transmit less for higher frequencies.
2. Photoconductive switch performance is determined, among other parameters, by pulse duration, pulse intensity, antenna geometry and antenna alignment.
3. Likewise, ZnTe performance is determined by pulse power, pulse duration, crystal thickness, beam alignment, and performance of our balanced photodetectors.
4. We have some issues with electronic noise in our labs due to grounding issues.
5. We measure relatively small differential changes in our samples. As such the bandwidth depends on the measured sample and sampling time, since some samples show larger $\Delta E/E$ than others.

While we cannot say exactly to which extend these factors influence our bandwidth, they are all possible explanations for why we do not achieve the 0.2-2.5 THz bandwidth of similar THz-TDS systems.

4.5 Other Measurement Techniques

In this final section we briefly introduce the other measurement techniques used in this thesis to characterize our nanotubes and nanowires.

4.5.1 UV-Vis and FTIR Spectroscopy

Ultraviolet-visible (UV-Vis) and Fourier-transform infrared (FTIR) spectroscopy are two common non-contact methods for extracting the electronic bandstructure of a material, which observes how molecules within a material selectively absorb light of certain wavelengths. Both techniques measure the transmittance of the material for a range of wavelengths spanning the ultraviolet and optical (UV-Vis), and the infrared (FTIR). As for THz-TDS, both techniques require measurement of the sample as well as an appropriate reference, typically a bare substrate or an empty sample-holder. The transmittance is then given by the ratio I/I_0,

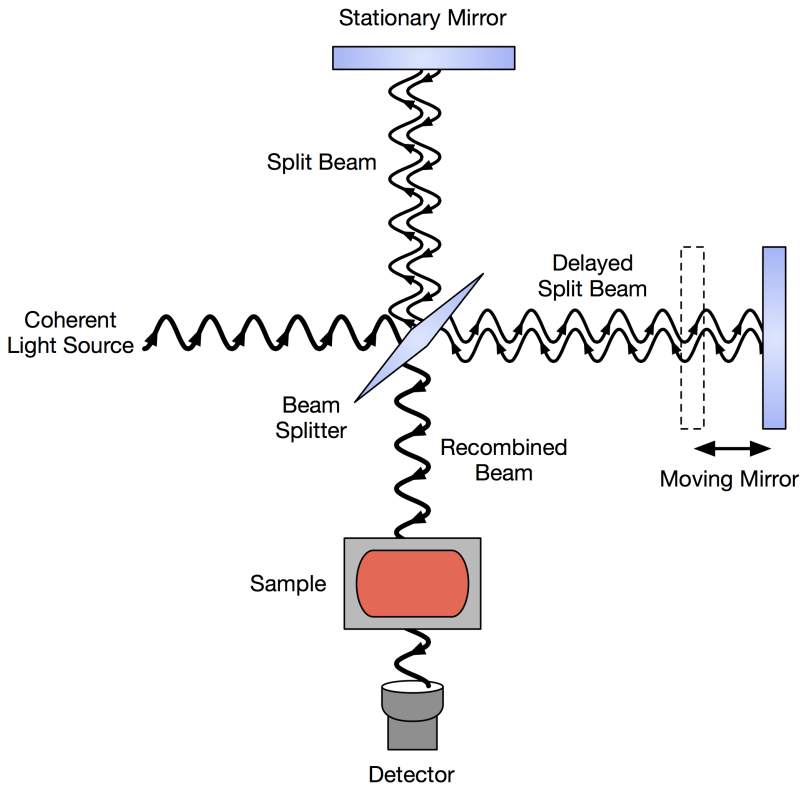

Figure 4.12: Diagram of a Michelson interferometer, used for FTIR. Image source: www.wikimedia.org.

where I and I_0 is the intensity of transmitted light for the sample and reference, respectively. The basic parts of a UV-Vis spectrometer are a light source, a holder for the sample, a diffraction grating in a monochromator or a prism to separate the different wavelengths of light, and a detector. The radiation source is often a tungsten filament (300-2500 nm), a deuterium arc lamp (190-400 nm), or a Xenon arc lamp (160-2000 nm). The detector is typically a photomultiplier tube, a photodiode, a photodiode array, or a charge-coupled device (CCD) [205]. A typical FTIR spectrometer is based on the Michelson interferometer. An infrared beam is emitted from a source and passed through a beam splitter, creating two seperate beams, where one beam has a fixed path-length, while the other beam's path-length is controlled with a movable end mirror, see 4.12. By varying the path-length of the second beam, it is phase-shifted with respect to the first beam, resulting in constructive and destructive interference of specific wavelengths as the two recombine at the sample and detector. By measuring the intensity of the beam as a function of the path-length difference, an interferogram can be constructed and the transmittance of the sample can be obtained as

a function of wavelength, using Fourier transformation. Since the electronic structure of each CNT chirality is largely unique in terms of the energy levels of optical transitions, broadband transmittance measurements obtained from UV-Vis and FTIR are useful for determining the sample composition of a CNT film [206, 207], especially due to the fact that nanotubes are always produced as mixtures of different diameters and electronic types.

4.5.2 Scanning Electron Microscopy

Scanning electron microscopy (SEM) plays an indispensable role in nanoscience and nanotechnology because of its high efficiency and high spatial resolution in characterizing nanomaterials [14]. Figure 4.13a shows a schematic of a typical scanning electron microscope. The electron beam emitted from the cathode tip is accelerated and focused by the anode and magnetic lens, respectively and the focused electron beam scans the specimen point-by-point via scanning coils. The secondary electrons (SEs) are produced by the electron bombardment and collected by the SE detector sequentially. The imaging using the SE signals is called the SE mode of SEM. The SE mode is the most commonly used mode and produces a grayscale image, with the gray value representing the intensity of the SE signal. Such an SEM image contains the surface information, including the topography, the material, and the local surface charge, which are the three main contributors to SE emission, see figure 4.13b. Due to the finite size of the electron beam, SEM cannot reveal the precise dimensions of nanomaterials with diameters around 1 nm. Even so, it can still be quite useful for checking the purity and geometry of prepared CNT films, i.e. whether the CNT network in the film is well-dispersed and without aggregated CNTs [208].

4.5.3 Raman Spectroscopy

Raman spectroscopy is widely-used tool for studying the fundamental properties of 1D nanomaterials, as well as characterizing the their structural properties in terms of purity and defects [208–210]. Similar to THz-TDS, Raman spectroscopy is a contactless optical technique, allowing for direct probing of the nanomaterial response without the need of any invasive contacts. The technique probes the vibrational and rotational modes within a material by measuring the inelastic scattering of monochromatic light off phonons in the material. Raman scattering occurs when a photon is absorbed and scattered by a molecule, following a change in the vibrational, rotational or electronic energy of said molecule. In most cases this scattering event will be elastic (Rayleigh scattering), however a small percentage of incident photons will experience a decrease (Stokes) or increase (anti-Stokes) in energy after the scattering event, where the change in energy coincides with the energy-difference between two

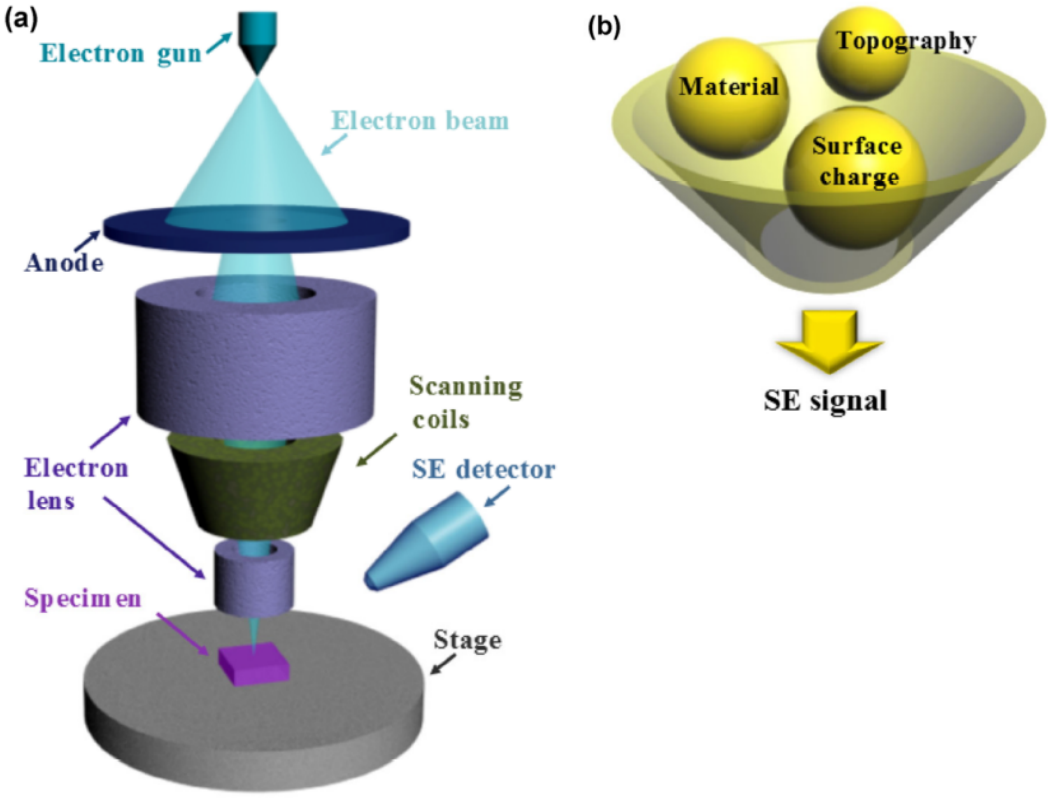

Figure 4.13: Schematic of (a) a typical SEM and (b) the main contributors to the SE signal. Image source: [14].

vibrational or rotational states in the molecule. In quantum mechanical terms the scattering event can be described as an excitation to a virtual state, followed by a relaxation to another vibrational state, see figure 4.14.

Raman spectroscopy is widely used to determine the diameter of CNTs by measuring their so-called "radial breathing mode" (RBM), i.e. where all atoms of the tube vibrate in-phase in the radial direction [211]. Here the RBM frequency scales roughly linearly with the inverse tube diameter. Raman spectroscopy is also used in conjunction with SEM to determine the quality of fabricated CNTs, specifically the defect-density [208]. The defect-density is estimated from the ratio of the G-band at $\sim$1593 cm^{-1}, originating from the longitudinal optical phonons of semiconducting CNTs, and the D-band at $\sim$1335 cm^{-1} (G/D ratio), which has been found to be a good estimate of the defect density for CNTs with diameters of $1-2$ nm, assuming the samples are non-aggregated and without adsorbed molecules [208, 212].

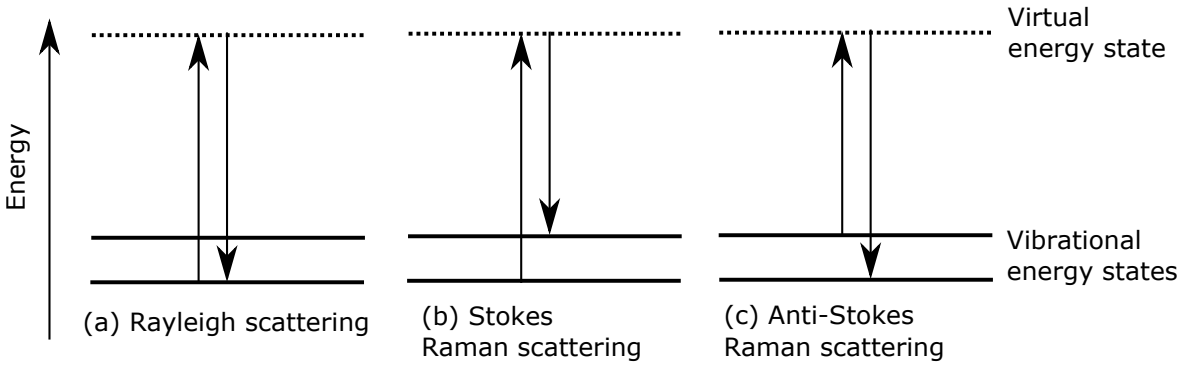

Figure 4.14: Energy level diagram for Raman scattering; (a) Rayleigh scattering, (b) Stokes Raman scattering, and (c) anti-Stokes Raman scattering.

Chapter 5

Analysis of THz-TDS and OPTP Measurements

In this chapter we present the data-analysis methods used in later chapters to extract the dielectric properties of our samples, as well as a general method for analysing the applicability of various approximations used when extracting the dielectric properties. The Matlab and Mathematica source code for these methods are found in appendix B.

5.1 Background

THz-TDS and OPTP are powerful tools for studying the ultrafast charge-carrier dynamics of materials on a femtosecond to nanosecond time-scale, and has successfully been applied to a range of different materials including semiconductors, carbon nanotubes, nanowires, and polymers [15, 66, 156, 197]. The power of this method lies in the extraction of the complex material parameters (represented by a complex permittivity, refractive index or conductivity) from photoinduced changes to the THz transmission/reflection of a sample [198–200]. This approach has allowed the study of a wealth of photo-species and phenomena, including exciton dynamics [201], plasmon formation [202], coulomb screening [203] and carrier scattering [204].

While the equilibrium material parameters of a sample are fairly trivial to extract through THz-TDS in the majority of cases, the same is not true for the non-equilibrium material parameters of a sample in an OPTP experiment. These require full wave solutions to Maxwell's equations, which must be numerically solved [213, 214]. However, depending on the geometry and dimensions of the sample, in some cases a set of simplified equations may be used to obtain approximate material parameters of the photoexcited sample, as shown in [200]. The most commonly used approaches assume either a very thin or thick sample relative to the

wavelength of the incident THz radiation, and have been used by numerous groups throughout the literature for a variety of thin- [215–232] and thick-films [199, 233–235]. Less simplified approximations have also been used for more complex geometries [66, 201, 236–241]. All of these approximations are based on a number of assumptions and approximations in terms of the probe wavelength and the magnitude of the relative change in transmission/reflection due to photoexcitation. It is important to note that improper use of these simplified equations can give a significant deviation from the expected material parameters, which may in turn lead to incorrect conclusions regarding the underlying charge-carrier dynamics of the material [199]. However, assessing the appropriate approximation for a given sample is not always trivial, since there are no clear boundaries for validity.

In this chapter, we present the methods used in later chapters to obtain the equilibrium and non-equilibrium material parameters of our samples. We also present a general method for evaluating the accuracy of various approximations for any particular sample geometry. We achieve the latter by using a modified transfer matrix method to simulate the transmitted and reflected fields of a photoexcited, multilayer structure, where the thickness of each layer and the photoinduced change in the complex refractive index are treated as input parameters. We then use these fields to extract approximate solutions for the complex refractive index of the material, which we compare to the input parameters, allowing us to assess ranges of validity. Using this method we calculate the relative error of the most commonly used approximations for a broad range of sample geometries, where the probe wavelength ranges from much smaller to much larger than the optical penetration depth of the pump beam in the material. Somewhat surprisingly, we find that these approximations are truly valid only in extreme cases where the optical thickness of the sample is several orders of magnitude smaller or larger than the probe wavelength. We then go beyond the most commonly applied approximations, using a general numerical approach based on the transfer matrix method, which exhibits a much broader range of validity.

5.2 The Transfer Matrix Method

In standard THz-TDS and OPTP experiments the material of interest will typically be part of some multilayer structure. For example, the sample can be placed on a substrate or in a cuvette. For THz-TDS, the THz transmission/reflection of this entire multilayer structure is measured, along with an appropriate reference. This gets further complicated on photoexcitation, where part or all of this multilayer structure experiences a changes in optical parameters, and the photoexcited change in the THz transmission/reflection of the entire structure is measured. One therefore wants a full wave solution capable of determining the

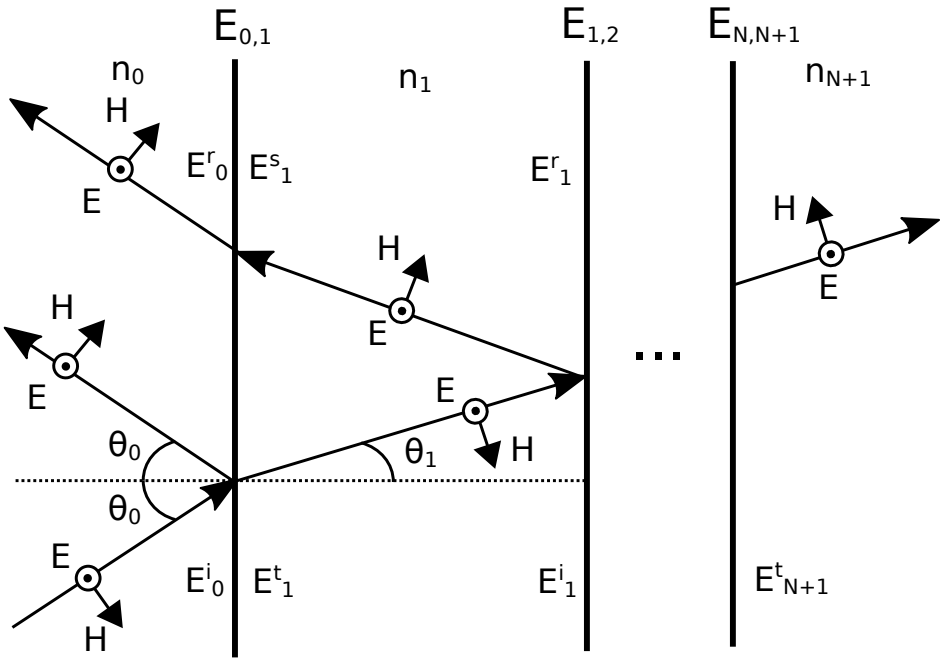

Figure 5.1: Wave propagation of TE-polarized field with incident angle θ_0 through a multilayer structure of N layers, each with a refractive index n_j, where $j = 0, 1, 2, \ldots, N+1$. The continuous THz field at each interface $E_{j,j+1}$ is determined by the incident (E^i, E^s), reflected (E^r) and transmitted (E^t) fields at each side of the interface, with $E^-_{j,j+1} = E^i_j + E^r_j$ and $E^+_{j,j+1} = E^t_{j+1} + E^s_{j+1}$ for the left and right side respectively.

complex transmission and reflection coefficients of arbitrary multilayers of differing index. The most straightforward approach here uses the *transfer matrix method* (TMM). Below, we summarize the important definitions and equations, but a full derivation can be found in any introductory textbook on optics, for example Pedrotti et al. [242, Chapter 22].

Figure 5.1 shows a general N-layer structure consisting of homogeneous layers of thickness d_j and complex refractive index n_j, where $j = 0, 1, 2, \ldots, N+1$. Here layer 0 and $N+1$ are the semi-infinite incident and transmitted regions, respectively. The electric (E) and magnetic (H) fields at interfaces j and $j+1$ are related through

$$\begin{pmatrix} E_{j-1,j} \\ Z_0 H_{j-1,j} \end{pmatrix} = \begin{pmatrix} \cos\delta_j & \frac{-i\sin\delta_j}{\gamma_j} \\ -i\gamma_j \sin\delta_j & \cos\delta_j \end{pmatrix} \begin{pmatrix} E_{j,j+1} \\ Z_0 H_{j,j+1} \end{pmatrix}, \tag{5.1}$$

where Z_0 is the free-space impedance, $\delta_j = \omega n_j d_j \cos\theta_j / c$ is the complex phase (including absorption) accumulated through the j'th layer, θ_j is the incident angle on the j'th interface, ω is the angular frequency of the fields, and $\gamma_j^{TE} = n_j \cos\theta_j$ and $\gamma_j^{TM} = \cos\theta_j / n_j$ for TE-

and TM-polarization, respectively. We define the transfer matrix for the j-th layer as

$$M_j \equiv \begin{pmatrix} \cos\delta_j & \frac{-i\sin\delta_j}{\gamma_j} \\ -i\gamma_j \sin\delta_j & \cos\delta_j \end{pmatrix}. \tag{5.2}$$

The fields transmitted through the entire multilayer structure are related to the incident fields via the relation

$$\begin{aligned} \begin{pmatrix} E_{01} \\ Z_0 H_{01} \end{pmatrix} &= M_1 M_2 \cdots M_N \begin{pmatrix} E_{N,N+1} \\ Z_0 H_{N,N+1} \end{pmatrix} \\ &= M_{tot} \begin{pmatrix} E_{N,N+1} \\ Z_0 H_{N,N+1} \end{pmatrix}, \end{aligned} \tag{5.3}$$

where M_{tot} is the total transfer matrix of the system, given by

$$M_{tot} = \begin{pmatrix} m_{11} & m_{12} \\ m_{21} & m_{22} \end{pmatrix}. \tag{5.4}$$

Equation (5.3) can be rewritten in terms of E_0^i, E_0^r and E_{N+1}^t:

$$\begin{pmatrix} E_0^i + E_0^r \\ (E_0^i - E_0^r)\gamma_0 \end{pmatrix} = M_{tot} \begin{pmatrix} E_{N+1}^t \\ \gamma_j E_{N+1}^t \end{pmatrix}. \tag{5.5}$$

The reflection (r) and transmission (t) coefficients for the entire structure can then be found from (5.5)

$$r = \frac{E_0^r}{E_0^i} = \frac{\gamma_0 m_{11} + \gamma_0\gamma_t m_{12} - m_{21} - \gamma_t m_{22}}{\gamma_0 m_{11} + \gamma_0\gamma_t m_{12} + m_{21} + \gamma_t m_{22}}, \tag{5.6}$$

$$t = \frac{E_{N+1}^t}{E_0^i} = \frac{2\gamma_0}{\gamma_0 m_{11} + \gamma_0\gamma_t m_{12} + m_{21} + \gamma_t m_{22}}. \tag{5.7}$$

If n_j and d_j is known for each layer, it is fairly straight-forward to calculate the transmitted and reflected fields of the multilayer structure. The reverse is also possible, i.e. equation (5.6) or (5.7) can be solved for an unknown n_j, assuming the incident and transmitted/reflected fields are known, which is normally the case in THz-TDS and OPTP experiments. However, without further approximations of equations (5.6) and (5.7), these must be found numerically, which can be resource and time intensive, depending on the complexity of the multilayer structure.

5.3 Analysis of THz-TDS Measurements

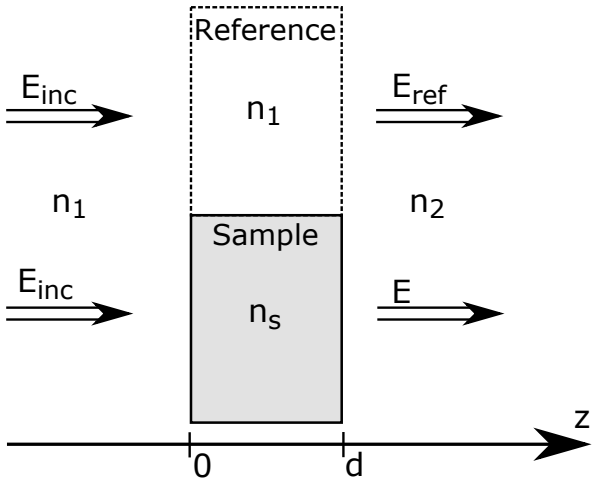

Figure 5.2: Diagram of typical THz-TDS experimental scenario. A THz pulse E_{inc} is incident on a sample with refractive index n_s, surrounded by an incident (n_1) and transmitted medium (n_2). By measuring the transmitted THz pulse of the system with/without the sample, E and E_{ref}, respectively, the dielectric properties of the sample can be obtained.

In most THz-TDS experiments, one typically deals with a simple three layer structure: The sample of interest, n_s, surrounded by two mediums, n_1 and n_2, which we can consider semi-infinite for the purpose of our analysis, see figure 5.2. By measuring the transmitted THz pulse of the system with/without the sample, E and E_{ref}, respectively, the dielectric properties of the sample can be obtained. While one can use the TMM formalism in section 5.2 for the geometry in figure 5.2, for such a relatively simple system it is often easier to derive E and E_{ref} from the Fresnel equations. The Fresnel transmission and reflection coefficients for normal incidence are given by

$$t_{ij} = \frac{2n_i}{n_i + n_j}, \tag{5.8}$$

$$r_{ij} = \frac{n_i - n_j}{n_i + n_j}, \tag{5.9}$$

where i and j are the incident and transmitted mediums at the interface. As mentioned in section 5.2, the complex phase accumulated through the j'th layer is given by $\delta_j = \omega n_j d_j / c$. The transmitted fields in figure 5.2 (including multiple internal reflections in the sample) are

then given by

$$E(\omega) = \frac{t_{1s}t_{s2}e^{i\delta_s}}{1 - r_{s1}r_{s2}e^{2i\delta_s}} E_{inc}(\omega), \tag{5.10}$$

$$E_{ref}(\omega) = t_{12}e^{i\delta_1} E_{inc}(\omega), \tag{5.11}$$

where the denominator in equation (5.10) represents multiple reflections in the sample (Fabry-Perot resonance):

$$\sum_{i=0}^{k} r_{s1}r_{s2}e^{2i\delta_s} \xrightarrow{k\to\infty} \frac{1}{1 - r_{s1}r_{s2}e^{2i\delta_s}}, \tag{5.12}$$

where we have assumed that the reflections inside the sample (k) go to infinity. This leads to

$$\frac{E(\omega)}{E_{ref}(\omega)} = \frac{t_{1s}t_{s2}}{t_{12}} \frac{e^{i(\delta_s - \delta_1)}}{1 - r_{s1}r_{s2}e^{2i\delta_s}}. \tag{5.13}$$

Equation (5.13) can then be solved numerically for the unknown n_s (and thus the permittivity, ϵ, and conductivity, σ, see equations (2.2) and (2.3)), assuming the thickness of the sample, d, is known. If the phase accumulated through the sample is small, i.e. $\delta_s << 1$, it is possible to obtain an analytical expression by Taylor-expanding the exponentials in equation (5.13). For the majority of our samples in later chapters this is not the case, so we choose to solve (5.13) numerically. However, the time and resources needed to solve equation (5.13) are minimal for any modern low-end computer.

5.4 Analysis of OPTP Measurements

The goal of an OPTP experiment is to determine the photoinduced change in the THz optical properties of a sample. This is done by measuring either the transmitted or reflected electric field of the photoexcited sample E_{exc}, as well as an appropriate reference, usually the unexcited sample E. From these two measurements, the non-equilibrium refractive index of the photoexcited sample n_{exc} can be determined by solving the equation

$$\frac{E_{exc}(\omega, n_{exc})}{E(\omega)} = \frac{t_{exc}(\omega, n_{exc})}{t(\omega)}, \tag{5.14}$$

where t and t_{exc} are the complex transmission functions of the unexcited and photoexcited multilayer structure. Equation 5.14 is commonly written in terms of the change in transmitted

electric field $\Delta E = E_{exc} - E$:

$$\frac{\Delta E(\omega, n_{exc})}{E(\omega)} = \frac{t_{exc}(\omega, n_{exc})}{t(\omega)} - 1. \tag{5.15}$$

Assuming the equilibrium refractive index and thickness of each layer of the multilayer structure are known, and that the dynamics of relaxation are slow compared the period of the THz radiation, one can solve equation (5.15) as a function of the non-equilibrium index n_{exc} for a given angular frequency ω. In figure 5.3 we consider a common scenario of a sample with refractive index n_s, surrounded by an incidence (n_1) and transmission medium (n_2). If the sample is photoexcited, one expects a non-equilibrium index that varies spatially through the sample, depending on the penetration of the pump pulse into the sample. At this point we will briefly switch to consider the permittivity $\epsilon = n^2$, since this parameter is easier to describe in terms of the photo-induced changes in the sample, $\Delta\epsilon$. If pump absorption is linear, and the amplitude of the THz response also varies linearly with the density of photospecies, the photoinduced change in permittivity $\Delta\epsilon$ (and conductivity $\Delta\sigma$) is expected to decay exponentially in the propagation direction, following the attenuation of the incident pump, and described by a decay length defined by a penetration depth d_p of the pump light, as assumed in [15, 76, 200]:

$$\Delta\epsilon(z) = \Delta\epsilon_0 e^{-z/d_p}, \tag{5.16}$$

where $\Delta\epsilon_0$ is the change in permittivity at the surface of the sample, which is assumed to be sufficiently small so that it scales linearly with the incident pump light. Equation 5.16 can then be rewritten in terms of the change in refractive index $\Delta n(z) \equiv n_{exc}(z) - n_s$ using the fact that $n + \Delta n = (\epsilon + \Delta\epsilon)^{1/2}$:

$$\Delta n(z) = (n_s^2 + \Delta\epsilon_0 e^{-z/d_p})^{1/2} - n_s \tag{5.17}$$

$$= (n_s^2 + (\Delta n_0 + 2n_s)\Delta n_0 e^{-z/d_p})^{1/2} - n_s, \tag{5.18}$$

where we have similarly assumed a small Δn_0. In this case, the spatially varying refractive index can be approximated by dividing the sample into N homogeneous layers, each with a refractive index $n_{exc}(z)$ determined by the distance z into the sample. Using equations (5.7), (5.15) and (5.17) it is then possible to determine Δn_0 from the experimentally obtained $\Delta E/E$, given that thickness (d), penetration depth (d_p) and refractive index (n_s) of the sample is known. However no analytical solution exists for Δn_0 in its current form, so a solution must be obtained numerically, which can be resource and time consuming depending

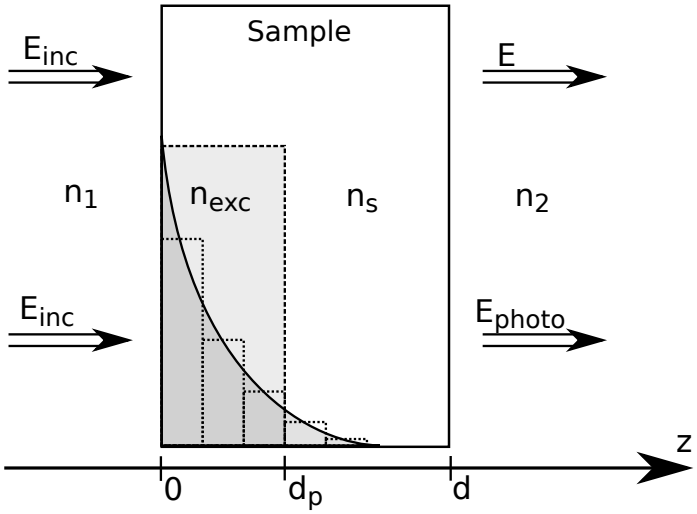

Figure 5.3: Diagram of typical pump-probe experimental scenario. A sample with refractive index n_s, surrounded by an incident (n_1) and transmitted medium (n_2), is photoexcited due to an incident pump pulse with penetration depth d_p, resulting in a new photoexcited refractive index at the surface of the sample n_{exc}. Here E_{exc} and E are the transmitted fields through the photoexcited and unexcited sample, respectively. The photoexcitation decays exponentially within the sample due to attenuation of the incident pump, where d_p is the distance at which the pump intensity has decayed to $1/e$. We represent this by dividing the sample into N homogeneous layers, each with a refractive index $n_{exc}(z)$ determined by the distance z into the sample. This is commonly approximated as a single homogeneous layer of thickness d_p and refractive index n_{exc}.

on the size of N.

A common approximation is to represent the photoexcitation as a single homogeneous layer of thickness d_p and constant photoexcited refractive index n_{exc}. This four-layer system can then be solved numerically as before using equations (5.7) and (5.15). Depending on the size of the wavelength inside the sample $\lambda_s = \lambda_0/Re(n)$ compared to the thickness and penetration depth of the sample, various approximations can be made, which result in a simpler solution for Δn [199, 200, 243]. In order to obtain an analytical solution, the most common approximations assume a small perturbation of the photoexcited sample, i.e. $\Delta E/E << 1$ and $\Delta n/n_s << 1$, and that the wavelength is much shorter or much larger than the thickness and penetration depth of the sample, i.e. $\lambda_s/d_p << 1$ or $\lambda_s/d >> 1$

[15, 199, 233, 234, 243]:

$$\Delta n \xrightarrow{\lambda_s/d_p \to 0} -\frac{ic}{\omega d}\frac{\Delta E}{E} \qquad \text{(short } \lambda \text{ limit)}, \tag{5.19}$$

$$\Delta n \xrightarrow{\lambda_s/d_p \to \infty} -\frac{n_s}{(n_1+n_2)}\frac{ic}{2\omega d}\frac{\Delta E}{E} \qquad \text{(long } \lambda \text{ limit)}. \tag{5.20}$$

Equation (5.19) is known as the short wavelength limit or thin-film approximation, and equation (5.20) is known as the long wavelength limit or thick sample approximation and in the following section we will give a full derivation, along with equivalent expressions written in terms of either the complex permittivity or the complex conductivity, which some authors tend to use instead. In the case of a thick sample with a thin photoexcited region compared to the wavelength, i.e. $\lambda_s/d_p >> 1$ and $\lambda_s/d << 1$, a similar expression to equation (5.20) can be derived where n_2 and d is replaced by n_s and d_p, respectively.

5.4.1 Derivation of the Short- and Long-Wavelength Limit

The short- and long-wavelength limit in equations (5.19) and (5.20) can be derived from the Fresnel equations under the assumption that the photo-induced change in the dielectric properties of the sample are small, i.e. $\Delta E/E << 1$ and $\Delta n/n << 1$. Furthermore, we assume a homogeneous excitation of the entire sample shown in figure 5.3. The Fresnel transmission and reflection coefficients for normal incidence are given by equations (5.8) and (5.9). For the geometry shown in figure 5.3 the transmitted electric field through the photoexcited (E_{exc}) and unexcited (E) sample is then given by

$$E = \frac{t_{1s}t_{s2}e^{i\delta_s}}{1 - r_{s1}r_{s2}e^{2i\delta_s}}, \tag{5.21}$$

$$E_{exc} = \frac{t_{1e}t_{e2}e^{i\delta_e}}{1 - r_{e1}r_{e2}e^{2i\delta_e}}, \tag{5.22}$$

where the indices e and s denotes the photoexcited and unexcited sample, respectively, and $\delta_j = \omega n_j d/c$ is the accumulated phase through layer j. In equations (5.21) and (5.22), the numerator represents direct transmission through the sample, while the denominator represents multiple internal reflections in the sample. The relative change in the transmitted electric field $\Delta E/E$ is then given by

$$\frac{\Delta E}{E} = \frac{t_{1e}t_{e2}e^{i(\delta_e-\delta_s)}}{t_{1s}t_{s2}}\frac{(1 - r_{s1}r_{s2}e^{2i\delta_s})}{(1 - r_{e1}r_{e2}e^{2i\delta_e})} - 1. \tag{5.23}$$

In order to solve equation (5.23) for Δn analytically, we need to Taylor expand the exponentials by assuming $\delta_e, \delta_s << 1$:

$$\begin{aligned}\frac{\Delta E}{E} =& \frac{t_{1e}t_{e2}(1+i\delta_e-i\delta_s)}{t_{1s}t_{s2}} \\ &\times \frac{1-r_{s1}r_{s2}(1+2i\delta_s)}{1-r_{e1}r_{e2}(1+2i\delta_e)} - 1\end{aligned} \tag{5.24}$$

Equation (5.24) can then be reduced by discarding higher order terms of Δn, and subsequently solved for Δn:

$$\Delta n = \frac{c(c(n_1+n_2)+id(n_1-n_2)(n_2-n_s)\omega)}{d\omega(2icn_s+d(n_1-n_s)(n_2-n_s)\omega)}\frac{\Delta E}{E} \tag{5.25}$$

By taking the limit of $d \to 0$ and $d \to \infty$, the approximations in equations (5.19) and (5.20) are obtained:

$$\Delta n \xrightarrow{d\to\infty} -\frac{ic}{\omega d}\frac{\Delta E}{E} \qquad \text{(short } \lambda \text{ limit)} \tag{5.26}$$

$$\Delta n \xrightarrow{d\to 0} -\frac{n_s}{(n_1+n_2)}\frac{ic}{2\omega d}\frac{\Delta E}{E} \qquad \text{(long } \lambda \text{ limit).} \tag{5.27}$$

Equations (5.26) and (5.27) can be rewritten in terms of the complex permittivity using $\Delta\epsilon = (n_s+\Delta n)^2 - n_s^2$:

$$\Delta\epsilon_{short} = -\frac{2icn_s}{\omega d}\frac{\Delta E}{E}, \tag{5.28}$$

$$\Delta\epsilon_{long} = -\frac{ic(n_1+n_2)}{\omega d}\frac{\Delta E}{E}, \tag{5.29}$$

where we have discarded the second order term of $\Delta E/E$ under the assumption that $\Delta E/E << 1$. Likewise, the complex conductivity can be found from equations (5.28) and(5.29) using $\Delta\sigma = -i\omega\epsilon_0\Delta\epsilon$:

$$\Delta\sigma_{short} = -\frac{2c\epsilon_0 n_s}{d}\frac{\Delta E}{E}, \tag{5.30}$$

$$\Delta\sigma_{long} = -\frac{c\epsilon_0(n_1+n_2)}{d}\frac{\Delta E}{E}, \tag{5.31}$$

It is important to note that for the long wavelength limit in equations (5.27), (5.29) and (5.31) we have assumed that the wavelength is much larger than the thickness of the sample. However, it is straightforward to derive a similar expression, where we consider a thin photoexcited region of thickness $d << \lambda$ at the surface of a semi-infinite sample, which is

another common approximation in OPTP. In this case, n_2 and d become the refractive index of the sample n_s, and the thickness of the photoexcited region d_p, respectively. Likewise the d in equations (5.26), (5.28) and (5.30) can be interchanged with the penetration depth d_p in the case where we are no longer considering a homogeneous excitation of the entire sample.

5.4.2 Evaluation of Analysis Methods

We now examine the relative error of the four different cases mentioned so far, specifically the short and long wavelength limits from equations (5.19) and (5.20), the full TMM approach described earlier using $N = 10$ layers to represent the photoexcited sample, and the full TMM approach but with the photoexcited region of the sample approximated as a single homogeneous layer of thickness d_p and refractive index n_{exc}. However, we emphasize that this analysis approach is a general evaluation method for any of the approximations found in the literature for these types of experiments [200], applied to any sample geometry that can be represented as a multilayer structure. The entire analysis and calculations were performed using Mathematica, see appendix B for the source-code and further details on how the figures in this section were produced.

In order to analyse the relative error of the different approximations, we simulate an experiment of a photoexcited sample of known thickness d, penetration depth $d_p = d/4$, and refractive index $n_s = 3 + 1i$, with the incident region being air ($n_1 = 1$), and the transmitted region being a quartz substrate ($n_2 \approx 2$)[244]. The photoinduced response $\Delta n(z)$ is modelled according to equation (5.17), where we choose $N = 100$ and $\Delta n_0 = (1 + 1i) \times 10^{-6}$ so that $\Delta E/E << 1$ for all wavelengths ranging from $\lambda_s/d = 10^{-2}$ to $\lambda_s/d = 10^4$. We then feed the generated $\Delta E/E$ into the various analysis methods and compare the resulting Δn_0^{out} with the input value of Δn_0. The resulting relative error, $(\Delta n_0^{out} - \Delta n_0)/\Delta n_0$, is plotted in figure 5.4a as a function of the wavelength normalized to the thickness of the sample λ_s/d, see appendix B for details of the calculations. As predicted, there is a significant error when the wavelength becomes comparable with the sample thickness, i.e. $\lambda_s/d \approx 1$, with a 20–50% relative error for the approximations in equation (5.19) and (5.20), and a 11% relative error when using the TMM approach while assuming a homogeneous photoexcited layer. The short and long wavelength approximations converge to the 2% relative error for $\lambda_s/d << 1$ and $\lambda_s/d >> 1$, respectively, but more surprisingly their relative error quickly becomes significant as λ_s/d approaches 10^{-1} and 10^3, respectively. This underlines the danger of using these approximations without properly analysing their applicability for a given sample. Furthermore, we note that the error of these approximations will scale with the relative variation between n_s and the surrounding mediums (n_1, n_2), where in this case

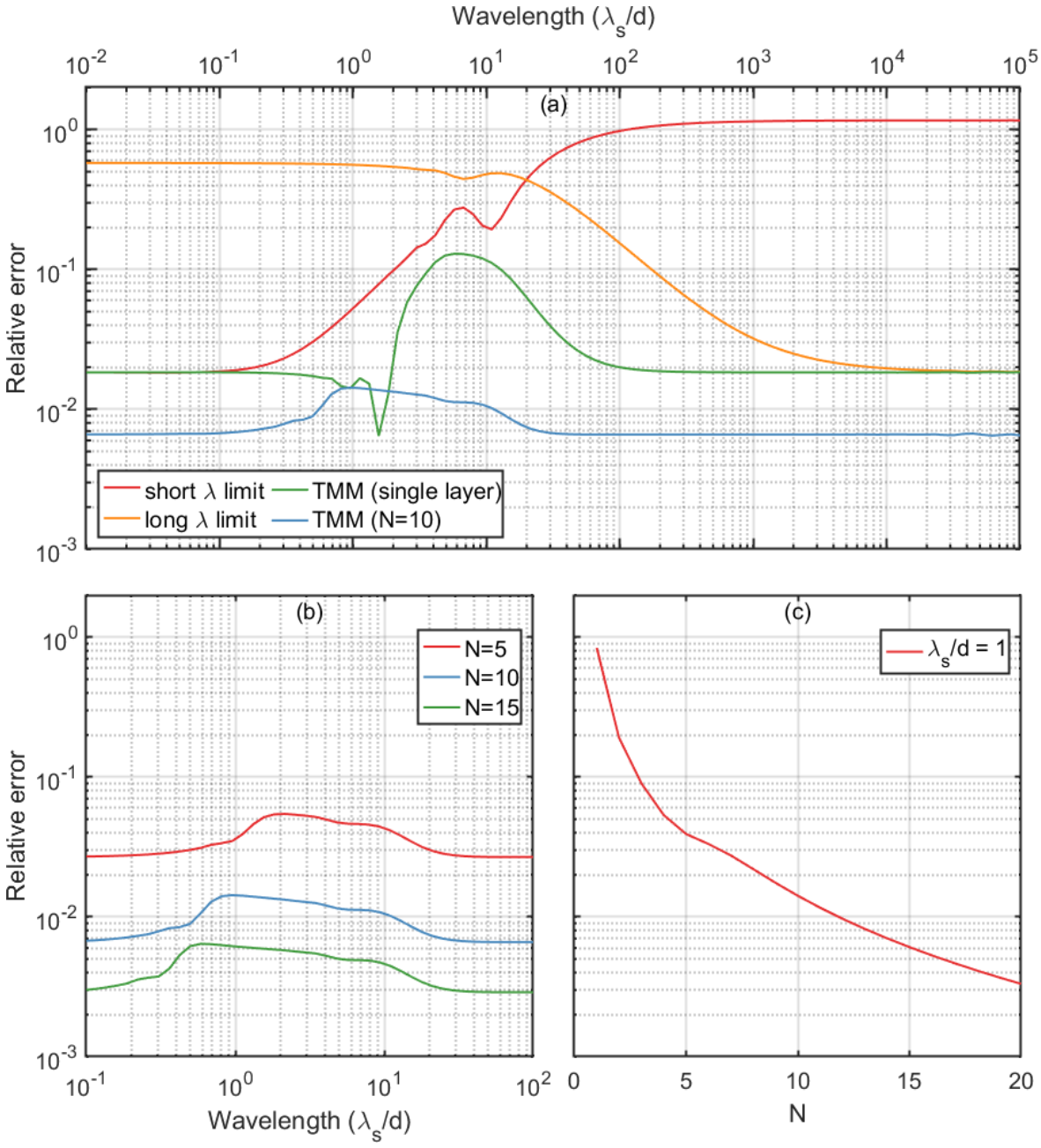

Figure 5.4: **(a)** Relative error of the different approximations of Δn_0 from the true value as a function of wavelength inside the sample λ_s/d. Here "short λ limit" and "long λ limit" are the short and long wavelength limit, "TMM (N = 10)" is the numerical transfer matrix method approach with the photoexcited sample represented by $N = 10$ layers, and "TMM single layer" uses the same transfer matrix method approach but with the photoexcitation being approximated as a single homogeneous layer of thickness d_p and refractive index n_{exc}. Furthermore, the relative error of the transfer matrix method approach is plotted **(b)** as a function of λ_s/d for $N = 5, 10, 15$, and **(c)** as a function of N for $\lambda_s/d = 1$.

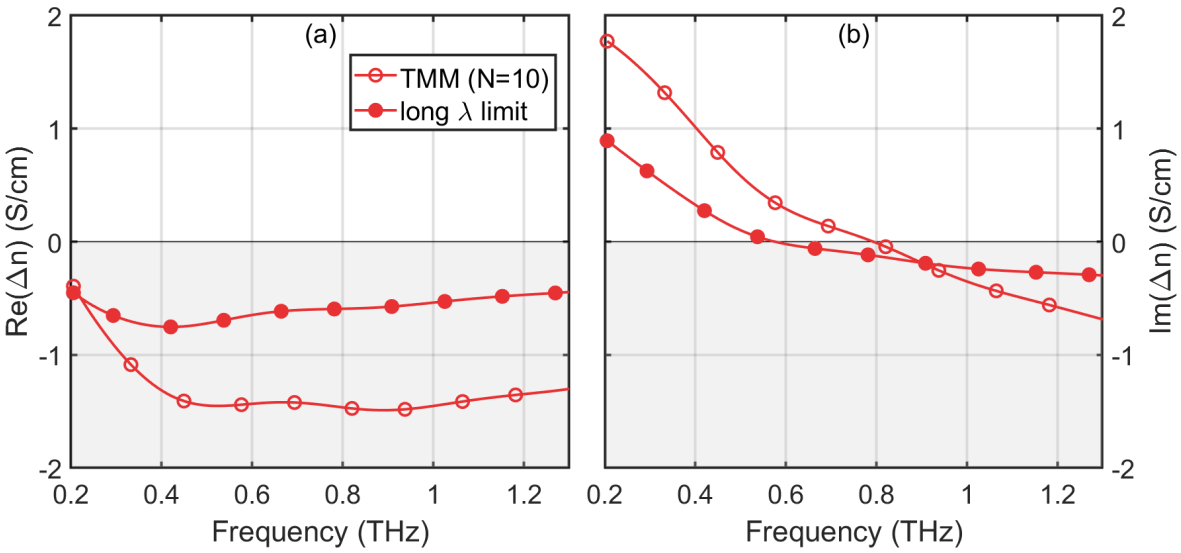

Figure 5.5: The extracted photo-induced change in refractive index **(a)** $\mathrm{Re}(\Delta n)$ and **(b)** $\mathrm{Im}(\Delta n)$ of a thin-film of carbon nanotubes with thickness $d = 700$ nm, penetration depth $d_p = 285$ nm, and refractive index $n_s = 13 + 9i$ at 1 THz, corresponding to $\lambda_s/d = 37$ for 1 THz, placed on a quartz substrate. We compare the resulting Δn using the long wavelength limit with using the full TMM approach for $N = 10$.

we have chosen a relatively small complex refractive index for the sample. Using the TMM approach with $N = 10$ achieves a relative error of less than 2% for $\lambda_s/d = 1$ in this case, and in figures 5.4b-5.4c we compare how the error converges as a function of N. We see that for $\lambda_s/d = 1$, the TMM approach converges relatively quickly for $N < 5$, but slows down beyond that, achieving a relative error less than of 1% for $N \geq 12$. This demonstrates that the TMM approach is valid for all wavelengths as long as N is large enough. Thus TMM is a valid option in the case where no other approximation is applicable, with the only limitation being computation time and memory requirement, which will scale with N.

Finally in figure 5.5 we examine a specific case of experimentally obtained data from a typical OPTP experiment, in this case a film of single-walled carbon nanotubes of thickness 700 nm and average tube length of 1 μm on a quartz substrate, where we have probed $\Delta E/E$ two picoseconds after photoexcitation with an 800 nm, 100 fs pump pulse, see chapters 6 and 7 for details of the sample preparation and the experimental setup. The sample geometry is the same as in figure 5.3, where the refractive index of the sample at 1 THz is approximately $n_s = 13 + 9i$, $n_1 = 1$ and $n_2 = 1.96$. In this case $\Delta E/E \leq 4\%$, $\lambda_s/d = 37$ for 1 THz, and the penetration depth d_p is 285 nm. A first guess might be to use the long wavelength limit in equation (5.20), since the wavelength is 10 times larger than the sample thickness,

so in figure 5.5 we plot the obtained complex photo-induced change in refractive index Δn, extracted using the long wavelength limit and using the full TMM approach with $N = 10$. We see that the two methods give remarkably different signals in terms of the frequency behaviour and the magnitude, which illustrates the error that can occur with improper use of these methods. To get a better estimate of the relative error of either approach, the next step would then be to use the calculated Δn (or simply choose an initial guess for Δn) to simulate $\Delta E/E$ using TMM and then compare the resulting Δn with the original result. If the method is accurate, the result should be the same as the original input value of Δn.

5.5 Conclusion

In conclusion we have formulated a general method for evaluating the applicability of any approximation used for obtaining the photoinduced change in dielectric properties of a sample in OPTP experiments. The method is valid for any given multilayer geometry and wavelength. Using this method we evaluate three of the most commonly used approximations and show that they quickly become invalid as the wavelength becomes comparable with the sample thickness. This demonstrates the need to properly analyse the applicability of an approximation for a given sample geometry, since improper use of these approximations can lead to significant errors, which in turn can lead to an incorrect interpretation of the photoexcited response.

Chapter 6

Influence of Nanotube Length and Density on the Plasmonic Terahertz Response of Single-Walled Carbon Nanotubes

We begin by acknowledging the contributions of our collaborators to the content presented in this chapter. The WS_2 nanotubes (INT) were provided by Reshef Tenne at the Department of Materials and Interfaces, Weizmann Institute of Science, Israel. The *s*-, *m*-, *met*-, and *sem*-CNT films, as well as the $m-$CNT/INT composites were prepared by Dzmitry I. Yuko and Mikhail Shuba at the Institute for Nuclear Problems, Belarus State University. The *l*-CNT films were provided by Albert G. Nasibulin at the Skolkovo Institute of Science and Technology, Moscow, and Department of Applied Physics, Aalto University, Finland. The 99% semiconducting CNTs were provided by Patrizia Lamberti at the Department of Information and Electrical Engineering and Applied Mathematics, University of Salerno, Italy. Chris Beckerleg (University of Exeter) assisted with the SEM measurements in figure 6.4. Mikhail Shuba provided the theoretical analysis of the CNTs in section 6.2, including the calculated conductivity spectra in figures 6.2 and 6.3. Furthermore, he and Dzmitry I. Yuko supplied the Raman spectra in figure 6.5; the broadband optical density and conductivity spectra in figures 6.6, 6.7, and 6.10; and the high temperature (>300 K) THz conductivity spectra in figure 6.9.

6.1 Background

Optical and electronic properties of single-walled carbon nanotubes (CNTs) have been under investigation for over two decades due to their fascinating physical properties and exciting potential for advanced applications [28–32]. Subsequent studies in the low-frequency, far infrared, terahertz and gigahertz ranges, led to proposing CNT-based composites as effective functional materials with tailored electromagnetic properties for these ranges [245–247].

One significant observation that has attracted much attention is a peak in the conductivity of CNT-based composites in the THz range, observed for the first time, to our knowledge, by Bommeli et al. [248]. Two different mechanisms of its origin have been debated in literature. An interband transition corresponding to a small THz-range gap inherent to metallic CNTs [94] (*finite radius effect*) has been proposed as a possible mechanism of a non-Drude-like behaviour of CNTs in THz range [249, 250]. An alternative mechanism has been proposed by Akima and Slepyan et al. [251, 252] as manifestation of the localized plasmon resonance in finite-length CNTs, which we denote the *finite-length effect*. Theoretical modelling [253] and experimental observations [254, 255] substantiates the dominant role of the finite-length effect in the THz peak origin, at least at room temperature. While the two explanations are not mutually exclusive, understanding the true origin of this THz peak is key to a number of potential CNT applications [246]. However, due to the inherent difficulty in fabricating isolated CNT samples, most measurements have been carried out on mixtures of CNTs with various distributions in length, density, thickness, chirality and bundle-size, and fabricated using a variety of techniques [149, 249, 253, 254, 256–258]. Moreover, different temperature dependencies of the THz conductivity for CNTs have been reported [255, 259–261] demonstrating the temperature dependence to be frequency dependent. Zhang et al. [255] shows a weak temperature variation in the CNT films conductivity below 3 THz, while the temperature has been shown to have a much more significant effect on the electronic transport properties of (i) nanotube composites at GHz frequencies [258, 262], and (ii) CNT-films in the mid-infrared range [263].

In this chapter, using THz-TDS, we investigate the influence of tube length and density on the temperature dependence of the THz conductivity spectra for thin-films comprising single-walled CNTs. Using films with different tube concentration we observe a plasmonic THz peak which is related to the effective length of conducting pathways in the CNT network. Due to this plasmonic behaviour, the frequency dependent conductivity is influenced by both tube length and density. This can in turn determine the response as a function of temperature, giving rise to a THz conductivity that increases and decreases with increasing temperature for the cases of low and high tube density, respectively.

6.2 Theoretical Background

All theoretical analysis and calculations in this section was provided by our collaborator, Mikhail Shuba, at the Institute for Nuclear Problems, Belarus State University. Since the theory and number of steps involved with these calculations are quite extensive, we limit ourselves to a brief overview here. Furthermore, throughout this chapter, we choose to describe the frequency dependent electromagnetic response of the CNT-films in terms of the real part of the complex effective conductivity, $\mathrm{Re}(\sigma(\nu))$, and real part of the relative permittivity, $\mathrm{Re}(\epsilon(\nu))$, as in references [249, 250, 253, 254, 264, 265]. These are related through equation (2.3):

$$\epsilon(\nu) = 1 + \frac{i\sigma(\nu)}{2\pi\nu\epsilon_0}, \tag{6.1}$$

where $\epsilon_0 = 8.85\times10^{-12} Fm^{-1}$ is the vacuum permittivity and ν is the frequency. We note that equation (6.1) assumes an isotropic conducting dielectric material. Since our films consist of unaligned CNTs oriented mainly in the plane of the film, their in-plane effective conductivity and permittivity can be considered to be isotropic, with their relation described by equation (6.1).

We begin our theoretical analysis by considering how tube length is expected to influence the THz conductivity resonance (referred to here as the *finite-length effect*). It is straightforward to show that tube length is expected to determine the peak frequency, as well as the temperature dependence of the conductivity spectra. Our carbon nanotubes samples (see Sec. 6.3) contain mostly bundled CNTs, which are assembled into a percolating network. For now, we consider only a diluted composite containing isolated, randomly oriented CNT bundles. We will show that for this composite the temperature dependence of the THz conductivity spectra is affected by the finite-length effect in the CNTs. We use an effective medium model, *the Waterman-Truell formula*, to estimate the effective relative permittivity of the composite material. The Waterman-Truell formula uses a statistical approach to approximate the multiple scattering effects that occur for an incident electromagnetic wave on an array of randomly distributed and randomly oriented, anisotropic inclusions in a host material [266, 267]. This has been adapted for CNTs to give the following expression for the effective permittivity [253]:

$$\epsilon_{eff}(\nu) = \epsilon_h(\nu) + \frac{1}{3\epsilon_0}\sum_j \int_0^\infty \alpha_j(\nu, L) N_j(L) dL, \tag{6.2}$$

where the function $N_j(L)$ describes the number density of the CNT bundles of type j with radius R_j and length L, and ϵ_h is the relative permittivity of the host material. The factor

1/3 in equation (6.2) is due to the random orientations of the inclusions; and α_j is the axial polarizability of a CNT bundle, calculated using the integral equation approach described in [268]. We note that equation (6.2) ignores the electromagnetic interactions between inclusions in the composites. The real part of the effective conductivity can then be found as $\mathrm{Re}(\sigma_{eff}) = 2\pi\nu\epsilon_0\mathrm{Im}(\epsilon_{eff})$.

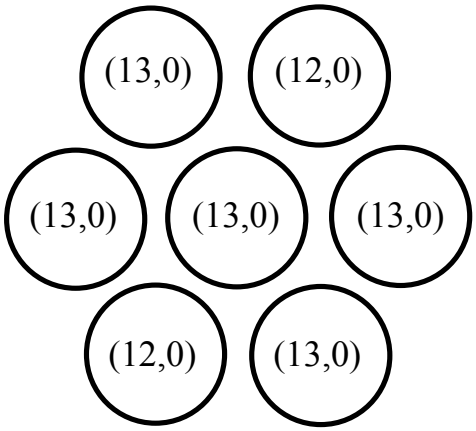

Figure 6.1: Cross-sectional schematic of the bundle of CNTs used in our numerical calculations. Each bundle contains five semiconducting (13,0) CNTs and two metallic (12,0) CNTs.

In our calculations we use $\epsilon_h = 1$ and the volume fraction occupied by the inclusions is $\phi = 20\%$. For simplicity we calculate the effective conductivity of a composite comprising identical bundles of either 1 μm or 10 μm in length. Each bundle consists of 7 tubes: two metallic tubes (12,0) and five semiconducting tubes (13,0) with energy gap of 0.816 eV and chemical potential of 0 eV, see figure 6.1. The axial conductivity of the metallic CNT is approximated by the Drude formula [269], defined by an electron relaxation time $\tau = 1/\gamma$, where γ is the electron scattering rate [253]. The THz conductivity of the semiconducting CNTs is supposed to be negligibly small and does not contribute to the THz response of the bundle.

Figure 6.2 shows $\mathrm{Re}(\epsilon_{eff})$ and $\mathrm{Re}(\sigma_{eff})$ of the CNT composite for different lengths L and electron scattering rates γ. The resonance at 5 THz for $L = 1$ μm and the broad peak at 0.8 THz for $L = 10$ μm are due to the well known finite-length effect in CNTs [252, 253]. Interestingly, the largest variation in both $\mathrm{Re}(\epsilon_{eff})$ and $\mathrm{Re}(\sigma_{eff})$ occurs in the locality of the THz resonance. In the range $\nu \in (0.1, 1)$ THz, dependencies of the conductivity on the scattering rate for short and long tubes are different: both $\mathrm{Re}(\epsilon_{eff})$ and $\mathrm{Re}(\sigma_{eff})$ decrease as γ increases for long-length tubes ($L = 10$ μm), while the opposite occurs for shorter tubes ($L = 1$ μm) as highlighted by the insets. This behaviour arises due to the difference in response on and off resonance.

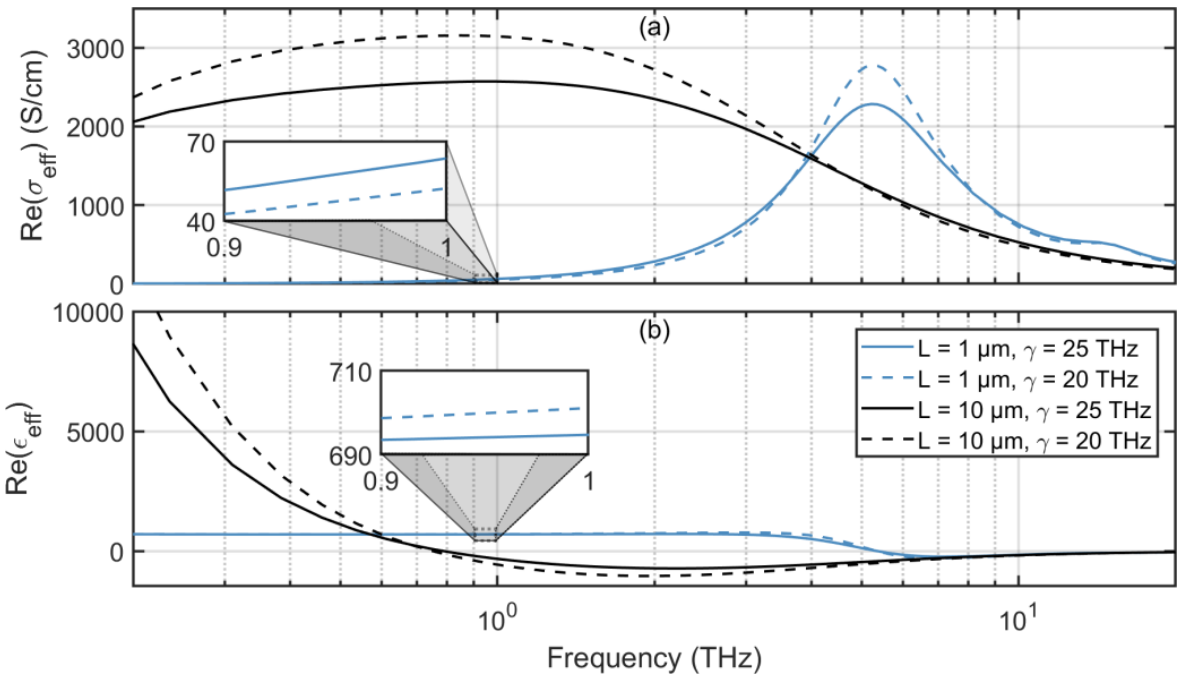

Figure 6.2: Calculated frequency dependence of (a) Re(σ_{eff}) and (b) Re(ϵ_{eff}) at different carbon nanotube lengths L and electron scattering rates γ. The insets show a zoomed area of their respective plots, highlighting the subtle differences for $L = 1$ μm when varying the scattering rate.

Since the dominant scattering mechanism for CNTs is expected to be acoustic phonon scattering [270] (i.e. the scattering rate is expected to increase with increasing temperature, T) we can conclude that, if the effective conductivity is plasmonic in origin, its temperature dependence will be determined by CNT length. For long tubes (tens of microns) the finite-length effect is negligibly small in the THz range and the effective conductivity decreases with increasing temperature. This is expected for the intrinsic conductivity of an individual tube [270]. For shorter tubes, the temperature dependence will be weaker and the conductivity may even increase with increasing temperature in the THz region. This behaviour can be characterized by a crossover frequency, where the value of $\partial \mathrm{Re}(\sigma_{eff})/\partial T$ changes sign.

As was recently shown [263], the temperature induced modification of the infrared conductivity spectra of thin CNT films can occur due to the strong temperature dependence of unintentionally doped semiconducting tubes with Fermi energy located close to the top of the valence band. To demonstrate possible contribution of these tubes to the THz conductivity spectra, we calculated the same CNT-composite as in figure 6.2, but assuming that (13,0) CNTs with energy gap of 0.816 eV has a chemical potential of 0.4 eV and electron scattering

rate for all the tubes in the bundle is $\gamma = 25$ THz. For this case the static conductivity of the semiconducting CNTs, calculated using the model presented in [263], is about 8 times smaller than that of metallic CNTs.

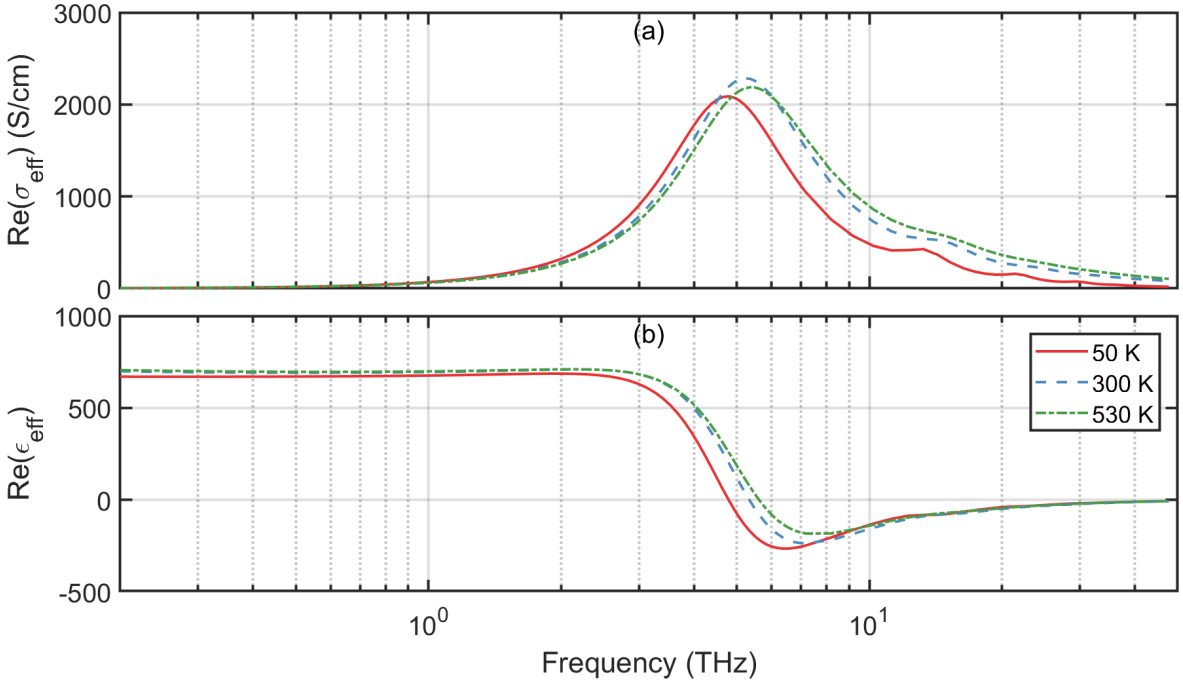

Figure 6.3: Calculated frequency dependence of (a) Re(σ_{eff}), and (b) the Re(ϵ_{eff}) at 50, 300, and 530 K for the composite medium with bundled CNTs. Each bundle comprises doped semiconducting tubes.

In figure 6.3, we present the values of Re(ϵ_{eff}) and Re(σ_{eff}) for a composite containing identical bundles of 1 μm in length at 50 K, 300 K, and 530 K, i.e. the temperature induced change in the conductivity is due to varying the electron Fermi-distribution function of the system. We note that in reality the scattering rate is expected to increase with temperature [271, 272], however in this case we choose a single scattering rate to show the effect of the Fermi distribution. One can see in figure 6.3 that the THz peak is expected to blue-shift slightly on increasing the temperature. In absence of a temperature dependent scattering rate, this effect arises due to an increase of the conductivity of the semiconducting tubes with temperature and, consequently, to the increase of the surface wave velocity in the CNT bundle [273]. The model predicts no temperature induced shift of the THz peak for composite comprising individual doped CNTs. This is confirmed in section 6.6, where we compare the data for bundled and unbundled CNT samples. Similar results were claimed in [268] with respect to the doping effect: substitutional doping leads to the blue-shift of the THz

conductivity peak for a composite comprising bundled tubes; there is no shift if tubes are individual.

6.3 Sample Preparation

To study the influence of tube length on the temperature induced modification of THz conductivity spectra we prepared three types of films comprising CNTs in bundled form, where the average lengths of the CNT bundles in the films varies significantly, see table 6.1. Additionally, to study the influence of bundling (and chirality in chapter 7), we prepared films of individual (unbundled), enriched metallic and semiconducting CNTs:

Sample	D (nm)	L (μm)	d (nm)	sem.	met.
l-CNT	42	2–100 (10)	1.3–2	33%	66%
m-CNT	500	0.3–2 (1)	0.8–1.2	66%	33%
s-CNT	600	< 0.3	0.8–1.2	66%	33%
sem-CNT	500	0.1–1	0.8–1.2	99%	1%
met-CNT	500	0.1–1	0.8–1.2	5%	95%

Table 6.1: Summary of our CNT films; thickness (D), length (L) (average length in parenthesis), diameter (d), and content of semiconducting (sem.) and metallic (met.) CNTs.

1. Free-standing films comprising long length single-walled CNTs (l-CNT, $L \approx 10$ μm, film thickness of 42 nm) with diameters of approximately 1.6 nm was prepared via the aerosol chemical vapour deposition method [274, 275]. These were provided by our collaborator, Albert G. Nasibulin, at the Skolkovo Institute of Science and Technology, Moscow, and Department of Applied Physics, Aalto University, Finland.

2. Free standing films comprising medium length single-walled CNTs (m-CNT, $L \in (0.3, 2)$ μm, average length of about 1 μm, film thickness of 500 nm) were prepared via the vacuum filtration technique [147]. Briefly, a material of non-purified High Pressure Carbon Monoxide (HiPco) CNTs with diameters of 0.8–1.2 nm (NanoIntegris Inc.) were dispersed by ultrasonic treatment (Ultrasonic device UZDN-2T, 44 kHz, maximum power) for 1 hour in an aqueous suspension with 1% Sodium-Dodecyl-Sulfate (SDS). Ultrasonic treatment cut the initially long tubes down to a length of up to 1–2 μm [139]. Then, the suspension was centrifuged at 10000g for 15 minutes. Strong centrifugation leads to purification of the tubes and removes aggregated tubes. The suspension was then filtrated through a membrane, causing a film to collect on the filter. This film was then washed to remove all surfactant. Finally, the filter paper was dissolved by acetone

and the film was transferred on to a metallic frame with a hole of 8 mm in diameter. These films were prepared by our collaborators, Dzmitry I. Yuko and Mikhail Shuba, at the Institute for Nuclear Problems, Belarus State University.

3. Thin films of short length single-walled CNTs (s-CNT, $L < 300$nm, film thickness of 600 nm) were also prepared via the vacuum filtration technique. To obtain short tubes, highly purified (99%) HiPco CNTs with diameters of 0.8–1.2nm (NanoIntegris Inc.), were cut by ultrasonic treatment of the material in a mixture of nitric and sulfuric acids [145]. Like the m-CNT films, these were prepared by our collaborators, Dzmitry I. Yuko and Mikhail Shuba.

4. Free standing films comprising medium length, individual, enriched semiconducting (99%) and metallic (95%) single-walled CNTs, respectively (sem- and met-CNT, $L \in (0.1, 1)$ μm, purchased from NanoIntegris Inc.). These samples were also prepared via the vacuum filtration technique by Dzmitry I. Yuko and Mikhail Shuba. The 99% semiconducting CNTs were provided by Patrizia Lamberti at the Department of Information and Electrical Engineering and Applied Mathematics, University of Salerno, Italy.

Since the observation of a conductivity threshold in polymer/carbon nanotube composites [148] much research has been dedicated to fabricating CNT-based composite materials with percolated networks and understanding their optical and electrical responses [149]. An ongoing issue with preparing CNT composite materials is aggregation, since tubes tend to be electrostatically attracted to each other instead of dispersing uniformly throughout the host material. To study the influence of the tube density on the temperature induced modification of the THz conductivity, we prepared a hybrid composite material consisting of well-dispersed and non-aggregated m-CNTs mixed with non-conductive inorganic WS_2 nanotubes (INT). INTs were synthesized in the large scale fluidized bed reactor (see details in [153]). INTs have diameters 20–180 nm and lengths 1–10 μm; they are semiconducting with a bandgap of 2 eV, and are transparent and non-conductive for THz frequencies. INT material was dispersed in 1% SDS aqueous solution for 30 min by ultrasonication and then the suspension was immediately centrifugated for 15 min at 300g to remove aggregated INTs. The suspensions of INTs and m-CNTs were mixed in different proportions and then filtrated to obtain thin films with thickness between 0.7 and 12 μm. The quantity of both m-CNTs and INTs in suspensions before mixing was controlled via ultraviolet-visible spectroscopy (RV2201 spectrophotometer, ZAO SOLAR, Belarus). This provided us with films of different volume fractions of CNTs. The films were transferred to 10 μm thick PTFE and 1 mm thick quartz substrates for tera-

hertz and microwave measurements. Finally the films on quartz substrates were annealed at 500°C for 30 minutes. Film thickness was measured with the profilometer Veeco Dektak 6 M. The INTs were provided by Reshef Tenne at the Department of Materials and Interfaces, Weizmann Institute of Science, Israel.

6.4 Characterization of Sample Purity and Crystalline Quality

We investigate crystalline quality and purity of our CNT films and CNT/INT composites using a combination of Scanning Electron Microscopy (SEM) and Raman spectroscopy. SEM was used to check the purity of our samples, specifically if the CNTs are well-dispersed and non-aggregated, and if there are any carbonaceous impurities present, since these can effect the Raman intensity of the CNT samples [208]. Figure 6.4 shows SEM images of the m-CNT/INT and met-CNT/INT composites with varying volume fractions. For both types of composites and for all volume fractions, the samples show successful dispersion and non-aggregation of the CNTs among the INTs, since the nanotubes are dispersed evenly in the sample and no dense particles compromising ten or more nanotubes, or any carbonaceous impurities, can be observed, indicating relatively high purity of our samples. Furthermore, we see that as the volume fraction of CNTs increases, the density of the CNT network increases evenly as well, thereby demonstrating the potential of the preparation-method for achieving high quality CNT/INT composites with a tunable, well-dispersed and non-aggregated CNT network.

The Raman spectra were supplied by our collaborators, Dzmitry I. Yuko and Mikhail Shuba, at the Institute for Nuclear Problems, Belarus State University, and obtained using a Raman spectrometer combined with a confocal microscope Nanofinder High End (Tokyo Instruments) at an excitation wavelength of 532 nm. Figure 6.5 shows the Raman spectra for pure m- and l-CNT films. The defect density is estimated from the ratio of the G-band at 1593 cm^{-1}, originating from the longitudinal optical phonons of semiconducting CNTs, and the D-band at 1335 cm^{-1} (G/D ratio), which has been found to be a good estimate of the defect density for CNTs with diameters of 1-2 nm, assuming the samples are non-aggregated and without adsorbed molecules [208, 212]. The G/D ratio is approximately 10 for the m-CNT films and 100 for the l-CNT film, indicating very high crystalline quality in the latter.

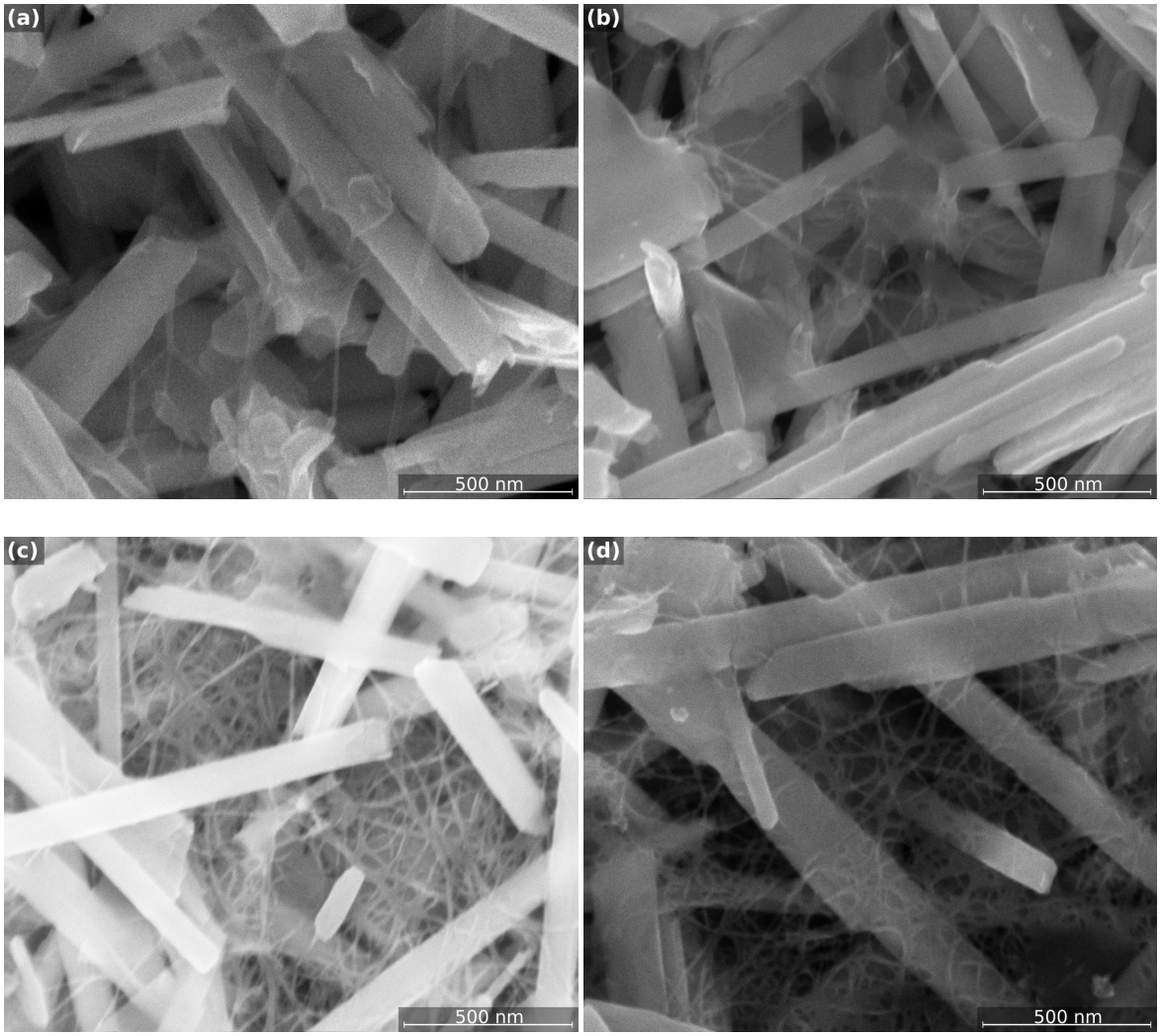

Figure 6.4: SEM images of samples comprising INTs and (a)-(c) met-CNTs with varying volume fractions of $\phi = 0.24\%, 0.49\%, 1.90\%$, respectively, and (d) m-CNTs with volume fraction $\phi = 2.4\%$. The thick white tubes are INTs and the thin white curves are the CNT network. Note that the CNTs are well dispersed among the INTs for all CNT volume fractions.

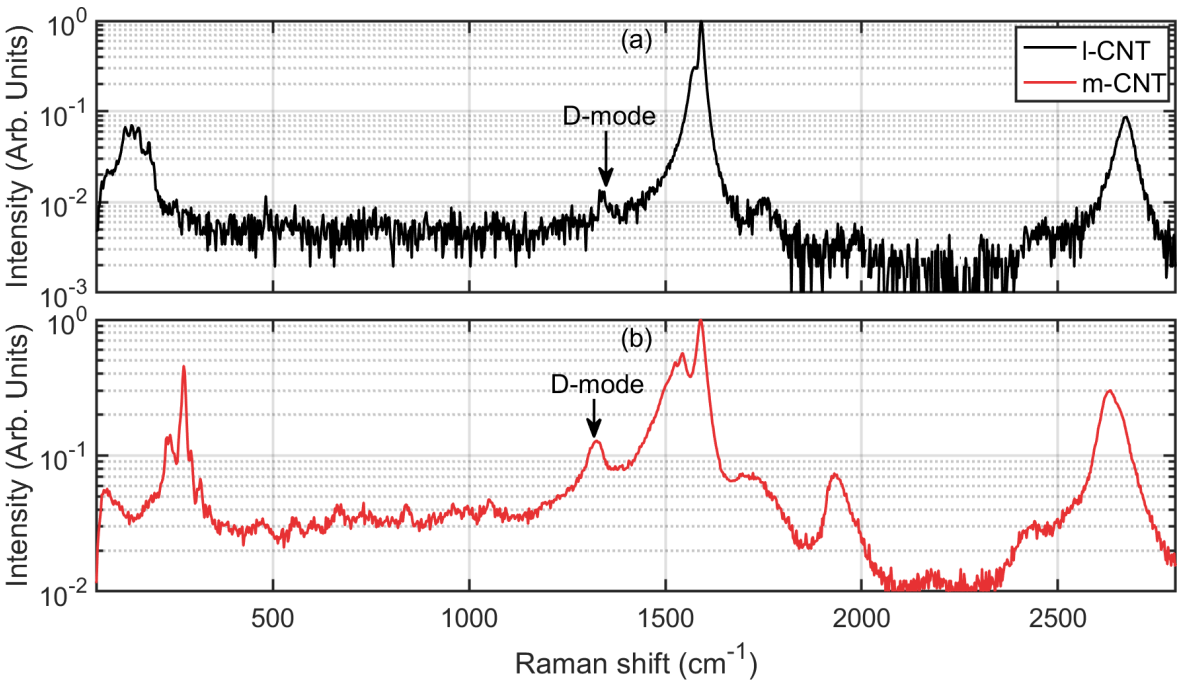

Figure 6.5: Raman spectra of (a) l-CNT and (b) m-CNT films. Note the very small D-mode at 1335 cm^{-1}, indicating high crystalline quality of the l-CNTs.

6.5 Experimental Measurement and Analysis

With normally incident light, the optical density spectra were obtained in the ranges 0.1–2 THz, 2–270 THz, and 270–1000 THz using THz-TDS (EKSPLA, Lithuania), a Fourier-transform infrared spectrometer Vertex 70 (Bruker), and an RV2201 spectrophotometer (ZAO SOLAR, Belarus), respectively. Data obtained in the range 1.5–3 THz has an error of about 20% because of high level of noise.

To investigate the temperature dependence of the THz conductivity in the range 10–300 K, we employed our THz-TDS setup with access to a closed cycle helium cryostat (ARS) [15], see section 4.4.1. THz pulses with a bandwidth of 0.3–2 THz were generated and detected by commercially available Photoconductive Antennas (PCAs) from Batop using a 40 MHz, 1064nm, femtosecond fibre laser from Ekspla. From direct measurement of the complex transmission coefficient of our samples, the conductivity and permittivity was obtained using the method described in chapter 5.

The same THz measurements in the range 300–530 K were done in air using a home-made furnace-style heating sample-holder. In order to remove doping effects from air molecules such as H_2O and O_2, which are non-covalently attached to the CNT walls, each sample was

maintained at temperature of 530 K for 10 min resulting in a reduction of sample conductivity of approximately 20%, before starting the measurements, and subsequently cooled from 530 K to 300 K while performing the THz measurements. We note that the sample conductivity was restored in one day after the heating due to the adsorption of air molecule on the CNTs. The microwave measurements at 30 GHz were performed at room temperature by waveguide method [276–278] using a scalar network analyzer R2-408R (ELMIKA, Vilnius, Lithuania). Static electrical (DC) conductivity of thin films was measured using a four-point linear probe technique. Both the high-temperature THz measurements, the broadband optical density measurements, and the DC and microwave measurements were supplied by our collaborators, Dzmitry I. Yuko and Mikhail Shuba, at the Institute for Nuclear Problems, Belarus State University.

6.6 Experimental Results and Discussion

6.6.1 The Finite-Length Effect

While many groups have observed a broad THz conductivity peak in CNTs, its origin has been debated for some time [249, 250, 253–255]. The peak was claimed to be associated either with a small-gap interband transition [249, 250] or with a localized plasmonic resonance [252–255]. However, both mechanisms contribute simultaneously and cause the appearance only one terahertz peak [253]. As was shown in [253], the contribution of the finite-length effect is dominant at room temperature, when the gap energy is less than or comparable to the average thermal energy. The dependence of the THz peak frequency on CNT length has been experimentally shown in [254], giving clear evidence of a plasmonic resonance in these materials.

In the present section we demonstrate experimentally the influence of the tube length on the temperature dependence of the THz conductivity spectra for CNT thin films. Good qualitative agreement of the experimental results with theoretical predictions made in section 6.2 confirm the plasmonic nature of the CNT response in the terahertz range. Figure 6.6a shows the optical density spectra for s-, m- and l-CNT films at 323 and 473 K. From this we can use Kramers-Kronig analysis [255, 259] to obtain the real part of the effective conductivity $\mathrm{Re}(\sigma_{eff})$ and the real part of the effective permittivity $\mathrm{Re}(\epsilon_{eff})$ as shown in figures 6.6b and 6.6c, respectively. Here we observe a shift of the THz peak to lower frequencies with increasing length: the spectra for m- and s-CNT have a broad peak at 4 THz and 10 THz, respectively, while the l-CNT demonstrates Drude-like behaviour.

We note that the average diameter of l-CNTs differs from that of m-, and s-CNTs. It

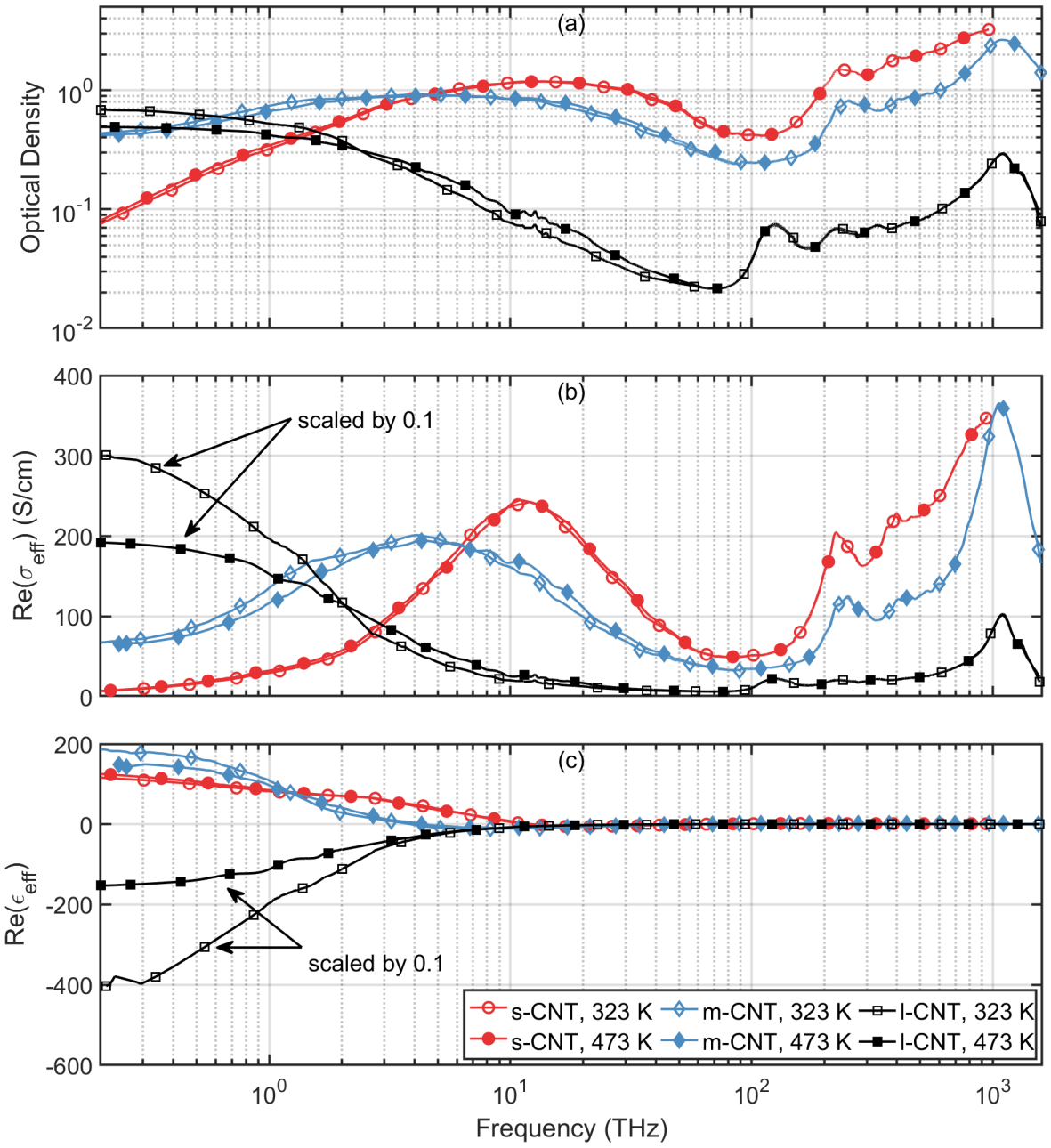

Figure 6.6: Frequency dependence of **(a)** the optical density, **(b)** the real part of the effective conductivity $\mathrm{Re}(\sigma_{eff})$, and **(c)** the real part of the effective permittivity $\mathrm{Re}(\epsilon_{eff})$, obtained from broadband optical density measurements at 323 K and 473 K for *s*-, *m*-, and *l*-CNT films. Note that in **(b)**-**(c)**, the data for the *l*-CNTs have been scaled by 0.1.

has been demonstrated previously that the polarizability and conductance of an individual single-walled CNT slightly depends on its diameter in the frequency range below interband transitions [253]. In terms of the effective conductivity of the CNT film, the tube diameter can influence this via intertube tunnelling or by varying the tube number density in the samples, however its contribution to the frequency of the terahertz peak is much smaller than from the finite-length effect. This was shown experimentally for samples with different average tube diameters of 0.8, 1, and 1.4 nm [254].

The temperature dependencies of the calculated spectra in figure 6.2 and measured spectra in figure 6.6 are very similar. Namely, in the range 0.3–1 THz, (i) long tubes *l*-CNTs ($L \approx 10\mu$m) demonstrate stronger temperature dependence than shorter tubes *m*- and *s*-CNTs ($L < 2\mu$m), (ii) The conductivity of *l*- and *m*-CNTs decreases with increasing temperature, while the opposite is true for *s*-CNTs. This can be explained by a decrease of the electron scattering rate with increasing temperature. As predicted from the model of localized plasmon resonance in figure 6.2, the THz peak shifts to higher frequencies as the length decreases, resulting in a weakening of the temperature response.

As shown in figure 6.6 for *m*- and *s*-CNTs, the THz peak shifts to a slightly higher frequency with increasing temperature. The shift arises for bundled tubes due to the temperature dependence of the conductivity of some fraction of doped semiconducting CNTs with a Fermi level located close to the top of the valence band [263]. This effect was demonstrated in figure 6.3 for a composite comprising bundled tubes. As follows from the model, this shift does not happen for individual tubes. This is supported by our measurements conducted for individual electronically separated tubes in figure 6.7, where we compare the effective conductivity $\mathrm{Re}(\sigma_{eff})$ of the bundled *m*-CNT and unbundled *met*-CNT films. We observe no blueshift of the THz peak for *met*-CNTs, as opposed to *m*-CNTs, which further demonstrates that the blueshift only occurs for bundled CNTs. Note that the *met*-CNT film shows an order of magnitude higher conductivity than the *m*-CNT film in the THz region, which is mainly due to the higher content of metallic CNTs in the former. This is in keeping with previous measurements of the THz conductivity for metallic and semiconducting CNT films [255], where the former shows 2-3 times higher conductivity at the THz peak frequency.

Figure 6.8 shows spectra of $\mathrm{Re}(\sigma_{eff})$ and $\mathrm{Re}(\epsilon_{eff})$ measured for *s*-, *m*-, and *l*-CNT films at 100 K and 300 K. The behaviour of the conductivity and permittivity for these films are qualitatively the same as in high temperature range 300–530 K (figure 6.6) and agrees well with the predicted finite-length response in figure 6.2 showing opposite temperature dependencies for short and long CNTs.

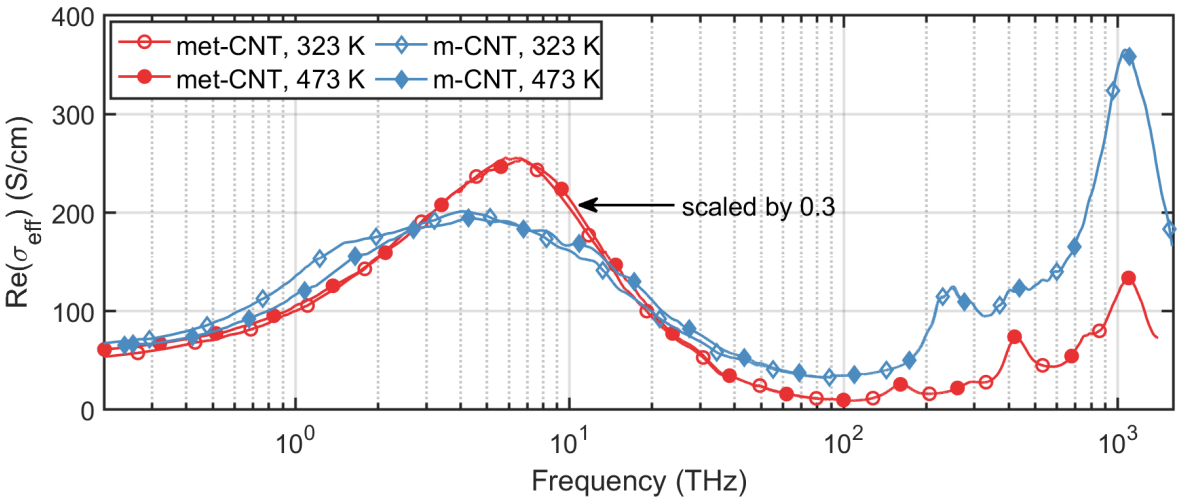

Figure 6.7: Frequency dependence of the real part of the effective conductivity Re(σ_{eff}), obtained from broadband optical density measurements at 323 K and 473 K for *met*-,and *m*-CNT films. Note that the data for the *met*-CNTs have been scaled by 0.3.

6.6.2 Electron Scattering Rate in Long-Length CNTs

In general, the THz conductivity spectra of CNT films are fitted with a Drude-Lorentz function containing the Drude and Lorentz terms with two and three unknown parameters, respectively [255, 259]. The Drude term describes the contribution from "infinite" length tubes while the Lorentz term is due to the localized plasmon resonance in finite-length CNTs. If the Drude- and Lorentz terms are overlapped with each other, some ambiguity in the determination of unknown parameters appears in the fitting procedure. If the tube length is large enough then the contribution from the Drude term dominates and we can fit the terahertz conductivity of the CNT film using just Drude term with two unknown parameters: the plasma frequency and electron scattering rate. For this case, the effective conductivity of the film is a sum of the intrinsic tube conductance in the unit volume, with a factor responsible for orientation of CNTs in the film. In this approximation we can conclude that the electron scattering rate in the Drude term of the CNT film effective conductivity is equal to the electron scattering rate in the individual CNTs. Our *l*-CNT sample comprises mainly long tubes and, consequently, demonstrates Drude-like behaviour in the terahertz range.

From our Drude fits of the effective conductivity for *l*-CNT samples in the range 0.3–2 THz at different temperatures, we found that the plasma frequency remains temperature independent, while the electron scattering rate γ shows a clear temperature dependence. This result indicates that the temperature dependence of the intrinsic CNT conductivity is not related to the energy dependent density of states of the CNT, but can instead be attributed

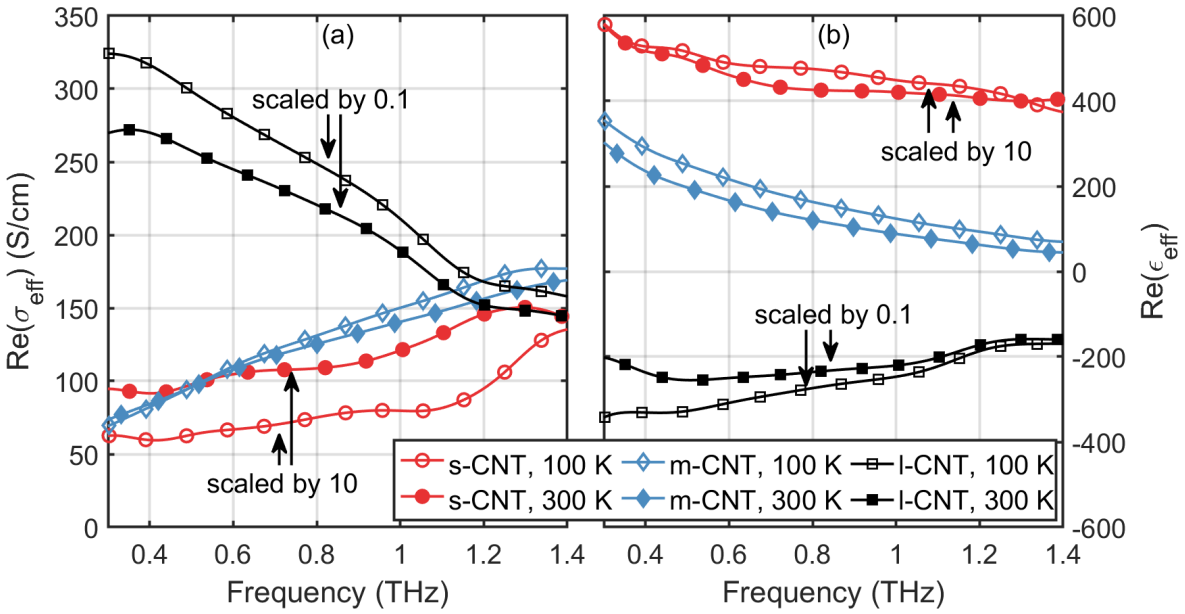

Figure 6.8: Frequency dependence of (a) Re(σ_{eff}), and (b) Re(ϵ_{eff}), obtained from THz-TDS measurements of s-, m-, and l-CNT films at 100 K and 300 K. Note that the data for l- and s-CNT have been scaled by 0.1 and 10, respectively.

to temperature dependent electron scattering processes. As seen in figure 6.5, Raman spectra of the l-CNTs show a very small D-mode, demonstrating a low defect density in the l-CNTs. Thus, we shall omit possible electron scattering by defects in our further consideration.

Figure 6.9a and 6.9b shows experimental and associated Drude-fits of the temperature dependence of Re(σ_{eff}) and Re(ϵ_{eff}) for l-CNT in the range 0.3–2 THz, along with the obtained electron scattering rate γ in figure 6.9c. For temperatures below 500 K, the scattering rate from acoustic phonons is known to have a linear temperature dependence [271, 272, 279, 280], $\gamma_{e-ph} = \alpha T/d$, where d is tube diameter and α is a constant. For our l-CNTs, the average diameter is 1.6 nm, giving $\alpha = 49$ m/(Ks) from fitting γ in the range 293–500 K (see dashed line in figure 6.9c). This value of α corresponds to an electron mean free path of 109 nm at room temperature, which is close to that of graphite [281]. The observed linear dependence $\gamma \propto T$ in this temperature range agrees well with this prediction, however the experimentally reported value of $\alpha = 12$ m/(Ks) by Zhou et al. [272] is four times smaller than our obtained value for α, indicating the electron-acoustic phonon scattering rate to be much smaller for their samples. The reason for this discrepancy is not currently known, but might be in part explained by the influence of contact-resistance in the measurements of [272].

In figure 6.9d, the obtained electron–acoustic phonon term has been subtracted from the scattering rate $\gamma - \gamma_{e-ph}$. We see that at low temperatures (< 200 K) there is a signifi-

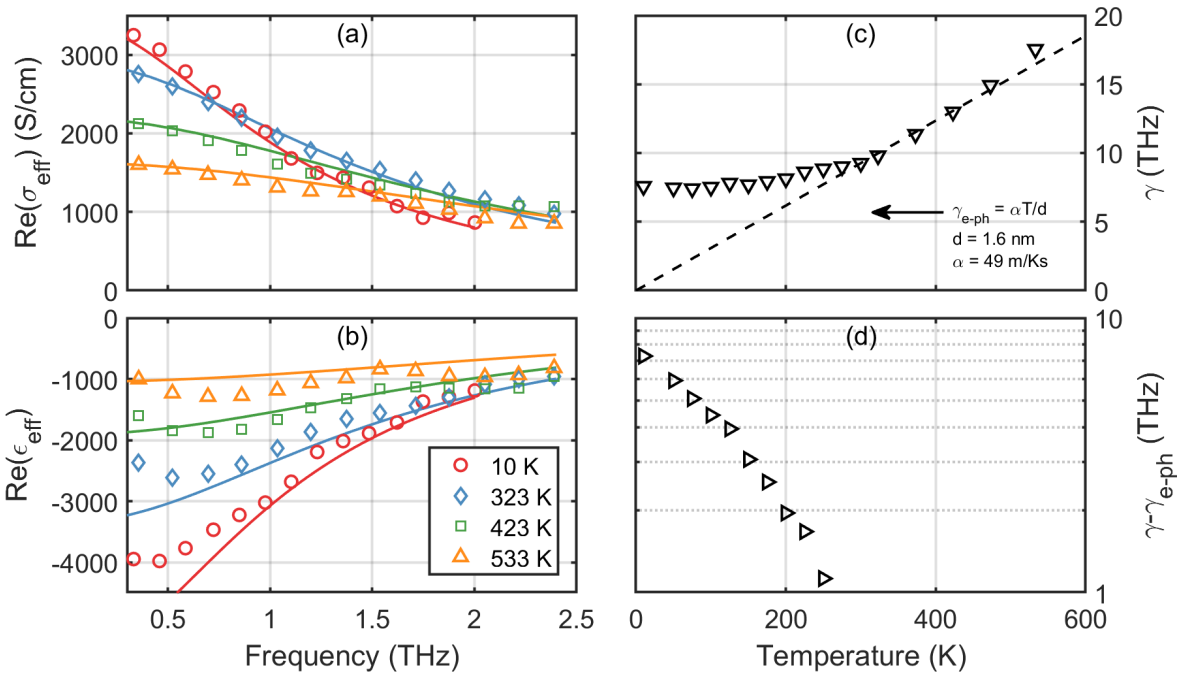

Figure 6.9: Frequency dependence of (a) Re(σ_{eff}), and (b) Re(ϵ_{eff}), obtained from THz-TDS measurements of l-CNT film at 10 K, 323 K, 423 K and 533 K, along with their associated Drude fits (full lines). (c) Temperature dependence of the scattering rate γ ($\triangledown$) obtained from Drude fits of measured spectra Re($\sigma_{eff}(\omega)$) and Re($\epsilon_{eff}(\omega)$) in the range 0.3–2 THz for l-CNT film. The data has been fitted in the range 300–500 K with a linear function $\gamma_{e-ph} = \alpha T/d$ (dashed line), where d = 1.6 nm is the mean diameter of our CNTs, and α = 49 m/Ks is a fitting constant. (d) Temperature dependence of the value $\gamma - \gamma_{e-ph}$ calculated from the data in (c).

cant contribution from scattering mechanisms which do not originate from electron-acoustic phonon scattering or defect scattering, however at present time we do not know the origin of this scattering. We note that this temperature-dependent behaviour remained constant through multiple heating and cooling cycles, meaning it is reversible. Further investigation is required to determine the physical mechanisms responsible for this temperature dependence.

6.6.3 Percolation Effects

While it is clear that temperature dependent scattering effects are sufficient to explain the conductivity temperature dependences of our CNT samples with tubes of varying length, this cannot by itself account for the huge variety of temperature dependences reported in the literature [250, 255, 259–262]. One cannot avoid the fact that in reality most CNT samples are percolating networks, with charge-carriers being able to travel between CNTs

through electrical tunnelling [282, 283]. The electrical properties of INT- and CNT/INT-composites have previously been studied from impedance measurements in the frequency range 0–10^6 Hz, showing significant dependence on the nanotube concentration [151, 284]. Therefore the influence of percolation must be included. In order to investigate this, the effective conductivity of m-CNT/INT-composites of varying nanotube volume fractions, ϕ, were measured at 0 GHz, 30 GHz, 0.3 THz, and 1 THz, see figure 6.10. The volume fraction was roughly estimated from the known CNT density ρ_{CNT} of our film using the relation $\phi = \rho_{CNT}/\rho_{graphite}$, where $\rho_{graphite} = 2.226$ g/cm^3 is the density of graphite. A significant result is the fact that our m-CNT/INT films show one order of magnitude higher conductivities compared with that reported for CNT-based composites of similar average volume fractions [285, 286]. This is due to the CNTs being non-aggregated and well dispersed among the INTs, as demonstrated earlier in section 6.4. Furthermore, let us note that the addition of fullerene-like WS_2 nanoparticles was recently shown to be efficient as an alternative route to produce well-dispersed CNT-based polymer nanocomposite [287, 288].

The conductivity in figure 6.10 is shown to follow a power-law dependence $\sigma(\phi) = \sigma_0(\phi - \phi_0)^\beta$, where σ_0 is an arbitrary scaling factor, ϕ is the volume fraction of the CNT network, ϕ_0 is the percolation threshold below which the sample effectively consists of isolated CNT bundles. Our fits of the data in figure 6.10 agrees with conductivity measurements of similar percolating nanotube networks showing a universal power-law scaling with frequency, which is common for systems with randomly distributed barriers [256, 258, 285, 289, 290]. From our fits we obtain $\beta = 1.6, 1.3, 1.2, 1.1$ and $\phi_0 = 0.06\%, 0.05\%, 0\%, 0\%$ for DC, 30 GHz, 0.3 THz and 1 THz, respectively. The DC percolation threshold agrees well with similar studies on CNT-composite systems [256, 285] and the difference in percolation thresholds and the decreasing β for higher frequencies is expected due to an increasing sensitivity to the intrinsic conductivity of the nanotube [256, 283].

In addition to affecting the frequency dependence of the conductivity, percolation also influences the temperature dependence, which is illustrated in figure 6.11, where $\mathrm{Re}(\sigma_{eff})$, obtained via THz-TDS, is plotted vs temperature for different CNT volume fractions ϕ. It can be seen that as ϕ increases, the temperature dependence reverses. This appears, as in our model from section 6.2, because the THz resonance shifts to lower frequencies for increasing ϕ. This can again be explained by the finite-length effect, where the increasing CNT volume fraction results in an increasing number of contact points between nanotubes, thereby increasing the "effective" nanotube length. Thus, our data for m-CNT shows (i) that percolation can strongly affect the temperature dependence for the effective conductivity in the THz range, (ii) the proportionality $\mathrm{Re}(\sigma_{eff}) \propto \phi$ is true in the range 0.2–1 THz giving us a method to determine CNT volume fraction from THz-TDS measurements [291]. (iii) The

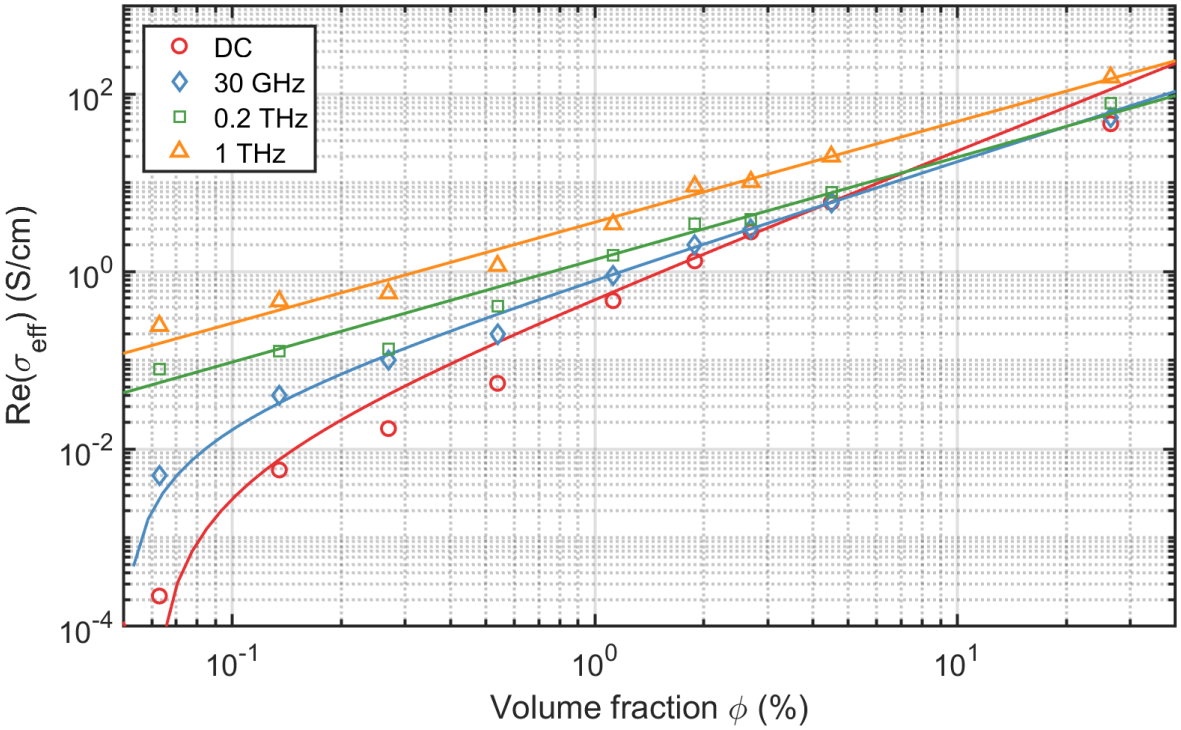

Figure 6.10: Effective conductivity $\mathrm{Re}(\sigma_{eff})$ of m-CNT/INT-composites vs CNT volume fraction ϕ for frequencies DC, 30 GHz, 0.3 THz and 1 THz. Points are experimental data and lines are fitted power functions of the form $\sigma(\phi) = \sigma_0(\phi - \phi_0)^\beta$, with $\beta = 1.6, 1.3, 1.2, 1.1$ and $\phi_0 = 0.06\%, 0.05\%, 0\%, 0\%$ for DC, 30 GHz, 0.3 THz and 1 THz, respectively.

volume fraction (or density) of the CNTs can strongly influence effective tube length and thus the location of the effective THz conductivity peak. Finally, since INTs demonstrate low conductivity below 3 THz and high temperature stability, they can be used as an "inert" material for the fabrication of hybrid films with randomly dispersed elongated conductive nanoparticles. Here we have demonstrated for the first time that such hybrid films are a great tool for studying the percolation effect in a wide range of temperatures, frequencies and concentrations.

6.7 Conclusion

In summary, free-standing films comprising single-walled CNTs of various lengths, and CNT/WS_2 INT composites of varying CNT densities on quartz, were prepared and their effective conductivities and permittivities measured in the ranges (i) 0.2–1000 THz for 300–530 K, and (ii) 0.3–2 THz for 10–530 K. We observe a peak in the THz conductivity spectra of the CNT films

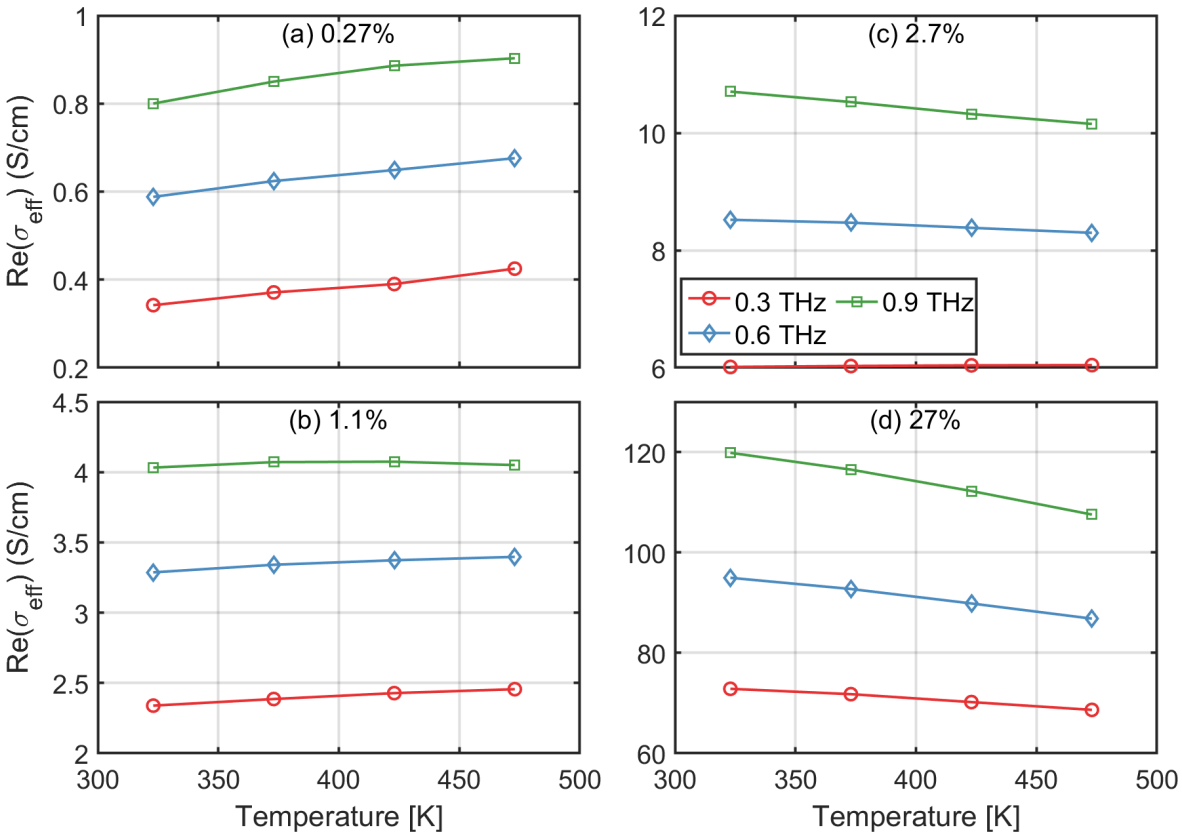

Figure 6.11: Effective conductivity $\mathrm{Re}(\sigma_{eff})$ for m-CNT/INT-films versus temperature for volume fractions $\phi \in (0.27\%, 1.1\%, 2.7\%, 27\%)$.

which is shown to be plasmonic in nature, in agreement with recent literature, and shifting in frequency with the CNT length as predicted by our model of the localized plasmon resonance. Drude fits of the THz conductivity spectra for long ($L \approx 10$ μm) CNTs show a linear dependence of the electron scattering rate $\gamma \propto$ T for 300–500 K, revealing electron-acoustic phonon scattering as the main scattering mechanism in the individual CNTs in this range [271, 272]. Due to the plasmonic nature of the response of shorter tubes ($L \leq 1$ μm), we observe an unexpected variation with temperature, where the effective conductivity of the films in the THz frequency range is shown to increase with temperature, while we observe a decrease in temperature for longer tubes. This temperature-induced effect arises indirectly from the variation of the electron scattering rate, which determines plasmon losses and thus broadening of the conductivity resonance. Moreover, by studying composites of varying CNT densities, we show that the change in conductivity with temperature depends not only on tube length, but also varies with tube density: as the temperature increases, we observe an

effective conductivity in the range 0.3–1 THz that increases/decreases for low/high density samples. This effect accounts for the apparent discrepancies in literature regarding temperature dependent conductivity of CNT composites [250, 255, 259–262], and occurs due to the density dependence of the effective length of conducting pathways in the composite films, which again leads to a shift and temperature dependent broadening of the THz conductivity resonance.

Chapter 7

Sign Inversion in the Terahertz Photoconductivity of Single-Walled Carbon Nanotube Films

We begin by acknowledging the contributions of our collaborators to the content presented in this chapter. The *s*-, *m*-, *met*-, and *sem*-CNT films were prepared by Dzmitry I. Yuko and Mikhail Shuba at the Institute for Nuclear Problems, Belarus State University. The *l*-CNT films were provided by Albert G. Nasibulin at the Skolkovo Institute of Science and Technology, Moscow, and Department of Applied Physics, Aalto University, Finland. The 99% semiconducting CNTs were provided by Patrizia Lamberti at the Department of Information and Electrical Engineering and Applied Mathematics, University of Salerno, Italy. Mikhail Shuba and Dzmitry I. Yuko the broadband optical density spectra in figure 7.1.

7.1 Background

The optical and electronic properties of single-walled carbon nanotubes (CNTs) have been intensely investigated for several decades due to their fascinating physical properties and potential for advanced applications [28–32]. Understanding the ultrafast dynamics of photoexcited charge-carriers in CNTs is critical due to their potential applications in photonics and optoelectronics [33–36]. For this reason, many groups have utilized time-resolved measurements to study the ultrafast response of CNTs due to optical photoexcitation, documenting, for example, the presence of excitons in photoexcited CNTs [37, 38, 38–42].

While visible pulses can detect the presence of excitons, THz pulses are ideal for probing low energy excitations such as free-carriers and plasmons, since each of these species have

distinct features in the THz photoconductivity [15]. Thus, a proper understanding of the THz response of CNTs is key to understanding the ultrafast charge-carrier mechanisms in CNTs. Many groups have utilized optical pump - THz probe time-domain spectroscopy to investigate the ultrafast charge-carrier dynamics in CNTs [41, 249, 257, 292–294]; however, there are conflicting reports of the sign and frequency dependence of the observed photoconductivity. This discrepancy has led to wildly different interpretations and conclusions about the photoinduced THz response. For example, Xu et al. [257] deduced that excitons are the dominant photogenerated species detected in these experiments, while Luo et al. [41] concluded the ultrafast THz response originates from transitions between exciton states. Beard et al. [292] and, more recently Jensen et al. [294], have meanwhile concluded that free carriers are the dominant photoexcited species, an interpretation broadly shared by Kampfrath et al. [249, 293], with small-gap interband transitions also contributing to the THz response. While most of these measurements have been carried out on samples of mixed chirality (i.e. mixed semiconducting and metallic CNTs) it is important to note that Beard et al. [292] found THz photoconductivities of samples containing 94% semiconducting and 93% metallic CNTs to be similar. Moreover, discrepancies persist even for nominally similar samples, with Luo et al. [41] and Xu et al. [257] reporting a photoconductivity of different sign for samples of predominately small-diameter semiconducting CNTs.

Since all of these groups have measured CNTs under similar excitation and preparation conditions, these discrepancies must originate from a difference in the measured samples themselves. The key to understanding these discrepancies lies in the observation of a broad peak in the THz conductivity of CNTs, observed for the first time, to our knowledge, in [248]. While there has been some discussion regarding the nature of this resonance, with some groups proposing an interband transition of small-gap CNTs [249, 250, 259, 265], more recent papers [254, 255, 295, 296] show clear evidence that it results from a localized plasmon in finite-length CNTs, which we denote the *finite-length effect*, first proposed in [251, 252]. Theoretical modelling [253] and experimental observations [254, 255, 295, 296] substantiates the dominant role of the finite-length effect in the equilibrium THz response. Understanding the true origin of this THz resonance is also key to understanding the ultrafast charge-carrier dynamics of CNTs. However, due to the inherent difficulty in fabricating isolated CNT samples, most measurements have been carried out on mixtures of CNTs with various distributions in length, thickness, chirality and bundle-size, all fabricated using a variety of techniques [149, 249, 253, 254, 256, 257, 292].

In this chapter we use THz-TDS and OPTP to systematically investigate the influence of tube length and chirality on the THz photoconductivity of thin-films comprising single-walled CNTs. We observe explicitly that the THz photoconductivity of CNT films is a

highly variable quantity which correlates with the length of the CNTs, while the chirality distribution (i.e. the relative concentration of metallic vs semiconducting tubes) has very little influence. Moreover, by comparing the photo-induced change in THz conductivity ($\Delta\sigma_{ph}$) to the change on heating from 10 K to 300 K ($\Delta\sigma_{heat}$), we show that both occur primarily due to the temperature-induced modification of Drude electron relaxation rate, which results in a broadening of the plasmonic resonance present in finite-length metallic and doped semiconducting CNTs.

7.2 Sample Preparation

To study the influence of tube length and chirality, we prepared five types of films comprising CNTs in either bundled or individual form, where the average lengths of the CNTs and the chirality distributions of the films varies significantly, see table 7.1. The details of the sample preparation can be found in section 6.3 of the previous chapter.

Sample	D (nm)	L (μm)	d (nm)	sem.	met.
sem-CNT	500	0.1–1	0.8–1.2	99%	1%
met-CNT	500	0.1–1	0.8–1.2	5%	95%
l-CNT	55	2–100 (10)	1.3–2	33%	66%
m-CNT	500	0.3–2 (1)	0.8–1.2	66%	33%
s-CNT	800	< 0.3	0.8–1.2	66%	33%

Table 7.1: Summary of our CNT films; thickness (D), length (L) (average length in parenthesis), diameter (d), and content of semiconducting (sem.) and metallic (met.) CNTs.

7.3 Experimental Measurement and Analysis

In order to observe the influence of the broad THz peak on the photoconductivity of CNTs, it is important to probe at or below the resonance frequency, which typically lies in the range 1-10 THz [254]. We carried out both transmission and photoconductivity measurements over the range 0.2–1.3 THz, where THz pulses were incident normal to our samples. Transmission spectra were obtained using our THz-TDS setup described in section 4.4.1, where THz pulses were generated and detected by commercially available Photoconductive Antennas (PCAs) [167] from Batop using a 40 MHz, 1064 nm, femtosecond fibre-laser from Ekspla. To investigate the photoexcited THz response of our samples, we employed our OPTP setup described in section 4.4.2, which consists of a 100 fs, 1050 Hz repetition rate, 800 nm Ti:Sapphire amplified laser, where THz pulses were generated and detected by optical rectification [180]

and electro-optic sampling [189], respectively, in 1mm thick ZnTe crystals. To photoexcite the sample, we again use 800 nm pulses, with fluences in the range of 0.018–169 μJ/cm^2. By analysing the frequency dependent transmission amplitude and phase of a sample as described in chapter 5, we can determine its complex equilibrium effective conductivity, $\sigma(\nu)$, as in references [255, 257, 292], where ν is the frequency. Similarly, by recording the difference in transmission, $\Delta E = E_{exc} - E$, between a photoexcited (E_{exc}) and unexcited sample (E), a complex photoconductivity $\Delta\sigma_{ph}(\nu, \Delta\tau)$ can be obtained as a function of pump-probe delay-time $\Delta\tau$ (again, see chapter 5). To investigate the temperature dependence of the THz conductivity in the range 10–300 K, we employed a closed cycle helium cryostat (ARS)[15] with quartz windows. Note that the relatively narrow bandwidth of our measurements is determined by the transmission through this cryostat system, as well as the vibrations of the cryostat when measuring at low temperatures. The transmittance of our samples at 800 nm were determined using an UV-Vis spectrometer by comparing the transmittance at 800 nm our samples and an empty sample holder. From the transmittance and thickness of our samples, we were then able to determine their penetration depth d_p using the Lambert-Beer law, and their absorbed photon density N for a given incident pump-fluence.

7.4 Experimental Results and Discussion

7.4.1 Decay-Dynamics

When photoexciting CNTs, an important first step is to check whether the pump-wavelength overlaps with any of the optical transitions in the CNTs, see section 2.7, since photoexciting on- or off-resonance may lead to different responses [41]. In figure 7.1 we plot the broadband optical density spectra of the CNT films, obtained following the procedure described in section 6.5. Firstly, we observe that the l-CNT optical transitions are significantly shifted to lower frequencies, compared with the other CNT spectra. This is due to the larger diameters of the l-CNTs, see table 7.1, since the diameter largely determines the energy levels of the optical transitions, as seen in section 6.2. Secondly, we note that the 800 nm photoexcitation occurs off-resonance from the optical transitions in the CNTs, specifically the first (S11) and second (S22) optical transition in semiconducting CNTs, and the first optical transition in metallic CNTs (M11). In case of the $s-$ and $m-$CNTs, the 800 nm pump overlaps with the edge of the S22 transition, meaning only a small subset of the semiconducting CNTs are photoexcited on-resonance. Therefore we do not expect these "on-resonance" semiconducting CNTs to contribute significantly to the overall photoconductivity, compared to the rest of the CNTs.

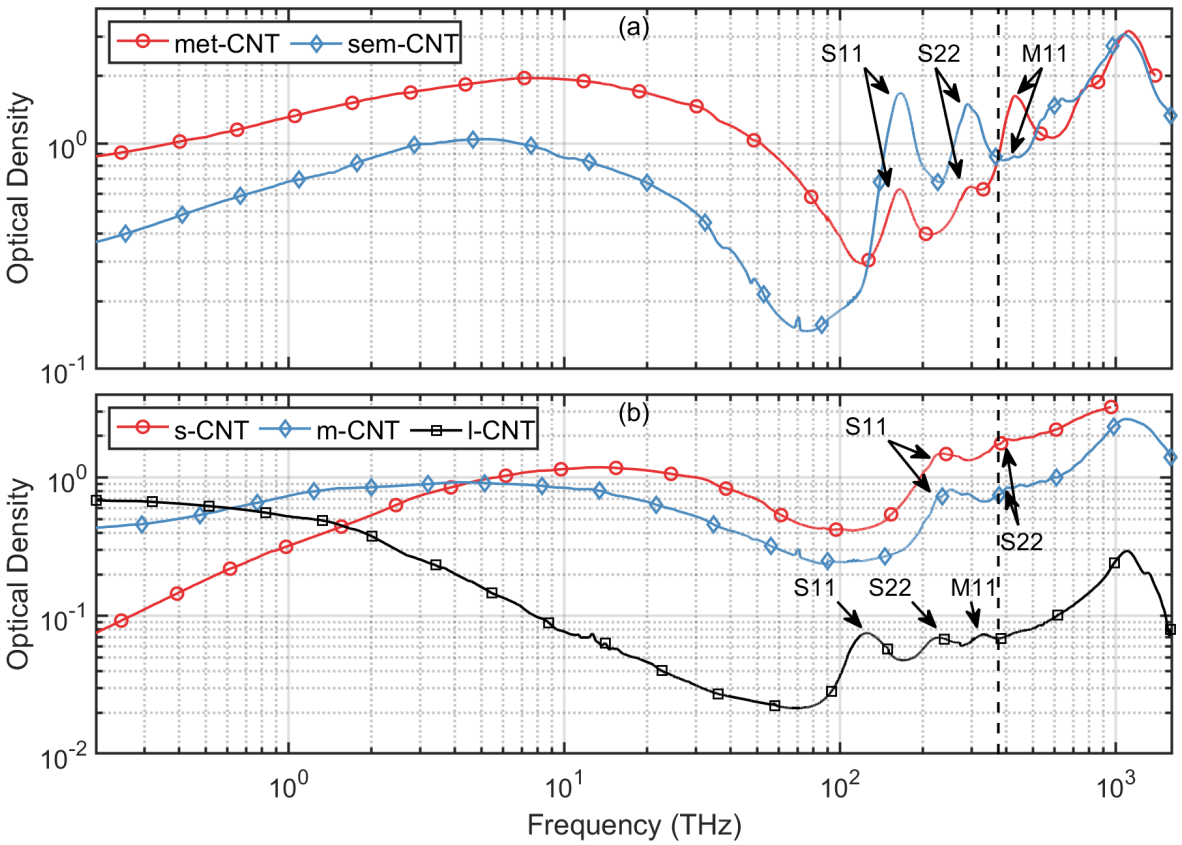

Figure 7.1: Optical density of **(a)** *met*− and *sem*−CNT and **(b)** *s*−, *m*− and *l*−CNT, measured at 323 K. The vertical dashed line corresponds to the mean frequency of the 800 nm pump pulse, and the arrows indicate the first (S11) and second (S22) optical transitions in the semiconducting CNTs and the first optical transition in the metallic CNTs (M11).

In figure 7.2, we plot the photoinduced change in transmission ($\Delta E/E$) as a function of pump-probe delay time $\Delta\tau$ and normalized to the absorbed photon density N, for the *met*− and *sem*−CNT (7.2a), and the *l*−, *m*− and *s*−CNT films (7.2b). We note that in order to facilitate comparison of photoconductivities of similar order, the incident fluence F used for the *l*−CNT is two orders of magnitude smaller than for the other samples, due to the relatively large photo-response of *l*−CNT. However, later on we show that the dynamics and conductivity spectra are observed to be relatively fluence independent for our samples, so the sample responses are still comparable. We observe that the decay dynamics of all the films are quite similar, with decay-times in the range of 1.6-1.9 ps, comparable to previous reports [257, 293, 294, 297, 298], which has previously been attributed to Auger recombination of the photoexcited electron-hole pairs [257, 298]. A key signature of this recombination mechanism is a strong fluence dependence of the decay times, which are expect to increase significantly

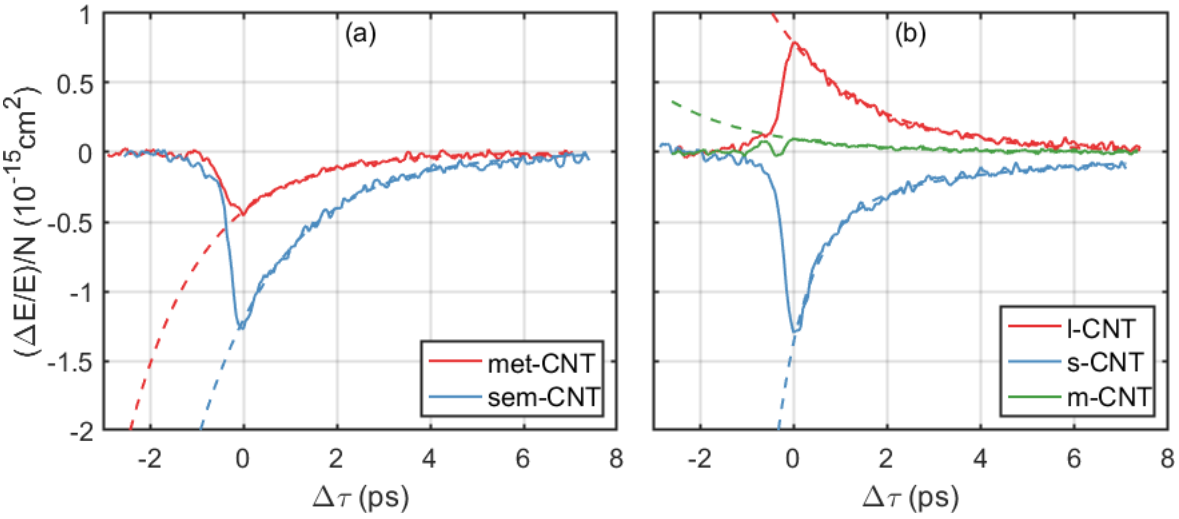

Figure 7.2: The photo-induced relative change in the THz transmission $\Delta E/E$ due to 800 nm photoexcitation at 300 K of **(a)** *met*− and *sem*−CNT, and **(b)** *l*−, *m*− and *s*−CNT, vs pump-probe delay time $\Delta\tau$ and normalized by the absorbed photon density N. The incident fluence is 15 μJ/cm^2 for all films except *l*−CNT, where the fluence is 0.7 μJ/cm^2. The full lines are the experimentally obtained data, and the dashed lines are exponential fits. The decay time τ is found to be 1.8 ps, 1.6 ps, 1.9 ps, and 1.9 ps for *sem*−, *met*−, *l*−, and *m*−, respectively. For *s*−CNT, an initial fast decay of 0.7 ps is observed, followed by a slow decay of 4.4 ps.

with increasing fluence. Thus, in figure 7.3 we plot $\Delta E/E$ for different incident fluences in the range of approximately 0.2–54 μJ/cm^2. For the majority of the films, the relaxation dynamics and the normalized photoresponse remains unchanged, except for relatively high fluences, where the signal becomes saturated and the decay time is observed to increase slightly. The exception is *met*-CNT in figure 7.3a, where we observe an increased saturation of the signal for all incident fluences, which is likely due to the high charge-carrier concentration in these metallic CNTs. A curious oscillatory behaviour is observed for the *m*-CNT film in figure 7.3d immediately after photoexcitation, however it is difficult to make any meaningful interpretation about this feature, since it occurs on a sub-picosecond timescale. It could very likely be an artefact from our measurement technique [73]. Since we observe little fluence dependence in the decay times of the various CNT films, we rule out Auger recombination as a significant relaxation mechanism for our films. Instead we associate the THz photoresponse and decay times with cooling of the CNT electronic system and lattice, which will become evident later on. While the decay dynamics of the different films are similar, a quite significant feature of figures 7.2 and 7.3 is that the magnitude of $\Delta E/E$ varies significantly between the samples, and even changes sign. It is the origin of this large variation in photoresponse that

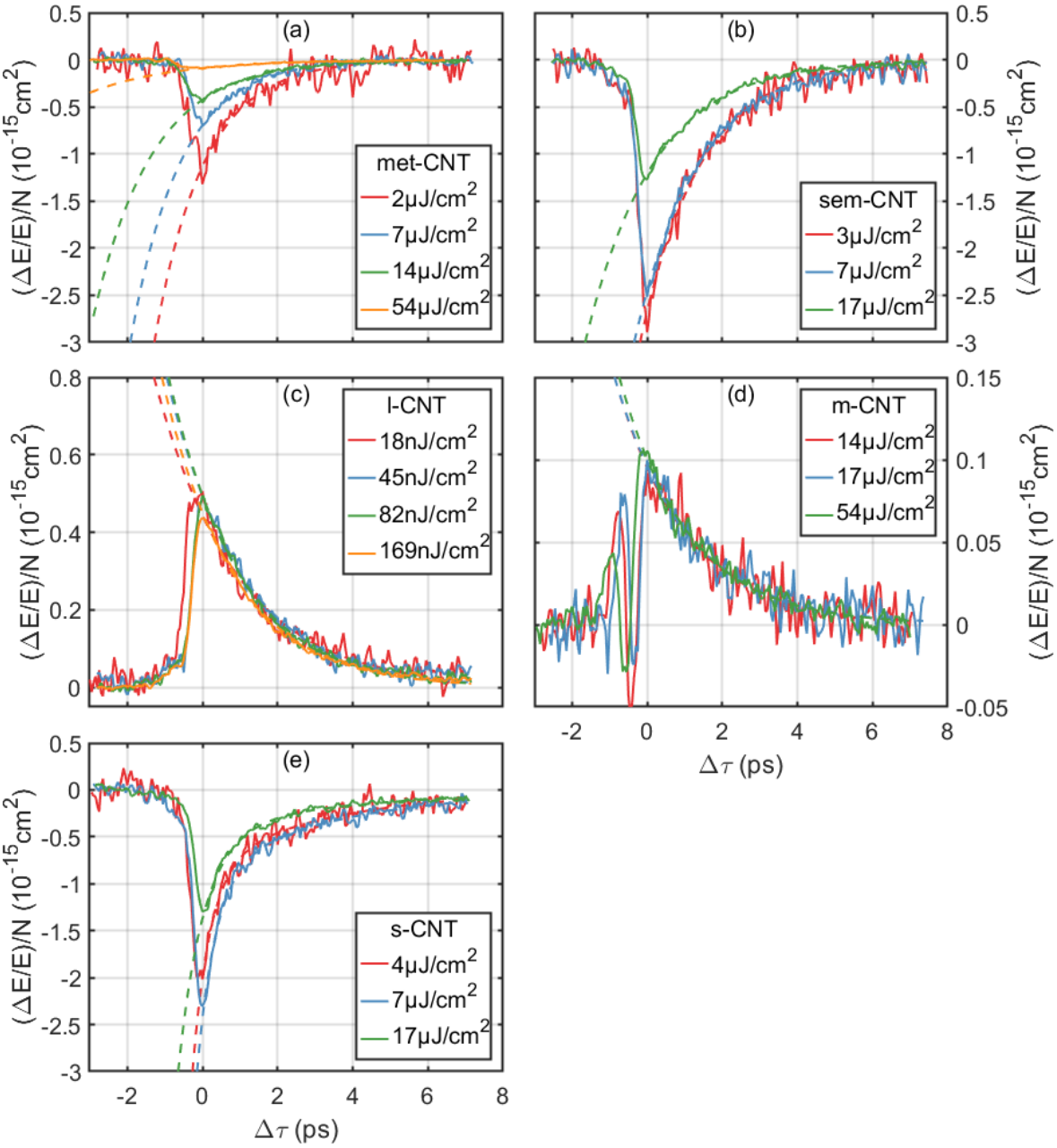

Figure 7.3: The photo-induced relative change in the THz transmission $\Delta E/E$ due to 800 nm photoexcitation at 300 K of **(a)** *met*−CNT, **(b)** *sem*−CNT, **(c)** *l*−CNT, **(d)** *m*−CNT, and **(e)** *s*−CNT, vs pump-probe delay time $\Delta\tau$ and fluence, and normalized by the absorbed photon density N. The solid lines are the experimentally obtained data, and the dashed lines are exponential fits. The decay time for each CNT film is **(a)** 1.3-2.2 ps, **(b)** 1.6-1.8 ps, **(c)** 1.9-2.2 ps, **(d)** 1.8-1.9 ps, and **(e)** 0.5-0.6 ps and 3.5-4.4 ps for the fast and slow decay, respectively, where the decay time is observed to slightly increase with increasing fluence.

forms the basis of this chapter. In order to understand this behaviour, we therefore move on to consider the influence of chirality and length on the complex photoconductivity σ_{ph}.

7.4.2 Photoconductivity

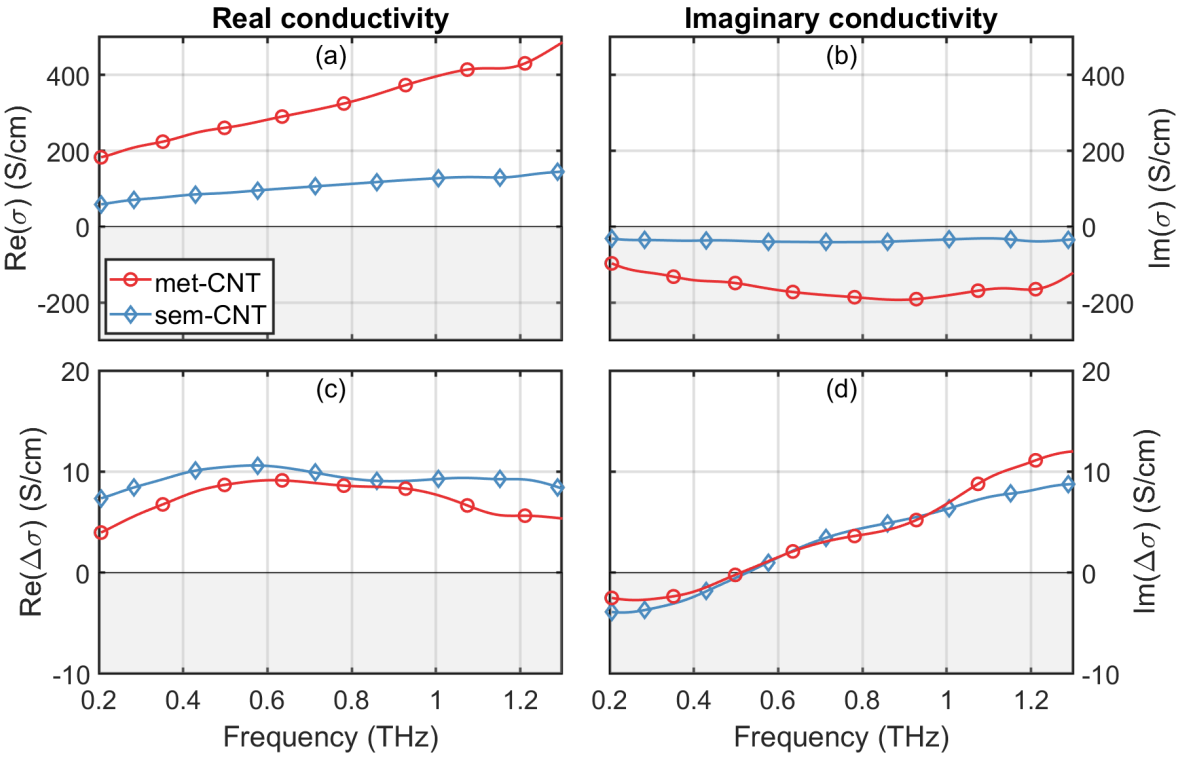

Figure 7.4: Effective conductivity **(a)** Re(σ) and **(b)** Im(σ) of *met*− and *sem*−CNT at 300 K, and change in effective conductivity **(c)** Re($\Delta\sigma$) and **(d)** Im($\Delta\sigma$) due to 800 nm photoexcitation at pump-probe delay time $\Delta\tau = 1$ ps. The incident fluence is 15 μJ/cm^2. The negative region of the second axis in (a)-(d) have been shaded to highlight the difference in sign of σ and $\Delta\sigma$.

We begin by considering the influence of chirality on the effective THz conductivity of the CNT films. In figures 7.4a and 7.4b we plot the real and imaginary parts of $\sigma(\nu)$ for the predominantly semiconducting (*sem*−CNT) and metallic (*met*−CNT) films, extracted following the method outlined in chapter 5. The films show similar conductivities in terms of frequency dependence and sign, resulting from driven oscillation of the plasmon resonance at higher frequency [254, 255]. We observe a factor of three difference in conductivity between *sem*-CNTs and *met*-CNTs due to the higher free charge density in metallic tubes. However, as we discussed in section 2.7, the frequency of the plasmon resonance is not expected to

depend on the density of free charges for CNTs with a linear bandstructure [75], i.e. the metallic CNTs, while we expect the semiconducting CNTs to have some density dependence. When we photoexcite the films away from the optical resonances, we see that the similarity in the responses persists, as previously reported by Beard et al. [292]: in figures 7.4c-7.4d we plot the photoconductivity of each film, $\Delta\sigma_{ph}$, measured 1 ps after excitation ($\Delta\tau = 1$ ps). This similarity suggests that the variation in ultrafast CNT photoconductivities reported in the literature [41, 249, 257, 292–294] is not directly linked to a variation in the chirality-distribution of the samples. In figure 7.5 we plot the fluence-dependence of $\Delta\sigma_{ph}$ for $\Delta\tau = 1$ ps. We observe little to no change in the frequency-dependence of $\Delta\sigma_{ph}$, only an increase in the magnitude of the signal. Here the *met*-CNT shows a weaker scaling with increasing fluence, which agrees with the saturated behaviour observed in figure 7.3. Again we note that we do not expect any fluence-dependence of the resonance frequency of the *met*-CNTs, which agrees with figure 7.5c-7.5d.

Since variation in chirality distribution is unable to explain the photoconductivity discrepancies in the literature, we therefore move on to consider influence of nanotube length, where we compare the $l-$, $m-$ and $s-$ CNT films in figure 7.8, defined by average lengths 10 μm, 1 μm and < 0.3 μm, respectively. We previously discussed these CNT films in chapter 6, where we observed a drastic difference in the real and imaginary parts of $\sigma(\nu)$. To reiterate: for l-CNT, we observe a typical free electron (Drude) response (dotted line), indicating that, in this sample, the carriers are free to move along the tube length, while the m- and s-CNT both display a typical plasmonic resonance, located above 1.3 THz, due to the finite-length effect [253, 254, 299]. Likewise, the photo-induced THz response is quite variable for these samples of different length CNTs, as seen in figure 7.8c-7.8d. For short tubes (s-CNT), we observe a photoconductivity $\Delta\sigma_{ph}$, measured at $\Delta\tau = 1$ ps, which has a positive real component and a negative imaginary component for all frequencies in our range. The medium length tubes (m-CNT) display a real component of photoconductivity, which changes sign at approximately 0.7 THz, while the longest tubes (l-CNT) display a real component of the photoconductivity which is negative for all frequencies in our range. It is interesting to note that the photoconductivity observed for the $l-$CNT film is similar to that observed in the literature by Xu et al. [257], and the $m-$CNT is similar to the observation by Kampfrath et al.[249], while the behaviour of films $s-$, $sem-$ and $met-$CNT are similar to that observed by Beard et al. and Jensen et al. [292, 294]. Thus the photoconductivities observed for our films extend across the full range of photo-responses observed previously in the literature. In figure 7.7 we plot the fluence-dependence of $\Delta\sigma_{ph}$ for $\Delta\tau = 1$ ps. As for the *sem*- and *met*-CNTs, we observe little to no change in the frequency-dependence of $\Delta\sigma_{ph}$, only an increase in the magnitude of the signal. From what we have showed so far, it is clear that the

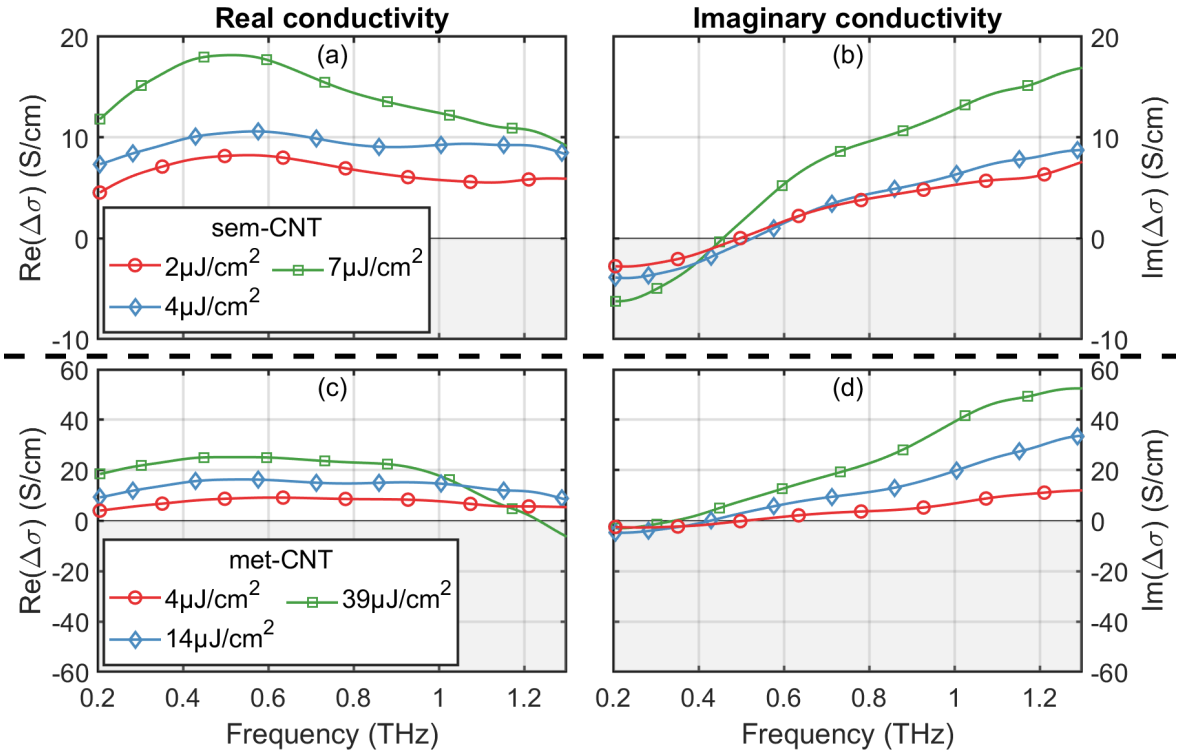

Figure 7.5: Change in effective conductivity Re($\Delta\sigma$) and Im($\Delta\sigma$) vs fluence for **(a)-(b)** $l-$CNT, **(c)-(d)** $m-$CNT, **(e)-(f)** $s-$CNT, **(g)-(h)** $met-$CNT, and **(i)-(j)** $sem-$CNT, due to 800 nm photoexcitation at pump-probe delay time $\Delta\tau = 1$ ps. Change in effective conductivity **(k)** Re($\Delta\sigma$) and **(l)** Im($\Delta\sigma$) of $met-$ and $sem-$CNT due to heating from 10 K – 300 K (filled symbols), compared with the same $\Delta\sigma_{ph}$ data as in **(g)-(j)** for incident fluence 4 $\mu J/cm^2$ (open symbols).

length of the CNTs strongly influences their photoconductivity, just as we observed for the effective conductivity in chapter 6. In order to elucidate the exact mechanism behind this response, we compare $\Delta\sigma_{ph}$ with the changes in conductivity that occur from heating our CNT samples from 10 K to 300 K and show that these two mechanisms give quite similar responses.

7.5 Heating Effects

After illumination with a femtosecond optical stimulus, the electron and phonon temperatures in CNTs are thought to rise by several hundred kelvin [300, 301], and the heating of electron and phonon systems occurs even at low pulse fluence, e.g. 5 μJ/cm^2, as shown for graphite film in [302]. Therefore, to elucidate the origin of this rather peculiar variation in behaviour,

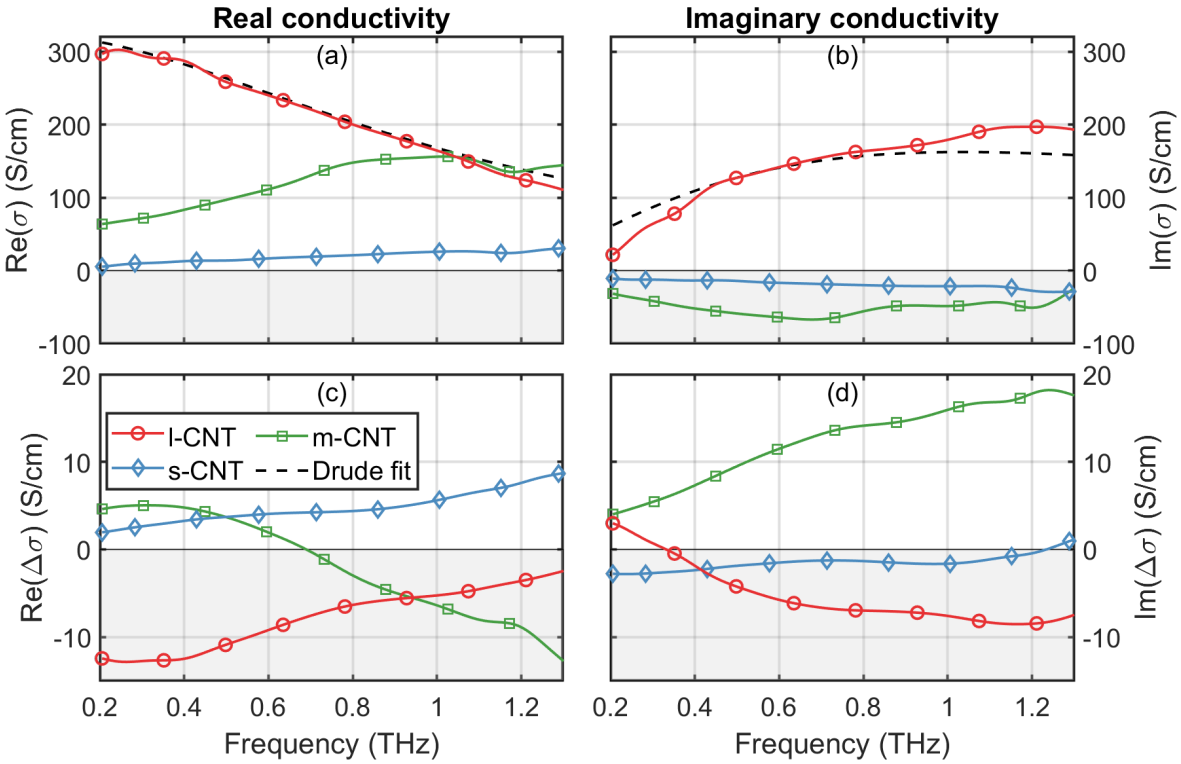

Figure 7.6: Change in effective conductivity $\mathrm{Re}(\Delta\sigma)$ and $\mathrm{Im}(\Delta\sigma)$ vs fluence for **(a)-(b)** $l-$CNT, **(c)-(d)** $m-$CNT, **(e)-(f)** $s-$CNT, due to 800 nm photoexcitation at pump-probe delay time $\Delta\tau = 1$ ps.

we also investigate the change in conductivity on heating our samples. In figures 7.8a-7.8d we compare $\Delta\sigma_{ph}$ to the change induced by heating from 10K to 300 K, ($\Delta\sigma_{heat}$), for our CNT films. The similarity in the change in the frequency response for heating compared to photoexcitation is striking. In figures 7.8a-7.8b, the only notable difference between $sem-$ and $met-$CNT is a four times increase in the magnitude of $\mathrm{Re}(\Delta\sigma_{heat})$, which is expected due to bandgap of the latter. Likewise, in figures 7.8c-7.8d, the only notable difference is between $\mathrm{Im}(\Delta\sigma_{ph})$ and $\mathrm{Im}(\Delta\sigma_{heat})$ for $s-$CNT (we discuss this later on). Our observations suggest that $\Delta\sigma_{ph}$ and $\Delta\sigma_{heat}$ likely originate from the same underlying mechanism, one that is related to heating induced changes in the conductivity. Furthermore, we note that the intrinsic THz conductivity of metallic CNTs with diameters less than 2 nm follows the Drude law, where the plasma frequency does not depend on the temperature [269, Equation (24)]. A dominant heating effect may arise from electron scattering by hot optical-phonons [302] as well as acoustical phonons, which have a linear temperature dependence of the Drude scattering rate in CNTs below 500 K [272, 299], as we demonstrated in section 6.6.2. However,

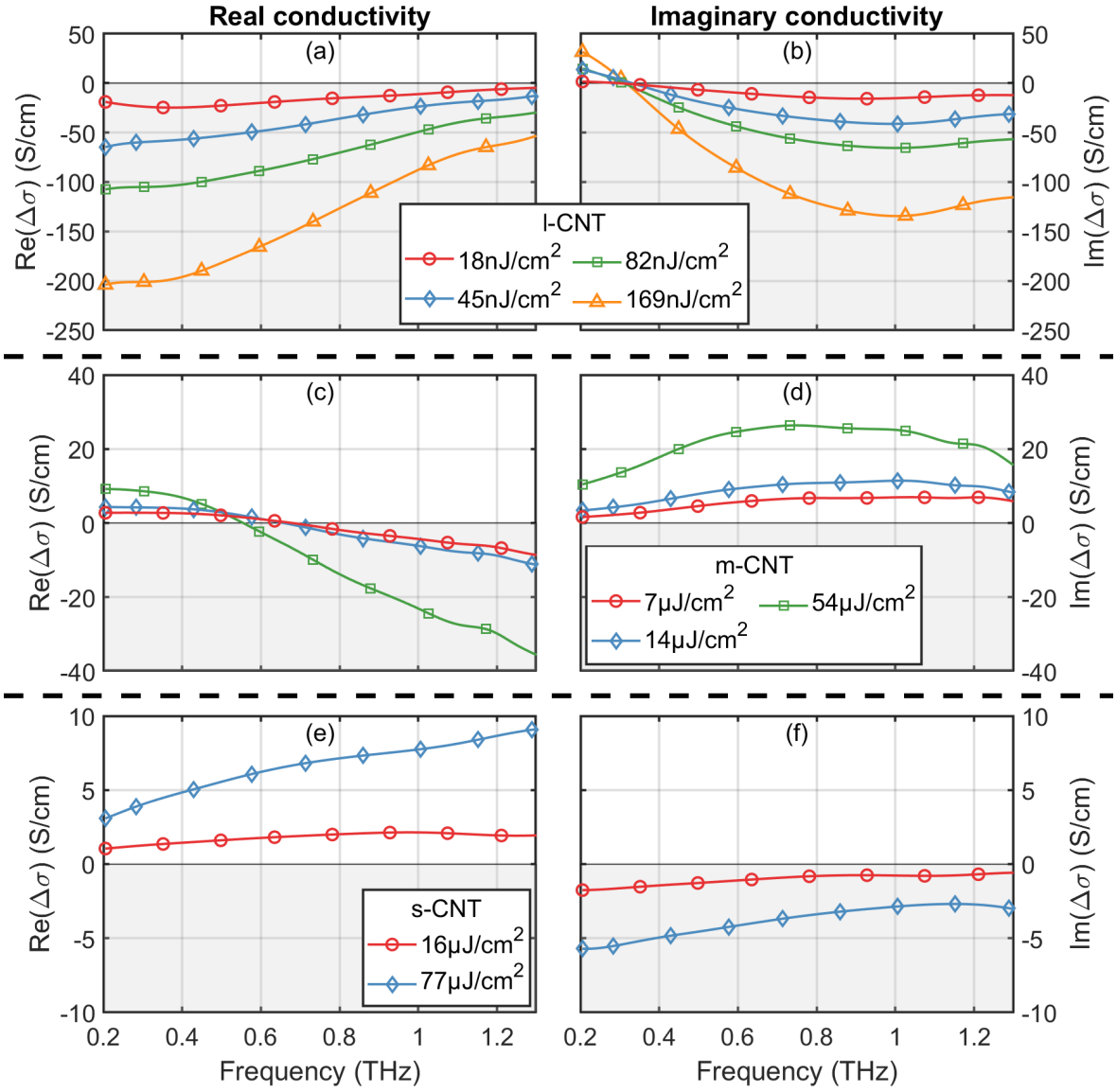

Figure 7.7: Change in effective conductivity $\mathrm{Re}(\Delta\sigma)$ and $\mathrm{Im}(\Delta\sigma)$ vs fluence for **(a)-(b)** $l-$CNT, **(c)-(d)** $m-$CNT, and **(e)-(f)** $s-$CNT, due to 800 nm photoexcitation at pump-probe delay time $\Delta\tau = 1$ ps.

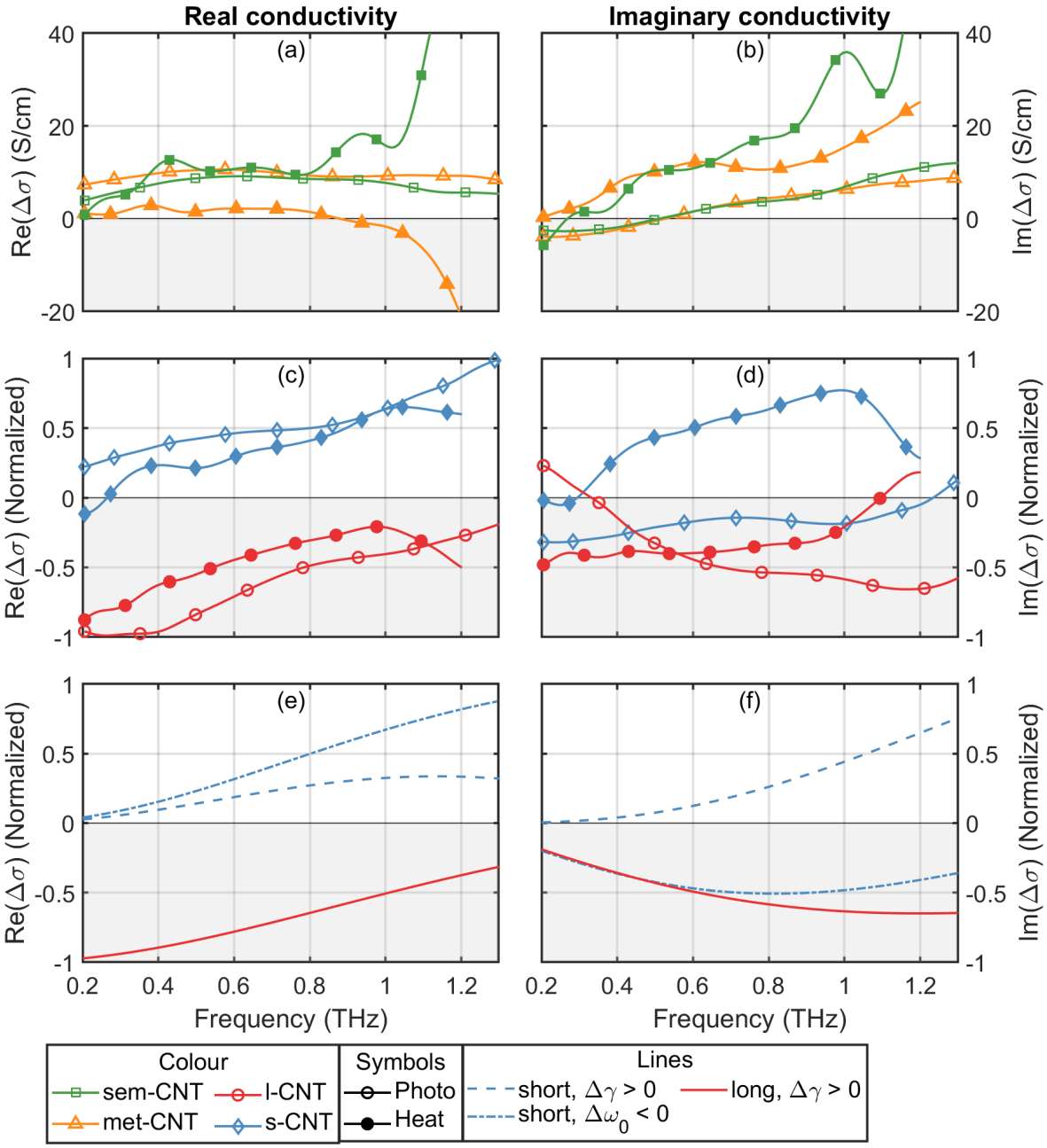

Figure 7.8: Change in effective conductivity ($\mathrm{Re}(\Delta\sigma)$ and $\mathrm{Im}(\Delta\sigma)$) of **(a)-(b)** *sem-* and *met*-CNT, and **(c)-(d)** $l-$ and $s-$CNT, due to heating from 10 K – 300 K (filled symbols), compared with the same $\Delta\sigma_{ph}$ data as in figures 7.4 and 7.6 (open symbols). The calculated change in conductivity **(e)** $\mathrm{Re}(\Delta\sigma)$ and **(f)** $\mathrm{Im}(\Delta\sigma)$ for two simple Lorentzian resonances *long* and *short* at resonance frequency $\omega_0 = 2\pi \times 10^{-2}$ THz and $\omega_0 = 2\pi \times 10$ THz, respectively, to illustrate the difference in $\Delta\sigma$ when increasing the scattering rate $\Delta\gamma > 0$ and when decreasing the resonance frequency $\Delta\omega_0 < 0$. Here we have chosen $\gamma = 2$ THz and $\gamma = 50$ THz, for the *long* and *short* resonance, respectively, and $\Delta\gamma = 1$ THz and $\Delta\omega_0 = 1$ THz. Note that all data in **(c)-(f)** have been normalized by the maximum absolute value of each $\Delta\sigma$ in the displayed frequency region to make the overall frequency behaviour more comparable.

the influence that this has on the THz conductivity will depend on the frequency and oscillator strength of the THz plasmon resonance. In general, one would expect heating to induce a broadening of the THz peak. However, depending on the frequency of the resonance, this can lead to either an increase or decrease of the effective conductivity of the CNT-film in the THz range, as we saw in chapter 6. To illustrate this effect, in figures 7.8e and 7.8f we plot the differential conductivity expected for a Lorentzian resonator, given by

$$\sigma(\omega) = -i\omega\epsilon_0 \left(\frac{A}{\omega^2 - \omega_0^2 + i\omega\gamma} \right), \tag{7.1}$$

where A is the oscillator strength, $\epsilon_0 = 8.85 \times 10^{-12} Fm^{-1}$ is the vacuum permittivity, and γ is the scattering rate. We note that this simple model ignores contributions to the scattering rate from inhomogeneous broadening over CNT length [253, Equations (1) and (2)]. We choose two Lorentzians with resonance frequencies located at $\omega_0 = 2\pi \times 10$ THz and $\omega_0 = 2\pi \times 10^{-2}$ THz, representing *short* and *long* CNTs, respectively. It is straightforward to qualitatively reproduce the general trends of the observed real $\Delta\sigma = (\partial\sigma/\partial\gamma)\Delta\gamma$ in figure 7.8c by assuming a heat induced increase in the scattering rate, γ. This gives rise to a change in real part of the conductivity which is negative for a low frequency resonator ($\omega_0 = 2\pi \times 10^{-2}$ THz) and positive for a high frequency resonator ($\omega_0 = 2\pi \times 10$ THz). Based on this simple consideration we conclude that both $\Delta\sigma_{ph}$ and $\Delta\sigma_{heat}$ are determined predominantly from heat induced changes to electron scattering.

It is interesting to note that the opposite signs of $\mathrm{Im}(\Delta\sigma_{heat})$ and $\mathrm{Im}(\Delta\sigma_{ph})$ for $s-$CNT indicate that thermal heating and photo-excitation bring about slightly different changes to the carrier distribution. In order to reproduce this sign change, we must additionally introduce a small change to the resonance frequency, shifting to lower frequency after photoexcitation (see blue dash-dotted line for $\Delta\sigma = (\partial\sigma/\partial\omega_0)\Delta\omega_0$ in figures 7.8g-7.8h). The origin of this effect can be understood as follows: In such a percolated CNT network, the plasmon resonance frequency is determined not by the physical length of each tube, but by an effective length of conductivity pathways in the network, which we also discussed in chapter 6. On photoexcitation with optical light, some energetic carriers will be able to escape local energy minima, become more delocalized, and increase the average effective length. Such an effect will be most important for short length tubes, as we observed in experiment.

7.6 Conclusion

In conclusion, using optical pump - THz probe time-domain spectroscopy we measured the photo-induced change in THz conductivity, $\Delta\sigma_{ph}$, in free-standing carbon nanotube (CNT)

films of different lengths and chirality distributions. By comparing CNT films with average individual tube lengths ranging from 0.3 μm to 10 μm, we demonstrated that drastic variations in $\Delta\sigma_{ph}$ observed for various films primarily originates from changes to the plasmonic resonance observed in finite length CNTs due to expected heat-induced changes to electron scattering. Thus we conclude that the photoexcited ultrafast THz response is predominately plasmonic in nature, and that the length of the CNTs is what determines the frequency-dependent behaviour. This explains the conflicting reports presented in [41, 249, 257, 292–294], and underlines the need to carefully consider the length of the CNTs when analysing their ultrafast THz response.

Chapter 8

Influence of Diameter and Oxygen Content on the Terahertz Conductivity of Tungsten-Oxide Nanowires

We begin by acknowledging the contributions of our collaborators to the content presented in this chapter. WO_x nanowire fabrication, preparation and structural characterisation described in section 8.2, was performed by Kunyapat Thummavichai, under supervision of Prof. Yanqiu Zhu, at the College of Engineering, University of Exeter.

8.1 Background

In recent years, 1D nanomaterials have provided a means to investigate the effects of low dimensionality on their physical and chemical properties. Because of their unique architectures, 1D materials also offer an opportunity to fabricate certain nanodevices [105, 106, 303, 304]. Among the metal oxide materials, tungsten oxide (WO_x, $2 < x < 3$), is an important semiconductor material with a wide band gap ranging from 2.62 eV to 3.25 eV, is of great interest because of its practical applications in smart windows [47], photocatalysts [48, 49], and gas/temperature sensors [50, 51]. Therefore, much effort has been expended to synthesize 1D tungsten oxide materials with various morphologies and phases using either physical or chemical routes [52–63].

As detailed in section 2.8, WO_3 is a transition metal oxide made up of perovskite-like

units, and is well-known for its nonstoichiometric properties, as the lattice can withstand a considerable amount of oxygen deficiency [43]. Only a partial loss of the WO_3 oxygen content is needed to affect its electronic band structure and increase its conductivity by a large amount [8, 44]. Fully oxidized WO_3 is a n-type semiconductor with an indirect bandgap E_g corresponding to the difference between the energy levels of the valence band, originating from filled O 2p orbitals, and the conduction band originating from empty W 5d orbitals [8, 45, 46]. In the bulk, tungsten oxide exhibits a strong color change upon intercalation of small ions such as Li^+ or H^+ or due to oxygen deficiency [104]. In the case of WO_x, which generally has a strong blue color, a variety of oxygen-deficient stoichiometries can be obtained, e.g., $WO_{2.72}$ ($W_{18}O_{49}$), $WO_{2.8}$ (W_5O_{14}), $WO_{2.83}$ ($W_{24}O_{68}$), and $WO_{2.9}$ ($W_{20}O_{58}$). These are ordered phases with precise stoichiometries. For $2.9 < x < 3$ in bulk WO_x, the electrical and optical properties are dominated by localized electrons involved in polarons, which are quasiparticles consisting of a charge carrier and its polarization field in a lattice. Bulk WO_x undergoes a metal-insulator transition at $x = 2.9$, as the localized polaronic wave functions begin to overlap and form delocalized states [116]. This transition corresponds to the Fermi-level shifting from the band-gap and up into the conduction band [8], as seen in figure 2.21. As a result, for $x < 2.9$ in bulk WO_x, the electrical and optical properties are dominated by free electrons. The metal-insulator transition has been firmly established in bulk WO_x, both theoretically [8] and experimentally by a combination of temperature-dependent conductivity measurements [117], reflectivity measurements of the bulk plasma frequency [118], and X-ray photoelectron spectroscopy (XPS) [119]. Thus, there is a wide range of known phenomena from the bulk that may exhibit interesting size- and shape-dependent behavior at the nanoscale.

Studies of nanoscale WO_x have so far led to some contradictory results. For instance, $WO_{2.72}$ nanowires appear to be semiconducting on the basis of electrical transport [120] and photoluminescence studies [53, 121–125]. At the same time there is some evidence that $WO_{2.72}$ bulk is characterized by a metal-like dependence of electrical resistivity on temperature [118], which has also been confirmed theoretically [8]. Likewise, $WO_{2.8}$ nanowires appear to be metallic on the basis of XPS and electrical transport measurements [126], and it was demonstrated that nanoscale $WO_{2.83}$ can support strong localized surface plasmon resonances (LSPRs) [127], which can only appear in materials with a relatively high charge-carrier concentration. The reason for this discrepancy between bulk and nanowire $WO_{2.72}$ may to some extend be explained by the limitations of the experimental techniques used so far, specifically the static electrical (DC) resistance measurements and the photoluminescence measurements. The former technique is limited by the overall conductivity of the percolating nanowire network, which is heavily influence by the contact resistance between neighbouring nanowires,

the density of the network, and the contact resistance of the applied electrodes. Similarly, while photoluminescence measurements can reveal information about optical transitions and the lifetimes of radiative recombination in a material, it cannot say anything about the intraband conductivity, which is the relevant parameter for determining the transport properties of the material, and a critical factor for any optoelectronic applications. In this regard, terahertz time-domain spectroscopy (THz-TDS) is an ideal tool for probing the local intraband conductivity of WO_xNWs due to the non-invasive and local nature of the method, and the low energy of the transient terahertz (THz) pulses (1 THz $\sim$ 4.1 meV $\sim$ 1 ps), which typically coincides with a number of phonon resonances and scattering events in these types of materials [16, 156, 299]. Similarly, by photoexciting the NWs beforehand using an optical pump pulse (OPTP) it is possible to probe the photoexcited ultrafast charge-carrier dynamics on a picosecond timescale [15, 66, 238, 305–307]. Yet despite the usefulness of THz-TDS and its widespread use for similar nanowire materials, there is so far only one instance in the literature of THz-TDS being applied to WO_x nanomaterials, specifically WO_3 nanograins and nanoparticles [308], and in general there are very few measurements of the transient properties of WO_3 [308–311].

In this chapter we use THz-TDS and OPTP to systematically investigate the influence of oxygen-content and nanowire diameter on the THz conductivity and photoconductivity of thin-films comprising tungsten-oxide nanowires. To the best of our knowledge, we present the first experimental evidence of the predicted metal-to-insulator transition for $WO_{2.72} \rightarrow WO_3$ nanowires, which so far has only been shown to occur for bulk WO_x [8]. Specifically, we observe that the THz conductivity of our $WO_{2.72}$ nanowires drops by several orders of magnitude after oxidization ($x = 2.72 \rightarrow 3$), which we attribute to a shift in the Fermi level from the conduction-band down into the bandgap. Moreover, by comparing the equilibrium THz conductivity with the photo-induced change in THz conductivity (photoconductivity) due to 266 nm photoexcitation, we show that the THz photoconductivity is similarly influenced by the oxygen content, and to a lesser extend the diameter. Finally, to the best of our knowledge, we present the first experimental measurements of the photoexcited charge-carrier dynamics of WO_x nanowires on a picosecond timescale and map the influence of oxygen-content and nanowire diameter. From this we show that the decay-dynamics of the nanowires is characterized by a fast decay of <1 ps, followed by slow decay of 3-10 ps, which we attribute to saturable carrier trapping at the surface of the nanowires.

8.2 Sample Preparation and Characterization

All samples were fabricated and their structural properties characterized by our collaborators, Kunyapat Thummavichai and Yanqiu Zhu, at the College of Engineering, University of Exeter. To study the influence of oxygen content and diameter, four types of films comprising WO_x nanowires were prepared, where the diameter and oxygen content (x) of the individual NWs varies significantly, see table 8.1. Essentially, small and large diameter $WO_{2.72}$NWs were prepared and characterized using THz-TDS and OPTP. These films were afterwards baked in an oven at 500 °C for 1 hour to fully oxidize the $WO_{2.72}$NWs into WO_3 [52, 312], and the resulting changes in their THz properties were measured. The synthesis, sample preparation and structural characterization of the small-diameter $WO_{2.72}$NWs ($s-WO_{2.72}$) can be found in [304] and follows the procedure outlined in [52]. Likewise, the details of the large-diameter $WO_{2.72}$NWs ($l-WO_{2.72}$) can be found in [155]. In the following paragraph we give the details of the sample fabrication and preparation.

Bundles of oxygen deficient tungsten oxide nanowires $W_{18}O_{49}$ ($WO_{2.72}$) with individual diameters of approximately 4 nm were synthesized using a solvo-thermal method [52, 304], with tungsten hexachloride (WCl_6) as the precursor. Briefly, a 0.003 M well-dissolved WCl_6 in cyclohexanol solution was transferred to a 100 mL Teflon-lined stainless steel autoclave for solvothermal synthesis at 200 °C for 6 hours. The resulting final product was collected after being thoroughly rinsed with deionized water, ethanol, and acetone several times to remove the solvent residues, and dried at 80°C for 12 hours for later use. 0.1 g dried powder of $WO_{2.72}$ nanowires was dissolved in 2 ml ethanol, well mixed via ultrasonic bath for 30 min. 0.2 ml well-mixed solution was dropped and well-spun on the quartz substrate (1.5×1.5 cm^2) and then natural dried at room temperature to get a homogeneous nanowire thin film. Similar $WO_{2.72}$ nanowires with mean diameters of 100 nm were synthesized using the following approach (see [155] for details): 0.1 g dry WS2-IF powder [313] was well-dissolved in 2 ml ethanal, then 0.2 ml well-mixed solution was deposited on 1.5×1.5 cm^2 quartz substrate and left to dry at room temperature. The dry WS_2-IF thin film was then placed into a 1 m long quartz tube situated inside a horizontal furnace. Ar was used to flush the quartz tube at a flow rate of 150 sccm to thoroughly remove the air residue in the tube. The thin film on quartz substrate was initially located outside the heating zone when raising the temperature. After reaching the reaction temperature at 950°C, the sample was moved to the central hot zone; meanwhile, water vapor was introduced into the reaction tube by Ar bubbling though a wash bottle containing deionized water. The Ar flow rate was controlled at 40 sccm by a mass flow meter. The thin film was shifted out of the reaction zone and cooled to room temperature rapidly after 1 h reaction time to achieve large-diameter $WO_{2.72}$ nanowires

Sample	D (μm)	L (μm)	d (nm)	WO_x (x)
$l-WO_{2.72}$	$\sim$1	10 – 100	60 – 150	2.72
$l-WO_3$	$\sim$1	10 – 100	60 – 150	3
$s-WO_{2.72}$	$\sim$0.1	$\sim$2	2 – 5	2.72
$s-WO_3$	$\sim$0.1	$\sim$2	2 – 5	3

Table 8.1: Summary of our WOxNW films; thickness (D), length (L) (average length in parenthesis), individual diameter (d), and oxygen deficiency WO_x (x).

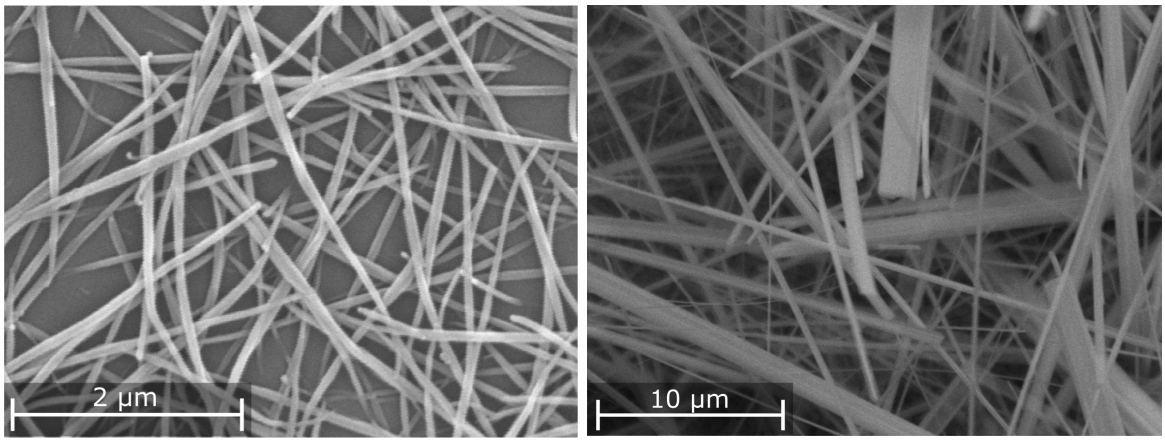

(a) (b)

Figure 8.1: SEM image of **(a)** $s-WO_{2.72}$ and **(b)** $l-WO_{2.72}$.

(nanorods). Finally, selected thin films of both small- and large-diameter $WO_{2.72}$NWs were oxidized into WO_3NWs via a low annealing treatment technique by baking the NWs at 350°C for 3 hours in an open-air condition [52, 312].

The thickness of the films coated on quartz was measured using a stylus profilemeter. Their structure and morphology were measured using a combination of X-ray diffraction (XRD) from 10 to 60° in the 2θ range, scanning electron microscopy (SEM; a Philips XL-30 machine operated at a voltage of 20 kV), see figure 8.1, and tunnelling electron microscopy, as detailed in [52, 155, 304].

8.3 Experimental Methods

We carried out both transmission and photoconductivity measurements over the range 0.2–1.5 THz, where THz pulses were incident normal to our samples. Transmission spectra were obtained using our THz-TDS setup described in section 4.4.1, where THz pulses were generated and detected by commercially available Photoconductive Antennas (PCAs) [167]

Sample	$\tau_{1,300K}$ (ps)	$\tau_{2,300K}$ (ps)	$\tau_{1,10K}$ (ps)	$\tau_{2,10K}$ (ps)
$l-WO_{2.72}$	-	9.2	0.2	2.8
$l-WO_3$	0.1	5.4	0.3	2.9
$s-WO_{2.72}$	0.3	11.3	0.4	9.8
$s-WO_3$	0.1	2.8	0.2	2.7

Table 8.2: Summary of the experimentally obtained decay-dynamics for our WO_xNW films; Fast decay time τ_1 and slow decay time τ_2 at 300 K and 10 K.

from Batop using a 40 MHz, 1064 nm, femtosecond fibrelaser from Ekspla. To investigate the photoexcited THz response of our samples, we employed our OPTP setup described in section 4.4.2, consisting of a 100 fs, 1050 Hz repetition rate, 800 nm Ti:Sapphire amplified laser, where THz pulses were generated and detected by optical rectification [180] and electro-optic sampling [189], respectively, in 1mm thick ZnTe crystals. To photoexcite the sample, we use 266 nm pulses with fluences in the range of 59–68 $\mu J/cm^2$, converted from the 800 nm pulses by way of second- and third-harmonic generation using BBO-crystals purchased from Eksma Optics. By analysing the frequency dependent transmission amplitude and phase of our samples (see chapter 5), we can determine its complex equilibrium effective conductivity, $\sigma(\nu)$, where ν is the frequency. Similarly, by recording the difference in THz transmission, $\Delta E = E_{exc} - E$, between the photoexcited (E_{exc}) and unexcited sample (E), a complex photoconductivity $\Delta\sigma_{photo}(\nu, \Delta\tau)$ can be obtained as a function of pump-probe delay-time $\Delta\tau$ (again, see chapter 5). To investigate the temperature dependence of the THz conductivity in the range 10–300 K, we employed a closed cycle helium cryostat (ARS)[15] with quartz windows. The 266 nm transmittance of our samples were determined by comparing the transmitted 266 nm pump power of our samples and a bare quartz substrate. From the transmittance and thickness of our samples, we were then able to determine their penetration depth d_p using the Lambert-Beer law, and their absorbed photon density N for a given incident pump-fluence.

8.4 Results

In figure 8.2 we plot the photo-induced relative change in THz transmission ($\Delta E/E$) of the WO_xNW films due to photoexcitation with an incident 266 nm pump-pulse, normalized to the absorbed photon density N, as a function of pump-probe delay time $\Delta\tau$ and for temperatures of 300 K (figure 8.2a) and 10 K (figure 8.2b). For 300 K in figure 8.2a we see that all samples except $l-WO_{2.72}$ exhibit an initial fast decay τ_1, followed by a much slower decay τ_2. The same is generally true at 10 K in figure 8.2b, although now all samples except $l-WO_3$ show

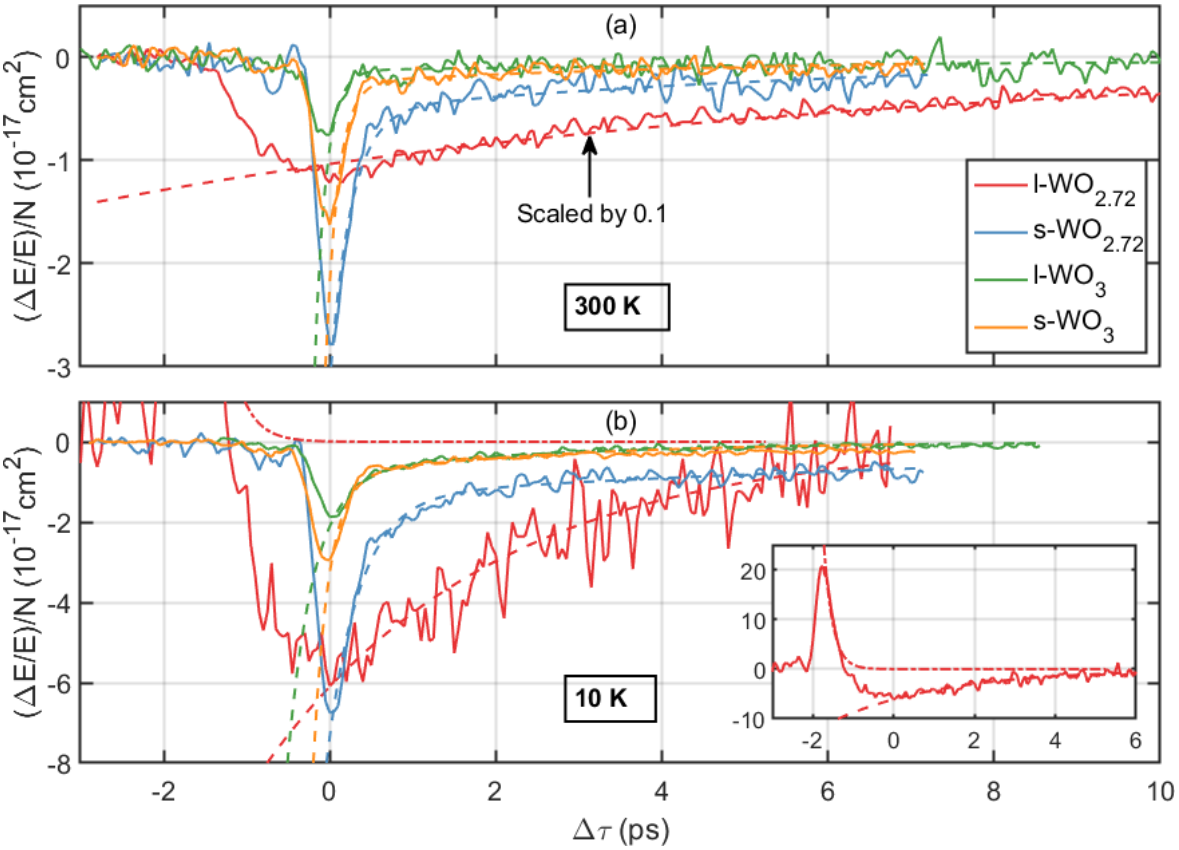

Figure 8.2: The photo-induced relative change in the THz transmission $\Delta E/E$ due to 266 nm photoexcitation at **(a)** 300 K and **(b)** 10 K of $s-$ and $l-WO_3$, and $s-$ and $l-WO_{2.72}$, vs pump-probe delay time $\Delta\tau$ and normalized by the absorbed photon density N. The incident fluence is 68 $\mu J/cm^2$, 59 $\mu J/cm^2$, 63 $\mu J/cm^2$, and 63 $\mu J/cm^2$ for $l-WO_{2.72}$, $s-WO_{2.72}$, $l-WO_3$ and $s-WO_3$, respectively. The full lines are the experimentally obtained data, and the dashed lines are exponential fits. Note that the data for $l-WO_{2.72}$ has been scaled by a factor of 0.1 in **(a)**. The inset in **(b)** shows a zoomed out plot of the $l-WO_{2.72}$ data at 10 K.

a fast and slow decay. Notably, at 10 K the $l-WO_{2.72}$ now shows an initial increase in THz transmission ($\Delta E/E > 0$), which quickly decays and reverses sign to the previously observed slowly decaying negative signal, which has weakened in magnitude to approximately half the size of the 300 K signal. Table 8.2 shows the extracted decay times from our exponential fits to $\Delta E/E$. In general, $WO_{2.72}$ has a noticeably slower decay time than WO_3 for both small and large NWs. Similarly, the decay-times of the small diameter NWs are either comparable or slightly faster than the large NWs at 300 K.

In previous studies, it was determined from spectroscopic measurements on the picosecond

time scale that the rate of electron trapping was on the order of 100 ps [309], while the rate of recombination was on the order of several hundred nanoseconds. Furthermore, time-resolved microwave conductivity studies have found that ∼80% of recombination occurs in WO_3 within 500 ns [314]. Regan et al. [308] used OPTP to measure the photoexcited THz response of spherical WO_3 nanoparticles, from which they observed a distribution of lifetimes, which they attributed to the inhomogeneity of their nanoparticles. They reported an average decay-time of 2 ps, which they attributed to carrier trapping. Similarly, recombination and trapping via surface states were shown to be the main decay dynamic in GaAs, InAs, and InP NWs [305], which was strongly dependent on NW diameter in the case of GaAs. Furthermore, the GaAs NWs displayed a deviation from mono-exponential behaviour at early photoexcitation times, which has been attributed to saturable carrier trapping at the nanowire surface [315]. Since our NWs show similar deviation from monoexponential behaviour, and the slow decays τ_2 of our NWs are comparable to the 2 ps decay time of the WO_3 nanoparticles observed by Regan et al. [308], we therefore associate the observed decay dynamics in figure 8.2 with saturable trapping of the photoexcited carriers. The reason we observe slightly slower decay times than the 2 ps of Regan et. al. [308] is likely due to the difference in geometry and surface to volume ratio between our nanowires and their nanoparticles. Similarly, the faster decay-times of the small-diameter NWs at 300 K is likely due to their increased surface to volume ratio, leading to increased scattering via trap states, as has been observed for other GaAs and InAs nanowires [305]. The observed difference in decay-times between $l-WO_{2.72}$ and $l-WO_3$ cannot be explained by this mechanism however, since the two samples have the exact same geometry. The faster decay-times of $l-WO_3$ must therefore originate from a different mechanism, which we are unable to determine at this time, however we propose that it may be related to the metal-insulator transition in WO_x at $x = 2.9$ [116]. Finally, the reason for the curious sign-reversal of $\Delta E/E$ for $l-WO_{2.72}$ at early $\Delta\tau$ at 10 K is not immediate obvious. We therefore move on to consider the conductivity and photoconductivity of the NWs.

In figure 8.3a we plot the effective conductivity (σ) of four prepared $l-WO_{2.72}$NW films to check the reproducibility. While there is a large variation in the magnitude of the samples, likely due to a variation in NW density, the overall frequency dependence is practically identical, showing a typical plasmonic Lorentzian response with a resonance frequency located above 1.5 THz, indicative of the localized nature of the system. In figure 8.3b, we examine the temperature-dependence for $l-WO_{2.72}$ film #2, which is the same sample plotted in figure 8.2 and the rest of this chapter. Re(σ) is observed to increase when cooling to 10 K, which agrees with previous DC conductivity measurements [116, 117], and is indicative of the metallic behaviour of this sample. We were unable to obtain reliable conductivity data at

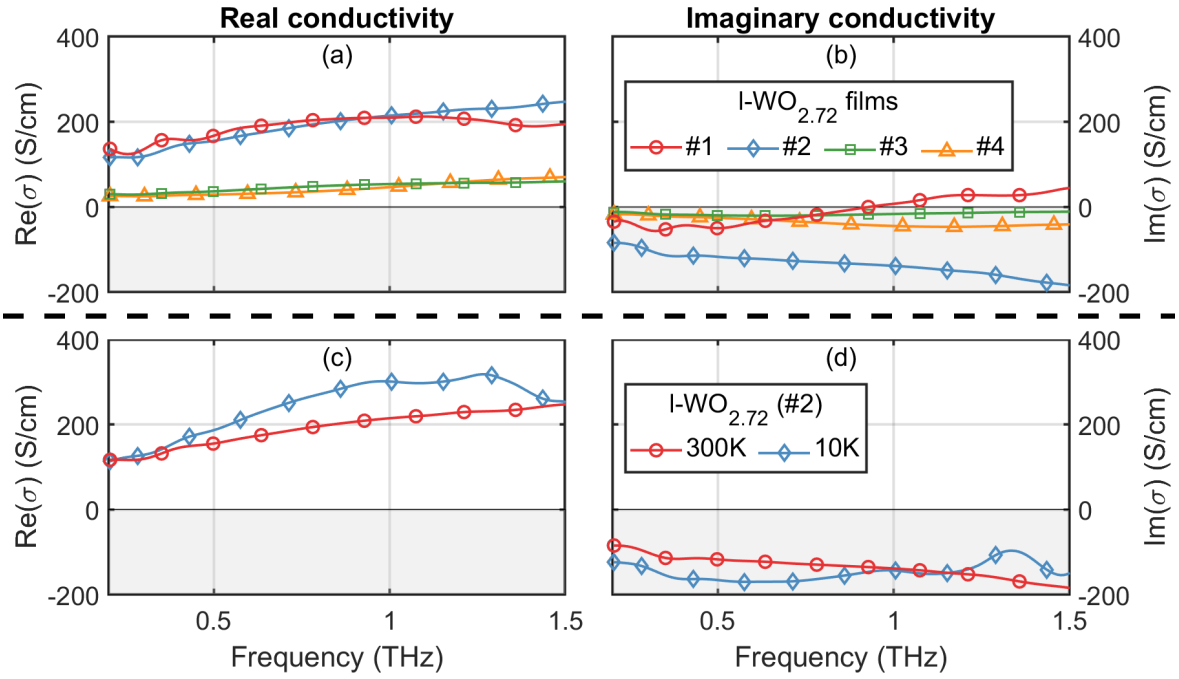

Figure 8.3: Effective conductivity **(a)** Re(σ) and **(b)** Im(σ) of four prepared $l-WO_{2.72}$ films at 300 K. Effective conductivity **(c)** Re(σ) and **(d)** Im(σ) of $l-WO_{2.72}$ film #2 at 300 K and 10 K. Note that the average thickness of each prepared film #1-4 is, respectively, 9 μm, 1 μm, 11 μm, and 7 μm.

this temperature for the rest of the NW films due to the small THz absorption of these, and the increased noise from running our cryostat, however we note that the DC conductivity of WO_3 has previously been observed to decrease at low temperatures [116, 117, 316], indicative of its semiconducting behaviour.

In figures 8.4a-8.4b we plot the effective conductivity σ of the WO_xNW films at 300 K. The frequency-dependency of σ for the rest of our NWs also display a typical plasmonic behaviour of positive Re(σ) and negative Im(σ), indicating a resonance frequency beyond 1.5 THz, which is common in 1D nanomaterials with a presence of free carriers [299, 305]. The difference in Re(σ) between large- and small-diameter NWs might be explained by an oxidization of the nanowire surface as proposed by Migas et al. [8], however the difference might simply be due to a variation in NW density as seen in figure 8.1. Furthermore, as we showed in figure 8.3, the effective conductivity of similarly produced $l-WO_{2.72}$ samples displayed some variation in magnitude of σ, with some of them displaying values closer to that of $s-WO_{2.72}$. Again, this may be due to a variation in NW concentration, as well as NW diameter distribution, and uncertainty in the overall thickness of the NW films determined

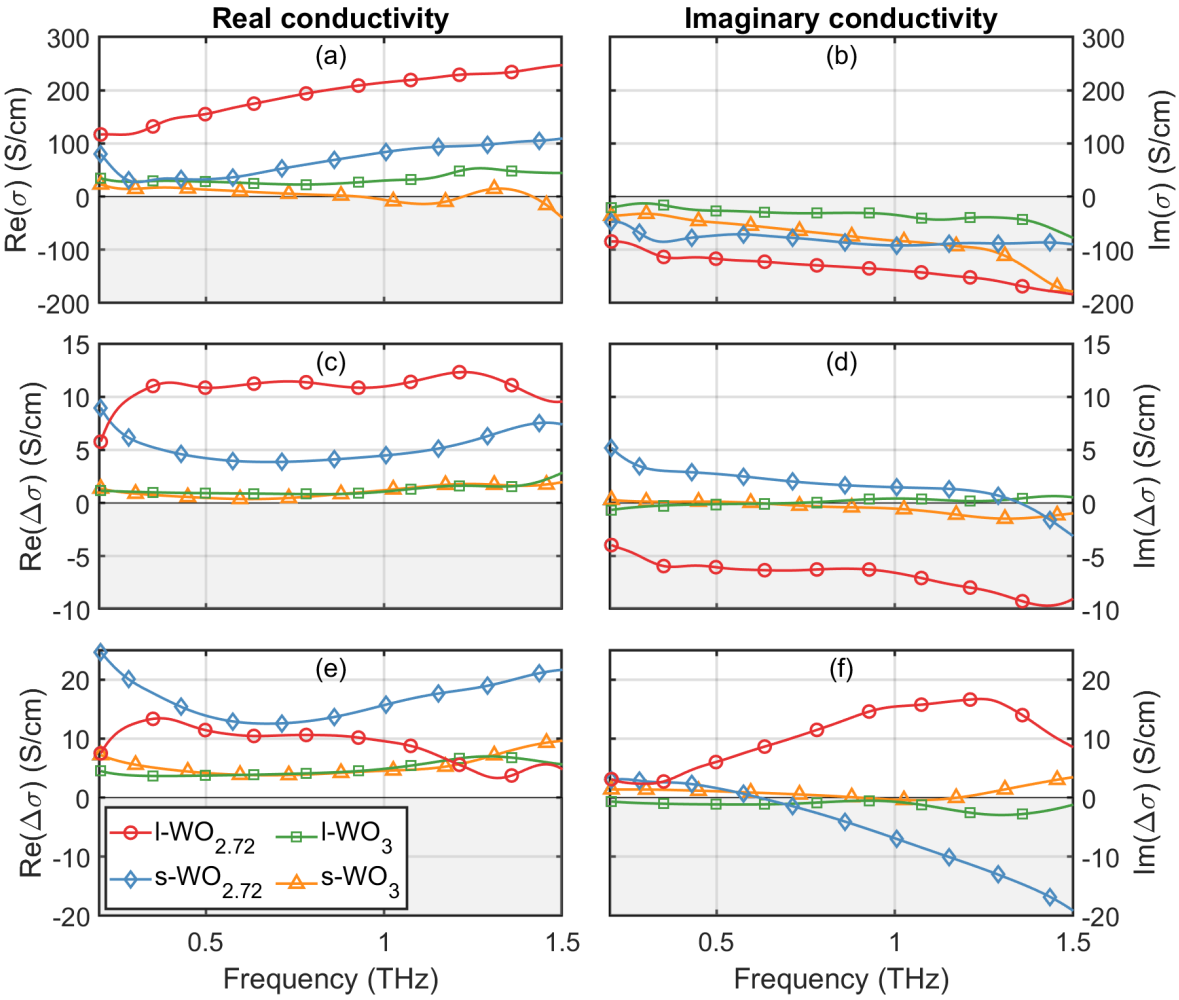

Figure 8.4: Effective conductivity **(a)** Re(σ) and **(b)** Im(σ) of $s-$ and $l-WO_{2.72}$, and $s-$ and $l-WO_3$ at 300 K, and change in effective conductivity **(c)** Re($\Delta\sigma$) and **(d)** Im($\Delta\sigma$) due to 266 nm photoexcitation at pump-probe delay time $\Delta\tau = 0.2$ ps. The incident fluence is 68 μJ/cm^2, 59 μJ/cm^2, 63 μJ/cm^2, and 63 μJ/cm^2 for $l-WO_{2.72}$, $s-WO_{2.72}$, $l-WO_3$ and $s-WO_3$, respectively. For the $s-WO_3$ in **(a)** we attribute the small oscillations of Re(σ) around zero as noise from our measurement. Note that the data for $l-WO_3$ has been scaled by a factor of 10 in all plots.

using the stylus profilemeter. However, the most notable result is that we observe significant drop in Re(σ) for both the large- and small-diameter NWs, approximately 200 S/cm to 3 S/cm for $l-WO_{2.72} \rightarrow l-WO_3$ at 1 THz, and ~80 S/cm to ~0 S/cm for $s-WO_{2.72} \rightarrow s-WO_3$. We can rule out factors such as sample-to-sample variation in the conductivity, since we measure the exact same NW samples before and after they were baked. Since the THz conductivity, to a first approximation, is proportional to the free-carrier density in a sample, and our

THz radiation exclusively probes the *intraband* conductivity of our samples, this reduction in conductivity must be due to a shift in Fermi level from the conduction band down into the bandgap as shown in figure 2.21. This is clear evidence of the predicted metal-to-insulator transition in WO_xNWs around $x = 2.9$ [8], which has so far only been observed in bulk WO_x [117–119].

In figures 8.4c-8.4d and 8.4e-8.4f we plot the photo-induced change in the effective conductivity $\Delta\sigma$ for 300 K and 10 K, respectively, immediate after 266 nm photoexcitation ($\Delta\tau = 0.2$ ps). While the frequency-dependence of $\mathrm{Re}(\Delta\sigma)$ is more or less the same for both temperatures and for all NW films, we observe a factor 10^2 reduction in $\mathrm{Re}(\Delta\sigma)$ at 300 K between the l-$WO_{2.72}$ and l-WO_3 NWs, just as we observed for $\mathrm{Re}(\sigma)$. For the small-diameter NWs the effect is much less pronounced with only a factor 2 reduction in $\mathrm{Re}(\Delta\sigma)$ from s-$WO_{2.72}$ to s-WO_3. This indicates that $\Delta\sigma$ is less influenced by oxygen-content as the diameter decreases and is likely due to the increased surface-to-volume ratio of the small-diameter NWs. In this case trapping and recombination via surface defects become the dominant effects, as observed for similar semiconductor NWs [305, 315], which likely limits the conductivity of photoexcited carriers immediately after photoexcitation. In terms of the temperature dependence of $\Delta\sigma$, all of the NW films show a general increase in $\mathrm{Re}(\Delta\sigma)$ as the temperature decreases, which is due to the increased life-times of the photoexcited carriers. Again the most curious change is observed for $l-WO_{2.72}$, which has a sign-reversal of $\mathrm{Im}(\Delta\sigma)$ from 300 K to 10 K, however we are not able to explain this behaviour at this point in time.

To study the time-evolution of the photoconductivity we plot $\Delta\sigma$ vs $\Delta\tau$ for each NW film at 10 K in figure 8.5. We do this partly to investigate the curious sign-reversal of $\Delta E/E$ for $l-WO_{2.72}$, and partly because for many of the NW films, the photoinduced signal is too weak to obtain reliable conductivity data at later $\Delta\tau$ at room temperature. For each film $\Delta\sigma$ becomes more or less flat at later $\Delta\tau$, and $\Delta\sigma$ shows the same frequency-dependency for almost every film. The exception here is the $l-WO_{2.72}$ film, which shows a strong decrease in $\mathrm{Re}(\Delta\sigma)$ above 1 THz for $\Delta\tau = -1.5$ ps, corresponding to the fast decay observed in figure 8.2b. We are unable to explain this behaviour at present time, but it would appear to be an additional mechanism that only occurs immediately after photoexcitation, and only at low temperatures. We only observe this behaviour for $l-WO_{2.72}$, so it may be related to the metallic nature of these NWs, since a negative $\mathrm{Re}(\Delta\sigma)$ has previously been observed in another metallic 1D system, specifically our finite-length carbon nanotubes chapter 7.

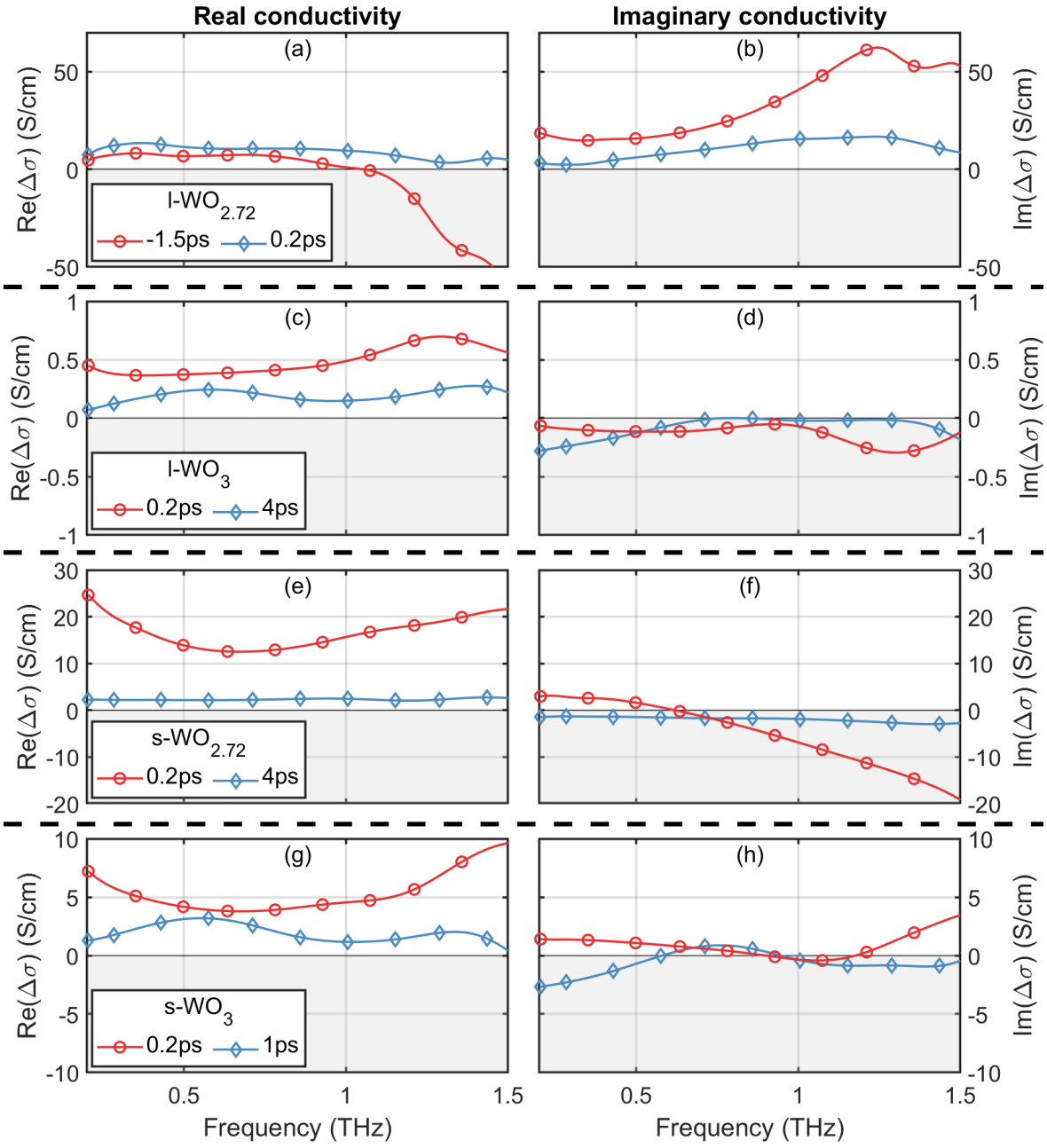

Figure 8.5: Change in effective conductivity ($\mathrm{Re}(\Delta\sigma)$ and $\mathrm{Im}(\Delta\sigma)$) of **(a)-(b)** $l-\mathrm{WO}_{2.72}$, **(c)-(d)** $l-\mathrm{WO}_3$, **(e)-(f)** $s-\mathrm{WO}_{2.72}$, and **(g)-(h)** $s-\mathrm{WO}_3$ at 10 K due to 266 nm photoexcitation vs pump-probe delay time $\Delta\tau$. The incident fluence is 68 μJ/cm^2, 63 μJ/cm^2, 59 μJ/cm^2, and 63 μJ/cm^2 for $l-\mathrm{WO}_{2.72}$, $l-\mathrm{WO}_3$, $s-\mathrm{WO}_{2.72}$ and $s-\mathrm{WO}_3$, respectively. Note that the early and later $\Delta\tau$ in each plot corresponds to region of fast and slow decay for each film as shown in figure 8.2b.

8.5 Conclusion

In conclusion we measured the terahertz conductivity and photoconductivity spectra of thin films compromising small- and large-diameter tungsten-oxide (WO_x) nanowires, and oxygen deficiencies $WO_{2.72}$ and WO_3 using THz-TDS and OPTP, as well as the decay-dynamics of the photoexcited carriers on a picosecond timescale. The $WO_{2.72}$NWs and large-diameter WO_3NWs displayed a typical plasmonic behaviour in the THz conductivity, which is common for 1D nanostructured systems with a significant presence of free carriers [299, 305]. For both small- and large-diameter NWs we observed a significant THz conductivity for $WO_{2.72}$, indicative of the metallic nature of the material. Furthermore we observe a massive drop in THz conductivity as the oxygen content is increased ($x = 2.72 \rightarrow 3$), which we attribute to the metal-to-insulator transition at $x = 2.9$, which so far has only been observed for bulk WO_3 [8, 116]. Furthermore we present the first experimental measurements of the photoexcited charge-carrier dynamics of WO_x nanowires on a picosecond timescale and map the influence of oxygen-content and nanowire diameter. For all NWs except the large-diameter $WO_{2.72}$ we observe an initial fast decay of $<$1 ps, followed by a slower decay of 3-10 ps. By comparing our data with similar measurements performed on WO_3 nanoparticles [308], and GaAs, InAs, and InP nanowires [305, 315], we attribute the observed decay-dynamics of our NW films to saturable carrier trapping at the surface of the nanowires. The decay-times were observed to decrease as the NW diameter decreases, and for small-diameter NWs the photoconductivity was less influenced by changes in oxygen content, which is likely due to the increased dominance of surface effects [305, 315]. Thus we have made significant progress in understanding the conductive properties of WO_xNWs and their decay-dynamics on the picosecond timescale, and are therefore one step closer in realizing efficient opto-electronic devices using nanostructured tungsten-oxide.

Chapter 9

Conclusion and Future Work

In conclusion, the charge-carrier dynamics of two 1D nanomaterials, single-walled carbon nanotubes and tungsten-oxide nanowires, have been investigated using THz-TDS and OPTP, with particular focus on how nanotube geometry and morphology influences their optoelectronic THz responses. Through these efforts, we have illuminated the nature of these types of materials in the THz frequency range, and thus helped pave the way for their applications in future optoelectronic devices. While this thesis has focused primarily on CNTs and WO_xNWs, many of the considerations and methods documented in this work are relevant for many other 1D semiconductor nanomaterials.

To summarize, in chapter 5 we formulated a general method for evaluating the applicability of any approximation used for obtaining the photoinduced change in dielectric properties of a sample, measured using OPTP. The method is valid for any given multilayer geometry and wavelength. Using this method we evaluated three of the most commonly used approximations and showed that they quickly become invalid as the wavelength becomes comparable with the sample thickness. The results of this analysis has huge implications for the study of charge-carrier dynamics using OPTP, since it demonstrates the need to properly analyse the applicability of an approximation for a given sample geometry. Improper use of these approximations can lead to significant errors, which in turn can lead to an incorrect interpretation of the photoexcited response. This method is therefore a huge achievement of this thesis in terms of quantifying the applicability of a given approximation for a given system.

In chapter 6, we then moved on to examine the influence of length and density on the effective conductivity of free-standing films comprising single-walled CNTs of various lengths, and CNT/WS_2 INT composites of varying CNT densities on quartz. Their effective conductivities and permittivities were measured in the ranges (i) 0.2–1000 THz for 300–530 K, and (ii) 0.3–2 THz for 10–530 K, and we observed a peak in the THz conductivity spectra of the

CNT films, which is shown to be plasmonic in nature, in agreement with recent literature, and shifting in frequency with the CNT length as predicted by our model of the localized plasmon resonance. Due to the plasmonic nature of the response of shorter tubes ($L \leq 1$ μm), we observed an unexpected variation with temperature, where the effective conductivity of the films in the THz frequency range is shown to increase with temperature, while we observed a decrease with temperature for longer tubes. This temperature-induced effect was shown to arise indirectly from the variation of the electron scattering rate, which determines plasmon losses, and therefore broadening of the conductivity resonance. Moreover, by studying composites of varying CNT densities, we showed that the change in conductivity with temperature depends not only on tube length, but also varies with tube density: as the temperature increases, we observe an effective conductivity in the range 0.3–1 THz that increases/decreases for low/high density samples. This effect accounts for the apparent discrepancies in literature regarding temperature dependent conductivity of CNT composites [250, 255, 259–262], and occurs due to the density dependence of the effective length of conducting pathways in the composite films, which again leads to a shift and temperature dependent broadening of the THz conductivity resonance. The observed influence of length and density on the effective conductivity of CNTs and CNT based composites presented in this thesis is a significant contribution to properly understanding the nature of the THz resonance in CNTs. Furthermore, the length- and density-influence have huge implications for the performance of any optoelectronic devices based on CNTs, such as photodetectors, polarizers, microwave shields, and so on, especially in the THz-range. Thus, careful consideration of CNT geometry is required when designing these types of CNT-based devices.

In chapter 7 we measured the photo-induced change in THz conductivity, $\Delta\sigma_{ph}$, in free-standing carbon nanotube (CNT) films of different lengths and chirality distributions. By comparing CNT films with average individual tube lengths ranging from 0.3 μm to 10 μm, we demonstrated that drastic variations in $\Delta\sigma_{ph}$ observed for various films primarily originates from changes to the plasmonic resonance observed in finite length CNTs due to expected heat-induced changes to electron scattering. From this we concluded that the photoexcited ultrafast THz response is predominately plasmonic in nature, and that the length of the CNTs is what determines the frequency-dependent behaviour. This explains the conflicting reports presented in [41, 249, 257, 292–294], and underlines the need to carefully consider the length of the CNTs when analysing their ultrafast THz response, and more importantly, when developing nanotube-based optoelectronic devices such as photodetectors [317] and ultrafast polarization modulators [318], since the CNT geometry in these devices will have a huge influence on their performance. To this end, we have also shown OPTP to be a simple and efficient technique for predicting the geometry of CNT films, which currently requires careful

statistical measurements with electron microscopy.

In chapter 8 we measured the terahertz conductivity and photoconductivity spectra of thin films compromising small- and large-diameter tungsten-oxide (WO_x) nanowires, and oxygen deficiencies $WO_{2.72}$ and WO_3 using THz-TDS and OPTP, as well as the decay-dynamics of the photoexcited carriers on a picosecond timescale. The $WO_{2.72}$NWs and large-diameter WO_3NWs displayed a typical plasmonic behaviour in the THz conductivity, which is common for 1D nanostructured systems with a significant presence of free carriers [299, 305]. For both small- and large-diameter NWs we observed a significant THz conductivity for $WO_{2.72}$, indicative of the metallic nature of the material. As the oxygen content increased ($x = 2.72 \rightarrow 3$), we observed a massive drop in THz conductivity, which we attributed to the metal-to-insulator transition at $x = 2.9$, which so far has only been observed for bulk WO_3 [8, 116]. Furthermore we presented the first experimental measurements of the photoexcited charge-carrier dynamics of WO_x nanowires on a picosecond timescale and mapped the influence of oxygen-content and nanowire diameter. For all NWs except the large-diameter $WO_{2.72}$ we observed an initial fast decay of <1 ps, followed by a slower decay of 3-10 ps. By comparing our data with similar measurements performed on WO_3 nanoparticles [308], and GaAs, InAs, and InP nanowires [305, 315], we attributed the observed decay-dynamics of our NW films to saturable carrier trapping at the surface of the nanowires. The decay-times were observed to decrease as the NW diameter decreases, and for small-diameter NWs the photoconductivity was less influenced by changes in oxygen content, which is likely due to the increased dominance of surface effects [305, 315]. Thus we have made significant progress in understanding the conductive properties of WO_xNWs and their decay-dynamics on the picosecond timescale, and are therefore one step closer in realizing efficient optoelectronic devices using nanostructured tungsten-oxide.

In conclusion, the work presented in this thesis has helped illuminate field of charge-carrier dynamics in 1D nanomaterials and thus contributed to their future development as components in novel optoelectronic devices.

9.1 Future Work

The work in this thesis has many possible roads for continued study. The general method for evaluating analysis approximations of OPTP, presented in chapter 5, is limited in so far that the modelling approach uses homogeneous slabs to represent the sample geometry. More complex geometries such as spatially inhomogeneous or nanostructured samples cannot be accurately modelled using this approach. Thus a next step could be to develop a model which can incorporate these types of geometries.

In terms of the CNTs in chapters 6 and 7, there are still many unexplored topics, for example the puzzling low temperature behaviour of the scattering rate. While the CNT/INT composites have huge potential in future optoelectronic devices, their photoexcited responses remain unexplored. In this thesis we have also limited ourselves to considering the effective conductivity of our CNT films: It may be of interest to use an effective medium model to extract the intrinsic conductivity of the CNTs in order to see how nanotube geometry and density influences this parameter. For our non-equilibrium experiments we have also limited ourselves to probing the off-resonance photoresponse of our CNTs. It would be quite relevant to probe the photoconductivity for on-resonance excitations, and below the optical transitions of the CNTs. The latter case might prove useful in observing the predicted small-gap interband transitions in quasi-metallic CNTs: Because the plasmonic THz resonance in CNTs clearly dominates the photoconductive response, no one has so far managed to observe the small-gap interband transition in experiment.

Regarding the WO_xNWs in chapter 8, we were limited to measuring two different diameters with oxygen contents of $x = 2.72$ and $x = 3$. A natural next step would be to examine the other Magnéli phases of tungsten-oxide, essentially mapping the THz conductivity and photoconductivity as a function of oxygen content, x (and diameter), in order to verify the predicted metal-insulator transition around $x = 2.9$. Furthermore, the nature of the WO_xNW photoconductive responses are still relatively unexplored, especially the curious behaviour the large-diameter $WO_{2.72}$NWs at low temperature.

Finally, our time-resolved THz measurements have been fairly limited in their frequency bandwidth due to a number of factors, mainly the cryostat. Thus, it would be quite relevant to map the optoelectronic responses of the CNTs and WO_xNWs for a broader frequency range. Thus, the field of charge-carrier dynamics in 1D nanomaterials is still open for many avenues of research.

Appendix A

Experimental Setups: Additional Information

This appendix contains additional information and pictures of the THz-TDS and OPTP setups described in section 4.4. Figure A.1 shows our PCA based THz-TDS, with the cryostat raised above the setup. Closeups of the cryostat are shown in figures A.2 and XXX. Figure A.4 shows our OPTP setup, along with a zoomed in picture of the dry-air box in figure A.5.

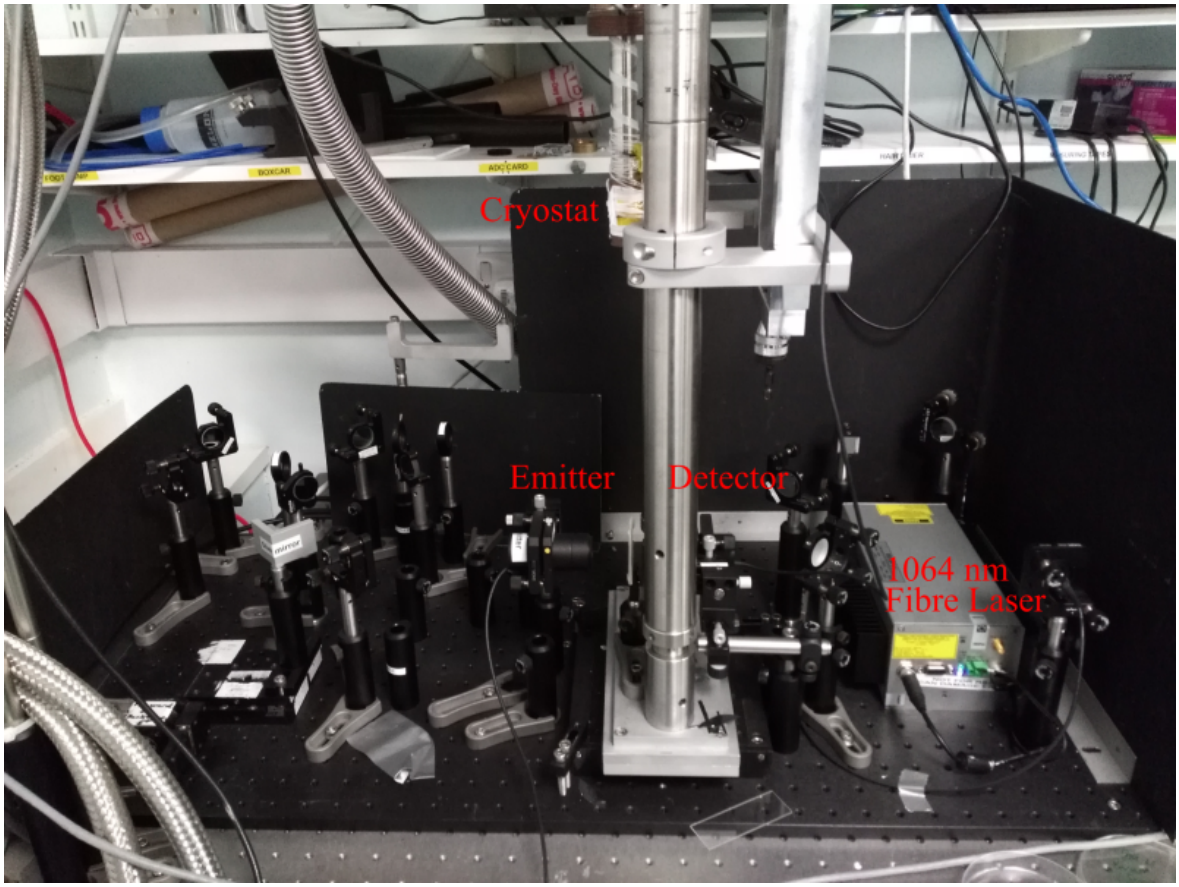

Figure A.1: Picture of the THz-TDS setup shown in figure 4.8. The two large pillars, situated between the PCAs in the middle of the setup, are part of the cryostat holder. The cryostat is raised above the setup.

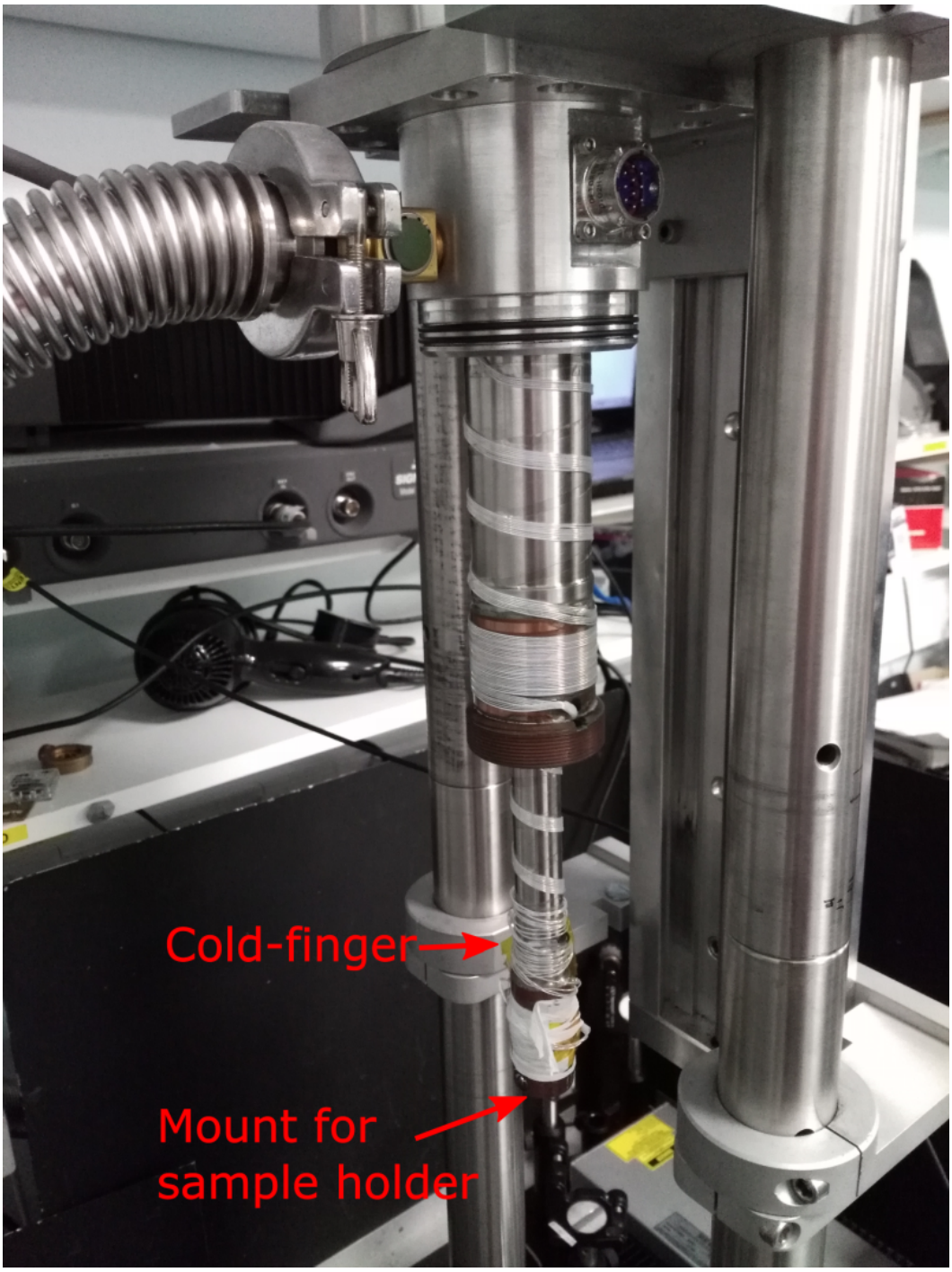

Figure A.2: Picture of the cryostat cold-finger, without sleeve. A sample holder can be mounted to the bottom of the coldfinger, and the temperature is controlled using heating wires and a temperature sensor mounted near the bottom of the cold-finger.

Figure A.3: Cryostat sleeves and radiation shield, which fits over the coldfinger.

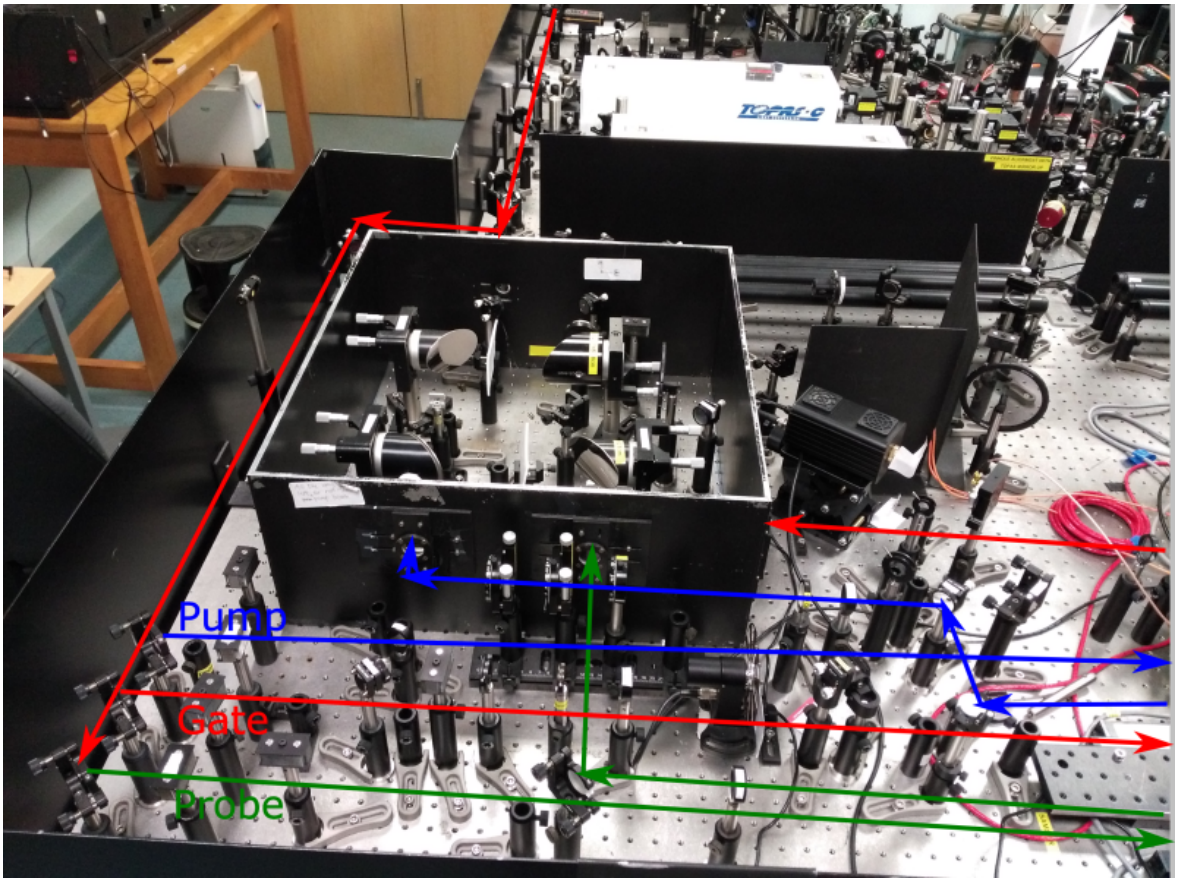

Figure A.4: Picture of the OPTP setup shown in figure 4.10. The OPTP setup is shown in the foreground, and the 800 nm femtosecond laser is in the background (just outside the picture), along with two other setups.

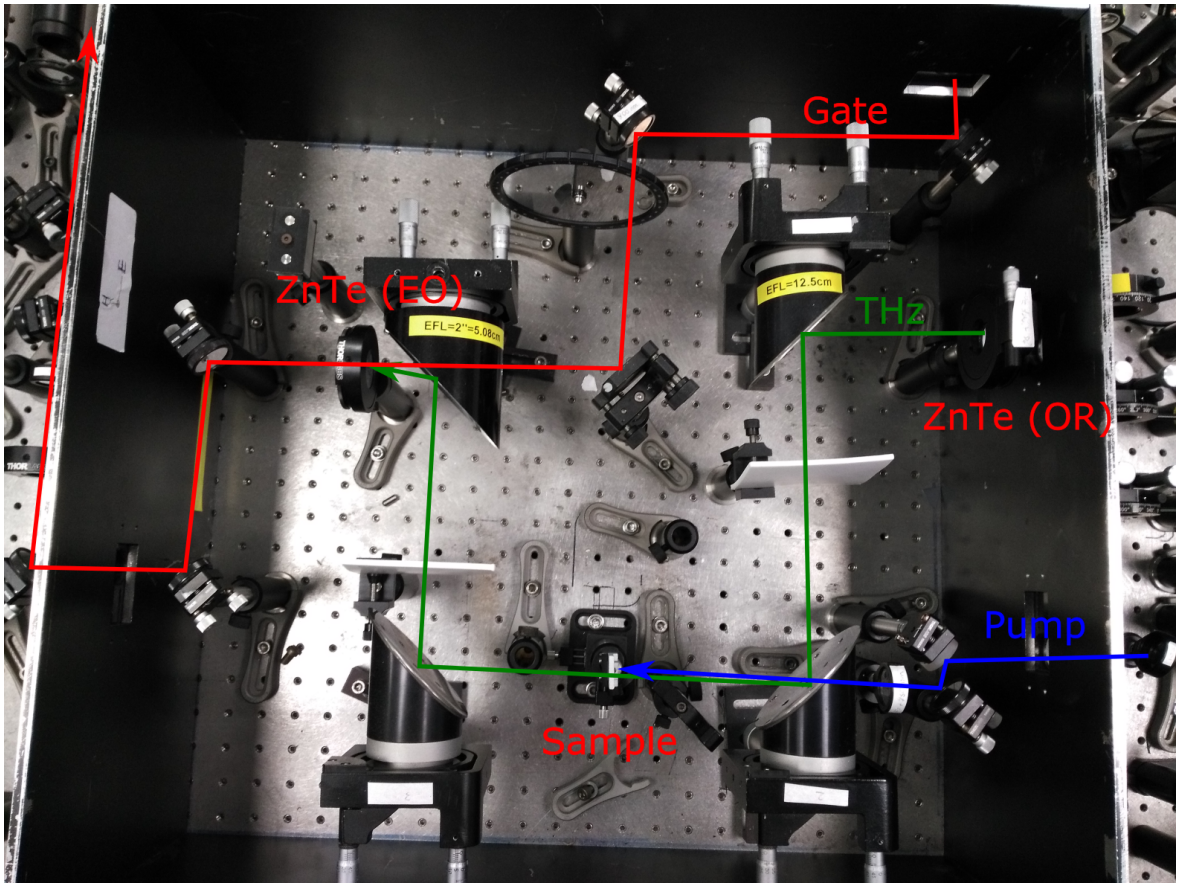

Figure A.5: Picture of the inside of our dry-air box used in the OPTP setup shown in figure 4.10. The green, red and blue arrows indicate the THz, gate, and pump-pulse, respectively. Note that the cryostat was removed from the setup when this picture was taken.

Appendix B

Source Code

This appendix chapter contains the Matlab and Mathematica source code used in chapters 5-8 to extract the dielectric properties of our samples and generate the results in figure 5.4.

B.1 Matlab Source Code

This section presents the Matlab functions used in chapters 5-8 to extract dielectric properties of our samples. Two functions were written for this purpose:

- **Conductivity_Fresnel**, which utilizes the Fresnel equations approach described in section 5.3 to extract the dielectric properties of a 3-layer structure.
- **ConductivityTMM**, which utilizes the Transfer Matrix Method (TMM) approach described in section 5.2 to extract the photoexcited dielectric properties.

B.1.1 Conductivity_Fresnel

```
1  function [ ntable] =...
2      Conductivity_Fresnel( f, fT, d, n_sub,varargin)
3  % Calculate permitivity, refractive index and conductivity of a
4  % 3-layer system using Fresnel equations.
5  %
6  % REQUIRED INPUT ARGUMENTS:
7  % -> f is an array of frequencies in units of THz.
8  % -> fT is an array containing the complex transmission of the pulse
9  %     in the frequency spectrum.
10 % -> d is a single value containing the thickness of the sample in units
11 %     of meters.
12 % -> n_sub is the refractive index of the sample substrate.
```

```
13 %
14 % OPTIONAL ARGUMENTS:
15 % -> initguess is the initial guess used by the numerical routine to find
16 %    the refractive index.
17 % -> FP is a boolean. If true, accounts for the Fabry-Perot resonance.
18 % -> flimit sets the frequency range that we wish to calculate for
19 % -> ff is the fillfraction for the sample, default value is 1.
20 % -> dvar is the difference between the thickness of the reference
21 %    substrate and the substrate of the sample
22 %
23 % OUTPUT:
24 % -> ntable is the outputted table containing frequency, refractive index,
25 % permittivity and conductivity.
26 %% Parameters
27 c=299792458; %[m/s] speed of light
28 eps0=8.854e-12; % [F/m] vacuum permittivity
29 n_air=1; % refractive index of light
30
31 %% Parse input
32 p = inputParser;
33 p.KeepUnmatched = true;
34
35 def_flimit=[0.2 1.2];
36 def_FP=true;
37 def_fillfraction=1;
38 def_initguess=2+2i;
39 def_substrate_thickness_variance=0;
40
41 addRequired(p,'f');
42 addRequired(p,'fT');
43 addRequired(p,'d');
44 addRequired(p,'n_sub');
45 addParameter(p,'flimit',def_flimit,@isnumeric);
46 addParameter(p,'ff',def_fillfraction,@isnumeric);
47 addParameter(p,'initguess',def_initguess,@isnumeric);
48 addParameter(p,'dvar',def_substrate_thickness_variance,@isnumeric);
49 addParameter(p,'FP',def_FP,@islogical);
50
51 parse(p,f,fT,d,n_sub,varargin{:})
52 struct2vars(p.Results)
53
54
55 %% Start calculation
56 index1=find(f>=flimit(1),1,'first');
```

```
index2=find(f>flimit(2),1,'first');

f3=f(index1:index2)'*1e12;
Tf = @(e1,e2) 2*e1/(e1+e2);
Rf = @(e1,e2) (e1-e2)/(e1+e2);
n_eff = @(e1,ff)sqrt(ff*e1^2+(1-ff)*n_air^2);
% Rf = @(e1,e2) (e2-e1)/(e1+e2);

T=(fT(index1:index2));
n_vpa=zeros(length(f3),1);
syms n_p
syms nr ki
for i=1:length(f3)
    fi=f3(i);
    if FP==true
        haps = vpasolve( T(i) == (Tf(n_air,n_eff(n_p,ff))...
            * Tf(n_eff(n_p,ff), n_sub)/Tf(n_air,n_sub)...
            * exp(1i*(d*(n_eff(n_p,ff)-n_air)-dvar*(n_sub-n_air))...
            *2*pi*fi/c))/(1 - Rf(n_eff(n_p,ff),n_sub)...
            * Rf(n_eff(n_p,ff), 1)* exp(2i*n_eff(n_p,ff)*2*pi*fi*d/c)),...
            n_p,initguess);
    else
        haps = vpasolve( T(i) == (Tf(n_air,n_eff(n_p,ff))...
            * Tf(n_eff(n_p,ff), n_sub)/Tf(n_air,n_sub)...
            * exp(1i*(d*(n_eff(n_p,ff)-n_air)-dvar*(n_sub-n_air))...
            *2*pi*fi/c)),n_p,initguess);
    end
    %         dispstat(['i=',num2str(i)])
    if isempty(haps)
        n_vpa(i)=NaN;
        continue
    else
        n_vpa(i)=haps;
        initguess = n_vpa(i);
    end
    dispstat(['i=',num2str(i),', f=',num2str(fi*1e-12),...
        ', guess=',num2str(initguess)])
end
n=n_vpa;
eps=n.^2;
conduct=-2*pi*1i*f3.*eps0.*(eps-1); %[S/m] conductivity
ntable = table(f3*1e-12, n, eps,conduct);
ntable.Properties.VariableNames = {'f_THz',...
    'n','eps','cond'};
```

```
101 end
```

B.1.2 ConductivityTMM

```
1  function [ Tout, dTout] =...
2      conductivityTMM(f, tratio, nList, nListRef, dList, initguess, varargin)
3  %conductivityTMM calculates the dielectric properties of a specific unknown
4  % layer in a multilayer system using the Transfer Matrix Method. This works
5  % for two types of geometries:
6  % 1) a single layer of unknown n.
7  % 2) An unknown change "dn" a single layer with known n due to
8  % photoexcitation. In this case, the penetration depth (dp) of the
9  % exponentially decaying photoconductivity into the layer must be
10 % specified as well.
11 % REQUIRED INPUT ARGUMENTS:
12 % -> "f" is an array containing the frequencies [Hz] of interest.
13 % -> "tratio" is the ratio of the transmitted complex electric field of our
14 %    multilayer system including our sample, and a similar system
15 %    corresponding to a suitable reference. Each element should correspond
16 %    to the given frequency in "f".
17 % -> "nList" and "nListRef" should contain the refractive index for each
18 %    layer of the system (FRONT TO BACK), including incident and
19 %    transmitted region. In nList, the layer of interested should set as
20 %    "NaN", i.e. nList(unknownLayer)=NaN. Also note that the incident layer
21 %    cannot be complex, i.e. no absorbtion or gain. Finally, if any layer
22 %    has a frequency-dependent refractive index, nList should given as a
23 %    (n,m) array, where n corresponds to each frequency of f(n), and m
24 %    corresponds to each layer.
25 % -> "dList" should contain the thickness of each layer given in meters.
26 %    The incident and transmitted region must be specified as Inf, i.e.
27 %    dList([1,end])=Inf.
28 % -> initguess is the initial guess used by the routine when solving the
29 %    system of equations for the unknown n using the routine "vpasolve".
30 % OPTIONAL ARGUMENTS:
31 % -> "theta0" is the angle of incidence, theta0=0 is normal incidence,
32 %    theta0=pi/2 for glancing. theta0 should be real. Default value is 0.
33 % -> "dp" is the penetration depth of the exponential decaying
34 %    photoexcitation. Leave unspecified to assume a homogeneous change in
35 %    refractive index of the layer of interest.
36 % -> "NLayer" is the number of layers which we use to represent the
37 %    exponentially decaying photoexcitation, deps(z)=deps*exp(-z/dp), in
38 %    our layer of interest. Larger NLayer increases accuracy at the cost of
39 %    computation time. Default is 10 layers.
```

```
40 % -> "fLimit" is the frequency range of interest. Default calculates for
41 %     all frequencies given in "f".
42 % -> "useParfor", when true, uses parallel computing to decrease
43 %     calculation time for "vpasolve", however in this case the program will
44 %     always use "initguess" as the initial guess for each frequency,
45 %     instead of updating the initial guess to the result obtained for the
46 %     previous iteration.
47 % OUTPUT
48 % -> "Tout" is a table containing the frequency, refractive index,
49 %     permittivity and conductivity (S/m) for the layer of interest.
50 % -> "dTout" is a table containing the frequency, and relative change in
51 %     refractive index, permittivity and conductivity (S/m) for the layer
52 %     of interest.
53
54 % Parse input
55 p = inputParser;
56 p.KeepUnmatched = true;
57
58 check_theta0 = @(x) (0<=x) && (x<=pi/2);
59 check_dList = @(x) isinf(x(1)) && isinf(x(end));
60 check_nList = @(x) isreal(x(:,1)) && any(any(isnan(x)));
61 check_nListRef = @(x) isreal(x(:,1));
62
63 addRequired(p,'f');
64 addRequired(p,'tratio');
65 addRequired(p,'nList',check_nList);
66 addRequired(p,'nListRef',check_nListRef);
67 addRequired(p,'dList',check_dList);
68 addRequired(p,'initguess',@isfloat);
69 addParameter(p,'theta0',0,check_theta0);
70 addParameter(p,'dp',[],@isreal);
71 addParameter(p,'NLayer',[],@isscalar);
72 % addParameter(p,'fLimit',[],@isreal);
73 addParameter(p,'useParfor',false,@islogical);
74
75 parse(p,f,tratio,nList,nListRef,dList,initguess,varargin{:})
76 struct2vars(p.Results)
77
78 %% Start Program
79 c=299792458; %[m/s] speed of light
80 eps0=8.854e-12; % [F/m] vacuum permittivity
81
82 % frequency
83 if isrow(f)
```

```
84      f = f.';
85  end
86  omega = 2*pi*f; %Angular frequency
87  fpoints = length(f);
88
89  % Calculate the transmission of the reference geometry
90  tref = zeros(1,fpoints);
91  for i=1:fpoints
92      if size(nListRef,1) > 1
93          tref(i) = tstotal(nListRef(i,:), dList, theta0, omega(i));
94      else
95          tref(i) = tstotal(nListRef, dList, theta0, omega(i));
96      end
97  end
98  % Locate index of layer and replace NaN with symbolic value "nG" used in
99  % the numerical solver "vpasolve":
100 nG = sym('nG');
101
102 [row,col,v] = find(isnan(nList(1,:)));
103 iL = col;
104 if length(iL)~=1
105     error('There should be exactly one NaN layer in "nList"')
106 end
107 nList = sym(nList);
108 nList(:,iL) = nG;
109 nRef = nListRef(:,iL);
110
111 % calculate exponential decay of n in photoexcited layer (if applicable),
112 % and divide the layer of interest into NLayer #layers.
113 % Modify nList and dList to reflect this.
114 if ~isempty(dp) && ~isempty(NLayer)
115     d_sample = dList(iL);
116     dz = d_sample/NLayer;
117     zLayer = zL(dz,NLayer);
118     nExcz = @(z,n,nexc,dp)...
119         (n.^2 + ((nexc-n).^2 + 2.*n.*(nexc-n)).*exp(-z./dp)).^(1/2);
120
121     sz = size(nListRef,1);
122     for i=1:sz
123         nListNew(i,:) = nExcz(zLayer,nListRef(i,iL),nG,dp);
124     end
125
126     nList = [nList(:,1:iL-1), nListNew, nList(:,iL+1:end)];
127     dList = [dList(1:iL-1), dz*ones(1,NLayer), dList(iL+1:end)];
```

```
128 end
129 %% Numerically solve for unknown n
130 n=zeros(fpoints,1);
131 sz = size(nList,1);
132 sz_ini = length(initguess);
133
134 if sz_ini==fpoints
135     initguess_i = initguess;
136 elseif sz_ini==1
137     initguess_i = initguess.*ones(1,fpoints);
138 else
139     error(['initial guess must either be a single value, or have a ',...
140         'corresponding value for each frequency'])
141 end
142 % Decide if we want to use parallel computing.
143 if useParfor == true
144     % Progress monitor, doesnt currently work
145 %     javaaddpath('D:\Google Drev\Matlab\Functions\ParforProgMon')
146 %     ppm = ParforProgMon('conductivityTMM', fpoints);
147 %     disp(ppm)
148     theta = theta0;
149     if sz>1
150         parfor i=1:fpoints
151             if any(isempty(nList(i,:))) || any(isnan(nList(i,:)))
152                 n(i)=NaN;
153                 continue
154             end
155             guess = vpasolve(tratio(i) == ...
156                 tstotal(nList(i,:),dList,theta,omega(i))./...
157                 tref(i),nG,initguess_i(i));
158             if isempty(guess)
159                 %disp(['No solution was found for i=',num2str(i),'/',...
160                 %num2str(fpoints)])
161                 guess = NaN(1);
162             end
163             n(i) = guess;
164 %             ppm.increment(); %update progress for progress monitor
165         end
166     else
167         parfor i=1:fpoints
168             if any(isempty(nList(i))) || any(isnan(nList(i)))
169                 n(i)=NaN;
170                 continue
171             end
```

```
172             guess = vpasolve(tratio(i) == ...
173                 tstotal(nList,dList,theta,omega(i))./...
174                 tref(i),nG,initguess_i(i));
175             if isempty(guess)
176                 %disp(['No solution was found for i=',num2str(i),'/',...
177                 %num2str(fpoints)])
178                 guess = NaN(1);
179             end
180             n(i) = guess;
181 %             ppm.increment(); %update progress for progress monitor
182         end
183     end
184 else
185     if sz>1
186         for i=1:fpoints
187             if any(isempty(nList(i,:))) || any(isnan(nList(i,:)))
188                 n(i)=NaN;
189                 continue
190             end
191             guess = vpasolve(tratio(i) == ...
192                 tstotal(nList(i,:),dList,theta0,omega(i))./...
193                 tref(i), nG,initguess_i(i));
194             if isempty(guess)
195                 disp(['No solution was found for i=',num2str(i),'/',...
196                     num2str(fpoints)])
197                 guess = NaN(1);
198             end
199             n(i) = guess;
200 %             initguess_i = guess;
201             dispstat(['i=',num2str(i),'/',num2str(fpoints),...
202                 ', n=',num2str(n(i))])
203         end
204     else
205         for i=1:fpoints
206             if any(isempty(nList(i))) || any(isnan(nList(i)))
207                 n(i)=NaN;
208                 continue
209             end
210             guess = vpasolve(tratio(i) == ...
211                 tstotal(nList,dList,theta0,omega(i))./...
212                 tref(i), nG,initguess_i(i));
213             if isempty(guess)
214                 disp(['No solution was found for i=',num2str(i),'/',...
215                     num2str(fpoints)])
```

```
216                 guess = NaN(1);
217             end
218             n(i) = guess;
219 %             initguess_i = guess;
220             dispstat(['i=',num2str(i),'/',num2str(fpoints),...
221                 ', n=',num2str(n(i))])
222         end
223     end
224 end
225 
226 % Calculate permittivity and conductivity and save everything in a table
227 eps = n.^2;
228 cond = -1i.*omega.*eps0.*(eps-1);
229 
230 VarN = {'f_THz','n','eps','cond'};
231 Tout = table(f*1e-12,n,eps,cond,'VariableNames',VarN);
232 
233 % Calculate change in dielectric properties and save everything in a table
234 epsRef = nRef.^2;
235 condRef = -1i.*omega.*eps0.*(epsRef-1);
236 
237 VarN = {'f_THz','n','eps','cond'};
238 dTout = table(f*1e-12,(n-nRef),(eps-epsRef),(cond-condRef),...
239     'VariableNames',VarN);
240 
241 end
242 
243 %% Subroutines
244 % find position for middle of each sublayer
245 function zLayer = zL(dz,NLayer)
246     zLayer=zeros(1,NLayer);
247         for i=1:NLayer
248             zLayer(i) = dz*(i-1/2);
249         end
250 end
251 
252 % Call function TMMCalc and return tstotal
253 function out = tstotal(nList, dList, theta0, omega)
254     S = TMMCalc(nList, dList, theta0, omega);
255     out = S.tstotal;
256 end
```

B.2 Mathematica Source Code

In this section we present the Mathematica source code used to generate the results in figure 5.4. The code starts with the Transfer Matrix Method routine used for calculating the transmitted electric fields of a layered stack for a given wavelength and angle. This is followed by applying the routine to the specific case shown in section 5.4.2.

Transfer Matrix Method

Source: Pedrotti[3] - Introduction to Optics

TMM of Stacked layers

This code finds the E-fields and transmission coefficients for a sample on semi-infinite substrate, and the photoexcited sample on the same substrate using the Transfer Matrix Method for normal incidence. These fields and transmission coefficients simulate the typical measurement obtained in a pump-probe time-domain spectroscopy experiment. We then use the typical analysis model to calculate the change in refractive index Δn of the sample due to photoexcitation, which people typically use for this experiment when the refractive index of the sample and substrate is known. We then compare our obtained value with the original true value Δn. Depending on the ratio of the wavelength and the thickness of the sample λ/l, one should either use the refractive index of the substrate or the sample in the model.

Parameters

```
ClearAll["Global`*"];
imgsize = 400;
fntsize = 14;
SetOptions[ListLogLinearPlot, BaseStyle → {FontSize → fntsize}, ImageSize → imgsize];
SetOptions[ListLogLogPlot, BaseStyle → {FontSize → fntsize}, ImageSize → imgsize];
c = 299 792 458;
Z0 = 377; (*Ohm*)
SetDirectory[NotebookDirectory[]];
```

Functions

```
logspace[a_, b_, n_] := 10.0^Range[a, b, (b - a) / (n - 1)];
repeat[m_, n_Integer?Positive] := Sequence @@ ConstantArray[m, n];
RelDev[x_, x0_] := (x - x0) / x0;
```

(∗Assumes solutions of the form exp[–*ı*ω*t*],
i.e. N=n+*ı*κ. Positive κ is absorption, negative κ is gain.∗)

```
γTE[nj_, αj_] := nj Cos[αj];
δ[ωj_, nj_, dj_, αj_] := ωj nj dj Cos[αj] / c;
γTM[nj_, αj_] := nj / Cos[αj];

Mj[γj_, δj_] := {{Cos[δj], -ⅈ Sin[δj] / γj}, {-ⅈ γj Sin[δj], Cos[δj]}};
r[Mi_, γ0_, γt_] :=
  (γ0 * Mi[[1, 1]] + γ0 * γt * Mi[[1, 2]] - Mi[[2, 1]] - γt * Mi[[2, 2]]) /
   (γ0 * Mi[[1, 1]] + γ0 * γt * Mi[[1, 2]] + Mi[[2, 1]] + γt * Mi[[2, 2]]);
t[Mi_, γ0_, γt_] := (2 * γ0) /
   (γ0 * Mi[[1, 1]] + γ0 * γt * Mi[[1, 2]] + Mi[[2, 1]] + γt * Mi[[2, 2]]);
```

Take the dot-product of a list of matrices:

```
RepeatedDotProduct[ListOfMatrices_] :=
  Block[{n = Length[ListOfMatrices], index, SoFar},
   If[n == 0, Return[{{1, 0}, {0, 1}}]];
   SoFar = ListOfMatrices[[1]];
   For[index = 2, index ≤ n, index++, SoFar = SoFar.ListOfMatrices[[index]]];
   Return[SoFar];
  ];
```

Convert between n and ϵ:

```
ConvertΔϵToΔn[n_, dϵi_] = √(n^2 + dϵi) - n;
ConvertΔnToΔϵ[n_, dni_] = (n + dni)^2 - n^2;
```

The program

INPUTS:
⇒"nList" is the list of refractive indices, in the order that the light would pass through them. The first element of the list should
be the semi-infinite medium from which the light enters, the last element should be the semi-infinite medium to which the light
exits (if any exits). The first element must be real, otherwise there are program errors associated with the branch cut discontinuities
in ArcSin.
⇒"θ0" is the angle of incidence, θ0=0 is normal incidence, θ0=p/2 for glancing. θ0 should be real.
⇒"dList" is the list of layer thicknesses (front to back). It should correspond one-to-one to the elements of "nList".

Printed by Wolfram Mathematica Student Edition

⇒"λ0" is the vacuum wavelength of the light.

```
TMMCalc[nList_, dList_, θ0_, λ0_] :=
 Block[{NumMedia, ω, δList, θList, MTEList, MTMList, MTE, MTM, γTEList, γTMList,
   rstotal, rptotal, tstotal, tptotal, Rs, Rp, Ts, Tp, RUnpol, TUnpol, temp, ψ, Δ},
  NumMedia = Length[nList];
  ω = 2 π c / λ0;
  If[(Length[dList] ≠ NumMedia) || (dList[[1]] ≠ ∞) || (dList[[NumMedia]] ≠ ∞),
   Return["Error in d or n!"]];
  If[Im[nList[[1]]] ≠ 0 || Im[θ0] ≠ 0, Return[
    "Sorry, program does not work correctly for a dissipative incoming medium."]];
(*θList is a list with, for each layer, the angle that the light travels through the
layer. Computed with Snell's law. Note that the "angles" may be complex!*)
θList = ArcSin[nList[[1]] Sin[θ0] / nList];
(* δ is a list with,
  for each layer (except the semi-infinite top and bottom "layers"),
  the phase accrued by traveling through that layer.*)
  γTEList = Thread[γTE[nList, θList]];
  γTMList = Thread[γTM[nList, θList]];
  δList = Table[If[i == 1 || i == NumMedia, Null,
     δ[ω, nList[[i]], dList[[i]], θList[[i]]]], {i, 1, NumMedia}];
MTEList = Table[If[i == 1 || i == NumMedia, Null, Mj[γTEList[[i]], δList[[i]]]],
    {i, 1, NumMedia}];
  MTMList = Table[If[i == 1 || i == NumMedia, Null, Mj[γTMList[[i]], δList[[i]]]],
    {i, 1, NumMedia}];

(* MTE and MTM will be the matrix that you get by dot-producting all the Mj.*)
MTE = RepeatedDotProduct[Take[MTEList, {2, NumMedia - 1}]];
  MTM = RepeatedDotProduct[Take[MTMList, {2, NumMedia - 1}]];

  (*Net complex transmission and reflection amplitudes:*)
  rstotal = r[MTE, γTEList[[1]], γTEList[[NumMedia]]];
  rptotal = r[MTM, γTMList[[1]], γTMList[[NumMedia]]];
  tstotal = t[MTE, γTEList[[1]], γTEList[[NumMedia]]];
  tptotal = t[MTM, γTMList[[1]], γTMList[[NumMedia]]];

  (* Net transmitted and reflected power,as a proportion of the incoming light power,
  for polarized and unpolarized incoming light.Don't forget,Ts,
  Tp,TUnpol represent the light power that enters the final,
  semi-infinite medium. If that medium has a complex index of refraction,
  the light will further attenuate as it travels through that medium to
   your detector, and you should take that into account separately.*)

  Rs = Abs[rstotal^2];
  Rp = Abs[rptotal^2];
  Ts = Abs[tstotal^2] Re[nList[[NumMedia]] Cos[θList[[NumMedia]]]] /
       Re[nList[[1]] Cos[θList[[1]]]];
  Tp = Abs[tptotal^2] (Re[nList[[NumMedia]] Conjugate[Cos[θList[[NumMedia]]]]] /
       Re[nList[[1]] Cos[θList[[1]]]]);
  RUnpol = 1/2 (Rs + Rp);
```


Printed by Wolfram Mathematica Student Edition

```
TUnpol = 1/2 (Ts + Tp);
(* Next, ψ and Δ are the parameters measured in ellipsometry. Note that both are
 in RADIANS,not degrees. To get the value in degrees, divide by the degree symbol,
e.g. "ψ/°". (In Mathematica, the degree symbol is just treated as
     the number π/180~0.0175). ψ is defined to be between 0 and+π/2,
and Δ between -π and +π. Warning:There are different conventions for Δ in use,
you may need to use "π-Δ" or "2π-Δ" or "Δ-π", etc.,
to get agreement with your ellipsometer output. *)
ψ = ArcTan[Abs[rptotal / rstotal]];
Δ = Arg[-rptotal / rstotal];
Return[{Rs, Ts, Rp, Tp, rstotal, tstotal, rptotal, tptotal, RUnpol, TUnpol, ψ, Δ}];]
```

Define separate functions for the reflection and transmission for s-polarization, p-polarization, and unpolarized light.

```
Rs[nList_, dList_, θ0_, λ0_] := TMMCalc[nList, dList, θ0, λ0][[1]];
Ts[nList_, dList_, θ0_, λ0_] := TMMCalc[nList, dList, θ0, λ0][[2]];
Rp[nList_, dList_, θ0_, λ0_] := TMMCalc[nList, dList, θ0, λ0][[3]];
Tp[nList_, dList_, θ0_, λ0_] := TMMCalc[nList, dList, θ0, λ0][[4]];
rstotal[nList_, dList_, θ0_, λ0_] := TMMCalc[nList, dList, θ0, λ0][[5]];
tstotal[nList_, dList_, θ0_, λ0_] := TMMCalc[nList, dList, θ0, λ0][[6]];
rptotal[nList_, dList_, θ0_, λ0_] := TMMCalc[nList, dList, θ0, λ0][[7]];
tptotal[nList_, dList_, θ0_, λ0_] := TMMCalc[nList, dList, θ0, λ0][[8]];
RUnpol[nList_, dList_, θ0_, λ0_] := TMMCalc[nList, dList, θ0, λ0][[9]];
TUnpol[nList_, dList_, θ0_, λ0_] := TMMCalc[nList, dList, θ0, λ0][[10]];
ψ[nList_, dList_, θ0_, λ0_] := TMMCalc[nList, dList, θ0, λ0][[11]];
Δ[nList_, dList_, θ0_, λ0_] := TMMCalc[nList, dList, θ0, λ0][[12]];
```


Printed by Wolfram Mathematica Student Edition

Simulate Transmitted Electric Fields of a Thinfilm on Substrate

Define parameters

```
θin = 0;
dSample = 1 * 10^-6;
n0 = 1;
nCNT = 16 + i 6;
nSample = 3.415 + 1 i;
ϵSample = nSample^2;
nt = 1.96;

ΔϵExc = (1 + 1 i) 10^-6;
ϵExc = ϵSample + ΔϵExc;
nExc = ϵExc^1/2;
ΔnExc = nExc - nSample;

dExc = 0.25 * dSample;
dSampleExc = dSample - dExc;
ωpoints = 100;
λn = logspace[-2, 5, ωpoints]; (*λ0/1 (freespace wavelength/sample thickness)*)
λ0 = λn dSample;
λs = λn / Re[nSample];
ω = 2 π c / (λn dSample);
Print["n_sample = ", nSample]; Print["n_substrate = ", nt];
Print["Δn_sample = ", ΔnExc]; Print["Δϵ_sample = ", ΔϵExc];
```

$n_{sample} = 3.415 + 1. i$

$n_{substrate} = 1.96$

$\Delta n_{sample} = 1.74337 \times 10^{-7} + 9.53624 \times 10^{-8}\, i$

$\Delta \epsilon_{sample} = \frac{1}{1\,000\,000} + \frac{i}{1\,000\,000}$

Substrate

```
nListSub = {n0, n0, nt};
dListSub = {∞, dSample, ∞};
nList = nListSub;
dList = dListSub;
rsub = Table[rstotal[nList, dList, θin, λ0[[i]]], {i, 1, ωpoints}];
tsub = Table[tstotal[nList, dList, θin, λ0[[i]]], {i, 1, ωpoints}];
Rsub = Table[Rs[nList, dList, θin, λ0[[i]]], {i, 1, ωpoints}];
Tsub = Table[Ts[nList, dList, θin, λ0[[i]]], {i, 1, ωpoints}];
```


Printed by Wolfram Mathematica Student Edition

Unexcited sample on substrate

```
nListDark = {n0, nSample, nt};
dListDark = {∞, dSample, ∞};
nList = nListDark;
dList = dListDark;
rref = Table[rstotal[nList, dList, θin, λ0[[i]]], {i, 1, ωpoints}];
tref = Table[tstotal[nList, dList, θin, λ0[[i]]], {i, 1, ωpoints}];
Rref = Table[Rs[nList, dList, θin, λ0[[i]]], {i, 1, ωpoints}];
Tref = Table[Ts[nList, dList, θin, λ0[[i]]], {i, 1, ωpoints}];
tSample = tref / tsub;
```

Homogeneous Photoexcited sample on substrate

```
nListExc = {n0, nExc, nSample, nt};
dListExc = {∞, dExc, dSampleExc, ∞};
nList = nListExc;
dList = dListExc;
rexc = Table[rstotal[nList, dList, θin, λ0[[i]]], {i, 1, ωpoints}];
texc = Table[tstotal[nList, dList, θin, λ0[[i]]], {i, 1, ωpoints}];
Rexc = Table[Rs[nList, dList, θin, λ0[[i]]], {i, 1, ωpoints}];
Texc = Table[Ts[nList, dList, θin, λ0[[i]]], {i, 1, ωpoints}];
```

relative change of the transmission coefficient of the sample due to photoexcitation

$$\texttt{dtExc} = \frac{\texttt{texc} - \texttt{tref}}{\texttt{tref}};$$

```
tExcHomo = texc / tref;
```

Plot T, R and t

```
plt = ListLogLinearPlot[{Thread[{λs, Tref}], Thread[{λs, Texc}], Thread[{λs, Tsub}]},
  AxesLabel → {"λs/d", "T"}, PlotLabels → {"ref", "exc", "sub"},
  PlotLabel → "Transmittance", Joined → True, GridLines → Automatic,
  PlotLegends → LineLegend[{"ref", "exc", "sub"}]]
Export["T.pdf", plt];
plt = ListLogLinearPlot[{Thread[{λs, Rref}], Thread[{λs, Rexc}], Thread[{λs, Rsub}]},
  AxesLabel → {"λs/d", "R"}, PlotLabels → {"ref", "exc", "sub"},
  PlotLabel → "Reflectance", Joined → True, GridLines → Automatic,
  PlotLegends → LineLegend[{"ref", "exc", "sub"}]]
Export["R.pdf", plt];
plt = ListLogLinearPlot[
  {Thread[{λs, Abs[tref]}], Thread[{λs, Abs[texc]}], Thread[{λs, Abs[tsub]}]},
  AxesLabel → {"λs/d", "Abs(t)"}, PlotLabels → {"ref", "exc", "sub"},
  PlotLabel → "Abs(transmission)", Joined → True, GridLines → Automatic,
  PlotLegends → LineLegend[{"ref", "exc", "sub"}]]
Export["t_abs.pdf", plt];
plt = ListLogLinearPlot[
  {Thread[{λs, Arg[tref]}], Thread[{λs, Arg[texc]}], Thread[{λs, Arg[tsub]}]},
  AxesLabel → {"λs/d", "Arg(t)"}, PlotLabel → "Arg(transmission)",
  PlotLegends → LineLegend[{"ref", "exc", "sub"}], Joined → True, GridLines → Automatic]
Export["t_arg.pdf", plt];
```


Printed by Wolfram Mathematica Student Edition

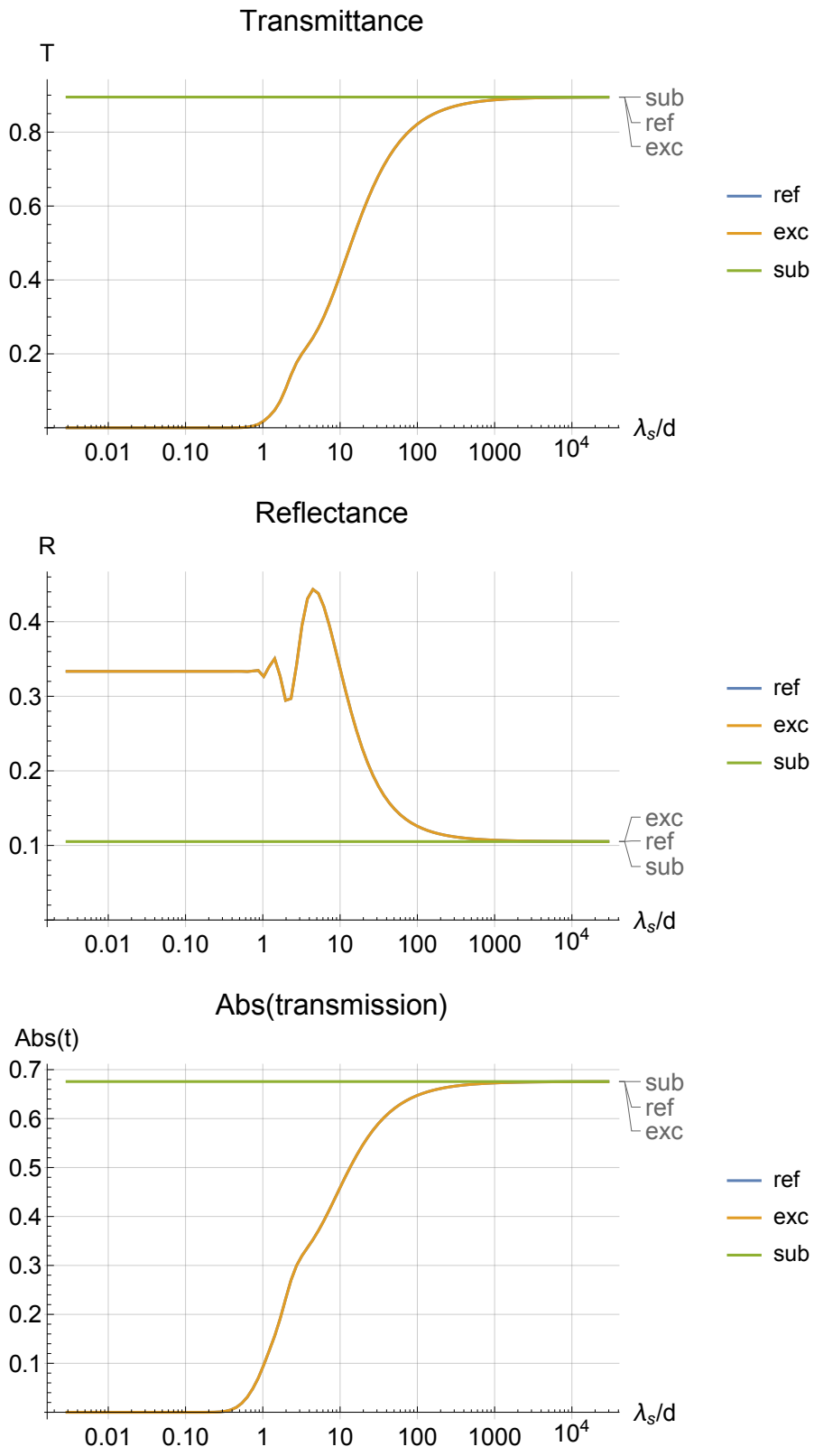

Printed by Wolfram Mathematica Student Edition

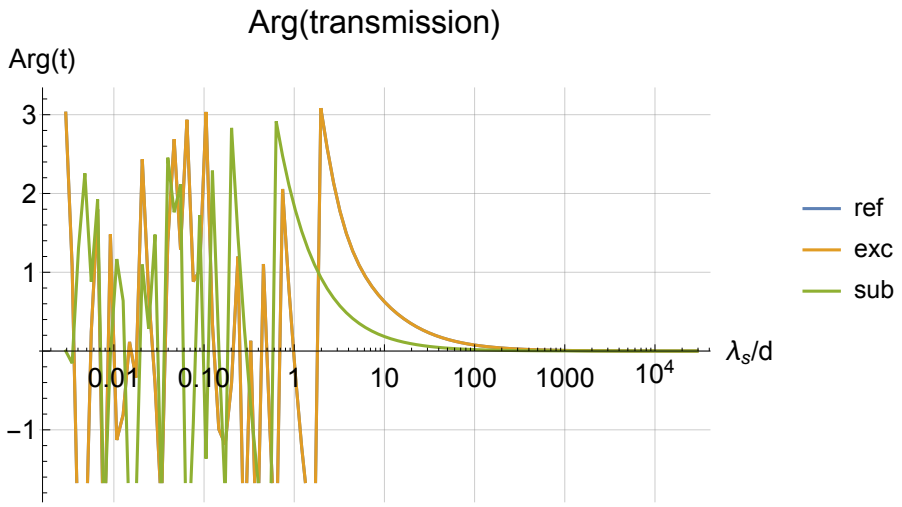

Exponentially decaying photoexcitation of a sample on substrate

Here we simulate an exponentially decaying photoconductivity $\Delta\sigma(z) = \Delta\sigma_{exc}\, e^{-\alpha z} \rightarrow$ $\Delta n(z) = (\epsilon_{dark} + \Delta\epsilon_{exc}\, e^{-\alpha z})^{1/2} - \epsilon_{dark}{}^{1/2}$, where $\Delta\epsilon \propto \Delta\sigma$ and $\alpha = 1/d_p$, where d_p is the penetration depth. We define the photoexcited region by the penetration depth d_p and divide the sample of thickness dSample into NLayer number of layers, each with a $\Delta n(z_i)$, where z_i is the position sampled in the middle of layer i.

```
NLayer = 100;
Δz = dSample / NLayer;
zL[Δz_, NLayer_Integer?Positive] := Table[Δz (i - 1/2), {i, NLayer}];
zLayer = zL[Δz, NLayer];
nExcz[z_, nDark_, ΔnExc_, dExc_] := (nDark^2 + (ΔnExc^2 + 2 nDark ΔnExc) Exp[-z/dExc])^(1/2);
nLayer = nExcz[#, nSample, ΔnExc, dExc] & /@ zLayer;
ΔnLayer = nLayer - nSample;
nListExcExp = Flatten[{n0, nLayer, nt}];
dListExcExp = {∞, repeat[Δz, NLayer], ∞};
nList = nListExcExp;
dList = dListExcExp;
rExcExp = Table[rstotal[nList, dList, θin, λ0[[i]]], {i, 1, ωpoints}];
tExcExp = Table[tstotal[nList, dList, θin, λ0[[i]]], {i, 1, ωpoints}];
RExcExp = Table[Rs[nList, dList, θin, λ0[[i]]], {i, 1, ωpoints}];
TExcExp = Table[Ts[nList, dList, θin, λ0[[i]]], {i, 1, ωpoints}];
```

relative change of the transmission coefficient of the sample due to photoexcitation

```
dtExcExp = (tExcExp - tref)/tref;
tExcExpRegion = tExcExp / tref;
(*The transmission coeffient of the photoexcited region E_exc/E_ref*)
```


Printed by Wolfram Mathematica Student Edition

Plot

```
plt = ListPlot[{Thread[{zLayer/dSample, Re[ΔnLayer]/Re[ΔnExc]}], Thread[{zLayer/dSample, Im[ΔnLayer]/Im[ΔnExc]}]},
  AxesLabel → {"z/d_Sample", "Δn (z)/Δn (0)"}, PlotLegends → LineLegend[{"Re(Δn)", "Im(Δn)"}],
  PlotLabel → "Photoexcitation Profile"]
Export["n_profile.pdf", plt];
plt =
 ListLogLinearPlot[{Thread[{λs, Tref}], Thread[{λs, TExcExp}], Thread[{λs, Tsub}]},
  AxesLabel → {"λ_s/d", "T"}, PlotLabels → {"ref", "exc", "sub"},
  PlotLabel → "Transmittance (Δσ(z)=Δσ_0 e^(-αz))", Joined → True,
  GridLines → Automatic, PlotLegends → LineLegend[{"ref", "exc", "sub"}]]
Export["T.pdf", plt];
plt =
 ListLogLinearPlot[{Thread[{λs, Rref}], Thread[{λs, RExcExp}], Thread[{λs, Rsub}]},
  AxesLabel → {"λ_s/d", "R"}, PlotLabels → {"ref", "exc", "sub"},
  PlotLabel → "Reflectance (Δσ(z)=Δσ_0 e^(-αz))", Joined → True,
  GridLines → Automatic, PlotLegends → LineLegend[{"ref", "exc", "sub"}]]
Export["R.pdf", plt];
plt = ListLogLinearPlot[
  {Thread[{λs, Abs[tref]}], Thread[{λs, Abs[tExcExp]}], Thread[{λs, Abs[tsub]}]},
  AxesLabel → {"λ_s/d", "Abs(t)"}, PlotLabels → {"ref", "exc", "sub"},
  PlotLabel → "Abs(transmission) (Δσ(z)=Δσ_0 e^(-αz))", Joined → True,
  GridLines → Automatic, PlotLegends → LineLegend[{"ref", "exc", "sub"}]]
Export["t_abs.pdf", plt];
plt = ListLogLinearPlot[
  {Thread[{λs, Arg[tref]}], Thread[{λs, Arg[tExcExp]}], Thread[{λs, Arg[tsub]}]},
  AxesLabel → {"λ_s/d", "Arg(t)"}, PlotLabel → "Arg(transmission) (Δσ(z)=Δσ_0 e^(-αz))",
  PlotLegends → LineLegend[{"ref", "exc", "sub"}], Joined → True, GridLines → Automatic]
Export["t_arg.pdf", plt];
```

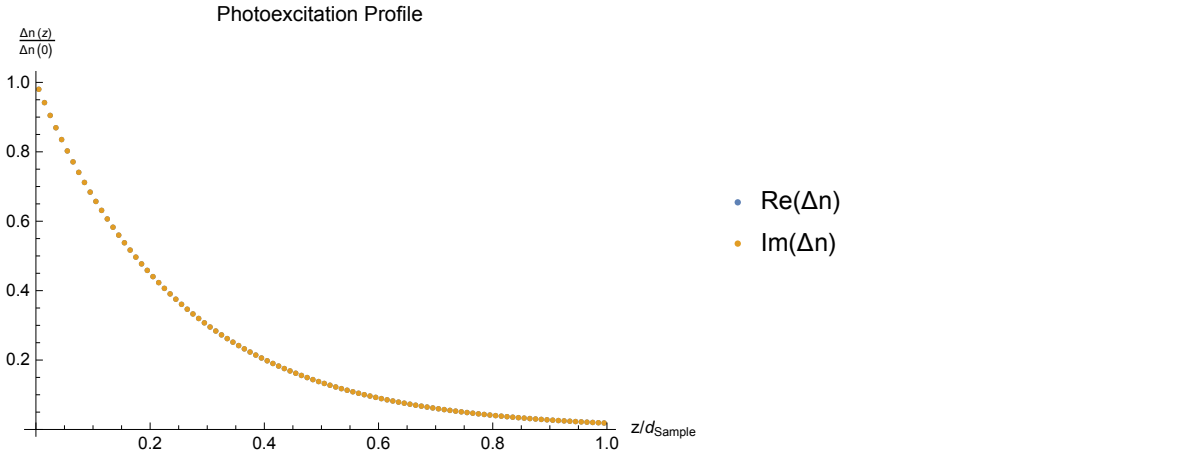

Printed by Wolfram Mathematica Student Edition

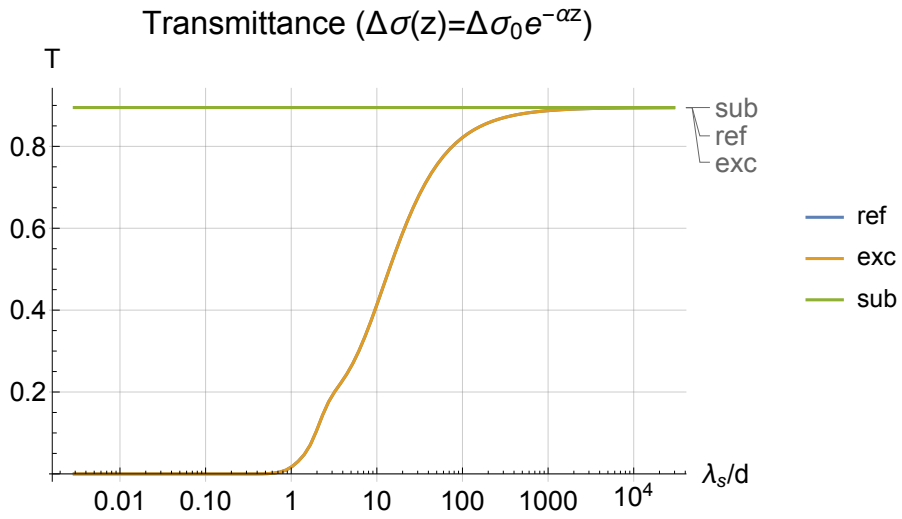

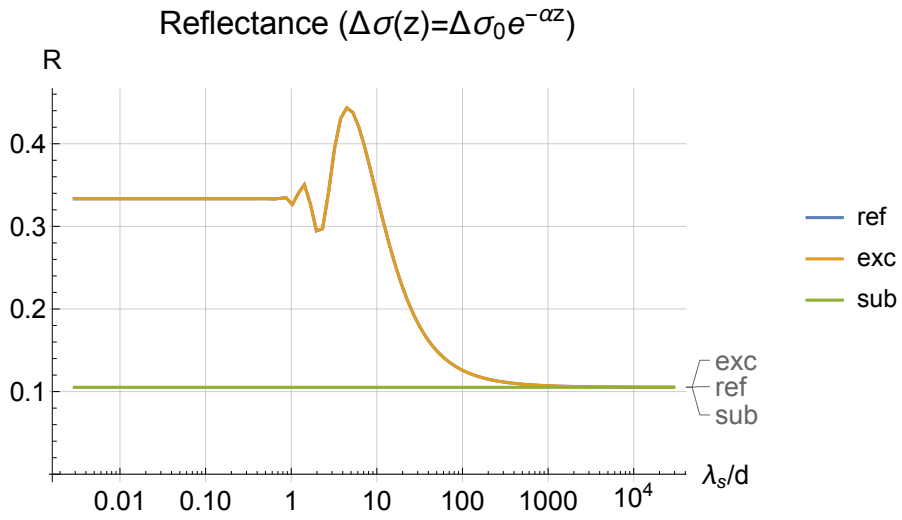

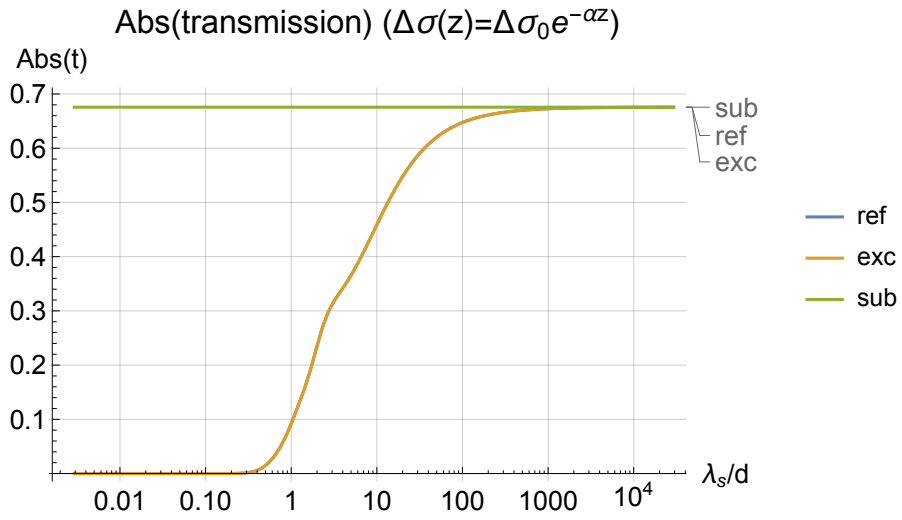

Printed by Wolfram Mathematica Student Edition

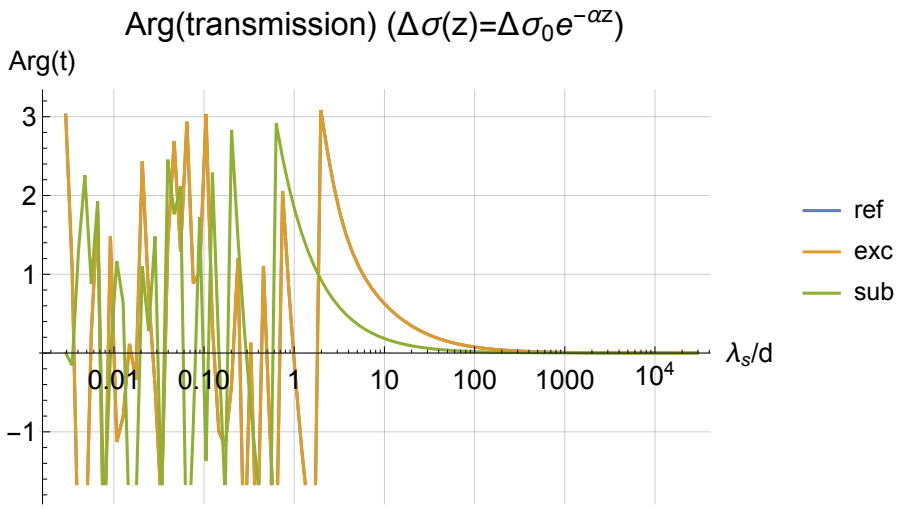

Find Full Matrix solution (Numerical solving)

Here we set up the full Transfer Matrix equation that we need to solve for the desired refractive index *n*, assuming all other parameters are known, i.e. thickness, penetration depth and electric field values in the transmitted region for each geometry. It is not possible to solve this equation analytically, so we must use numerical algorithms (FindRoot) to estimate a solution.

Define functions and Equations

Fresnel transmission/reflection coefficients from layer i→j. Assumes normal incidence and TE-polarized light

```
tf[ni_, nj_] := 2 ni / (ni + nj);
rf[ni_, nj_] := (ni - nj) / (ni + nj);
```

Phase delay inside layer j. Assumes normal incidence:

```
δ[ωj_, nj_, dj_] := i ωj nj dj / c;
```

Short and long wavelength approximation:

```
ΔϵShort[n_,dti_,dp_,ωi_] = -2 i c n dti / (dp ωi);
ΔϵLong[n_, dti_, dp_, ωi_] = -i c (1 + n) dti / (dp ωi);
```


Printed by Wolfram Mathematica Student Edition

Set up equations using TMMCalc

Unexcited sample and homogeneous excitation of sample

```
nDarkTMM[nj_, λ0_] := (nListDarkUnknown = nListDark;
  nListDarkUnknown[[2]] = nj;
  tstotal[nListDarkUnknown, dListDark, θin, λ0] / tstotal[nListSub, dListSub, θin, λ0]);

nExcTMM[nj_, λ0_] := (nListExcUnknown = nListExc;
  nListExcUnknown[[2]] = nj;
  tstotal[nListExcUnknown, dListExc, θin, λ0] / tstotal[nListDark, dListDark, θin, λ0]);
```

Exponentially decaying photo-excited region, $\epsilon_{exc}(z) = \epsilon_{dark} + \Delta\epsilon\, e^{-\alpha z}$

Set up equation for given wavelength λ0 using penetration depth "dExcG", lumber of layers "NLayerG", and photoexcited refractive index at the surface Δn.

```
ΔnExcTMMExp[ΔnG_, λ0_, NLayerG_, dExcG_] := (
  ΔzG = dSample / NLayerG;
  zLayerG = zL[ΔzG, NLayerG];
  nListExcExpG = nExcz[#, nSample, ΔnG, dExcG] & /@ zLayerG;
  nListExcExpG = Flatten[{n0, nListExcExpG, nt}];
  dListExcExpG = {∞, repeat[ΔzG, NLayerG], ∞};
  tj = tstotal[nListExcExpG, dListExcExpG, θin, λ0] / tstotal[nListDark, dListDark, θin, λ0];
  Return[tj]);
```

Estimate the refractive index of the photo-excited region

We compare our four approaches;
1) The short and long wavelength approximations.
2) Assuming a homogeneous photo-excited region of thickness d_p.
3) Assuming an exponentially decaying photoconductivity across the sample, $\Delta\sigma(z) = \Delta\sigma_{exc}\, e^{-\alpha z}$, which we divide into N_L layers.

We use these approaches to estimate Δn for an exponentially decaying photo-excited region, $\epsilon_{exc}(z) = \epsilon_{dark} + \Delta\epsilon\, e^{-\alpha z}$.

Printed by Wolfram Mathematica Student Edition

Estimate the refractive index at the surface of the exp. decaying photoexc. region ($\Delta n(0) = \Delta n_0$)

Use long and short wavelength limit

```
Δϵ𝙴𝚡𝚙𝙻𝚘𝚗𝚐 = Δϵ𝙻𝚘𝚗𝚐[𝚗𝚝, 𝚍𝚝𝙴𝚡𝚌𝙴𝚡𝚙, 𝚍𝙴𝚡𝚌, ω];
Δϵ𝙴𝚡𝚙𝚂𝚑𝚘𝚛𝚝 = Δϵ𝚂𝚑𝚘𝚛𝚝[𝚗𝚂𝚊𝚖𝚙𝚕𝚎, 𝚍𝚝𝙴𝚡𝚌𝙴𝚡𝚙, 𝚍𝙴𝚡𝚌, ω];
Δ𝚗𝙴𝚡𝚙𝙻𝚘𝚗𝚐 = 𝙲𝚘𝚗𝚟𝚎𝚛𝚝Δϵ𝚃𝚘Δ𝚗[𝚗𝚂𝚊𝚖𝚙𝚕𝚎, Δϵ𝙴𝚡𝚙𝙻𝚘𝚗𝚐];
Δ𝚗𝙴𝚡𝚙𝚂𝚑𝚘𝚛𝚝 = 𝙲𝚘𝚗𝚟𝚎𝚛𝚝Δϵ𝚃𝚘Δ𝚗[𝚗𝚂𝚊𝚖𝚙𝚕𝚎, Δϵ𝙴𝚡𝚙𝚂𝚑𝚘𝚛𝚝];
Δ𝚗𝙴𝚡𝚙𝙻𝚘𝚗𝚐𝚁𝚎𝚕𝙳𝚎𝚟 = 𝚁𝚎𝚕𝙳𝚎𝚟[Δ𝚗𝙴𝚡𝚙𝙻𝚘𝚗𝚐, Δ𝚗𝙴𝚡𝚌];
Δ𝚗𝙴𝚡𝚙𝚂𝚑𝚘𝚛𝚝𝚁𝚎𝚕𝙳𝚎𝚟 = 𝚁𝚎𝚕𝙳𝚎𝚟[Δ𝚗𝙴𝚡𝚙𝚂𝚑𝚘𝚛𝚝, Δ𝚗𝙴𝚡𝚌];
```

Assume homogeneous excited area of thickness d_p:

```
𝚒𝚗𝚒𝚝𝚐𝚞𝚎𝚜𝚜 = 𝚗𝙴𝚡𝚌;
𝚐𝚞𝚎𝚜𝚜 = 𝙿𝚊𝚛𝚊𝚕𝚕𝚎𝚕𝚒𝚣𝚎[
   𝚃𝚊𝚋𝚕𝚎[𝙵𝚒𝚗𝚍𝚁𝚘𝚘𝚝[𝚝𝙴𝚡𝚌𝙴𝚡𝚙𝚁𝚎𝚐𝚒𝚘𝚗[[i]] == 𝚗𝙴𝚡𝚌𝚃𝙼𝙼[𝚗𝚓, λ0[[i]]], {𝚗𝚓, 𝚒𝚗𝚒𝚝𝚐𝚞𝚎𝚜𝚜},
     𝚆𝚘𝚛𝚔𝚒𝚗𝚐𝙿𝚛𝚎𝚌𝚒𝚜𝚒𝚘𝚗 → 𝙼𝚊𝚌𝚑𝚒𝚗𝚎𝙿𝚛𝚎𝚌𝚒𝚜𝚒𝚘𝚗, 𝙼𝚊𝚡𝙸𝚝𝚎𝚛𝚊𝚝𝚒𝚘𝚗𝚜 → 50], {i, ωpoints}]];
𝚗𝙴𝚡𝚌𝙴𝚡𝚙𝚃𝙼𝙼𝙷𝚘𝚖𝚘 = 𝚗𝚓 /. 𝚐𝚞𝚎𝚜𝚜;
Δ𝚗𝙴𝚡𝚌𝙴𝚡𝚙𝚃𝙼𝙼𝙷𝚘𝚖𝚘𝚁𝚎𝚕𝙳𝚎𝚟 = 𝚁𝚎𝚕𝙳𝚎𝚟[𝚗𝙴𝚡𝚌𝙴𝚡𝚙𝚃𝙼𝙼𝙷𝚘𝚖𝚘 - 𝚗𝚂𝚊𝚖𝚙𝚕𝚎, Δ𝚗𝙴𝚡𝚌];
```

Assume exponentially decaying photoexcitation represented by 10 layers:

```
𝚍𝙴𝚡𝚌𝙶 = 𝚍𝙴𝚡𝚌;
𝙽𝙻𝚊𝚢𝚎𝚛𝙶 = 10;
𝚒𝚗𝚒𝚝𝚐𝚞𝚎𝚜𝚜 = Δ𝚗𝙴𝚡𝚌;
𝚐𝚞𝚎𝚜𝚜 = 𝙿𝚊𝚛𝚊𝚕𝚕𝚎𝚕𝚒𝚣𝚎[𝚃𝚊𝚋𝚕𝚎[𝙵𝚒𝚗𝚍𝚁𝚘𝚘𝚝[
     𝚝𝙴𝚡𝚌𝙴𝚡𝚙𝚁𝚎𝚐𝚒𝚘𝚗[[i]] == Δ𝚗𝙴𝚡𝚌𝚃𝙼𝙼𝙴𝚡𝚙[Δ𝚗𝙶, λ0[[i]], 𝙽𝙻𝚊𝚢𝚎𝚛𝙶, 𝚍𝙴𝚡𝚌𝙶], {Δ𝚗𝙶, 𝚒𝚗𝚒𝚝𝚐𝚞𝚎𝚜𝚜},
     𝚆𝚘𝚛𝚔𝚒𝚗𝚐𝙿𝚛𝚎𝚌𝚒𝚜𝚒𝚘𝚗 → 𝙼𝚊𝚌𝚑𝚒𝚗𝚎𝙿𝚛𝚎𝚌𝚒𝚜𝚒𝚘𝚗, 𝙼𝚊𝚡𝙸𝚝𝚎𝚛𝚊𝚝𝚒𝚘𝚗𝚜 → 50], {i, ωpoints}]];
Δ𝚗𝙴𝚡𝚌𝙴𝚡𝚙𝚃𝙼𝙼𝙴𝚡𝚙 = Δ𝚗𝙶 /. 𝚐𝚞𝚎𝚜𝚜;
Δ𝚗𝙴𝚡𝚌𝙴𝚡𝚙𝚃𝙼𝙼𝙴𝚡𝚙𝚁𝚎𝚕𝙳𝚎𝚟 = 𝚁𝚎𝚕𝙳𝚎𝚟[Δ𝚗𝙴𝚡𝚌𝙴𝚡𝚙𝚃𝙼𝙼𝙴𝚡𝚙, Δ𝚗𝙴𝚡𝚌];
```

Export Data

```
𝙴𝚡𝚙𝚘𝚛𝚝["𝙴𝚡𝚙_𝚃𝙼𝙼_𝙴𝚡𝚙.𝚡𝚕𝚜", 𝚃𝚛𝚊𝚗𝚜𝚙𝚘𝚜𝚎[{Δ𝚗𝙴𝚡𝚌𝙴𝚡𝚙𝚃𝙼𝙼𝙴𝚡𝚙, Δ𝚗𝙴𝚡𝚌𝙴𝚡𝚙𝚃𝙼𝙼𝙴𝚡𝚙𝚁𝚎𝚕𝙳𝚎𝚟}]];
𝙴𝚡𝚙𝚘𝚛𝚝["𝙴𝚡𝚙_𝚃𝙼𝙼_𝙷𝚘𝚖𝚘.𝚡𝚕𝚜", 𝚃𝚛𝚊𝚗𝚜𝚙𝚘𝚜𝚎[{𝚗𝙴𝚡𝚌𝙴𝚡𝚙𝚃𝙼𝙼𝙷𝚘𝚖𝚘, Δ𝚗𝙴𝚡𝚌𝙴𝚡𝚙𝚃𝙼𝙼𝙷𝚘𝚖𝚘𝚁𝚎𝚕𝙳𝚎𝚟}]];
𝙴𝚡𝚙𝚘𝚛𝚝["𝙴𝚡𝚙_𝙰𝚙𝚙𝚛𝚘𝚡_𝚜𝚑𝚘𝚛𝚝.𝚡𝚕𝚜", 𝚃𝚛𝚊𝚗𝚜𝚙𝚘𝚜𝚎[{Δ𝚗𝙴𝚡𝚙𝚂𝚑𝚘𝚛𝚝, Δ𝚗𝙴𝚡𝚙𝚂𝚑𝚘𝚛𝚝𝚁𝚎𝚕𝙳𝚎𝚟}]];
𝙴𝚡𝚙𝚘𝚛𝚝["𝙴𝚡𝚙_𝙰𝚙𝚙𝚛𝚘𝚡_𝚕𝚘𝚗𝚐.𝚡𝚕𝚜", 𝚃𝚛𝚊𝚗𝚜𝚙𝚘𝚜𝚎[{Δ𝚗𝙴𝚡𝚙𝙻𝚘𝚗𝚐, Δ𝚗𝙴𝚡𝚙𝙻𝚘𝚗𝚐𝚁𝚎𝚕𝙳𝚎𝚟}]];
```


Printed by Wolfram Mathematica Student Edition

Plot

```
ALabels = {"λs/d", "Re(Δnguess − Δn / Δn)"};
ALabels2 = {"λs/d", "Im(Δnguess − Δn / Δn)"};
ALabels3 = {"λs/d", "Abs(Δnguess − Δn / Δn)"};
leg = {"TMM Exp", "TMM Homo", "Short", "Long"};
plt1 = ListLogLinearPlot[{Thread[{λs, Re[ΔnExcExpTMMExpRelDev]}],
    Thread[{λs, Re[ΔnExcExpTMMHomoRelDev]}],
    Thread[{λs, Re[ΔnExpShortRelDev]}],
    Thread[{λs, Re[ΔnExpLongRelDev]}]},
  AxesLabel → ALabels, PlotLabel → "Re(Δnexc)", Joined → True, GridLines → Automatic,
  PlotLegends → LineLegend[leg], PlotLabels → Placed[leg, Automatic], PlotRange → All]
plt2 = ListLogLinearPlot[{Thread[{λs, Im[ΔnExcExpTMMExpRelDev]}],
    Thread[{λs, Im[ΔnExcExpTMMHomoRelDev]}],
    Thread[{λs, Im[ΔnExpShortRelDev]}],
    Thread[{λs, Im[ΔnExpLongRelDev]}]},
  AxesLabel → ALabels2, PlotLabel → "Im(Δnexc)", Joined → True, GridLines → Automatic,
  PlotLegends → LineLegend[leg], PlotLabels → leg, PlotRange → All]
plt3 = ListLogLogPlot[{Thread[{λs, Abs[ΔnExcExpTMMExpRelDev]}],
    Thread[{λs, Abs[ΔnExcExpTMMHomoRelDev]}],
    Thread[{λs, Abs[ΔnExpShortRelDev]}],
    Thread[{λs, Abs[ΔnExpLongRelDev]}]},
  AxesLabel → ALabels3, PlotLabel → "Abs(Δnexc)", Joined → True, GridLines → Automatic,
  PlotLegends → LineLegend[leg], PlotLabels → leg, PlotRange → All]
Export["modeltest_Re.pdf", plt1];
Export["modeltest_Im.pdf", plt2];
Export["modeltest_abs.pdf", plt3];
```

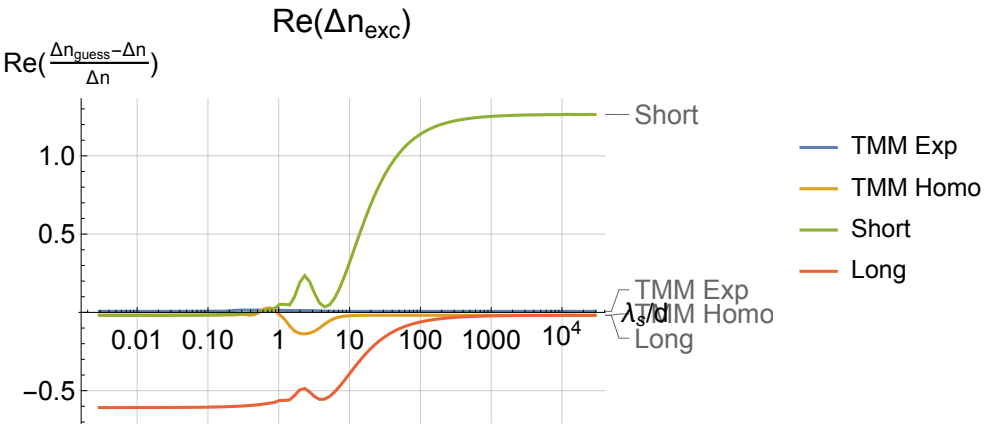

Printed by Wolfram Mathematica Student Edition

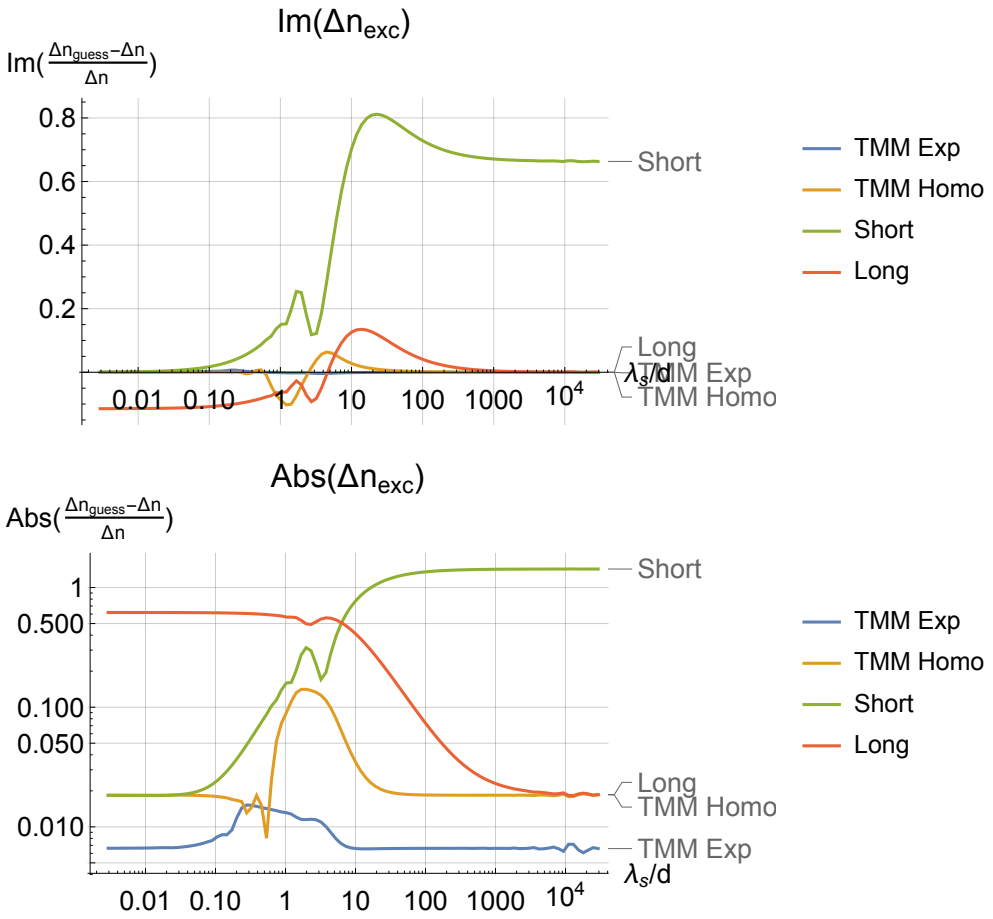

We see that the analytical approximation works fairly well at the extremes (2-4% deviation), however they quickly deviate in the intermediate wavelengths. Using TMM and assuming a homogeneous slab of photoexcitation, we get a more accurate result, but it still has 12% deviation for $\lambda_s/d \simeq 1$. Representing the photoexcited sample by 10 Layers gives around 1% deviation for all wavelengths, however it is still slightly less accurate when λ_s is the size of the sample.

Compare accuracy of estimation vs input parameters (d_p, N_L)

We compare the accuracy when using N_L number of layers to represent the exponentially decaying photoconductivity of our material.

Printed by Wolfram Mathematica Student Edition

Calculate vs NLayer for $\lambda_s / d = 1$

```
NL2 = Range[1, 20];
ii = Flatten[Position[λn, _?(# ≥ 1 &)]];
ii = ii[[1]];
NLayerTest2 = Parallelize[Table[(
      dExcG = dExc;
      initguess = ΔnExc;
      guess =
       FindRoot[tExcExpRegion[[ii]] == ΔnExcTMMExp[ΔnG, λ0[[ii]], NLayerG, dExcG],
        {ΔnG, initguess}, WorkingPrecision → MachinePrecision, MaxIterations → 100];
      ΔnGuess = ΔnG /. guess)
     , {NLayerG, NL2}]];
```

FindRoot::lstol : The line search decreased the step size to within tolerance specified by AccuracyGoal and PrecisionGoal but was unable to find a sufficient decrease in the merit function. You may need more than MachinePrecision digits of working precision to meet these tolerances.

Calculate for selected NLayer

```
NL = Range[5, 15, 5];
NLayerTest = Table[(
     dExcG = dExc;
     initguess = ΔnExc;
     guess = Parallelize[Table[FindRoot[tExcExpRegion[[i]] ==
          ΔnExcTMMExp[ΔnG, λ0[[i]], NLayerG, dExcG], {ΔnG, initguess},
         WorkingPrecision → MachinePrecision, MaxIterations → 100], {i, ωpoints}]];
     ΔnGuess = ΔnG /. guess)
    , {NLayerG, NL}];
```


Printed by Wolfram Mathematica Student Edition

Plot

```
NLTa = RelDev[#, ΔnExc] & /@ NLayerTest;
NLT = Map[Thread[{λs, #}] &, Abs[NLTa], {1}];
NLT2a = RelDev[NLayerTest2, ΔnExc];
NLT2 = Thread[{NL2, Abs[NLT2a]}];
leg = NL;
plt = ListLogLogPlot[NLT, AxesLabel → {"λs/d", "Abs(Δnguess − Δn / Δn)"},
  PlotLabel → "NLayer Test", Joined → True, GridLines → Automatic,
  PlotLegends → LineLegend[leg], PlotLabels → leg, PlotRange → Full]
Export["NTest_abs.pdf", plt];
plt = ListLogLogPlot[NLT2, AxesLabel → {"NLayers", "Abs(Δnguess − Δn / Δn)"},
  PlotLabel → "NLayer Test (λs/d=1)", Joined → True,
  GridLines → Automatic, PlotRange → Full]
Export["NTest2_abs.pdf", plt];
```

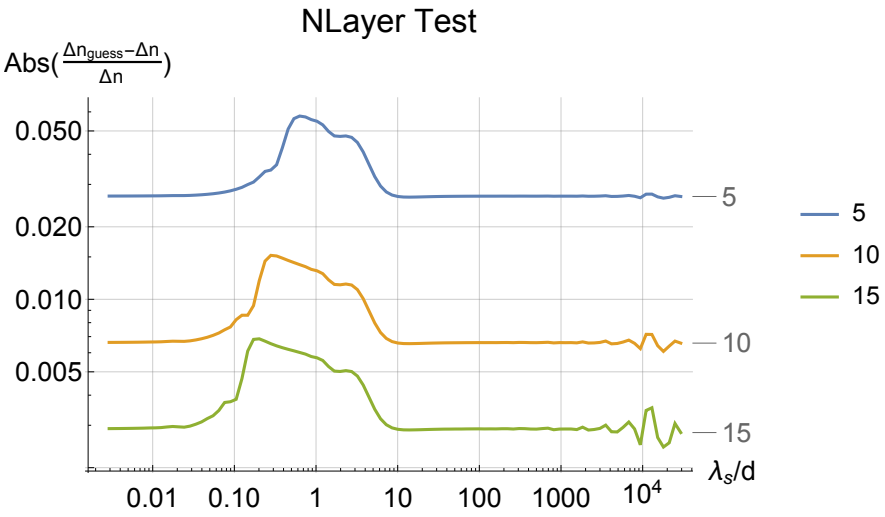

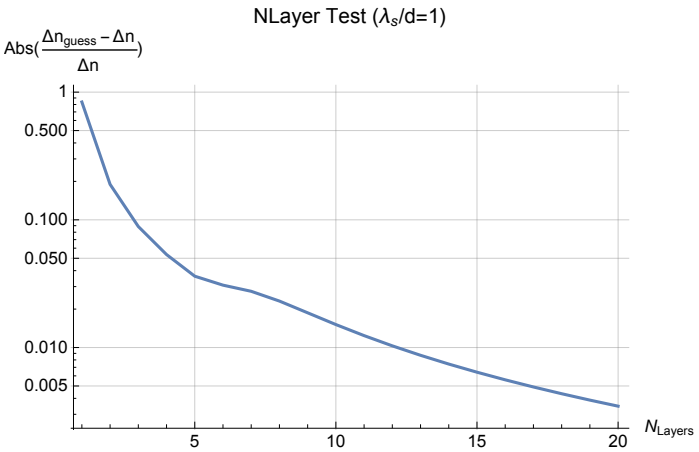

We see that the routine fairly quickly converges as N increases, with NLayer=10 giving roughly 1% deviation. As expected, the routine is less accurate when the wavelength is roughly the size of the individual layers.

Printed by Wolfram Mathematica Student Edition

Export the data

```
Export["lambda_n.xls", λn];
Export["NLayerTest.xls", Transpose[NLTa]];
Export["NLayerTest2.xls", NLT2a];
```


Printed by Wolfram Mathematica Student Edition

References

[1] Dyre, J.C. and Schrøder, T.B. Universality of ac conduction in disordered solids. *Reviews of Modern Physics*, **72**, 873 (2000). xv, 19, 27

[2] Seo, J., Forró, L., and Saito, S. *Carbon Nanotubes: Quantum Cylinders of Graphene*, volume 3 of *Contemporary Concepts of Condensed Matter Science*. Elsevier (2008). ISBN 9780444532763. xv, 2, 28, 29, 30, 31, 32, 33

[3] Charlier, J.C. and Roche, S. Electronic and transport properties of nanotubes. *Reviews of Modern Physics*, **79**, 677 (2007). xv, 2, 3, 28, 30, 31

[4] Ramana, C.V., Utsunomiya, S., Ewing, R.C., Julien, C.M., and Becker, U. Structural Stability and Phase Transitions in WO 3 Thin Films. *The Journal of Physical Chemistry B*, **110**, 10430 (2006). xv, 33, 34

[5] Huang, K. and Zhang, Q. Rechargeable lithium battery based on a single hexagonal tungsten trioxide nanowire. *Nano Energy*, **1**, 172 (2012). xv, 34

[6] Roussel, P., Labbé, P., and Groult, D. Symmetry and twins in the monophosphate tungsten bronze series $(PO_2)_4(WO_3)_{2m}(2 \leq m \leq 14)$. *Acta Crystallographica Section B Structural Science*, **56**, 377 (2000). xv, 35

[7] Frey, G., Rothschild, A., Sloan, J., Rosentsveig, R., Popovitz-Biro, R., and Tenne, R. Investigations of Nonstoichiometric Tungsten Oxide Nanoparticles. *Journal of Solid State Chemistry*, **162**, 300 (2001). xv, 35, 36

[8] Migas, D.B., Shaposhnikov, V.L., and Borisenko, V.E. Tungsten oxides. II. The metallic nature of Magnéli phases. *Journal of Applied Physics*, **108**, 093714 (2010). xvi, 3, 33, 35, 36, 37, 38, 39, 122, 123, 129, 131, 133, 137

[9] Kumar, M. Carbon Nanotube Synthesis and Growth Mechanism. In *Carbon Nanotubes - Synthesis, Characterization, Applications*. InTech (2011). ISBN 978-953-307-497-9. xvi, 41, 42

[10] Bronikowski, M.J., Willis, P.A., Colbert, D.T., Smith, K.A., and Smalley, R.E. Gas-phase production of carbon single-walled nanotubes from carbon monoxide via the HiPco process: A parametric study. *Journal of Vacuum Science & Technology A: Vacuum, Surfaces, and Films*, **19**, 1800 (2001). xvi, 43

[11] Strano, M.S., Moore, V.C., Miller, M.K., Allen, M.J., Haroz, E.H., Kittrell, C., Hauge, R.H., and Smalley, R.E. The Role of Surfactant Adsorption during Ultrasonication in the Dispersion of Single-Walled Carbon Nanotubes. *Journal of Nanoscience and Nanotechnology*, **3**, 81 (2003). xvi, 44

[12] Hayashi, S. and Kawase, K. Terahertz-wave parametric sources. In *Recent Optical and Photonic Technologies*, edited by K.Y. Kim, chapter 06. InTech, Rijeka (2010). xvi, 49

[13] Nemoto, N., Higuchi, T., Kanda, N., Konishi, K., and Kuwata-Gonokami, M. Highly precise and accurate terahertz polarization measurements based on electro-optic sampling with polarization modulation of probe pulses. *Optics Express*, **22**, 17915 (2014). xvii, 53

[14] Li, D., Zhang, J., He, Y., Qin, Y., Wei, Y., Liu, P., Zhang, L., Wang, J., Li, Q., Fan, S., and Jiang, K. Scanning electron microscopy imaging of single-walled carbon nanotubes on substrates. *Nano Research*, **10**, 1804 (2017). xviii, 65, 66

[15] Ulbricht, R., Hendry, E., Shan, J., Heinz, T.F., and Bonn, M. Carrier dynamics in semiconductors studied with time-resolved terahertz spectroscopy. *Reviews of Modern Physics*, **83**, 543 (2011). 1, 2, 9, 19, 25, 50, 56, 69, 75, 77, 93, 106, 108, 123, 126

[16] Lloyd-Hughes, J. and Jeon, T.I. A Review of the Terahertz Conductivity of Bulk and Nano-Materials. *Journal of Infrared, Millimeter, and Terahertz Waves*, **33**, 871 (2012). 1, 2, 22, 123

[17] Grischkowsky, D., Keiding, S., van Exter, M., and Fattinger, C. Far-infrared time-domain spectroscopy with terahertz beams of dielectrics and semiconductors. *Journal of the Optical Society of America B*, **7**, 2006 (1990). 1, 50

[18] Chatterjee, S., Grunwald, T., Köhler, D., Pierz, K., Golde, D., Kira, M., and Koch, S. THz measurements of the optical response in a two-dimensional electron gas. *Physica Status Solidi (C)*, **6**, 453 (2009). 1, 50

[19] Jeon, T.I., Kim, K.J., Kang, C., Maeng, I.H., Son, J.H., An, K.H., Lee, J.Y., and Lee, Y.H. Optical and electrical properties of preferentially anisotropic single-walled carbon-nanotube films in terahertz region. *Journal of Applied Physics*, **95**, 5736 (2004). 1, 50

[20] Groeneveld, R.H.M. and Grischkowsky, D. Picosecond time-resolved far-infrared experiments on carriers and excitons in GaAs-AlGaAs multiple quantum wells. *Journal of the Optical Society of America B*, **11**, 2502 (1994). 1, 50

[21] Leinss, S., Kampfrath, T., V.Volkmann, K., Wolf, M., Steiner, J.T., Kira, M., Koch, S.W., Leitenstorfer, A., and Huber, R. Terahertz Coherent Control of Optically Dark Paraexcitons in Cu_2O. *Physical Review Letters*, **101**, 246401 (2008). 1, 50

[22] Beard, M.C., Turner, G.M., and Schmuttenmaer, C.A. Measuring intramolecular charge transfer via coherent generation of THz radiation. *Journal of Physical Chemistry A*, **106**, 878 (2002). 1, 50

[23] Schall, M., Walther, M., and Uhd Jepsen, P. Fundamental and second-order phonon processes in CdTe and ZnTe. *Physical Review B*, **64**, 094301 (2001). 1, 50

[24] Ando, T. The electronic properties of graphene and carbon nanotubes. *NPG Asia Materials*, **1**, 17 (2009). 2, 28

[25] Iijima, S. Helical microtubules of graphitic carbon. *Nature*, **354**, 56 (1991). 3, 41

[26] Hu, L., Hecht, D.S., and Gruner, G. Carbon Nanotube Thin Films: Fabrication, Properties, and Applications. *Chemical Reviews*, **110**, 5790 (2010). 3, 41

[27] Park, S., Vosguerichian, M., and Bao, Z. A review of fabrication and applications of carbon nanotube film-based flexible electronics. *Nanoscale*, **5**, 1727 (2013). 3, 41

[28] Reich, S., Thomsen, C., and Maultzsch, J. *Carbon Nanotubes: Basic Concepts and Physical Properties*. Wiley (2008). ISBN 9783527618057. 3, 84, 105

[29] Portnoi, M., Kibis, O., and Rosenau da Costa, M. Terahertz applications of carbon nanotubes. *Superlattices and Microstructures*, **43**, 399 (2008).

[30] He, X., Fujimura, N., Lloyd, J.M., Erickson, K.J., Talin, A.A., Zhang, Q., Gao, W., Jiang, Q., Kawano, Y., Hauge, R.H., Léonard, F., and Kono, J. Carbon nanotube terahertz detector. *Nano letters*, **14**, 3953 (2014).

[31] Titova, L.V., Pint, C.L., Zhang, Q., Hauge, R.H., Kono, J., and Hegmann, F.A. Generation of Terahertz Radiation by Optical Excitation of Aligned Carbon Nanotubes. *Nano letters* (2015).

[32] Zubair, A., Tsentalovich, D.E., Young, C.C., Heimbeck, M.S., Everitt, H.O., Pasquali, M., and Kono, J. Carbon nanotube fiber terahertz polarizer. *Applied Physics Letters*, **108**, 141107 (2016). 3, 84, 105

[33] Nanot, S., Hároz, E.H., Kim, J.H., Hauge, R.H., and Kono, J. Optoelectronic properties of single-wall carbon nanotubes. *Advanced materials (Deerfield Beach, Fla.)*, **24**, 4977 (2012). 3, 105

[34] Avouris, P., Chen, Z., and Perebeinos, V. Carbon-based electronics. *Nature Nanotechnology*, **2**, 605 (2007).

[35] Avouris, P., Freitag, M., and Perebeinos, V. Carbon-nanotube photonics and optoelectronics. *Nature Photonics*, **2**, 341 (2008).

[36] Leonard, F. *The physics of carbon nanotube devices*. William Andrew (2009). ISBN 9780815515739. 3, 105

[37] Soavi, G., Scotognella, F., Lanzani, G., and Cerullo, G. Ultrafast Photophysics of Single-Walled Carbon Nanotubes. *Advanced Optical Materials*, **4**, 1670 (2016). 3, 105

[38] Wang, F., Dukovic, G., Brus, L.E., and Heinz, T.F. The Optical Resonances in Carbon Nanotubes Arise from Excitons. *Science*, **308**, 838 (2005). 3, 12, 105

[39] Srivastava, A., Htoon, H., Klimov, V.I., and Kono, J. Direct Observation of Dark Excitons in Individual Carbon Nanotubes: Inhomogeneity in the Exchange Splitting. *Physical Review Letters*, **101**, 087402 (2008).

[40] Chmeliov, J., Narkeliunas, J., Graham, M.W., Fleming, G.R., and Valkunas, L. Excitonexciton annihilation and relaxation pathways in semiconducting carbon nanotubes. *Nanoscale*, **8**, 1618 (2016).

[41] Luo, L., Chatzakis, I., Patz, A., and Wang, J. Ultrafast Terahertz Probes of Interacting Dark Excitons in Chirality-Specific Semiconducting Single-Walled Carbon Nanotubes. *Physical Review Letters*, **114**, 107402 (2015). 106, 108, 113, 119, 136

[42] Haugen, N.O., Phillips, A.B., Dykstra, T.E., Watthage, S., Heben, M.J., and Ellingson, R.J. Intraexciton Transitions Observed in High Stability Doped Single-Wall Carbon Nanotube Films and Solutions. *The Journal of Physical Chemistry C*, **118**, 25253 (2014). 3, 105

[43] Polaczek, A., Pekala, M., and Obuszko, Z. Magnetic susceptibility and thermoelectric power of tungsten intermediary oxides. *Journal of Physics: Condensed Matter*, **6**, 7909 (1994). 3, 32, 122

[44] Makarov, V.O. and Trontelj, M. Sintering and Electrical Conductivity of Doped WO_3. *Journal of the European Ceramic Society*, **16**, 791 (1996). 3, 33, 37, 122

[45] Gillet, M., Aguir, K., Lemire, C., Gillet, E., and Schierbaum, K. The structure and electrical conductivity of vacuum-annealed WO_3 thin films. *Thin Solid Films*, **467**, 239 (2004). 3, 122

[46] Gullapalli, S.K., Vemuri, R.S., and Ramana, C.V. Structural transformation induced changes in the optical properties of nanocrystalline tungsten oxide thin films. *Applied Physics Letters*, **96**, 171903 (2010). 3, 122

[47] Niklasson, G.a. and Granqvist, C.G. Electrochromics for smart windows: thin films of tungsten oxide and nickel oxide, and devices based on these. *Journal of Materials Chemistry*, **17**, 127 (2007). 3, 121

[48] Sayama, K., Mukasa, K., Abe, R., Abe, Y., and Arakawa, H. Stoichiometric water splitting into H2 and O2 using a mixture of two different photocatalysts and an IO3/I shuttle redox mediator under visible light irradiation. *Chemical Communications*, **0**, 2416 (2001). 3, 121

[49] HODES, G., CAHEN, D., and MANASSEN, J. Tungsten trioxide as a photoanode for a photoelectrochemical cell (PEC). *Nature*, **260**, 312 (1976). 3, 121

[50] Ho, J.J. Novel nitrogen monoxides (NO) gas sensors integrated with tungsten trioxide (WO_3)/pin structure for room temperature operation. *Solid-State Electronics*, **47**, 827 (2003). 3, 121

[51] Reyes, L.F., Hoel, A., Saukko, S., Heszler, P., Lantto, V., and Granqvist, C.G. Gas sensor response of pure and activated WO_3 nanoparticle films made by advanced reactive gas deposition. *Sensors and Actuators, B: Chemical*, **117**, 128 (2006). 3, 121

[52] Sun, S., Zhao, Y., Xia, Y., Zou, Z., Min, G., and Zhu, Y. Bundled tungsten oxide nanowires under thermal processing. *Nanotechnology*, **19**, 305709 (2008). 3, 47, 121, 124, 125

[53] Su, C.Y.Y. and Lin, H.C.C. Direct route to tungsten oxide nanorod bundles: Microstructures and electro-optical properties. *Journal of Physical Chemistry C*, **113**, 4042 (2009). 39, 122

[54] Li, Y., Bando, Y., and Golberg, D. Quasi-Aligned Single-Crystalline W18O49 Nanotubes and Nanowires. *Advanced Materials*, **15**, 1294 (2003).

[55] Jin, Y.Z., Zhu, Y.Q., Whitby, R.L., Nan Yao, N., Renzhi, M., Watts, P.C., Kroto, H.W., and Walton, D.R. Simple approaches to quality large-Scale tungsten oxide nanoneedles (2004).

[56] Zhou, J., Gong, L., Deng, S.Z., Chen, J., She, J.C., Xu, N.S., Yang, R., and Wang, Z.L. Growth and field-emission property of tungsten oxide nanotip arrays. *Applied Physics Letters*, **87**, 223108 (2005).

[57] Chi, L., Xu, N., Deng, S., Chen, J., and She, J. An approach for synthesizing various types of tungsten oxide nanostructure. *Nanotechnology*, **17**, 5590 (2006).

[58] Liu, J., Zhang, Z., Zhao, Y., Su, X., Liu, S., and Wang, E. Tuning the Field-Emission Properties of Tungsten Oxide Nanorods. *Small*, **1**, 310 (2005).

[59] Cheong, F.C., Varghese, B., Zhu, Y., Tan, E.P.S., Dai, L., Tan, V.B.C., Lim, C.T., and Sow, C.H. WO_{3-x} nanorods synthesized on a thermal hot plate. *Journal of Physical Chemistry C*, **111**, 17193 (2007).

[60] Yoo, S.J., Lim, J.W., Sung, Y.E., Jung, Y.H., Choi, H.G., and Kim, D.K. Fast switchable electrochromic properties of tungsten oxide nanowire bundles. *Applied Physics Letters*, **90**, 173126 (2007).

[61] Wang, X.P., Yang, B.Q., Zhang, H.X., and Feng, P.X. Tungsten Oxide Nanorods Array and Nanobundle Prepared by Using Chemical Vapor Deposition Technique. *Nanoscale Research Letters*, **2**, 405 (2007).

[62] Jeon, S. and Yong, K. Direct synthesis of W_18O_49 nanorods from W_2N film by thermal annealing. *Nanotechnology*, **18**, 245602 (2007).

[63] Wu, Y., Xi, Z., Zhang, G., Yu, J., and Guo, D. Growth of hexagonal tungsten trioxide tubes. *Journal of Crystal Growth*, **292**, 143 (2006). 3, 121

[64] Kittel, C. *Introduction to Solid State Physics*. Wiley, 8th edition (2004). ISBN 9780471415268. 10

[65] Scholes, G.D. and Rumbles, G. Excitons in nanoscale systems. *Nature Materials*, **5**, 683 (2006). 11, 26

[66] Joyce, H.J., Boland, J.L., Davies, C.L., Baig, S.A., and Johnston, M.B. Electrical properties of semiconductor nanowires: Insights gained from terahertz conductivity spectroscopy. *Semiconductor Science and Technology*, **31**, 1 (2016). 19, 56, 69, 70, 123

[67] Averitt, R.D. and Taylor, A.J. Ultrafast optical and far-infrared quasiparticle dynamics in correlated electron materials. *Journal of Physics: Condensed Matter*, **14**, R1357 (2002).

[68] Kaindl, R.A., Huber, R., Schmid, B.A., Carnahan, M.A., Hägele, D., and Chemla, D.S. Ultrafast THz spectroscopy of correlated electrons: from excitons to Cooper pairs. *physica status solidi (b)*, **243**, 2414 (2006).

[69] Kira, M., Hoyer, W., and Koch, S. Terahertz signatures of the exciton formation dynamics in non-resonantly excited semiconductors. *Solid State Communications*, **129**, 733 (2004). 19

[70] Garnett, J.C.M. Colours in Metal Glasses and in Metallic Films. *Philosophical Transactions of the Royal Society A: Mathematical, Physical and Engineering Sciences*, **203**, 385 (1904). 19, 27, 28

[71] Stroud, D. Generalized effective-medium approach to the conductivity of an inhomogeneous material. *Physical Review B*, **12**, 3368 (1975).

[72] Choy, T.C. *Effective Medium Theory*. Oxford University Press (2015). ISBN 9780198705093. 19, 27

[73] Nienhuys, H.K. and Sundström, V. Influence of plasmons on terahertz conductivity measurements. *Applied Physics Letters*, **87**, 012101 (2005). 19, 110

[74] Smith, N. Classical generalization of the Drude formula for the optical conductivity. *Physical Review B*, **64**, 155106 (2001). 19, 21

[75] Das Sarma, S. and Hwang, E.H. Collective Modes of the Massless Dirac Plasma. *Physical Review Letters*, **102**, 206412 (2009). 21, 113

[76] Kužel, P. and Němec, H. Terahertz conductivity in nanoscaled systems: effective medium theory aspects. *Journal of Physics D: Applied Physics*, **47**, 374005 (2014). 21, 27, 75

[77] Bass, J. Deviations from Matthiessen's Rule. *Advances in Physics*, **21**, 431 (1972). 22

[78] Kasap, S. and Capper, P. (editors). *Springer Handbook of Electronic and Photonic Materials*. Springer International Publishing, Cham (2017). ISBN 978-3-319-48931-5. 22

[79] Ramayya, E.B., Vasileska, D., Goodnick, S.M., and Knezevic, I. Electron transport in silicon nanowires: The role of acoustic phonon confinement and surface roughness scattering. *Journal of Applied Physics*, **104**, 063711 (2008). 23, 24

[80] Yu, S., Kim, K.W., Stroscio, M.A., and Iafrate, G.J. Electronacoustic-phonon scattering rates in cylindrical quantum wires. *Physical Review B*, **51**, 4695 (1995). 23

[81] Murphy-Armando, F., Fagas, G., and Greer, J.C. Deformation Potentials and Electron-Phonon Coupling in Silicon Nanowires. *Nano Letters*, **10**, 869 (2010). 23

[82] Low, F.E. and Pines, D. Mobility of Slow Electrons in Polar Crystals. *Physical Review*, **98**, 414 (1955). 23

[83] Bardeen, J. and Shockley, W. Deformation potentials and mobilities in non-polar crystals. *Physical Review*, **80**, 72 (1950). 23

[84] Conwell, E. and Weisskopf, V.F. Theory of Impurity Scattering in Semiconductors. *Physical Review*, **77**, 388 (1950). 24

[85] Chattopadhyay, D. and Queisser, H.J. Electron scattering by ionized impurities in semiconductors. *Reviews of Modern Physics*, **53**, 745 (1981). 24

[86] Unuma, T., Yoshita, M., Noda, T., Sakaki, H., and Akiyama, H. Intersubband absorption linewidth in GaAs quantum wells due to scattering by interface roughness, phonons, alloy disorder, and impurities. *Journal of Applied Physics*, **93**, 1586 (2003). 24

[87] Wang, J., Polizzi, E., Ghosh, A., Datta, S., and Lundstrom, M. Theoretical investigation of surface roughness scattering in silicon nanowire transistors. *Applied Physics Letters*, **87**, 043101 (2005).

[88] Martin, P., Aksamija, Z., Pop, E., and Ravaioli, U. Impact of Phonon-Surface Roughness Scattering on Thermal Conductivity of Thin Si Nanowires. *Physical Review Letters*, **102**, 125503 (2009). 24

[89] Yu, P.Y. and Cardona, M. *Fundamentals of Semiconductors*. Graduate Texts in Physics. Springer Berlin Heidelberg, Berlin, Heidelberg, fourth edition (2010). ISBN 978-3-642-00709-5. 25

[90] Bruggeman, D.A.G. Berechnung verschiedener physikalischer Konstanten von heterogenen Substanzen. I. Dielektrizitätskonstanten und Leitfähigkeiten der Mischkörper aus isotropen Substanzen. *Annalen der Physik*, **416**, 636 (1935). 27, 28

[91] Niklasson, G.a., Granqvist, C.G., and Hunderi, O. Effective medium models for the optical properties of inhomogeneous materials. *Applied Optics*, **20**, 26 (1981). 28

[92] Wallace, P.R. The band theory of graphite. *Physical Review*, **71**, 622 (1947). 29

[93] Blase, X., Benedict, L.X., Shirley, E.L., and Louie, S.G. Hybridization effects and metallicity in small radius carbon nanotubes. *Physical Review Letters*, **72**, 1878 (1994). 31

[94] Kane, C.L. and Mele, E.J. Size, shape, and low energy electronic structure of carbon nanotubes. *Phys. Rev. Lett.*, **78**, 1932 (1997). 31, 84

[95] Comfort, E. and Lee, J.U. Large Bandgap Shrinkage from Doping and Dielectric Interface in Semiconducting Carbon Nanotubes. *Scientific Reports*, **6**, 28520 (2016). 31

[96] Delaney, P., Choi, H.J., Ihm, J., Louie, S.G., and Cohen, M.L. Broken symmetry and pseudogaps in ropes of carbon nanotubes. *Nature*, **391**, 466 (1998). 31

[97] Collins, P.G., Bradley, K., Ishigami, M., and Zettl, A. Extreme Oxygen Sensitivity of Electronic Properties Extreme Oxygen Sensitivity of Electronic Properties of Carbon Nanotubes. *Science*, **287**, 1801 (2000). 31

[98] Zahab, A., Spina, L., Poncharal, P., and Marlière, C. Water-vapor effect on the electrical conductivity of a single-walled carbon nanotube mat. *Physical Review B*, **62**, 10000 (2000). 31

[99] Benedict, X., Louie, S.G., and Cohen, M.L. Static Polarizabilities of single-walled carbon nanotubes. *Physical Review B*, **52**, 8541 (1995). 32

[100] Jiang, J., Saito, R., Grüneis, a., Dresselhaus, G., and Dresselhaus, M.S. Optical absorption matrix elements in single-wall carbon nanotubes. *Carbon*, **42**, 3169 (2004). 32

[101] Kataura, H., Kumazawa, Y., Maniwa, Y., Umezu, I., Suzuki, S., Ohtsuka, Y., and Achiba, Y. Optical properties of single-wall carbon nanotubes. *Synthetic Metals*, **103**, 2555 (1999). 32

[102] Gerand, B., Nowogrocki, G., Guenot, J., and Figlarz, M. Structural study of a new hexagonal form of tungsten trioxide. *Journal of Solid State Chemistry*, **29**, 429 (1979). 33

[103] Bronzes, T. Monophosphate Tungsten Bronzes. A New Family of Low-Dimensional, Charge-Density-Wave Oxides. *Accounts of Chemical Research*, **5**, 219 (1996). 33

[104] Deb, S.K. Opportunities and challenges of electrochromic phenomena in transition metal oxides. *Solar Energy Materials and Solar Cells*, **25**, 327 (1992). 34, 38, 122

[105] Zheng, H., Ou, J.Z., Strano, M.S., Kaner, R.B., Mitchell, A., and Kalantar-zadeh, K. Nanostructured Tungsten Oxide - Properties, Synthesis, and Applications. *Advanced Functional Materials*, **21**, 2175 (2011). 46, 47, 121

[106] Cong, S., Geng, F., and Zhao, Z. Tungsten Oxide Materials for Optoelectronic Applications. *Advanced Materials*, **28**, 10518 (2016). 34, 121

[107] Niklasson, G.A., Berggren, L., and Larsson, A.L. Electrochromic tungsten oxide: the role of defects. *Solar Energy Materials and Solar Cells*, **84**, 315 (2004). 34

[108] Salje, E.K.H., Rehmann, S., Pobell, F., Morris, D., Knight, K.S., Herrmannsdörfer, T., and Dove, M.T. Crystal structure and paramagnetic behaviour of. *Journal of Physics: Condensed Matter*, **9**, 6563 (1997). 34

[109] Vogt, T., Woodward, P.M., and Hunter, B.A. The High-Temperature Phases of WO_3. *Journal of Solid State Chemistry*, **144**, 209 (1999). 34

[110] Boulova, M. and Lucazeau, G. Crystallite Nanosize Effect on the Structural Transitions of WO_3 Studied by Raman Spectroscopy. *Journal of Solid State Chemistry*, **167**, 425 (2002). 35

[111] Al Mohammad, A. and Gillet, M. Phase transformations in WO3 thin films during annealing. *Thin Solid Films*, **408**, 302 (2002). 35

[112] Glember, O. and Saurr, H. Über Wolframoxyde. *Zeitschrift für anorganische Chemie*, **252**, 144 (1943). 35

[113] Saenger, M.F., Höing, T., Robertson, B.W., Billa, R.B., Hofmann, T., Schubert, E., and Schubert, M. Polaron and phonon properties in proton intercalated amorphous tungsten oxide thin films. *Physical Review B*, **78**, 245205 (2008). 36

[114] Watanabe, H., Fujikata, K., Oaki, Y., and Imai, H. Band-gap expansion of tungsten oxide quantum dots synthesized in sub-nano porous silica. *Chemical Communications*, **49**, 8477 (2013). 37

[115] Zhang, Z., Wei, H.X., Ma, G.F., Li, Y.Q., Lee, S.T., and Tang, J.X. Interface energetics at WO$_x$ /organic interfaces: The role of oxygen vacancies. *Applied Physics Letters*, **103**, 133302 (2013). 37

[116] Salje, E. and Güttler, B. Anderson transition and intermediate polaron formation in WO_{3-x} Transport properties and optical absorption. *Philosophical Magazine Part B*, **50**, 607 (1984). 38, 122, 128, 129, 133, 137

[117] Sahle, W. and Nygren, M. Electrical conductivity and high resolution electron microscopy studies of WO3-x crystals with 0 x 0.28. *Journal of Solid State Chemistry*, **48**, 154 (1983). 38, 122, 128, 129, 131

[118] Viswanathan, K., Brandt, K., and Salje, E. Crystal structure and charge carrier concentration of W18O49. *Journal of Solid State Chemistry*, **36**, 45 (1981). 38, 39, 122

[119] Gehlig, R., Salje, E., Carley, A.F., and Roberts, M.W. XPS studies on $WO_{2.90}$ and $WO_{2.72}$ and the influence of metallic impurities. *Journal of Solid State Chemistry*, **49**, 318 (1983). 38, 122, 131

[120] Shi, S., Xue, X., Feng, P., Liu, Y., Zhao, H., and Wang, T. Low-temperature synthesis and electrical transport properties of W18O49 nanowires. *Journal of Crystal Growth*, **310**, 462 (2008). 39, 122

[121] Lee, K., Seo, W.S., and Park, J.T. Synthesis and optical properties of colloidal tungsten oxide nanorods. *Journal of the American Chemical Society*, **125**, 3408 (2003). 39, 122

[122] Feng, M., Pan, A.L., Zhang, H.R., Li, Z.A., Liu, F., Liu, H.W., Shi, D.X., Zou, B.S., and Gao, H.J. Strong photoluminescence of nanostructured crystalline tungsten oxide thin films. *Applied Physics Letters*, **86**, 141901 (2005).

[123] Li, Y.H., Zhao, Y.M., Ma, R.Z., Zhu, Y.Q., Fisher, N., Jin, Y.Z., and Zhang, X.P. Novel route to WO_x nanorods and WS2 nanotubes from WS2 inorganic fullerenes. *Journal of Physical Chemistry B*, **110**, 18191 (2006).

[124] Hong, K., Xie, M., Hu, R., and Wu, H. Synthesizing tungsten oxide nanowires by a thermal evaporation method. *Applied Physics Letters*, **90**, 173121 (2007).

[125] Hu, W., Zhao, Y., Liu, Z., Dunnill, C.W., Gregory, D.H., and Zhu, Y. Nanostructural Evolution: From One-Dimensional Tungsten Oxide Nanowires to Three-Dimensional Ferberite Flowers. *Chemistry of Materials*, **20**, 5657 (2008). 39, 122

[126] Remškar, M., Kovac, J., Viršek, M., Mrak, M., Jesih, A., and Seabaugh, A. W5O14 Nanowires. *Advanced Functional Materials*, **17**, 1974 (2007). 39, 122

[127] Manthiram, K. and Alivisatos, A.P. Tunable Localized Surface Plasmon Resonances in Tungsten Oxide Nanocrystals. *Journal of the American Chemical Society*, **8**, 8 (2012). 39, 122

[128] Ebbesen, T.W. and Ajayan, P.M. Large-scale synthesis of carbon nanotubes. *Nature*, **358**, 220 (1992). 41

[129] Ci, L., Zhao, Z., and Bai, J. Direct growth of carbon nanotubes on the surface of ceramic fibers. *Carbon*, **43**, 883 (2005). 41, 42

[130] Koziol, K., Boskovic, B.O., and Yahya, N. Synthesis of Carbon Nanostructures by CVD Method. In *Carbon and Oxide Nanostructures*, pages 23–49. Springer, Berlin, Heidelberg (2010). 41, 42

[131] Nikolaev, P., Bronikowski, M.J., Bradley, R.K., Rohmund, F., Colbert, D.T., Smith, K.a., and Smalley, R.E. Gas-phase catalytic growth of single-walled carbon nanotubes from carbon monoxide. *Chemical Physics Letters*, **313**, 91 (1999). 43

[132] Strano, M.S. Electronic Structure Control of Single-Walled Carbon Nanotube Functionalization. *Science*, **301**, 1519 (2003). 43, 44

[133] Matarredona, O., Rhoads, H., Li, Z., Harwell, J.H., Balzano, L., and Resasco, D.E. Dispersion of Single-Walled Carbon Nanotubes in Aqueous Solutions of the Anionic Surfactant NaDDBS. *The Journal of Physical Chemistry B*, **107**, 13357 (2003). 43

[134] Stahl, H., Appenzeller, J., Martel, R., Avouris, P., and Lengeler, B. Intertube coupling in ropes of single-wall carbon nanotubes. *Physical Review Letters*, **85**, 5186 (2000). 44

[135] Bandyopadhyaya, R., Nativ-Roth, E., Regev, O., and Yerushalmi-Rozen, R. Stabilization of Individual Carbon Nanotubes in Aqueous Solutions. *Nano Letters*, **2**, 25 (2002). 44

[136] Shin, J.Y., Premkumar, T., and Geckeler, K.E. Dispersion of single-walled carbon nanotubes by using surfactants: Are the type and concentration important? *Chemistry - A European Journal*, **14**, 6044 (2008). 44

[137] Rinzler, A., Liu, J., Dai, H., Nikolaev, P., Huffman, C., Rodríguez-Macías, F., Boul, P., Lu, A., Heymann, D., Colbert, D., Lee, R., Fischer, J., Rao, A., Eklund, P., and Smalley, R. Large-scale purification of single-wall carbon nanotubes: process, product, and characterization. *Applied Physics A: Materials Science & Processing*, **67**, 29 (1998). 44

[138] Wang, Y., Gao, L., Sun, J., Liu, Y., Zheng, S., Kajiura, H., Li, Y., and Noda, K. An integrated route for purification, cutting and dispersion of single-walled carbon nanotubes. *Chemical Physics Letters*, **432**, 205 (2006). 44

[139] Hennrich, F., Krupke, R., Arnold, K., Stütz, J.A., Lebedkin, S., Koch, T., Schimmel, T., and Kappes, M.M. The mechanism of cavitation-induced scission of single-walled carbon nanotubes. *Journal of Physical Chemistry B*, **111**, 1932 (2007). 45, 89

[140] Liu, J., Rinzler, A.G., Dai, H., Hafner, J.H., Kelley Bradley, R., Boul, P.J., Lu, A., Iverson, T., Shelimov, K., Huffman, C.B., Rodriguez-Macias, F., Shon, Y.S., Lee, T.R., Colbert, D.T., and Smalley, R.E. Fullerene pipes. *Science*, **280**, 1253 (1998). 45

[141] Simpson, J., Fagan, J., Becker, M., Hobbie, E., and Hight Walker, A. The effect of dispersant on defects in length-separated single-wall carbon nanotubes measured by Raman spectroscopy. *Carbon*, **47**, 3238 (2009). 45

[142] Fagan, J.A., Bauer, B.J., Hobbie, E.K., Becker, M.L., Hight Walker, A.R., Simpson, J.R., Chun, J., Obrzut, J., Bajpai, V., Phelan, F.R., Simien, D., Huh, J.Y., and Migler, K.B. Carbon Nanotubes: Measuring Dispersion and Length. *Advanced Materials*, **23**, 338 (2011). 45

[143] Arnold, M.S., Green, A.A., Hulvat, J.F., Stupp, S.I., and Hersam, M.C. Sorting carbon nanotubes by electronic structure using density differentiation. *Nature Nanotechnology*, **1**, 60 (2006). 45

[144] Huang, X., Mclean, R.S., and Zheng, M. High-Resolution Length Sorting and Purification of DNA-Wrapped Carbon Nanotubes by Size-Exclusion Chromatography. *Analytical Chemistry*, **77**, 6225 (2005). 45

[145] Shuba, M.V., Paddubskaya, A.G., Kuzhir, P.P., Maksimenko, S.A., Ksenevich, V.K., Niaura, G., Seliuta, D., Kasalynas, I., and Valusis, G. Soft cutting of single-wall carbon nanotubes by low temperature ultrasonication in a mixture of sulfuric and nitric acids. *Nanotechnology*, **23**, 495714 (2012). 45, 90

[146] Marshall, M.W., Popa-Nita, S., and Shapter, J.G. Measurement of functionalised carbon nanotube carboxylic acid groups using a simple chemical process. *Carbon*, **44**, 1137 (2006).

[147] Hennrich, F., Lebedkin, S., Malik, S., Tracy, J., Barczewski, M., Rösner, H., and Kappes, M. Preparation, characterization and applications of free-standing single walled carbon nanotube thin films. *Physical Chemistry Chemical Physics*, **4**, 2273 (2002). 45, 89

[148] Coleman, J.N., Curran, S., Dalton, A.B., Davey, A.P., McCarthy, B., Blau, W., and Barklie, R.C. Percolation-dominated conductivity in a conjugated-polymer-carbon-nanotube composite. *Phys. Rev. B*, **58**, R7492 (1998). 46, 90

[149] Bauhofer, W. and Kovacs, J.Z. A review and analysis of electrical percolation in carbon nanotube polymer composites. *Composites Science and Technology*, **69**, 1486 (2009). 46, 84, 90, 106

[150] Naffakh, M., Díez-Pascual, A.M., and Gómez-Fatou, M.A. New hybrid nanocomposites containing carbon nanotubes, inorganic fullerene-like WS2 nanoparticles and poly(ether ether ketone) (PEEK). *Journal of Materials Chemistry*, **21**, 7425 (2011). 46

[151] Ksenevich, V., Gorbachuk, N., Viet, H., Shuba, M., Kuzhir, P., Maksimenko, S., Paddubskaya, A., Valusis, G., Wieck, A., Zak, A., and Tenne, R. Electrical properties of carbon nanotubes/WS2 nanotubes (nanoparticles) hybrid films. *Nanosystems: Physics, Chemistry, Mathematics*, **7**, 37 (2016). 46, 100

[152] Eder, D. Carbon nanotube-inorganic hybrids. *Chemical Reviews*, **110**, 1348 (2010). 46

[153] Zak, A., Sallan-Ecker, L., Margolin, A., Genut, M., and Tenne, R. Insight Into the Growth Mechanism of Ws 2 Nanotubes in the Scaled-Up Fluidized-Bed Reactor. *Nano*, **04**, 91 (2009). 46, 90

[154] Rothschild, A., Sloan, J., and Tenne, R. Growth of WS_2 nanotubes phases. *Journal of the American Chemical Society*, **122**, 5169 (2000). 46

[155] Li, Y.H., Zhao, Y.M., Ma, R.Z., Zhu, Y.Q., Fisher, N., Jin, Y.Z., and Zhang, X.P. Novel route to WO_x nanorods and WS_2 nanotubes from WS_2 inorganic fullerenes. *Journal of Physical Chemistry B*, **110**, 18191 (2006). 47, 124, 125

[156] Jepsen, P., Cooke, D., and Koch, M. Terahertz spectroscopy and imaging - Modern techniques and applications. *Laser & Photonics Reviews*, **5**, 124 (2011). 50, 56, 69, 123

[157] Auston, D.H. and Smith, P.R. Generation and detection of millimeter waves by picosecond photoconductivity. *Applied Physics Letters*, **43**, 631 (1983). 50

[158] Auston, D.H., Cheung, K.P., and Smith, P.R. Picosecond Photoconducting Hertzian Dipoles. *Applied Physics Letters*, **45**, 284 (1984).

[159] Auston, D. and Nuss, M. Electrooptical generation and detection of femtosecond electrical transients. *IEEE Journal of Quantum Electronics*, **24**, 184 (1988). 50

[160] Williams, G.P. High-power terahertz synchrotron sources. *Philosophical Transactions of the Royal Society A: Mathematical, Physical and Engineering Sciences*, **362**, 403 (2004). 50

[161] Murdin, B.N. Far-infrared free-electron lasers and their applications. *Contemporary Physics*, **50**, 391 (2009). 50

[162] Scalari, G., Walther, C., Fischer, M., Terazzi, R., Beere, H., Ritchie, D., and Faist, J. THz and sub-THz quantum cascade lasers. *Laser & Photonics Review*, **3**, 45 (2009). 50

[163] Simoens, F. Thz bolometer detectors. *Springer Series in Optical Sciences*, **173**, 35 (2014). 50

[164] Schiselski, M., Laabs, M., Neumann, N., Kovalev, S., Green, B., Gensch, M., and Plettemeier, D. A planar Schottky diode based integrated THz detector for fast electron pulse diagnostics. In *2016 IEEE MTT-S International Microwave Symposium (IMS)*, volume 2016-Augus, pages 1–4. IEEE (2016). ISBN 978-1-5090-0698-4. 50

[165] Smith, P., Auston, D., and Nuss, M. Subpicosecond photoconducting dipole antennas. *IEEE Journal of Quantum Electronics*, **24**, 255 (1988). 50, 51

[166] Fattinger, C. and Grischkowsky, D. Point source terahertz optics. *Applied Physics Letters*, **53**, 1480 (1988).

[167] Fattinger, C. and Grischkowsky, D. Terahertz beams. *Applied Physics Letters*, **54**, 490 (1989). 107, 125

[168] Shan, J. and Heinz, T.F. Terahertz Radiation from Semiconductors. In *Ultrafast Dynamical Processes in Semiconductors*, pages 1–56. Springer, Berlin, Heidelberg (2004). ISBN 0303-4216. 50

[169] Shen, Y.C., Upadhya, P.C., Beere, H.E., Linfield, E.H., Davies, A.G., Gregory, I.S., Baker, C., Tribe, W.R., and Evans, M.J. Generation and detection of ultrabroadband terahertz radiation using photoconductive emitters and receivers. *Applied Physics Letters*, **85**, 164 (2004). 50, 51

[170] Cai, Y., Brener, I., Lopata, J., Wynn, J., Pfeiffer, L., Stark, J.B., Wu, Q., Zhang, X.C., and Federici, J.F. Coherent terahertz radiation detection: Direct comparison between free-space electro-optic sampling and antenna detection. *Applied Physics Letters*, **73**, 444 (1998). 50, 54

[171] Krökel, D., Grischkowsky, D., and Ketchen, M.B. Subpicosecond electrical pulse generation using photoconductive switches with long carrier lifetimes. *Applied Physics Letters*, **54**, 1046 (1989). 51

[172] McIntosh, K.A., Brown, E.R., Nichols, K.B., McMahon, O.B., DiNatale, W.F., and Lyszczarz, T.M. Terahertz photomixing with diode lasers in lowtemperaturegrown GaAs. *Applied Physics Letters*, **67**, 3844 (1995). 51

[173] Lloyd-Hughes, J., Castro-Camus, E., and Johnston, M.B. Simulation and optimisation of terahertz emission from InGaAs and InP photoconductive switches. *Solid State Communications*, **136**, 595 (2005).

[174] Gu, P., Tani, M., Kono, S., Sakai, K., and Zhang, X.C. Study of terahertz radiation from InAs and InSb. *Journal of Applied Physics*, **91**, 5533 (2002). 51

[175] Headley, C., Fu, L., Parkinson, P., Xu, X., Lloyd-Hughes, J., Jagadish, C., and Johnston, M.B. Improved Performance of GaAs-Based Terahertz Emitters via Surface Passivation and Silicon Nitride Encapsulation. *IEEE Journal of Selected Topics in Quantum Electronics*, **17**, 17 (2011). 51

[176] Johnston, M.B., Corchia, A., Dowd, A., Linfield, E.H., Davies, A.G., McLaughlin, R., Arnone, D.D., and Pepper, M. Magnetic-field-induced enhancement of terahertz emission from III-V semiconductor surfaces. *Physica E: Low-Dimensional Systems and Nanostructures*, **13**, 896 (2002). 51

[177] Johnston, M.B., Whittaker, D.M., Corchia, A., G. Davies, A., and Linfield, E.H. Theory of magnetic-field enhancement of surface-field terahertz emission. *Journal of Applied Physics*, **91**, 2104 (2002). 51

[178] Johnston, M.B., Dowd, A., Driver, R., Linfield, E.H., Davies, A.G., and Whittaker, D.M. Emission of collimated THz pulses from photo-excited semiconductors. *Semiconductor Science and Technology*, **19**, S449 (2004). 51

[179] Yamaguchi, S., Fukushi, Y., Kubota, O., Itsuji, T., Ouchi, T., and Yamamoto, S. Brain tumor imaging of rat fresh tissue using terahertz spectroscopy. *Scientific Reports*, **6**, 30124 (2016). 52

[180] Zhang, X., Jin, Y., and Ma, X.F. Coherent measurement of THz optical rectification from electrooptic crystals. *Applied Physics Letters*, **61**, 2764 (1992). 52, 107, 126

[181] Reimann, K. Table-top sources of ultrashort THz pulses. *Reports on Progress in Physics*, **70**, 1597 (2007). 52

[182] Ko, Y., Sengupta, S., Tomasulo, S., Dutta, P., and Wilke, I. Emission of terahertz-frequency electromagnetic radiation from bulk $Ga_xIn_{1-x}As$ crystals. *Physical Review B - Condensed Matter and Materials Physics*, **78**, 035201 (2008). 52

[183] Wilke, I. and Sengupta, S. Nonlinear Optical Techniques for Terahertz Pulse Generation and Detection-Optical Rectification and Electrooptic Sampling. *Terahertz Spectroscopy: Principles and Applications*, pages 41–68 (2008). 52, 53

[184] Nahata, A., Weling, A.S., and Heinz, T.F. A wideband coherent terahertz spectroscopy system using optical rectification and electrooptic sampling. *Applied Physics Letters*, **69**, 2321 (1996). 52

[185] Wu, Q. and Zhang, X.C. 7 terahertz broadband GaP electro-optic sensor. *Applied Physics Letters*, **70**, 1784 (1997). 52

[186] Kaindl, R.A., Eickemeyer, F., Woerner, M., and Elsaesser, T. Broadband phase-matched difference frequency mixing of femtosecond pulses in GaSe: Experiment and theory. *Applied Physics Letters*, **75**, 1060 (1999).

[187] Huber, R., Brodschelm, A., Tauser, F., and Leitenstorfer, A. Generation and field-resolved detection of femtosecond electromagnetic pulses tunable up to 41 THz. *Applied Physics Letters*, **76**, 3191 (2000).

[188] Tomasino, A., Parisi, A., Stivala, S., Livreri, P., Cino, A.C., Busacca, A.C., Peccianti, M., and Morandotti, R. Wideband THz Time Domain Spectroscopy based on Optical Rectification and Electro-Optic Sampling. *Scientific Reports*, **3**, 3116 (2013). 52, 53

[189] Wu, Q. and Zhang, X.C. 7 terahertz broadband GaP electro-optic sensor. *Applied Physics Letters*, **70**, 1784 (1997). 53, 108, 126

[190] Nahata, A., Auston, D.H., Heinz, T.F., and Wu, C. Coherent detection of freely propagating terahertz radiation by electro-optic sampling. *Applied Physics Letters*, **68**, 150 (1996).

[191] Cornet, M., Degert, J., Abraham, E., and Freysz, E. Terahertz-field-induced second harmonic generation through Pockels effect in zinc telluride crystal. *Optics Letters*, **39**, 5921 (2014).

[192] Keiber, S., Sederberg, S., Schwarz, A., Trubetskov, M., Pervak, V., Krausz, F., and Karpowicz, N. Electro-optic sampling of near-infrared waveforms. *Nature Photonics*, **10**, 159 (2016). 53

[193] Rungsawang, R., Marshall, O., Freeman, J.R., Beere, H.E., Malik, S., Alton, J., Barbieri, S., and Ritchie, D.A. Intensity detection of terahertz quantum

cascade laser radiation using electro-optic sampling. *Applied Physics Letters*, **93**, 191111 (2008). 53

[194] Nahata, A., Weling, A.S., and Heinz, T.F. A wideband coherent terahertz spectroscopy system using optical rectification and electrooptic sampling. *Applied Physics Letters*, **69**, 2321 (1996). 53

[195] Bakker, H.J., Cho, G.C., Kurz, H., Wu, Q., and Zhang, X.C. Distortion of terahertz pulses in electro-optic sampling. *Journal of the Optical Society of America B*, **15**, 1795 (1998). 54

[196] Tani, M., Horita, K., Kinoshita, T., Que, C.T., Estacio, E., Yamamoto, K., and Bakunov, M.I. Efficient electro-optic sampling detection of terahertz radiation via Cherenkov phase matching. *Optics Express*, **19**, 19901 (2011). 54

[197] Schmuttenmaer, C.A. Exploring dynamics in the far-infrared with terahertz spectroscopy. *Chemical Reviews*, **104**, 1759 (2004). 56, 69

[198] Duvillaret, L., Garet, F., and Coutaz, J.L.L. A reliable method for extraction of material parameters in terahertz time-domain spectroscopy. *IEEE Journal of Selected Topics in Quantum Electronics*, **2**, 739 (1996). 56, 69

[199] Nienhuys, H.K. and Sundström, V. Intrinsic complications in the analysis of optical-pump, terahertz probe experiments. *Physical Review B - Condensed Matter and Materials Physics*, **71**, 1 (2005). 70, 76, 77

[200] Kužel, P., Kadlec, F., and Němec, H. Propagation of terahertz pulses in photoexcited media: Analytical theory for layered systems. *The Journal of Chemical Physics*, **127**, 024506 (2007). 56, 69, 75, 76, 79

[201] Bergren, M.R., Palomaki, P.K.B., Neale, N.R., Furtak, T.E., and Beard, M.C. Size-Dependent Exciton Formation Dynamics in Colloidal Silicon Quantum Dots. *ACS Nano*, **10**, 2316 (2016). 56, 69, 70

[202] Huber, R., Kübler, C., Tübel, S., Leitenstorfer, A., Vu, Q.T., Haug, H., Köhler, F., and Amann, M.C. Femtosecond Formation of Coupled Phonon-Plasmon Modes in InP: Ultrabroadband THz Experiment and Quantum Kinetic Theory. *Physical Review Letters*, **94**, 027401 (2005). 56, 69

[203] Jensen, S.A., Tielrooij, K.J., Hendry, E., Bonn, M., Rychetský, I., and Němec, H. Terahertz Depolarization Effects in Colloidal TiO_2 Films Reveal Particle Morphology. *The Journal of Physical Chemistry C*, **118**, 1191 (2014). 56, 69

[204] Beard, M.C., Turner, G.M., and Schmuttenmaer, C.A. Transient photoconductivity in GaAs as measured by time-resolved terahertz spectroscopy. *Physical Review B - Condensed Matter and Materials Physics*, **62**, 15764 (2000). 56, 69

[205] Förster, H. *UV/VIS Spectroscopy*, volume 4. Springer, Berlin, Heidelberg (2004). ISBN 9783642774799. 64

[206] Bachilo, S.M. Structure-Assigned Optical Spectra of Single-Walled Carbon Nanotubes. *Science*, **298**, 2361 (2002). 65

[207] Backes, C. and Stemmler, I. Absorption Spectroscopy as a Powerful Technique for the Characterization of Single-Walled Carbon Nanotubes. *Perkinelmer.Co.Uk*, pages 4–9 (2013). 65

[208] Miyata, Y., Mizuno, K., and Kataura, H. Purity and Defect Characterization of Single-Wall Carbon Nanotubes Using Raman Spectroscopy. *Journal of Nanomaterials*, **2011**, 1 (2011). 65, 66, 91

[209] Thomsen, C. and Reich, S. Raman Scattering in Carbon Nanotubes. In *Light Scattering in Solid IX*, pages 115–234. Springer Berlin Heidelberg, Berlin, Heidelberg (2006).

[210] De Luca, M. and Zardo, I. Semiconductor Nanowires: Raman Spectroscopy Studies. In *Raman Spectroscopy and Applications*, pages 81–101. InTech (2017). ISBN 9789537619343. 65

[211] Maultzsch, J., Telg, H., Reich, S., and Thomsen, C. Radial breathing mode of single-walled carbon nanotubes: Optical transition energies and chiral-index assignment. *Physical Review B*, **72**, 205438 (2005). 66

[212] Jorio, A., Pimenta, M.A., Filho, A.G.S., Saito, R., Dresselhaus, G., and Dresselhaus, M.S. Characterizing carbon nanotube samples with resonance Raman scattering. *New Journal of Physics*, **5**, 139 (2003). 66, 91

[213] Hempel, H., Unold, T., and Eichberger, R. Measurement of charge carrier mobilities in thin films on metal substrates by reflection time resolved terahertz spectroscopy. *Optics Express*, **25**, 17227 (2017). 69

[214] Hempel, H., Redinger, A., Repins, I., Moisan, C., Larramona, G., Dennler, G., Handwerg, M., Fischer, S.F., Eichberger, R., and Unold, T. Intragrain charge transport in kesterite thin filmsLimits arising from carrier localization. *Journal of Applied Physics*, **120**, 175302 (2016). 69

[215] Cunningham, P.D. and Hayden, L.M. Carrier Dynamics Resulting from Above and Below Gap Excitation of P3HT and P3HT/PCBM Investigated by Optical-Pump Terahertz-Probe Spectroscopy. *The Journal of Physical Chemistry C*, **112**, 7928 (2008). 70

[216] Zajac, V., Němec, H., Kadlec, C., Ksová, K., Pelant, I., and Kužel, P. THz photoconductivity in light-emitting surface-oxidized Si nanocrystals: the role of large particles. *New Journal of Physics*, **16**, 093013 (2014).

[217] Xiao, Y., Zhai, Z.H., Shi, Q.W., Zhu, L.G., Li, J., Huang, W.X., Yue, F., Hu, Y.Y., Peng, Q.X., and Li, Z.R. Ultrafast terahertz modulation characteristic of tungsten doped vanadium dioxide nanogranular film revealed by time-resolved terahertz spectroscopy. *Applied Physics Letters*, **107**, 031906 (2015).

[218] Ziwritsch, M., Müller, S., Hempel, H., Unold, T., Abdi, F.F., van de Krol, R., Friedrich, D., and Eichberger, R. Direct Time-Resolved Observation of Carrier Trapping and Polaron Conductivity in $BiVO_4$. *ACS Energy Letters*, **1**, 888 (2016).

[219] Strothkämper, C., Schwarzburg, K., Schütz, R., Eichberger, R., and Bartelt, A. Multiple-Trapping Governed Electron Transport and Charge Separation in ZnO/In_2S_3 Core/Shell Nanorod Heterojunctions. *The Journal of Physical Chemistry C*, **116**, 1165 (2012).

[220] Němec, H., Nienhuys, H.K., Perzon, E., Zhang, F., Inganäs, O., Kužel, P., and Sundström, V. Ultrafast conductivity in a low-band-gap polyphenylene and fullerene blend studied by terahertz spectroscopy. *Physical Review B*, **79**, 245326 (2009).

[221] Němec, H., Fekete, L., Kadlec, F., Kužel, P., Martin, M., Mangeney, J., Delagnes, J.C., and Mounaix, P. Ultrafast carrier dynamics in Br^+-bombarded InP studied by time-resolved terahertz spectroscopy. *Physical Review B*, **78**, 235206 (2008).

[222] Strothkämper, C., Bartelt, A., Sippel, P., Hannappel, T., Schütz, R., and Eichberger, R. Delayed Electron Transfer through Interface States in Hybrid ZnO/Organic-Dye Nanostructures. *The Journal of Physical Chemistry C*, **117**, 17901 (2013).

[223] Nemec, H., Zajac, V., Rychetsky, I., Fattakhova-Rohlfing, D., Mandlmeier, B., Bein, T., Mics, Z., and Kuzel, P. Charge Transport in TiO_2 Films With Complex Percolation Pathways Investigated by Time-Resolved Terahertz Spectroscopy. *IEEE Transactions on Terahertz Science and Technology*, **3**, 302 (2013).

[224] Liu, H.W., Wong, L.M., Wang, S.J., Tang, S.H., and Zhang, X.H. Ultrafast insulatormetal phase transition in vanadium dioxide studied using optical pumpterahertz probe spectroscopy. *Journal of Physics: Condensed Matter*, **24**, 415604 (2012).

[225] Němec, H., Nienhuys, H.K., Zhang, F., Inganas, O., Yartsev, A., and Sundström, V. Charge carrier dynamics in alternating polyfluorene copolymer: Fullerene blends probed by terahertz spectroscopy. *Journal of Physical Chemistry C*, **112**, 6558 (2008).

[226] Cunningham, P.D. Accessing Terahertz Complex Conductivity Dynamics in the Time-Domain. *IEEE Transactions on Terahertz Science and Technology*, **3**, 494 (2013).

[227] Jnawali, G., Rao, Y., Yan, H., and Heinz, T.F. Observation of a transient decrease in terahertz conductivity of single-layer graphene induced by ultrafast optical excitation. *Nano letters*, **13**, 524 (2013).

[228] Terashige, T., Yada, H., Matsui, Y., Miyamoto, T., Kida, N., and Okamoto, H. Temperature and carrier-density dependence of electron-hole scattering in silicon investigated by optical-pump terahertz-probe spectroscopy. *Physical Review B*, **91**, 241201 (2015).

[229] Yettapu, G.R., Talukdar, D., Sarkar, S., Swarnkar, A., Nag, A., Ghosh, P., and Mandal, P. Terahertz Conductivity within Colloidal $CsPbBr_3$ Perovskite Nanocrystals: Remarkably High Carrier Mobilities and Large Diffusion Lengths. *Nano Letters*, **16**, 4838 (2016).

[230] Lui, K.P.H. and Hegmann, F.A. Ultrafast carrier relaxation in radiation-damaged silicon on sapphire studied by optical-pump terahertz-probe experiments. *Applied Physics Letters*, **78**, 3478 (2001).

[231] Prasankumar, R.P., Scopatz, A., Hilton, D.J., Taylor, A.J., Averitt, R.D., Zide, J.M., and Gossard, A.C. Carrier dynamics in self-assembled ErAs nanoislands embedded in GaAs measured by optical-pump terahertz-probe spectroscopy. *Applied Physics Letters*, **86**, 201107 (2005).

[232] Minami, Y., Horiuchi, K., Masuda, K., Takeda, J., and Katayama, I. Terahertz dielectric response of photoexcited carriers in Si revealed via single-shot optical-pump and terahertz-probe spectroscopy. *Applied Physics Letters*, **107**, 171104 (2015). 70

[233] Hendry, E., Koeberg, M., Schins, J.M., Nienhuys, H.K., Sundström, V., Siebbeles, L.D.A., and Bonn, M. Interchain effects in the ultrafast photophysics of a semiconducting polymer: THz time-domain spectroscopy of thin films and isolated chains in solution. *Physical Review B - Condensed Matter and Materials Physics*, **71**, 1 (2005). 70, 77

[234] Hendry, E., Koeberg, M., O'Regan, B., and Bonn, M. Local field effects on electron transport in nanostructured TiO_2 revealed by terahertz spectroscopy. *Nano Letters*, **6**, 755 (2006). 77

[235] Shan, J., Wang, F., Knoesel, E., Bonn, M., and Heinz, T.F. Measurement of the frequency-dependent conductivity in sapphire. *Physical review letters*, **90**, 247401 (2003). 70

[236] Zhang, W., Zeng, X., Su, X., Zou, X., Mante, P.A., Borgström, M.T., and Yartsev, A. Carrier Recombination Processes in Gallium Indium Phosphide Nanowires. *Nano Letters*, **17**, 4248 (2017). 70

[237] Bergren, M.R., Kendrick, C.E., Neale, N.R., Redwing, J.M., Collins, R.T., Furtak, T.E., and Beard, M.C. Ultrafast Electrical Measurements of Isolated Silicon Nanowires and Nanocrystals. *The Journal of Physical Chemistry Letters*, **5**, 2050 (2014).

[238] Parkinson, P., Dodson, C., Joyce, H.J., Bertness, K.A., Sanford, N.A., Herz, L.M., and Johnston, M.B. Noncontact Measurement of Charge Carrier Lifetime and Mobility in GaN Nanowires. *Nano Letters*, **12**, 4600 (2012). 123

[239] Němec, H., Kužel, P., and Sundström, V. Charge transport in nanostructured materials for solar energy conversion studied by time-resolved terahertz spectroscopy. *Journal of Photochemistry and Photobiology A: Chemistry*, **215**, 123 (2010).

[240] Němec, H., Nienhuys, H.K., Perzon, E., Zhang, F., Inganäs, O., Kužel, P., and Sundström, V. Ultrafast conductivity in a low-band-gap polyphenylene and fullerene blend studied by terahertz spectroscopy. *Physical Review B*, **79**, 245326 (2009).

[241] Fekete, L., Kužel, P., Němec, H., Kadlec, F., Dejneka, A., Stuchlík, J., and Fejfar, A. Ultrafast carrier dynamics in microcrystalline silicon probed by time-resolved terahertz spectroscopy. *Physical Review B*, **79**, 115306 (2009). 70

[242] Pedrotti, F.L., Pedrotti, L.M., and Pedrotti, L.S. *Introduction to Optics: International Edition*. Pearson, third edition (2006). ISBN 9780131971332. 71

[243] Knoesel, E., Bonn, M., Shan, J., Wang, F., and Heinz, T.F. Conductivity of solvated electrons in hexane investigated with terahertz time-domain spectroscopy. *Journal of Chemical Physics*, **121**, 394 (2004). 76, 77

[244] Naftaly, M. and Miles, R.E. Terahertz time-domain spectroscopy for material characterization. *Proceedings of the IEEE*, **95**, 1658 (2007). 79

[245] Brosseau, F. and Brosseau, C. A review and analysis of microwave absorption in polymer composites filled with carbonaceous particles. *Journal of Applied Physics*, **111**, 061301 (2012). 84

[246] Hartmann, R.R., Kono, J., and Portnoi, M.E. Terahertz science and technology of carbon nanomaterials. *Nanotechnology*, **25**, 322001 (2014). 84

[247] Shuba, M.V., Paddubskaya, A.G., Kuzhir, P.P., Maksimenko, S.A., Flahaut, E., Fierro, V., Celzard, A., and Valusis, G. Short-length carbon nanotubes as building blocks for high dielectric constant materials in the terahertz range. *Journal of Physics D: Applied Physics*, **50**, 08LT01 (2017). 84

[248] Bommeli, F., Degiorgi, L., Wachter, P., Bacsa, W.S., de Heer, W.A., and Forro, L. The optical response of carbon nanotubes. *Synthetic Metals*, **86**, 2307 (1997). 84, 106

[249] Kampfrath, T., von Volkmann, K., Aguirre, C.M., Desjardins, P., Martel, R., Krenz, M., Frischkorn, C., Wolf, M., and Perfetti, L. Mechanism of the Far-Infrared Absorption of Carbon-Nanotube Films. *Phys. Rev. Lett.*, **101**, 267403 (2008). 84, 85, 94, 106, 113, 119, 136

[250] Ugawa, A., Rinzler, A.G., and Tanner, D.B. Far-infrared gaps in single-wall carbon nanotubes. *Phys. Rev. B*, **60**, R11305 (1999). 84, 85, 94, 99, 103, 106, 136

[251] Akima, N., Iwasa, Y., Brown, S., Barbour, A., Cao, J., Musfeldt, J., Matsui, H., Toyota, N., Shiraishi, M., Shimoda, H., and Zhou, O. Strong anisotropy in the far-infrared absorption spectra of stretch-aligned single-walled carbon nanotubes. *Advanced Materials*, **18**, 1166 (2006). 84, 106

[252] Slepyan, G.Y., Shuba, M.V., Maksimenko, S.A., and Lakhtakia, A. Theory of optical scattering by achiral carbon nanotubes and their potential as optical nanoantennas. *Phys. Rev. B*, **73**, 195416 (2006). 84, 86, 94, 106

[253] Slepyan, G.Y., Shuba, M.V., Maksimenko, S.A., Thomsen, C., and Lakhtakia, A. Terahertz conductivity peak in composite materials containing carbon nanotubes: Theory and interpretation of experiment. *Phys. Rev. B*, **81**, 205423 (2010). 84, 85, 86, 94, 96, 106, 113, 118

[254] Shuba, M.V., Paddubskaya, A.G., Plyushch, A.O., Kuzhir, P.P., Slepyan, G.Y., Maksimenko, S.A., Ksenevich, V.K., Buka, P., Seliuta, D., Kasalynas, I., MacUtkevic, J., Valusis, G., Thomsen, C., and Lakhtakia, A. Experimental evidence of localized plasmon resonance in composite materials containing single-wall carbon nanotubes. *Physical Review B - Condensed Matter and Materials Physics*, **85**, 165435 (2012). 84, 85, 94, 96, 106, 107, 112, 113

[255] Zhang, Q., Hároz, E.H., Jin, Z., Ren, L., Wang, X., Arvidson, R.S., Lüttge, A., and Kono, J. Plasmonic nature of the terahertz conductivity peak in single-wall carbon nanotubes. *Nano letters*, **13**, 5991 (2013). 84, 94, 96, 97, 99, 103, 106, 108, 112, 136

[256] Kim, B., Lee, J., and Yu, I. Electrical properties of single-wall carbon nanotube and epoxy composites. *Journal of Applied Physics*, **94**, 6724 (2003). 84, 100, 106

[257] Xu, X., Chuang, K., Nicholas, R.J., Johnston, M.B., and Herz, L.M. Terahertz excitonic response of isolated single-walled carbon nanotubes. *Journal of Physical Chemistry C*, **113**, 18106 (2009). 106, 108, 109, 113, 119, 136

[258] Wen, B., Cao, M.S., Hou, Z.L., Song, W.L., Zhang, L., Lu, M.M., Jin, H.B., Fang, X.Y., Wang, W.Z., and Yuan, J. Temperature dependent microwave attenuation behavior for carbon-nanotube/silica composites. *Carbon*, **65**, 124 (2013). 84, 100

[259] Borondics, F., Kamarás, K., Nikolou, M., Tanner, D.B., Chen, Z.H., and Rinzler, A.G. Charge dynamics in transparent single-walled carbon nanotube films from optical transmission measurements. *Physical Review B*, **74**, 045431 (2006). 84, 94, 97, 99, 103, 106, 136

[260] Thirunavukkuarasu, K., Hennrich, F., Kamarás, K., and Kuntscher, C.A. Infrared spectroscopic studies on unoriented single-walled carbon nanotube films under hydrostatic pressure. *Phys. Rev. B*, **81**, 1 (2010).

[261] Morimoto, T., Ichida, M., Ikemoto, Y., and Okazaki, T. Temperature dependence of plasmon resonance in single-walled carbon nanotubes. *Phys. Rev. B*, **93**, 195409 (2016). 84

[262] Xu, H., Anlage, S.M., Hu, L., and Gruner, G. Microwave shielding of transparent and conducting single-walled carbon nanotube films. *Applied Physics Letters*, **90**, 3 (2007). 84, 99, 103, 136

[263] Shuba, M.V., Paddubskaya, A.G., Kuzhir, P.P., Maksimenko, S.A., Valusis, G., Poklonski, N.A., Bellucci, S., Kenanakis, G., and Kafesaki, M. Temperature induced modification of the mid-infrared response of single-walled carbon nanotubes. *Journal of Applied Physics*, **119**, 104303 (2016). 84, 87, 88, 96

[264] Kampfrath, T., Perfetti, L., von Volkmann, K., Aguirre, C.M., Desjardins, P., Martel, R., Frischkorn, C., and Wolf, M. Optical response of single-wall carbon nanotube sheets in the far-infrared spectral range from 1 THz to 40 THz. *Physica Status Solidi (B) Basic Research*, **244**, 3950 (2007). 85

[265] Nishimura, H., Minami, N., and Shimano, R. Dielectric properties of single-walled carbon nanotubes in the terahertz frequency range. *Applied Physics Letters*, **91**, 2005 (2007). 85, 106

[266] Waterman, P.C. and Truell, R. Multiple Scattering of Waves. *Journal of Mathematical Physics*, **2**, 512 (1961). 85

[267] Lakhtakia, A. Application of the Waterman-Truell approach for chiral composites. *International Journal of Electronics*, **75**, 1243 (1993). 85

[268] Nemilentsau, A.M., Shuba, M.V., Slepyan, G.Y., Kuzhir, P.P., Maksimenko, S.A., D'yachkov, P.N., and Lakhtakia, A. Substitutional doping of carbon nanotubes to control their electromagnetic characteristics. *Phys. Rev. B*, **82**, 235424 (2010). 86, 88

[269] Slepyan, G.Y., Maksimenko, S.A., Lakhtakia, A., Yevtushenko, O., and Gusakov, A.V. Electrodynamics of carbon nanotubes: Dynamic conductivity, impedance boundary conditions, and surface wave propagation. *Phys. Rev. B*, **60**, 17136 (1999). 86, 115

[270] Zhou, X., Park, J.Y., Huang, S., Liu, J., and McEuen, P.L. Band structure, phonon scattering, and the performance limit of single-walled carbon nanotube transistors. *Phys. Rev. Lett.*, **95**, 146805 (2005). 87

[271] Kane, C.L., Mele, E.J., Lee, R.S., Fischer, J.E., Petit, P., Dai, H., Thess, A., Smalley, R.E., Verschueren, A.R.M., Tans, S.J., and Dekker, C. Temperature-dependent resistivity of single-wall carbon nanotubes. *Europhysics Letters (EPL)*, **41**, 683 (1998). 88, 98, 102

[272] Zhou, X., Park, J.Y., Huang, S., Liu, J., and McEuen, P.L. Band Structure, Phonon Scattering, and the Performance Limit of Single-Walled Carbon Nanotube Transistors. *Phys. Rev. Lett.*, **95**, 146805 (2005). 88, 98, 102, 115

[273] Shuba, M.V., Maksimenko, S.A., and Lakhtakia, A. Electromagnetic wave propagation in an almost circular bundle of closely packed metallic carbon nanotubes. *Phys. Rev. B*, **76**, 155407 (2007). 88

[274] Nasibulin, A.G., Kaskela, A., Mustonen, K., Anisimov, A.S., Ruiz, V., Kivistö, S., Rackauskas, S., Timmermans, M.Y., Pudas, M., Aitchison, B., Kauppinen, M., Brown, D.P., Okhotnikov, O.G., and Kauppinen, E.I. Multifunctional free-standing single-walled carbon nanotube films. *ACS Nano*, **5**, 3214 (2011). 89

[275] Tian, Y., Timmermans, M.Y., Kivistö, S., Nasibulin, A.G., Zhu, Z., Jiang, H., Okhotnikov, O.G., and Kauppinen, E.I. Tailoring the diameter of single-walled carbon nanotubes for optical applications. *Nano Research*, **4**, 807 (2011). 89

[276] (2009). Standard test method for measuring relative complex permittivity and relative magnetic permeability of solid materials at microwave frequencies, ASTM D5568-08, 2009. 94

[277] Chung, B.K. Dielectric constant measurement for thin material at microwave frequencies. *Progress In Electromagnetics Research*, **75**, 239 (2007).

[278] Paddubskaya, A., Valynets, N., Kuzhir, P., Batrakov, K., Maksimenko, S., Kotsilkova, R., Velichkova, H., Petrova, I., Biró, I., Kertész, K., Márk,

G.I., Horváth, Z.E., and Biró, L.P. Electromagnetic and thermal properties of three-dimensional printed multilayered nano-carbon/poly(lactic) acid structures. *Journal of Applied Physics*, **119**, 135102 (2016). 94

[279] Suzuura, H. and Ando, T. Phonons and electron-phonon scattering in carbon nanotubes. *Phys. Rev. B*, **65**, 235412 (2002). 98

[280] Pennington, G., Goldsman, N., Akturk, A., and Wickenden, A.E. Deformation potential carrier-phonon scattering in semiconducting carbon nanotube transistors. *Applied Physics Letters*, **90** (2007). 98

[281] Philipp, H.R. Infrared optical properties of graphite. *Phys. Rev. B*, **16**, 2896 (1977). 98

[282] Gau, C., Kuo, C.Y., and Ko, H.S. Electron tunneling in carbon nanotube composites. *Nanotechnology*, **20**, 395705 (2009). 100

[283] Ounaies, Z., Park, C., Wise, K.E., Siochi, E.J., and Harrison, J.S. Electrical properties of single wall carbon nanotube reinforced polyimide composites. *Composites Science and Technology*, **63**, 1637 (2003). 100

[284] Lubineau, G., Mora, A., Han, F., Odeh, I., and Yaldiz, R. A morphological investigation of conductive networks in polymers loaded with carbon nanotubes. *Computational Materials Science*, **130**, 21 (2017). 100

[285] Li, N., Huang, Y., Du, F., He, X., Lin, X., Gao, H., Ma, Y., Li, F., Chen, Y., and Eklund, P.C. Electromagnetic Interference (EMI) shielding of single-walled carbon nanotube epoxy composites. *Nano Letters*, **6**, 1141 (2006). 100

[286] Gong, S., Zhu, Z.H., and Haddad, E.I. Modeling electrical conductivity of nanocomposites by considering carbon nanotube deformation at nanotube junctions. *Journal of Applied Physics*, **114**, 074303 (2013). 100

[287] Naffakh, M., Diez-Pascual, A.M., and Gomez-Fatou, M.A. New hybrid nanocomposites containing carbon nanotubes, inorganic fullerene-like ws2 nanoparticles and poly(ether ether ketone) (peek). *J. Mater. Chem.*, **21**, 7425 (2011). 100

[288] Dez-Pascual, A.M., Naffakh, M., Marco, C., and Ellis, G. Rheological and tribological properties of carbon nanotube/thermoplastic nanocomposites incorporating inorganic fullerene-like ws2 nanoparticles. *The Journal of Physical Chemistry B*, **116**, 7959 (2012). PMID: 22697425. 100

[289] Battisti, A., Skordos, A.A., and Partridge, I.K. Percolation threshold of carbon nanotubes filled unsaturated polyesters. *Composites Science and Technology*, **70**, 633 (2010). 100

[290] Sandler, J., Kirk, J., Kinloch, I., Shaffer, M., and Windle, A. Ultra-low electrical percolation threshold in carbon-nanotube-epoxy composites. *Polymer*, **44**, 5893 (2003). 100

[291] Peters, O., Busch, S.F., Fischer, B.M., and Koch, M. Determination of the Carbon Nanotube Concentration and Homogeneity in Resin Films by THz Spectroscopy and Imaging. *Journal of Infrared, Millimeter, and Terahertz Waves*, **33**, 1221 (2012). 100

[292] Beard, M.C., Blackburn, J.L., and Heben, M.J. Photogenerated Free Carrier Dynamics in Metal and Semiconductor Single-Walled Carbon Nanotube Films. *Nano*, **8**, 2 (2008). 106, 108, 113, 119, 136

[293] Perfetti, L., Kampfrath, T., Schapper, F., Hagen, A., Hertel, T., Aguirre, C.M., Desjardins, P., Martel, R., Frischkorn, C., and Wolf, M. Ultrafast Dynamics of Delocalized and Localized Electrons in Carbon Nanotubes. *Physical Review Letters*, **96**, 027401 (2006). 106, 109

[294] Jensen, S.A., Ulbricht, R., Narita, A., Feng, X., Müllen, K., Hertel, T., Turchinovich, D., and Bonn, M. Ultrafast photoconductivity of graphene nanoribbons and carbon nanotubes. *Nano letters*, **13**, 5925 (2013). 106, 109, 113, 119, 136

[295] Morimoto, T., Joung, S.K., Saito, T., Futaba, D.N., Hata, K., and Okazaki, T. Length-dependent plasmon resonance in single-walled carbon nanotubes. *ACS nano*, **8**, 9897 (2014). 106

[296] Falk, A.L., Chiu, K.C., Farmer, D.B., Cao, Q., Tersoff, J., Lee, Y.H., Avouris, P., and Han, S.J. Coherent Plasmon and Phonon-Plasmon Resonances in Carbon Nanotubes. *Physical Review Letters*, **118**, 257401 (2017). 106

[297] Lauret, J.S., Voisin, C., Cassabois, G., Delalande, C., Roussignol, P., Jost, O., and Capes, L. Ultrafast carrier dynamics in single-wall carbon nanotubes. *Physical review letters*, **90**, 057404 (2003). 109

[298] Wang, F., Dukovic, G., Knoesel, E., Brus, L.E., and Heinz, T.F. Observation of rapid Auger recombination in optically excited semiconducting carbon nanotubes. *Physical Review B*, **70**, 241403 (2004). 109

[299] Karlsen, P., Shuba, M., Beckerleg, C., Yuko, D., Kuzhir, P., Maksimenko, S.A., Ksenevich, V., Viet, H., Nasibulin, A., Tenne, R., and Hendry, E. Influence of nanotube length and density on the plasmonic terahertz response of single-walled carbon nanotubes. *Journal of Physics D: Applied Physics* (2017). 113, 115, 123, 129, 133, 137

[300] Hertel, T. and Moos, G. Electron-Phonon Interaction in Single-Wall Carbon Nanotubes: A Time-Domain Study. *Physical Review Letters*, **84**, 5002 (2000). 114

[301] Moos, G., Fasel, R., and Hertel, T. Temperature Dependence of Electron-to- Lattice Energy Transfer in Single-Wall Carbon Nanotube Bundles. *Journal of nanoscience and nanotechnology*, **3**, 145 (2002). 114

[302] Kampfrath, T., Perfetti, L., Schapper, F., Frischkorn, C., and Wolf, M. Strongly Coupled Optical Phonons in the Ultrafast Dynamics of the Electronic Energy and Current Relaxation in Graphite. *Physical Review Letters*, **95**, 187403 (2005). 114, 115

[303] Thummavichai, K., Xia, Y., and Zhu, Y. Recent progress in chromogenic research of tungsten oxides towards energy-related applications. *Progress in Materials Science*, **88**, 281 (2017). 121

[304] Thummavichai, K., Trimby, L., Wang, N., Wright, C.D., Xia, Y., and Zhu, Y. Low Temperature Annealing Improves the Electrochromic and Degradation Behavior of Tungsten Oxide (WO_x) Thin Films. *The Journal of Physical Chemistry C*, **121**, 20498 (2017). 121, 124, 125

[305] Joyce, H.J., Docherty, C.J., Gao, Q., Tan, H.H., Jagadish, C., Lloyd-Hughes, J., Herz, L.M., and Johnston, M.B. Electronic properties of GaAs, InAs and InP nanowires studied by terahertz spectroscopy. *Nanotechnology*, **24**, 214006 (2013). 123, 128, 129, 131, 133, 137

[306] Joyce, H.J., Parkinson, P., Jiang, N., Docherty, C.J., Gao, Q., Tan, H.H., Jagadish, C., Herz, L.M., and Johnston, M.B. Electron Mobilities Approaching Bulk Limits in "Surface-Free" GaAs Nanowires. *Nano letters*, **14**, 5989 (2014).

[307] Boland, J.L., Conesa-Boj, S., Parkinson, P., Ttncoglu, G., Matteini, F., Rffer, D., Casadei, A., Amaduzzi, F., Jabeen, F., Davies, C.L., Joyce, H.J., Herz, L.M., Fontcuberta i Morral, A., and Johnston, M.B. Modulation

doping of gaas/algaas coreshell nanowires with effective defect passivation and high electron mobility. *Nano Letters*, **15**, 1336 (2015). PMID: 25602841. 123

[308] Regan, K.P., Koenigsmann, C., Sheehan, S.W., Konezny, S.J., and Schmuttenmaer, C.A. Size-Dependent Ultrafast Charge Carrier Dynamics of WO_3 for Photoelectrochemical Cells. *The Journal of Physical Chemistry C*, **120**, 14926 (2016). 123, 128, 133, 137

[309] Bedja, I., Hotchandani, S., and Kamat, P.V. Photoelectrochemistry of quantized tungsten trioxide colloids: electron storage, electrochromic, and photoelectrochromic effects. *The Journal of Physical Chemistry*, **97**, 11064 (1993). 128

[310] Pesci, F.M., Cowan, A.J., Alexander, B.D., Durrant, J.R., and Klug, D.R. Charge Carrier Dynamics on Mesoporous WO_3 during Water Splitting. *The Journal of Physical Chemistry Letters*, **2**, 1900 (2011).

[311] Grigioni, I., Stamplecoskie, K.G., Selli, E., and Kamat, P.V. Dynamics of Photogenerated Charge Carriers in $WO_3/BiVO_4$ Heterojunction Photoanodes. *The Journal of Physical Chemistry C*, **119**, 20792 (2015). 123

[312] Pol, S.V., Pol, V.G., Kessler, V.G., Seisenbaeva, G.A., Solovyov, L.A., and Gedanken, A. Synthesis of WO_3 Nanorods by Reacting $WO(OMe)_4$ under Autogenic Pressure at Elevated Temperature Followed by Annealing. *Inorganic Chemistry*, **44**, 9938 (2005). 124, 125

[313] Xu, F., Wang, N., Chang, H., Xia, Y., and Zhu, Y. Continuous Production of IF-WS_2 Nanoparticles by a Rotary Process. *Inorganics*, **2**, 313 (2014). 124

[314] Patil, P.S., Patil, P.R., and Ennaoui, E.A. Characterization of ultrasonic spray pyrolyzed tungsten oxide thin films. *Thin Solid Films*, **370**, 38 (2000). 128

[315] Parkinson, P., Joyce, H.J., Gao, Q., Tan, H.H., Zhang, X., Zou, J., Jagadish, C., Herz, L.M., and Johnston, M.B. Carrier Lifetime and Mobility Enhancement in Nearly Defect-Free Core- Shell Nanowires Measured Using Time-Resolved Terahertz Spectroscopy. *Nano Letters*, **9**, 3349 (2009). 128, 131, 133, 137

[316] Vemuri, R., Bharathi, K.K., Gullapalli, S., and Ramana, C. Effect of Structure and Size on the Electrical Properties of Nanocrystalline WO_3 Films. *ACS Applied Materials & Interfaces*, **2**, 2623 (2010). 129

[317] Zhang, T.F., Li, Z.P., Wang, J.Z., Kong, W.Y., Wu, G.A., Zheng, Y.Z., Zhao, Y.W., Yao, E.X., Zhuang, N.X., and Luo, L.B. Broadband photodetector based on carbon nanotube thin film/single layer graphene Schottky junction. *Scientific Reports*, **6**, 38569 (2016). 136

[318] Docherty, C.J., Stranks, S.D., Habisreutinger, S.N., Joyce, H.J., Herz, L.M., Nicholas, R.J., and Johnston, M.B. An ultrafast carbon nanotube terahertz polarisation modulator. *J. Appl. Phys.*, **115**, 203108 (2014). 136